Faculty of Fundamental Problems of Technology
Wrocław University of Science and Technology

Beyond Lead: Pressure-Induced Electronic Tunability and Excitonic Control in 2D Tin and Copper Metal Halide Perovskites

Rafał Bartoszewicz

**Ph.D. thesis prepared
under the supervision of**

Prof. dr hab. inż. Robert Kudrawiec

Dr inż. Artur Herman

Wrocław 2026

I would like to express my sincere gratitude to my supervisor, Prof. Robert Kudrawiec, for his invaluable guidance, support, and patience throughout the preparation of this dissertation. His expertise and insightful feedback were essential to the completion of this work.

I am also deeply grateful to my co-supervisor, Dr. Artur Herman, for his constructive advice, and continuous support, both within and beyond the university environment. His encouragement helped me persevere through the most challenging stages of this research. Over the years, I have also come to value his friendship greatly.

I would like to thank my colleagues at the Department of Semiconductor Materials Engineering for their assistance and for creating a friendly and inspiring working environment. I am especially grateful to Dr. Jakub Ziembicki, Miłosz Rybak and Kamil Misztal with whom I shared many memorable moments both inside and outside the university.

Finally, I wish to express my heartfelt thanks to my family for their unwavering support, patience, and encouragement throughout the course of my doctoral thesis.

Streszczenie

Badania przedstawione w niniejszej rozprawie doktorskiej stanowią systematyczną analizę właściwości strukturalnych i elektronowych bezołowiowych, dwuwymiarowych (2D) hybrydowych organicznych-nieorganicznych perowskitów (Hybrid Organic-Inorganic Perovskites, HOIPs) w warunkach zmiennej temperatury oraz zmiennego ciśnienia hydrostatycznego. Zastępując dotychczas badane ołowiowe perowskity, które są toksyczne, alternatywnymi materiałami zawierającymi kationy Sn^{2+} oraz Cu^{2+}, wykazano, że wrodzona miękkość sieci krystalicznej tych materiałów może zostać wykorzystana do uzyskania szerokiej kontroli nad ich właściwościami optoelektronicznymi. Głównym celem pracy było zrozumienie wzajemnych zależności pomiędzy dynamiką sieci krystalicznej, szerokością pasma elektronowego oraz lokalizacją ekscytonów w warunkach ciśnienia hydrostatycznego sięgającego $\sim$11 GPa oraz temperatur w zakresie od 20 do 320 K.

Rozdział pierwszy przedstawia koncepcyjne oraz teoretyczne podstawy rozprawy, wraz z hipotezą badawczą. Omówiono w nim fundamentalne aspekty strukturalne HOIPs, ze szczególnym uwzględnieniem roli elastyczności oktaedrów oraz hybrydyzacji orbitali w kształtowaniu struktury pasmowej. Szczególną uwagę poświęcono hipotezie badawczej zakładającej, że miękkość sieci krystalicznej determinuje konkurencję pomiędzy poszerzaniem szerokości pasma elektronowego a energią relaksacji sieci. W rozdziale tym zidentyfikowano również kluczowe nierozwiązane problemy w tym obszarze, takie jak sprzeczne trendy zmian przerwy energetycznej pod wpływem ciśnienia czy stabilność ekscytonów samouwięzionych (self-trapped excitons, STEs) w warunkach silnej kompresji, co stanowi teoretyczną podstawę interpretacji wyników eksperymentalnych.

Rozdział drugi opisuje metody eksperymentalne zastosowane w badaniach tych materiałów. Przedstawiono integrację kowadła diamentowego z napędem membranowym (diamond anvil cell, DAC) z kriostatem helowym typu closed-cycle, co umożliwia precyzyjną kontrolę parametrów termodynamicznych. Istotna część rozdziału poświęcona jest systematycznej charakterystyce medium transmitującego ciśnienie Daphne 7575 oraz wyznaczeniu jego granic hydrostatyczności do temperatury 40 K. Omówiono również rygorystyczne procedury kalibracyjne zastosowane w pracy, obejmujące fluorescencję rubinu skorygowaną o wpływ temperatury oraz wzajemną weryfikację wyników uzyskanych metodami spektroskopii odbiciowej (R), transmisyjnej oraz fotoluminescencyjnej (PL), co umożliwiło wyznaczenie wrodzonych parametrów badanych materiałów.

Rozdział trzeci obejmuje cztery recenzowane artykuły naukowe prezentujące główne wyniki badań przeprowadzonych w ramach niniejszej pracy.

W badaniach przedstawionych w sekcji 3.1 oraz 3.2 analizowana jest możliwość strojenia właściwości elektronowych jodkowych perowskitów opartych na cynie, w szczególności $(4FP)_2SnI_4$ oraz TMA_2SnI_4. Wykazano, że układy zawierające Sn charakte-

ryzują się rekordowo wysokimi współczynnikami ciśnieniowymi, osiągającymi wartości do -187 meV/GPa, znacznie przewyższającymi analogiczne układy oparte na ołowiu. Uzyskane wyniki wskazują na liniowe zawężenie przerwy energetycznej do momentu przejścia fazowego, co czyni te kryształy obiecującymi materiałami do zastosowań w wysokoczułych optycznych sensorach ciśnienia.

Badania przedstawione w sekcji 3.3 dotyczą złożonej natury ekscytonów w związku $(4FPEA)_2SnBr_4$. Zaobserwowano wyraźny podział zachowania stanów ekscytonowych: podczas gdy emisja w pobliżu krawędzi pasma przesuwa się ku niższym energiom pod wpływem kompresji, emisja ekscytonów samouwięzionych wykazuje anomalne przesunięcie ku wyższym energiom. Wyniki te dostarczają mikroskopowego opisu mechanizmu powstawania małych polaronów, wskazując, że sztywność sieci krystalicznej zależna od rodzaju halogenku oraz ekranowanie dielektryczne determinują stabilizację zlokalizowanych i zdelokalizowanych stanów ekscytonowych.

Sekcja 3.4 poświęcona jest badaniu perowskitów opartych na miedzi, w szczególności $(PMA)_2CuX_4$ (X= Cl, Br). Praca ta podejmuje zagadnienie stabilności termodynamicznej tych materiałów oraz przedstawia porównawczą analizę efektów termochromizmu i piezochromizmu. Wykazano, że zarówno zmiany temperatury, jak i ciśnienia prowadzą do istotnych przesunięć widmowych ku niższym energiom, jednak mechanizmy odpowiedzialne za te zjawiska, rozszerzalność cieplna w przypadku temperatury oraz kompresja mechaniczna w przypadku ciśnienia, oddziałują z układem elektron-fonon w odmienny sposób, wpływając na stabilność strukturalną materiału pod wpływem ciśnienia dochodzącego do 11 GPa.

W końcowej części rozprawy przedstawiono syntetyczne podsumowanie uzyskanych wyników oraz sformułowano ogólne wnioski dotyczące perspektyw rozwoju optoelektroniki reagującej na bodźce zewnętrzne takie jak, temperatura i ciśnienie hydrostatyczne.

Podsumowując, niniejsza rozprawa dostarcza spójnego opisu zależności pomiędzy zaburzeniami mechanicznymi, strukturą elektronową oraz właściwościami ekscytonowymi w wybranych bezołowiowych dwuwymiarowych perowskitach. Uzyskane rezultaty stanowią istotny wkład w rozwój fizyki półprzewodników, wskazując, że miękkość sieci krystalicznej, często postrzegana jako ograniczenie, może być traktowana jako regulowany stopień swobody w inżynierii stanów kwantowych oraz projektowaniu nowej generacji adaptacyjnych urządzeń optoelektronicznych.

Abstract

The research presented in this dissertation provides a comprehensive investigation into the structural and electronic landscapes of Pb-free, two-dimensional (2D) hybrid organic-inorganic perovskites (HOIPs) under various temperatures and hydrostatic pressures. By replacing previously studied toxic Pb-based systems with Sn^{2+} and Cu^{2+} alternatives, this work demonstrates how the inherent lattice softness of these materials can be exploited to achieve unprecedented control over their optoelectronic properties. The primary objective is to understand the interplay between lattice dynamics, electronic bandwidth, and exciton localization when subjected to hydrostatic pressures up to $\sim$11 GPa and temperatures ranging from 20 to 320 K.

Chapter 1 establishes the conceptual and theoretical framework of the dissertation, including hypothesis. It introduces the structural fundamentals of HOIPs, emphasizing the consequences of octahedral flexibility and orbital hybridization for band structure formation. Particular attention is given to the scientific hypothesis that lattice softness governs the competition between electronic bandwidth broadening and lattice relaxation energy. This chapter identifies key unresolved questions in the field, such as contradictory pressure-dependent band gap trends and the stability of self-trapped excitons (STEs) under extreme compression, providing the theoretical foundation necessary to interpret the experimental results.

Chapter 2 details the experimental methodologies developed to prove these materials. It describes the integration of a membrane-driven diamond anvil cell (DAC) with closed-cycle helium cryostat, enabling precise thermodynamic control. A significant portion of this chapter is devoted to the systematic characterization of the Daphne 7575 pressure-transmitting medium, establishing its hydrostatic limits down to 40 K. The chapter also outlines the rigorous calibration protocols used, including temperature-corrected ruby fluorescence and the cross-validation of reflectance (R), transmission, and photoluminescence (PL) spectroscopy to ensure the extraction of intrinsic material parameters.

Chapter 3 comprises four peer-reviewed research articles that detail the primary findings of this work.

In the studies presented in Sections 3.1 and 3.2 the electronic tunability of tin-based iodide perovskites, specifically $(4FP)_2SnI_4$ and TMA_2SnI_4, is investigated. These works establish that Sn-based systems possess record-breaking pressure coefficients (up to -187 meV/GPa), significantly surpassing their Pb-based counterparts. The results demonstrate a linear band gap narrowing across structural phase transitions, positioning these materials as ideal candidates for high-sensitivity optical pressure sensors.

The work described in Section 3.3 explores the complex excitonic energy landscape in $(4FPEA)_2SnBr_4$. This study uncovers a striking excitonic dichotomy: while the near-band-edge emission redshifts under compression, the self-trapped exciton emission exhibits an

anomalous blueshift. This research provides a microscopic framework for understanding small polaron formation, demonstrating how halide-specific lattice rigidity and dielectric screening dictate the stabilization of localized versus delocalized excitonic states.

Section 3.4 transitions the investigation to Cu-based systems, specifically $(PMA)_2CuX_4$ (X= Cl, Br). This study addresses the critical challenge of thermodynamic stability and provides a comparative analysis of thermochromism versus piezochromism. It is demonstrated that while both temperature and pressure induce significant redshifts, the underlying mechanisms, thermal expansion versus mechanical compression, interact with the electron-phonon landscape in fundamentally different ways, influencing the structural resilience of the material up to 11 GPa.

Finally, the dissertation provides a summary of the findings and formulates overall conclusions regarding the future of stimuli-responsive optoelectronics.

In summary, this dissertation provides a coherent description of the relationships between mechanical perturbations, electronic structure, and excitonic behavior in selected Pb-free 2D perovskites. The results constitute a significant contribution to the development of semiconductor physics, proving that lattice softness, often viewed as a limitation, can function as a tunable degree of freedom for quantum-state engineering and the design of next-generation adaptive optoelectronic devices.

Contents

List of Figures

List of Tables

Acronyms

1D One-Dimensional. 7

2D Two-Dimensional. 7, 12, 14, 39, 77, 123–125

3D Three-Dimensional. 7, 23

ACI Alternating Cation Interlayer. 7–9

B-D Intralayer Bidentate. 7, 9, 10

CBM Conduction Band Minimum. 5

D-J Dion- Jacobson. 7–10

DAC Diamond Anvil Cell. 15, 24–34, 37, 99, X

DFT Density Functional Theory. 59, 77, 125

EPC Electron-Phonon Coupling. 5, 12, 14, 21–23

GB GloveBox. 17

HOIPs Hybrid Organic-Inorganic Perovskites. 1, 3–15, 17, 18, 22–24, 27, 39, 41, 77, 99, 123–125, IX

HP High-Pressure. 22–27, 29, 34, 37, 41, 59, 99, X

LED Light-Emitting Diode. 8, 124

NBE Near-Band-Edge. 39, 77

PL Photoluminescence. 12, 15, 18, 20, 21, 23, 26, 27, 29, 31–35, 41, 59, 77, IX, X

R Reflectance. 15, 18, 20, 21, 59, 99, 125

R-P Ruddlesden-Popper. 7–10

SOC Spin-Orbit Coupling. 1, 6, 11

STE Self-Trapped Exciton. 1, 6, 11, 12, 14, 39, 77, 124

VBM Valence Band Maximum. 5

XRD X-ray Diffraction. 41, 59

Introduction

This chapter establishes the conceptual and physical framework that underpins the investigation of Pb-free layered hybrid organic-inorganic perovskites (HOIPs) under hydrostatic pressure.

It introduces the structural and electronic fundamentals of HOIPs, emphasizing the consequences of lattice softness, octahedral flexibility, and orbital hybridization for band structure formation and exciton emission. Special attention is given to dimensional reduction and Pb substitution, as these parameters fundamentally modify spin-orbit coupling (SOC), dielectric confinement, and electron-phonon interactions.

The chapter further formulates the central scientific hypothesis of this thesis: **that lattice softness governs the competition between electronic bandwidth broadening and lattice relaxation energy, thereby controlling band gap evolution and self-trapped exciton (STE) stability under compression.**

By integrating structural physics, electronic theory, and thermodynamic control concepts, this chapter provides the theoretical foundation necessary to interpret temperature and high-pressure optical measurements presented in the following chapters.

Together, these considerations define a coherent work for understanding how mechanical perturbations can be harnessed to engineer electronic states in soft-lattice semiconductors.

1.1 Motivation and Scientific Hypothesis

The rapid development of perovskite solar cells over the past decade represents one of the most remarkable advances in modern photovoltaic research.[1, 2] The origins of this field can be traced in 2009, when the group of Tsutomu Miyasaka first introduced Hybrid Organic-Inorganic Perovskites (HOIPs) as light absorbers in dye-sensitized solar cells.[3] In that pioneering study, methylammonium lead halide perovskites, most notably $CH_3NH_3PbI_3$, were employed as sensitizers, enabling power conversion efficiencies of approximately 3.8 %.[3] Despite this promising initial demonstration, the early devices suffered from severe instability because the perovskite material rapidly decomposed in contact with the liquid electrolyte used in the cell architecture.[1, 3] As a result, these first-generation devices did not immediately attract widespread attention within the photovoltaic community.[4]

A major turning point occurred in 2012 with the introduction of solid-state perovskite solar cells.[5, 6] By replacing the liquid electrolyte with a solid hole-transport material, researchers significantly improved both the operational stability and the photovoltaic performance of the devices.[5, 6, 7, 8, 9, 10, 11, 12, 13] This architectural innovation transformed perovskites from a niche research curiosity into a highly promising class of photovoltaic materials.[1] In the years that followed, the field experienced explosive growth, with rapid improvements in device efficiency and an exponential increase in scientific publications (Figure 1.1).[1] Today, perovskite solar cells are widely recognized as one of the most promising next-generation photovoltaic technologies.[1, 14, 15, 16, 17, 18]

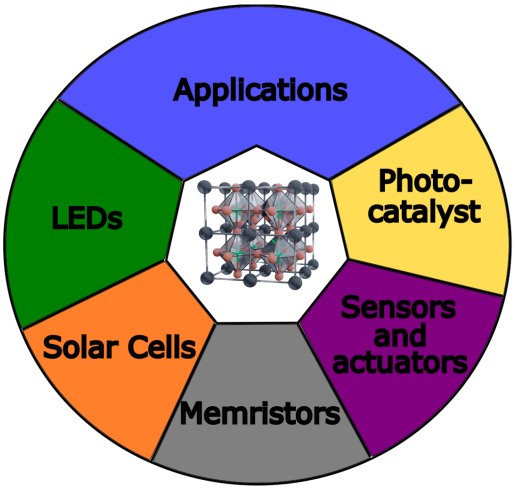

Figure 1.1: Overview of potential applications of HOIPs materials.

While solar energy remains the primary driver of research, the fundamental properties of the perovskite lattice, such as high defect tolerance and tunable band gap, have enabled a diverse range of secondary applications (see Figure 1.1):

- Light-Emitting Diodes (PeLEDs),

  HOIPs offer exceptional color purity and narrow emission linewidth. Green and red PeLEDs have already surpassed 20% external quantum efficiency, rivaling established OLED technologies.[19, 20]

- Radiation Detection,

  HOIPs are superior candidates for low-dose X-ray and gamma-ray imaging, potentially revolutionizing medical and security scanning.[21, 22]

- Neuromorphic Computing,

  Perovskites can act as memristors that mimic biological synapses. This allows for the development of energy-efficient AI hardware and visual memory sensors.[23]

- Sustainable Catalysis,

  Perovskites are being utilized for solar-to-fuel conversion, specifically for photocatalytic water splitting.[24]

- Chemical Sensing.

  Their high surface area allows for the detection of toxic gasses at room temperature, facilitating the creation of low-power, wearable environmental monitors.[25]

HOIPs have transformed the landscape of semiconductor physics by combining strong light-matter interaction with an unusually soft and deformable lattice.[26, 27] Their rapid emergence in photovoltaic and light-emitting applications is rooted in a rare convergence of properties: direct band gaps, high absorption coefficients, long carrier diffusion lengths, and remarkable defect tolerance.[26, 28, 29] These characteristics enable efficient charge generation and transport, even in materials processed using low-temperature solution-based techniques.[26]

At the same time, HOIPs differs fundamentally from conventional covalent semiconductors such as Si or GaAs.[27] Their ionic bonding character results in pronounced structural flexibility, strong electron-phonon coupling, and dynamic lattice disorder.[26, 30] These features give rise to complex physical phenomena, including ion migration, lattice anharmonicity, and strong coupling between structural and electronic degrees of freedom.[31, 30] While these properties contribute to the remarkable optoelectronic performance of perovskite materials, they also introduce new challenges related to long-term stability and device reliability.[1]

Understanding the interplay between structural dynamics, electronic structure, and optoelectronic properties is therefore essential for further advancement of perovskite-based technologies.[26, 27] In particular, the soft lattice and dynamic disorder characteristic of HOIPs play a critical role in determining charge-carried behavior, defect formation, and light-matter interactions.[26, 28] Elucidating these fundamental mechanisms is crucial not only for improving photovoltaic performance but also for enabling the broader application of perovskites in light-emitting diodes, photodetectors, and other optoelectronic devices.[27]

1.1.1 Scientific Hypothesis

This thesis is motivated by a central scientific challenge:

The softness of the HOIPs lattice depends on the type of cation and has a significant impact on how the band gap depends on temperature and hydrostatic pressure.

1.2 Fundamentals of Hybrid Organic-Inorganic Perovskites

1.2.1 Crystal Structure

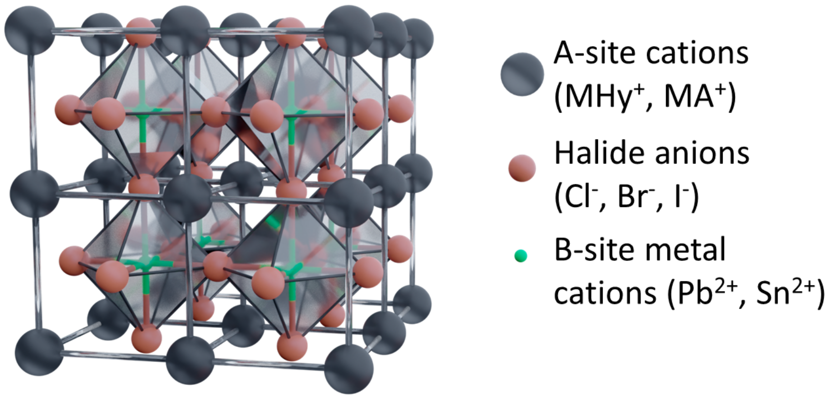

Figure 1.2: ABX_3 perovskite structure showing corner-sharing BX_6 octahedra (semi-transparent), A-site cations (grey), B-site metal cations (green) and halide ions (red).

HOIPs adopts the ABX_3 crystal structure, where A is a monovalent cation (e.g. methylammonium, formamidinium, methylhydrazinium), B a divalent metal (e.g., Pb^{2+}, Sn^{2+}, Cu^{2+}), and X a halide anion (Cl^-, Br^-, I^-).[32, 33, 34] The structure consists of corner-sharing BX_6 octahedra forming a three-dimensional network, with A-site cations occupying the cavities. The schematic example of such a structure is presented in Figure 1.2.

Structural stability of HOIPs is commonly described by the Goldschmidt tolerance factor:[35, 36]

$$t = \frac{r_A + r_X}{\sqrt{2}(r_B + r_X)}, \tag{1.1}$$

where r_A, r_B, r_X are the radius values of the corresponding parts in the ABX_3 formula.

Variations in ideal geometry ($t \approx 1$) induce octahedral tilting and symmetry lowering, which in turn modulate the electronic structure and band gap.[37, 38] Unlike classic semiconductors such as Si or GaAs, the octahedral structure in HOIPs can rotate and distort at low energetic cost. Consequently, the lattice responds readily to temperature, strain, and hydrostatic pressure.[37, 38, 39, 40] This flexibility underpins their large pressure coefficients, structural phase transitions, and enhanced electron-phonon coupling (EPC).[26, 41]

1.2.2 Electronic Structure and Spin-Orbit Coupling

The electronic structure of HOIPs emerges from orbital hybridization between B-site metal and halide orbitals.[42, 43] The valence band maximum (VBM) consists of an antibonding combination of metal s-orbitals and halide p-orbitals, while the conduction band minimum (CBM) is primarily composed of metal p-orbitals. This configuration

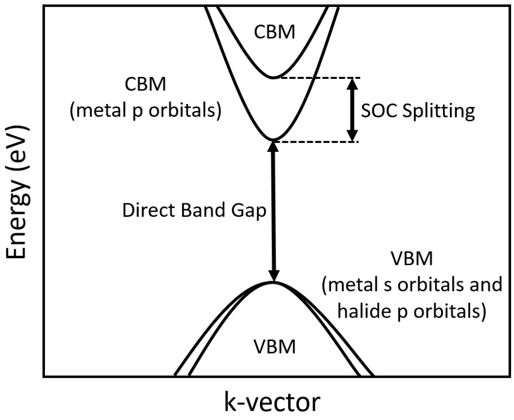

Figure 1.3: Schematic band structure of 3D ABX_3 perovskites showing orbital contributions and spin-orbit splitting of the conduction band.

typically leads to a direct band gap, which enables efficient light absorption and emission, crucial for optoelectronic applications.

Heavy metals such as Pb^{2+}, strongly influence SOC, which in result significantly lowers and splits the conduction band.[44, 45] Additionally SOC modifies effective masses, and excitonic structure. Substitution of Pb^{2+} with lighter metals such as Sn^{2+} or Cu^{2+} reduces SOC strength, modifies band gap and carrier localization.[33, 46] In Cu-based perovskites, partially filled Cu 3d orbitals introduce localized states that give rise to intra-ionic d-d transitions, leading to more localized excitations compared to Pb-based systems.

The electronic bandwidth emerging from orbital overlap competes directly with lattice relaxation energy. This competition governs whether carriers remain delocalized or localized into polarons or STEs.[47]

1.2.3 Dimensional Reduction

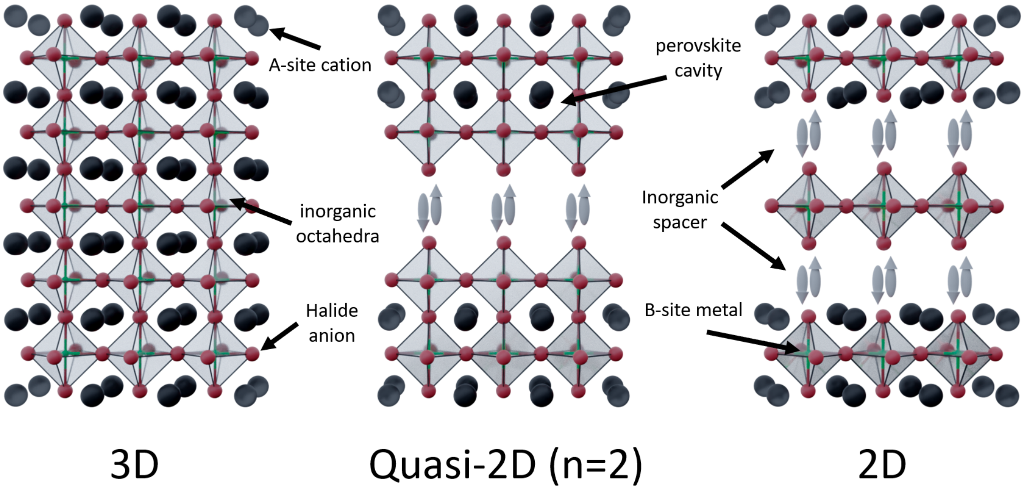

Figure 1.4: Dimensional reduction in HOIPs: 3D → quasi-2D (n=2) → 2D.

Dimensional engineering introduces an additional control parameter, as HOIPs exhibits a variety of dimensionalities from 3D, two-dimensional (2D), quasi-2D Ruddlesden-Popper phase, one-dimensional (1D), and zero-dimensional (0D).[48, 49, 50, 51, 52, 53] Reduction of the dimensionality introduces dielectric confinement, enhancing Coulomb interactions and resulting in increased exciton binding energies.[54] Enhanced exciton-lattice coupling facilitates self-trapping, a phenomenon of growing interest in optoelectronic applications.[26]

Layered HOIPs also presents enhanced pressure sensitivity, enabling larger band gap shifts under pressure,[55, 56, 57] and can stabilize Pb-free compositions by accommodating alternative B-site metals without compromising excitonic or optical performance.[58, 59]

Based on the nature of the organic spacer and its interaction with the inorganic lattice, several layered HOIPs families have been identified, including the Ruddlesden-Popper (R-P), Dion- Jacobson (D-J), alternating cation interlayer (ACI) and the recently proposed intralayer bidentate (B-D) phases.[60]

Ruddlesden-Popper Phase

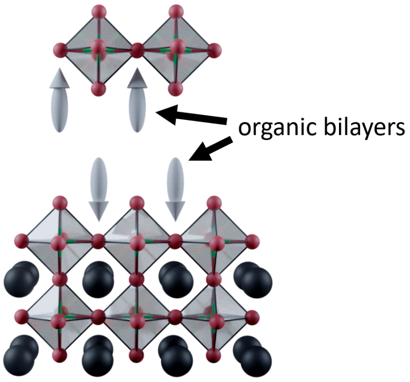

Figure 1.5: Representation of Ruddlesden-Popper Structure.

Layered HOIPs can adopt the R-P structure, which is represented by general formula:[61]

$$(A')_2 A_{n-1} B_n X_{3n+1} \tag{1.2}$$

In such a structure, the corner-sharing BX_6 octahedra form quasi-2D sheets separated by organic bilayers [62]. The organic spacers terminate the inorganic framework and break 3D connectivity, imposing steric constraints that reduce symmetry and enhance lattice flexibility.[63] In result such reduction produces structural anisotropy, with strong bonding in-plane and weak van der Waals interactions out-of-plane.[63]

Octahedral tilting and distortion are strongly enhanced relative to 3D systems.[61] Because electronic bandwidth is governed by B-X-B bond angles, these distortions directly modulate the band gap. The reduced structural rigidity also increases sensitivity to external perturbations such as hydrostatic pressure.[61, 64]

This reduction further introduces dielectric confinement. The dielectric constant of the inorganic sheets exceeds that of the organic spacer, generating electrostatic contrast that strengthens Coulomb interactions.[65]

Dion-Jacobson Phase

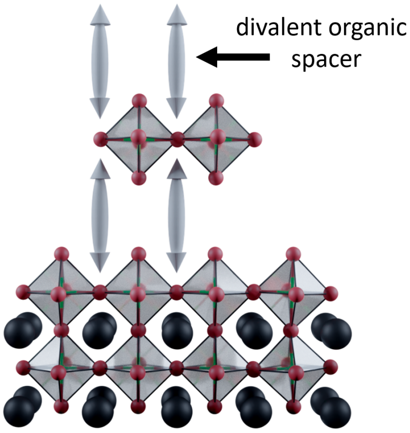

Figure 1.6: Representation of Dion-Jacobson Phase.

Another important class of layered HOIPs is the D-J phase, which incorporates divalent organic spacer cations.[60] The general formula of D-J perovskites can be expressed as:

$$(A'')A_{n-1}B_nX_{3n+1} \tag{1.3}$$

where A'' represents a diammonium organic spacer containing two ammonium groups capable of interacting simultaneously with adjacent inorganic layers.

In contrast to the R-P phase, where two monovalent organic cations form a bilayer spacer, the D-J structure contains a single divalent organic molecule that bridges two neighboring inorganic slabs. This configuration eliminates the van der Waals gap present in R-P perovskites and introduces stronger electrostatic interactions between the organic and inorganic components.

The enhanced interlayer coupling generally results in improved structural rigidity and stability compared with R-P structures. Additionally, the shorter interlayer distance facilitates more efficient charge transport perpendicular to the inorganic layers, which is beneficial for optoelectronic devices such as solar cells and light-emitting diodes (LEDs).

The ability to tune the molecular structure of diammonium spacers allows precise control of the interlayer spacing and octahedral distortions, providing an additional route for tailoring the electronic and optical properties of layered HOIPs.

Alternating Cation Interlayer Phase

A more recently identified layered configuration is the ACI phase.[60] In this architecture, two distinct organic cations occupy the interlayer space in an alternating arrangement rather than forming a uniform spacer layer.

A common example involves the combination of guanidinium (GA^+) and methylammonium (MA^+) cations. These cations alternate within the interlayer region and modify the packing of the organic components.

This structural arrangement influences the distortion of the inorganic octahedral framework and alters the electronic structure of the material. Compared with conven-

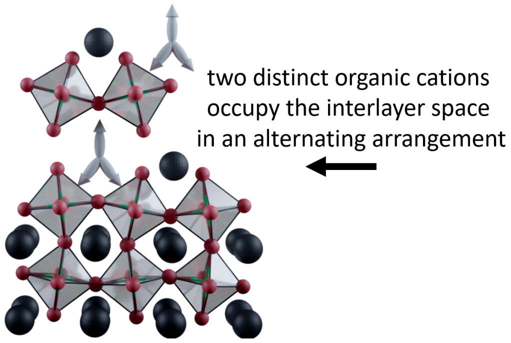

Figure 1.7: Representation of Alternating Cation Interlayer Phase.

tional R-P perovskites, ACI structures can exhibit improved structural ordering and enhanced stability due to more efficient packing of the interlayer species.

The presence of multiple cation species also modifies the dielectric environment surrounding the inorganic layers, which can influence excitonic confinement and charge transport properties. Consequently, ACI perovskites provide an additional strategy for tuning the structural and optoelectronic properties of layered HOIPs through careful selection of the interlayer cation composition.

Intralayer Bidentate Phase

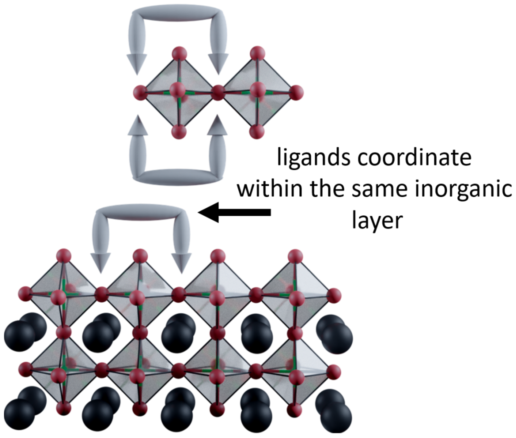

Figure 1.8: Representation of Intralayer Bidentate Phase.

Recently, a new structural motif termed the B-D phase has been proposed,[60] introducing a different binding configuration between organic ligands and the inorganic framework.

In contrast to both R-P and D-J phases, where organic cations interact with the inorganic lattice from the interlayer region, B-D ligands coordinate directly within the same inorganic layer. These ligands typically consist of a rigid molecular core with two ammonium-terminated arms positioned on the same side of the molecule, allowing simultaneous binding to adjacent A-site vacancies on the HOIPs surface.

The spacing between the ammonium groups is designed to match the separation between neighboring binding sites on the inorganic lattice, enabling intralayer bidentate coordination. This multidentate binding significantly strengthens the interaction between the organic ligand and the inorganic framework compared with conventional monodentate ligands used in R-P structures.

As a result, B-D phase perovskites exhibit enhanced structural stability and higher ligand detachment energies relative to both R-P and D-J analogs. The stronger anchoring of the ligand can suppress degradation pathways associated with ligand desorption and lattice reconstruction, which are common limitations in perovskite-based devices.

Furthermore, the strong ligand-lattice interaction can improve defect passivation and reduce non-radiative recombination, leading to enhanced photovoltaic performance and long-term stability in perovskite solar cells.

1.3 The Lead-Free Imperative

The rapid development of HOIPs has been primarily associated with Pb-based perovskites. As illustrated in Figure 1.9, the push toward Pb-free alternatives arises from both the intrinsic limitations of Pb-containing systems and the search for more sustainable materials platforms.

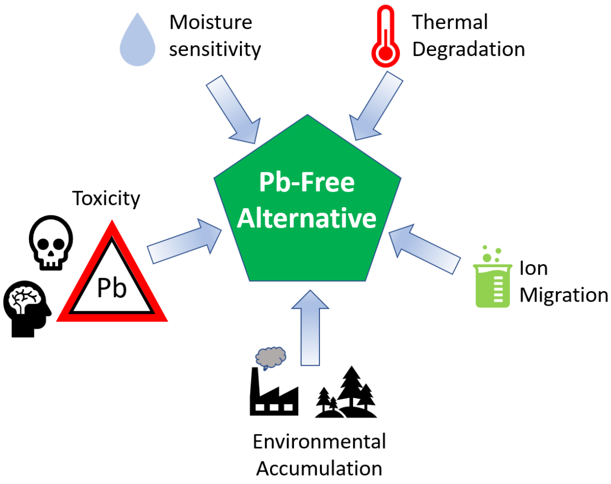

Figure 1.9: Schematic illustration highlighting the motivations for developing Pb-free HOIPs. The central element represents Pb-free alternatives, while surrounding arrows indicate key limitations of Pb-based perovskites.

The development of Pb-free HOIPs is motivated by both environmental responsibility and fundamental electronic physics. This section establishes the rationale for Pb replacement and examines the electronic consequences that define the limits and opportunities of Pb-free systems.

1.3.1 Environmental and Regulatory Drivers

Although Pb-based HOIPs have achieved remarkable optoelectronic performance, their long-term deployment is constrained by the toxicity and regulatory restrictions of Pb compounds. Pb is a cumulative neurotoxin, with well-documented environmental and health risks, particularly in the context of large-area device fabrication and end-of-life disposal.[66, 67] Regulatory frameworks, like the Restriction of Hazardous

Substances directive in the European Union, impose strict limits on Pb content in electronic devices.[68] While research-scale devices may currently operate under exemptions, full-scale commercialization will require compliance with increasingly stringent environmental standards.

Beyond toxicity, Pb-based systems exhibit chemical instability, ion migration, and degradation pathways that remain challenges for large-scale applications.[1] Lead-free development is therefore both a regulatory necessity and a scientific opportunity to interrogate the electronic origins of defect tolerance.

1.3.2 Electronic Consequences of Pb Replacement

The exceptional properties of Pb-based HOIPs emerges from the relativistically stabilized $6s^2$ lone pair of Pb^{2+}, which enhances covalency with halide p orbitals while maintaining antibonding character at valence band edge.[69] Replacing Pb modifies:[70, 71] SOC strength[70, 71, 72, 73], band curvature and dispersion, defect formation energies[74], electron-phonon coupling[75, 76, 77].

Sn^{2+} Substitution

Sn^{2+} retains the ns^2 lone pair, but its chemical stability differs markedly. Oxidation of Sn^{2+} to Sn^{4+} increases the population of Sn vacancies, leading to strong p-type self-doping.[1] Importantly, these vacancy-related states act as shallow acceptors, rather than deep defects. Background carrier concentrations can reach 10^{17}-10^{18} cm^{-3}, increasing nonradiative recombination.[71] Vacancy formation energies in Sn-based HOIPs are typically lower than those in Pb analogs, enhancing susceptibility to defect-mediated degradation.[71, 78, 79, 80, 81]

Cu^{2+} Substitution

Transition metals such as Cu^{2+} introduce partially filled 3d orbitals, which hybridize with halide p orbitals, increasing electronic localization and reducing bandwidth compared to Pb^{2+}[82]. Cu^{2+} represents a much weaker SOC, but the configuration d^9 induces pronounced Jahn-Teller distortions, which enhance electron-phonon coupling and can promote STE.[82] The formation energies of Cu vacancies are moderate, meaning that trap states are more likely than in Pb^{2+}. While Cu^{2+} can form stable HOIPs, these structural distortions and trap states impact both electronic transport and defect tolerance.[83, 84, 85]

1.4 Soft Lattice Physics and Exciton Self-Trapping

A defining characteristic of HOIPs is their mechanical softness. Bulk moduli typically range between 10-25 GPa, far lower than conventional semiconductors such as Si, GaAs, and wurzite GaN (98, 75, 205 GPa respectively).[86, 87, 88, 89, 90] This softness emerges from flexible octahedral connectivity and shallow potential energy surfaces. The lattice exhibits strong anharmonicity and dynamic disorder.[91] Large-amplitude vibrations persist even in crystallographically symmetric phases. Such structural fluctuations couple strongly to electronic excitations.

When a carrier forms, local lattice distortion lowers total energy. If the lattice relaxation energy exceeds carrier kinetic energy, self-trapping occurs. In 2D systems, reduced bandwidth and enhanced confinement increase the likelihood of self-trapping.

STE manifest experimentally as:

- Large Stokes shift[92, 93]
- Broadband emission[94]
- Strong temperature intensity[95, 96]

Thus, exciton behavior in HOIPs is governed by a competition between delocalization, (electronic bandwidth) and localization (lattice relaxation).[97]

1.5 Temperature as a Thermodynamic Control Parameter

HOIPs exhibit pronounced temperature-dependent optoelectronic behavior due to their soft lattice, strong EPC, and structural phase transitions if any.[96, 98] Temperature-dependent optical spectroscopy provides a direct means to disentangle structural, electronic, and excitonic contributions to the material response.

Structural Phase Transitions and Band Gap Evolution

Many HOIPs undergo temperature-driven structural phase transitions that modify lattice symmetry and orbital overlap, directly influencing the electronic band structure.[96, 98] Temperature-dependent transmission and reflectance measurements allow precise tracking of the absorption edge and extraction of the band gap energy.

Discontinuities or slope changes in the band gap versus temperature can indicate structural transitions. The evolution of the band gap was analyzed using the Varshni [99] and Bose-Einstein [100] model to separate contributions from lattice expansion and EPC, providing a quantitative understanding of thermally induced band gap shifts.

Exciton Stability and Recombination Dynamics

HOIPs have relatively high exciton binding energies, which decrease with increasing temperature.[96] As temperature rises, excitons dissociate into free carriers, non-radiative channels become activated, and trap-assisted recombination may dominate.

Temperature-dependent PL spectroscopy enables extraction of thermal activation energies for non-radiative processes via Arrhenius analysis, enabling quantitative determination of activation energies associated with non-radiative recombination pathways. These results are particularly relevant for optoelectronic devices, where thermal effects significantly impact performance.

Electron-Phonon Coupling and Lattice Dynamic Disorder

Temperature-dependent shifts in PL peak position and linewidth broadening provide a direct measure of EPC strength.[96] Linewidth broadening and peak shifts were analyzed using Varshni and Bose-Einstein phonon interaction models.

Understanding these processes provides insights into the interplay between lattice dynamics, carrier mobility, and exciton stability, all critical for device operation under realistic conditions.

Relevance to Device Stability and Performance

Thermal evolution of band gaps, excitonic behavior, and non-radiative recombination directly impacts device efficiency and operational stability in HOIPs-based optoelectronic devices.[98] The systematic temperature-dependent measurements presented here provide a quantitative framework for predicting material performance under realistic operating conditions.

1.6 Pressure as a Thermodynamic Control Parameter

Hydrostatic pressure provides a continuous and chemically clean and reversible method for tuning interatomic distances and bond angles. Unlike compositional substitution, pressure directly modifies distances and bond angles, enabling controlled interrogation of structure-property relationships.[71, 101] In the soft lattice of HOIPs, even small compression induces large changes in octahedral tilting, bond lengths, and phase stability.[102, 103, 104, 105] As a result, pressure has emerged as a powerful tool to tune band gap and excitons.[56]

Unfortunately, despite extensive investigations, pressure-induced phenomena in HOIPs remain not fully understood and they were not explored in Sn-based perovskites and in Cu-based perovskites. Reported trends in band gap tuning and emission behavior vary widely between studies,[64, 106, 107] suggesting that some competing structural mechanisms whose relative contributions are not yet resolved.

Under pressure, competing structural mechanisms occur:

- **Bond shortening**, which increases the orbital overlap between the metal and halide states. In result, this leads to the broadening of the electronic bandwidth [71].

- **Octahedral tilting and distortion**, which reduce effective overlap along certain directions and can narrow the bandwidth, leading to the reduction of the band gap.[108, 109, 110]

- **Pressure-Induced Phase Transitions**, at higher pressures, HOIPs frequently undergo structural phase transitions.[111, 112, 113] In some systems, amorphization occurs beyond a critical pressure, further complicating interpretation of data.

The relative dominance of these mechanisms determines whether the band gap increases or decreases with pressure.

Reports in the literature show contradictory trends - blueshift in some systems, redshift in others, and non-monotonic evolution in many cases.[114, 115, 116, 117] These different various behaviors suggest that the microscopic balance between bond-length contraction and distortion-driven bandwidth narrowing therefore remains debated.

1.7 Self-Trapped Excitons Under Extreme Conditions

STEs emerge from a balance between carrier kinetic energy and lattice relaxation energy. In this terms pressure is expected to strongly influence their stability. However, experimental observations are inconsistent with theory:

- Some studies report suppression or quenching of broadband emission under compression,[117] suggesting that increased electronic bandwidth destabilizes localized excitons. In such interpretation, bond shortening increases carrier kinetic energy and reduces STE energy.
- In contrast, other reports an enhanced broadband emission or increased Stokes shift under pressure.[118] Such behavior has been attributed to pressure-induced distortion or increased EPC.[119]
- Pressure-induced phase transitions often produce abrupt changes in emission spectra.[63] In certain cases, STE emission emerges only after symmetry breaking associated with a high pressure phase.[63]

The coexistence of STE quenching, and enhancement across similar material classes indicates that the microscopic mechanisms governing exciton localization under compression remain unresolved. It is therefore unclear whether pressure universally increases electronic bandwidth and suppresses localization, or whether enhanced lattice distortion strengthens self-trapping in layered HOIPs.

1.8 Research Objectives

Despite numerous publications, across HOIPs measurements under hydrostatic pressure, several critical questions remain open to discover, especially in layered Pb-free HOIPs:

1. What is the dominant factor of band gap narrowing under pressure in layered HOIPs: bond shortening or octahedral tilting?
2. Does pressure destabilize or enhance STEs in 2D lead-free systems?
3. How do pressure-induced phase transitions modify electron-phonon coupling strength?
4. Does pressure contribute to polaron formation?
5. To what extent do experimental conditions (hydrostaticity, pressure medium, sample morphology) contribute to contradictory reports?

To test hypothesis presented in this thesis, and try to answer to the questions above, this work systematically correlates high-pressure structural and optical measurements under controlled hydrostatic conditions.

Experimental Methods

The chapter outlines the experimental methodologies used to systematically investigate the structural, optical, and electronic properties of HOIPs samples under various temperature and hydrostatic pressure.

A detailed description of the sample origin, handling procedures, and environmental stability control is provided to ensure reproducibility and to suppress degradation pathways associated with moisture or oxygen exposure.

Optical characterization techniques, including reflectance (R), transmission, and photoluminescence (PL) spectroscopy, are introduced together with their underlying physical principles and corresponding instrumental configurations.

Temperature- and pressure-dependent measurements are presented in dedicated sections, including cryogenic setups and diamond anvil cell (DAC) configurations. Calibration strategies, pressure-transmitting medium selection, and accuracy are discussed to ensure accurate determination of thermodynamic and optoelectronic parameters.

Finally, procedures for data processing, baseline correction, peak fitting, and uncertainty estimation are described to ensure rigorous extraction of material parameters and reliable interpretation of results. All details not described in the articles included in this PhD thesis are presented herein.

Together, these methodologies provide a robust framework for understanding intrinsic optical phenomena in HOIPs under well-controlled experimental conditions.

2.1 Samples: Origin and Handling

The HOIPs samples investigated in this study were provided by three independent research institutions through collaborative projects resulting in joint publications. Material synthesis, precursor purification and compositional optimization were performed entirely by the respective collaborating laboratories and are described in detail in the associated publications.

The presented thesis focuses exclusively on post-fabrication physical characterization and advanced spectroscopic analysis.

Upon arrival, all samples were immediately transferred to a high-purity argon-filled glovebox (GB) to ensure controlled storage and handling conditions and to prevent exposure-induced degradation.

Table 2.1: Overview of the studied A_2MX_4-type layered halide compounds, presenting their composition, crystallographic structure (space group), optical properties (band gap and PL peak energies), and sample origin.

Material	Organic Cation (full name)	Abbrev.	Metal	Halide	Space group	Band gap [eV]	Pl peak [eV]	Source
$(4FP)_2SnI_4$	4-fluorophenethylammonium	(4FP)/ (4FPEA)	Sn	I	monoclinic P21/c	1.90	1.98	prof. Iván Mora-Seró Universitat Jaume in Spain
$(4FPEA)_2SnBr_4$				Br	triclinic P1	2.70	2.64	
TMA_2SnI_4	(2-thienyl)methylammonium	TMA		I	orthorhombic Pbca → Cmc21 (at 180 K)	2.00	1.99	dr. Łukasz Przypis Saule Technology
$(PMA)_2CuCl_4$	phenylmethylammonium	PMA	Cu	Cl	orthorhombic Pbca	2.33	2.12	dr. Muhammad Birowosuto Łukasiewicz PORT in Wroclaw
$(PMA)_2CuBr_4$				Br	hexagonal	2.23	-	

2.1.1 Handling and Environmental Stability

All samples were stored and prepared in an argon-filled GB maintained at the following conditions:

- Oxygen concentration: <0.5 ppm
- Moisture concentration: <0.5 ppm
- Temperature: 20-23 °C

Oxygen and moisture levels were continuously monitored using integrated electrochemical sensors. No samples were exposed to ambient laboratory air at any stage. Transfers between characterization instruments were performed using hermetically sealed containers to preserve the inert environment.

Optical measurements were conducted immediately upon taking the samples out of the GB to minimize environmental degradation effects, with the interval between removal and measurement kept below 20 minutes.

These procedures ensure that all reported properties reflect intrinsic material behavior rather than environmental or handling-induced artifacts.

2.2 Optical Spectroscopy

To comprehensively characterize the optical properties of the investigated HOIPs, three complementary spectroscopy techniques were employed: R, transmission (absorption), and PL.[120, 121]

- R spectroscopy provides information on the material-related optical response and electronic transitions, enabling identification of band-edge features and excitonic resonances,
- Transmission spectroscopy probes bulk optical behavior, allowing determination of absorption coefficient, band gap energy, and is insensitive to defects,
- PL directly measures radiative recombination processes, exciton energies, and is sensitive to defects.

For all spectroscopic measurements, optical alignment was verified prior to each measurement series to ensure reproducibility and minimize systematic deviations. All detectors and monochromators were wavelength-calibrated before data acquisition.

The combined application of R, transmission, and PL enables independent access to the complex dielectric response, absorption, and radiative recombination pathways. Their complementary nature allows cross-validation of band-edge energies and excitonic features while distinguishing intrinsic electronic transitions from defect-related contributions.

2.2.1 Reflectance Spectroscopy

Principle:

R spectroscopy measures the fraction of incident light reflected from a sample as a function of wavelength. Spectral features provide information about optical constants, electronic transitions, and is also sensitive to surface quality, i.e. mirror like surface is necessary for regular reflectance measurements. For non-mirror surface or powder samples diffusive reflectance can be applied, but in our case we were dealing with samples with mirror-like surface and therefore the set-up for diffusive reflectance is not described. Sharp peaks in the spectra often indicate band-edge transitions, excitonic resonances, or thin-film interference effects.

R spectra were measured in a near-normal "bright configuration" using a stabilized halogen lamp, fully covering the measured spectral range. The incident beam was mechanically modulated at 266 Hz, enabling phase-sensitive detection via lock-in amplification and significantly improving the signal-to-noise ratio, and directed onto the sample at a small incidence angle ($< 10^\circ$). Reflected light was collected in near-specular geometry and analyzed using a 0.5 m focal-length single-grating monochromator equipped with a 1200 lines/mm diffraction grating, providing a spectral resolution of approximately 0.5 nm.

The dispersed signal was detected using a calibrated Si photodiode covering 350-1100 nm spectral range. Samples were mounted on the cold finger of a closed-cycle helium cryostat. Phase-sensitive detection was performed using a lock-in amplifier synchronized

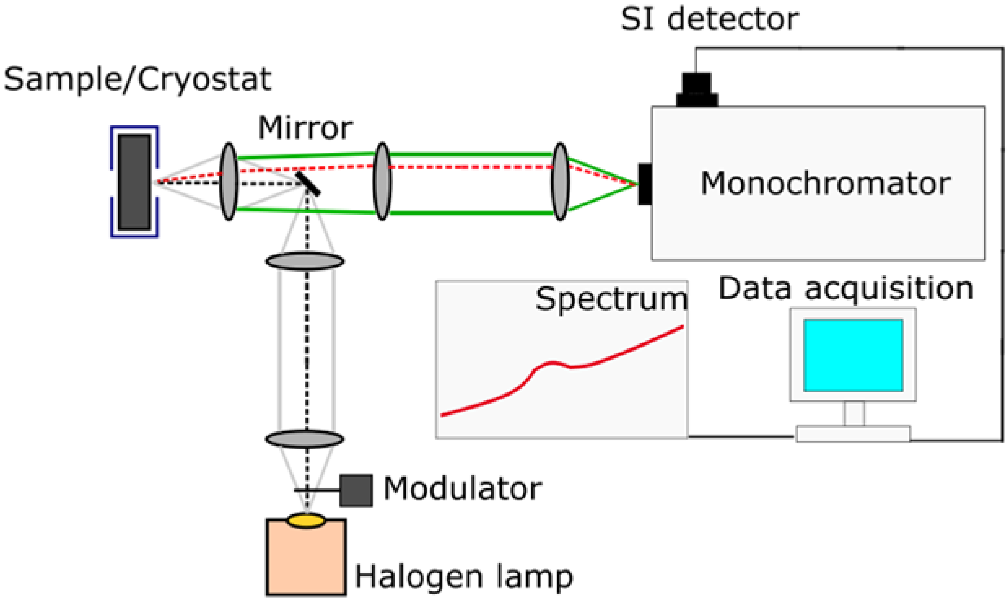

Figure 2.1: Schematic of the experimental setup used for temperature-dependent reflectance measurements. The incident beam is mechanically modulated and directed onto the sample at near-normal incidence. The reflected light is collected in near-specular geometry, spectrally dispersed by a monochromator, and detected using phase-sensitive lock-in amplification. Reprinted from Ref. J. Mater. Chem. C, 2025,13, 16929-16936 under CC-BY 3.0 license. Copyright 2025 R. Bartoszewicz et al.

to the chopper frequency. Absolute reflectance was obtained by normalization to a calibrated aluminum mirror measured under identical conditions:

$$R(\lambda) = \frac{R_{sample}(\lambda)}{R_{reference}(\lambda)}, \tag{2.1}$$

The beam spot diameter at the sample surface was approximately 1 mm.

2.2.2 Transmission (Absorption) Spectroscopy

Principle:

Transmission spectroscopy measures the wavelength-dependent intensity of light transmitted through a sample. The absorption coefficient, derived from the transmitted intensity, provides information on band gap energy and excitonic transition.

Measurements were performed in a "dark configuration", where the broadband halogen source was first dispersed by the monochromator before passing through the sample. The beam was incident normal to the sample surface and mechanically modulated at 270 Hz to enable phase-sensitive detection using a lock-in amplifier.

Transmitted light was detected using photodiodes selected according to the spectral range: Si (350-1100 nm), GaP (enhanced visible range), or PbS (near-infrared).

Sample thickness was measured prior to optical experiments using microscope with an uncertainty of ± 5 μm. The absorption coefficient was calculated according to:

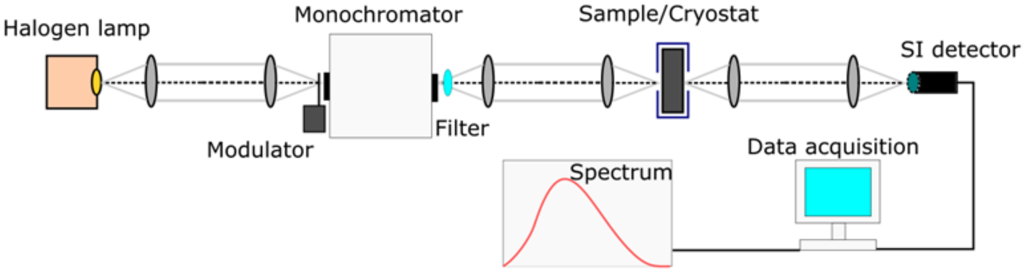

Figure 2.2: Schematic of the temperature-dependent transmission spectroscopy setup. The broadband halogen source is dispersed by a monochromator, mechanically modulated, and directed normally onto the sample mounted in a temperature-controlled cryostat. The transmitted signal is detected using wavelength-appropriate photodiodes and processed via lock-in amplification. Reprinted from Ref. J. Mater. Chem. C, 2025,13, 16929-16936 under CC-BY 3.0 license. Copyright 2025 R. Bartoszewicz et al.

$$\alpha = -\frac{1}{d} ln \frac{T}{(1-R)^2}, \tag{2.2}$$

where d is the sample thickness, T the transmitted intensity through the sample, and R is the reference signal.

This relation assumes negligible scattering losses, uniform sample thickness, and minimal multiple internal reflections. These conditions were verified by the absence of pronounced Fabry-Perot interference oscillations.

2.2.3 Photoluminescence Spectroscopy

Principle:

PL spectroscopy probes radiative recombination following above-band gap optical excitation. Spectra provide direct information on excitonic emission, and defect-assisted radiative features. Peak position, linewidth, and intensity evolution serve as sensitive indicators of structural quality, energetic disorder, and non-radiative recombination pathways.

PL measurements were performed in backscattering geometry using continuous-wave laser excitation at 405 or 325 nm. The excitation beam was focused onto the sample using a 10 cm focal-length lens, with power maintained between 20-150 μW. The emitted PL signal was collected by the same lens and analyzed using a 0.5 m monochromator with a 150 lines/mm diffraction grating blazed at 500 nm, achieving 1-2 nm spectral resolution. A long-pass filters suppressed scattered excitation light.

Detection was performed using a thermoelectrically cooled Si CCD camera. Spectral response was corrected using a calibrated reference lamp. The spectral axis was calibrated prior to each measurement series using known emission lines to ensure wavelength accuracy.

Cross-correlation of R, transmission, and PL spectra (absorption-like vs emission-like spectra) enables independent verification of band-edge energies and excitonic resonances. Agreement between techniques was used as an internal validation criterion to distinguish intrinsic electronic transitions from defect-related or measurement-induced artifacts like Fabry-Perot features attributed to optical transitions.

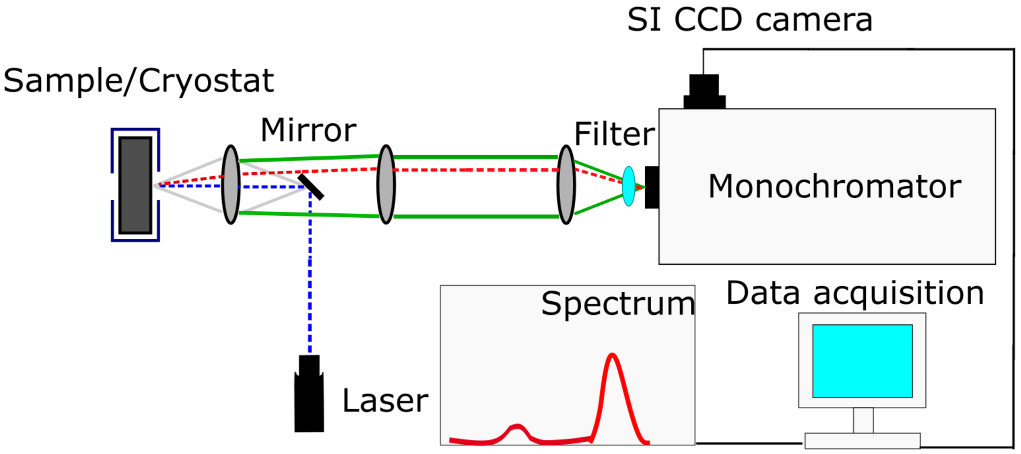

Figure 2.3: Schematic of the temperature-dependent photoluminescence setup. Continuous-wave laser excitation (405 or 325 nm) is focused onto the sample mounted in a temperature-controlled cryostat in backscattering geometry. The emitted PL is collected by the same lens, spectrally dispersed by a 0.5 m monochromator, and detected using a thermoelectrically cooled Si CCD camera. Long-pass filters suppress scattered excitation light.

2.3 Temperature-Dependent Measurements

In this study, temperature-dependent measurements were used to:

- Identify structural phase transitions and track band gap evolution.
- Quantify exciton stability and thermal activation of non-radiative recombination.
- Evaluate EPC and dynamic lattice disorder.
- Provide insights relevant to device performance and material optimization.

Transmission, R, and PL measurements as a function of temperature provide complementary information on the optical and electronic behavior of the samples.

2.3.1 Cryostat Configuration

All temperature-dependent measurements were performed using closed-cycle helium cryostats, which provide reliable temperature control over 20-320 K without liquid cryogens.

Samples were mounted on a brass sample holder thermally anchored to the cryostat cold finger. Brass was selected for its high thermal conductivity and mechanical stability under repeated thermal cycling.

To ensure uniform thermal contact and minimize mechanical tilt, silver paste was distributed along the sample edges using fine copper wire, thereby maintaining parallel alignment of the sample surface relative to the optical axis.

Each cryostat was equipped with four fused-silica optical windows arranged in a transmission geometry, allowing simultaneous access for excitation and detection. Prior to cooling, the sample chamber was evacuated using a turbomolecular pump. Maintaining high vacuum suppressed convective heat transfer and prevented condensation on the sample surface during low-temperature operation.

2.3.2 Temperature Control and Calibration

Temperature regulation was achieved using PID-controlled Lakeshore controllers. The temperature was monitored with a calibrated resistance sensor mounted directly on the sample holder at a distance of approximately 10 mm from the sample position.

To evaluate potential temperature gradients between the sensor and the sample, controlled heating ramps were performed. Under quasi-static conditions (< 2 K/min), the temperature offset between the sensor position and the sample was estimated to be below 0.5 K. This value is included in the overall temperature uncertainty.

At each temperature setpoint, temperature stability better than ± 0.1K was achieved. Stability was verified through continuous temperature logging over 6-minute intervals prior to data acquisition.

Heating rate was typically set between 2 and 5 K/min. Higher ramp rates introduced measurable thermal lag and were therefore excluded from quantitative analysis.

2.3.3 Measurement Protocol

A systematic temperature sweep protocol was implemented to ensure reproducibility and reliable detection of temperature-dependent optical changes. At each temperature setpoint, the system was allowed to stabilize for 5-10 minutes until temperature fluctuations were within ± 0.3 K. Data acquisition was initiated only after stabilization criteria were satisfied.

Measurements were performed in 20 K increments across the full investigated temperature range. The chosen step size was sufficient to resolve gradual band gap evolution and systematic spectral changes across the investigated temperature. In temperature regions where enhanced spectral evolution was observed, finer temperature steps were employed to resolve subtle changes.

The combination of controlled cryogenic conditions, systematic temperature stabilization, and reproducibility checks ensures reliable and reproducible determination of thermally induced optical changes in the investigated systems.

2.4 High Hydrostatic Pressure Measurements

High Hydrostatic Pressure (HP) experiments provide a powerful, non-invasive method to continuously tune the structural, electronic, and vibrational properties of HOIPs.[122] Unlike chemical substitution or compositional alloying, which may introduce disorder or defects, hydrostatic compression modifies interatomic distances and bonding interactions in a clean, reversible manner. This allows direct investigation of intrinsic structure-property relationships and exploration of emergent electronic phenomena.

HOIPs are characterized by soft ionic lattices, dynamic octahedral distortions, and strong EPC. Even moderate pressures (a few GPa) can induce substantial changes in band structure, lattice symmetry, and excitonic properties.[122, 123]

2.4.1 Fundamental Physical Principles

The response of HOIPs to pressure is governed by several mechanisms:

1. Lattice Compression and Bonding

   Hydrostatic pressure reduces unit-cell volume, affecting bond lengths, octahedral tilting, and interlayer spacing. Increased orbital overlap generally broadens electronic bands and reduces effective mass, while octahedral distortions can counteract this, producing non-monotonic band gap evolution.[124]

   Measured via: pressure-dependent PL and absorption spectroscopy, enabling tracking of band gap shifts and optical transitions.

2. EPC

   Soft phonon modes and anharmonic lattice dynamics dominate carrier behavior. Pressure typically stiffens phonons, modifies octahedral rotations, and alters polaron formation energies. These effects influence carrier mobility and recombination pathways.[122]

   Measured via: analysis of PL linewidth broadening and peak shifts under pressure, providing a quantitative assessment of lattice-carrier interactions.

3. Excitonic and Dielectric Effects

   Pressure changes dielectric screening by modifying lattice polarizability and ion displacements. In low-dimensional HOIPs, reduced interlayer spacing lowers exciton binding energy, while in 3D systems, compression simultaneously affects effective masses and screening, altering the free-carrier versus excitonic character.[123]

   Measured via: combined temperature- and pressure-dependent PL spectroscopy, allowing direct evaluation of exciton stability and dielectric response under compression.

2.4.2 Pressure-Induced Phenomena

HP studies reveal key material behaviors:

- Non-monotonic Band Gap Evolution[125, 126, 127, 128, 129, 130, 131],

  Initial narrowing due to orbital overlap may be followed by widening from octahedral distortion.

- Structural Phase Transitions[132, 133, 134, 135, 136, 137],

  Pressure can induce phase changes or amorphization, often accompanied by abrupt optical or electronic changes.

- Carrier Transport Modulation[138],

  Bandwidth, effective mass, and electron-phonon interactions evolve under compression, affecting mobility and polaron formation.

- Stability and Degradation[139, 140, 141, 142, 143]

  Mechanically driven instability, phase segregation, or structural collapse can be identified, informing material robustness.

Pressure therefore provides both a diagnostic tool and a predictive framework for designing HOIPs optoelectronic materials. All pressure-induced changes were verified to be reversible upon decompression, confirming that the observed phenomena reflect intrinsic lattice and electronic responses rather than sample degradation.

2.4.3 Diamond Anvil Cell Configuration

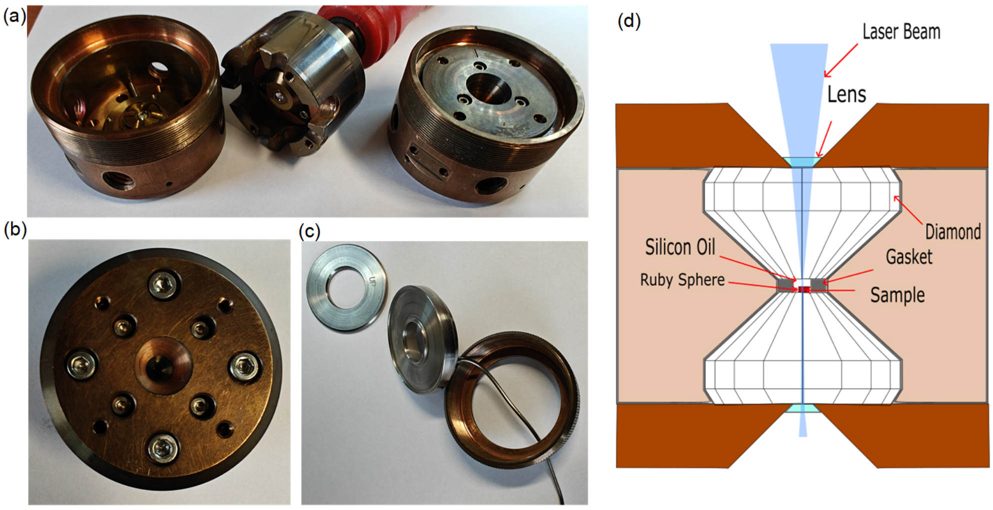

Figure 2.4: Membrane-driven DAC used for high-pressure optical measurements. (a) Front view of the assembled DAC, (b) rear view showing the membrane housing, (c) gas membrane for remote pressure control, (d) cross-sectional view of the DAC assembly illustrating the alignment of the diamond anvils, gasket, sample chamber, pressure-transmitting medium, and ruby sphere for pressure calibration.

HP optical measurements were performed using a membrane-driven Diacell diamond anvil cell (DAC) manufactured by Almax easyLab (Figures 2.4 a-c). The membrane-driven DAC design, first introduced by Letoullec,[144] enables fine, remote pressure tuning via a gas membrane, minimizing mechanical vibrations and drift during sensitive optical measurements. This configuration also allows experiments to be performed under temperature-controlled conditions without the iterative pressure cycling required for screw-driven DACs, where pressure must be adjusted at room temperature, followed by cooling, measurement, and reheating.

The DAC body is constructed from beryllium-copper alloy, providing the mechanical strength to withstand pressures up to 100 GPa while maintaining thermal stability during low-temperature operation. Symmetric type Ia diamond anvils with a culet diameter of 650 μm were used, allowing pressures up to 25 GPa while minimizing background fluorescence in optical spectroscopy. This culet size balances the achievable pressure with sample chamber dimensions, ensuring efficient optical access and compatibility with both transmission and backscattering geometries.

Figure 2.4 d presents a cross-sectional view of the assembled DAC, showing the alignment of the sample, pressure-transmitting medium, ruby sphere for pressure calibration, and gasket. This arrangement ensures reproducibility of high-pressure measurements and provides stable, well-defined optical paths.

2.4.4 Diamond Anvil Cell Closing and Pressure Medium

Gasket Material and Preparation

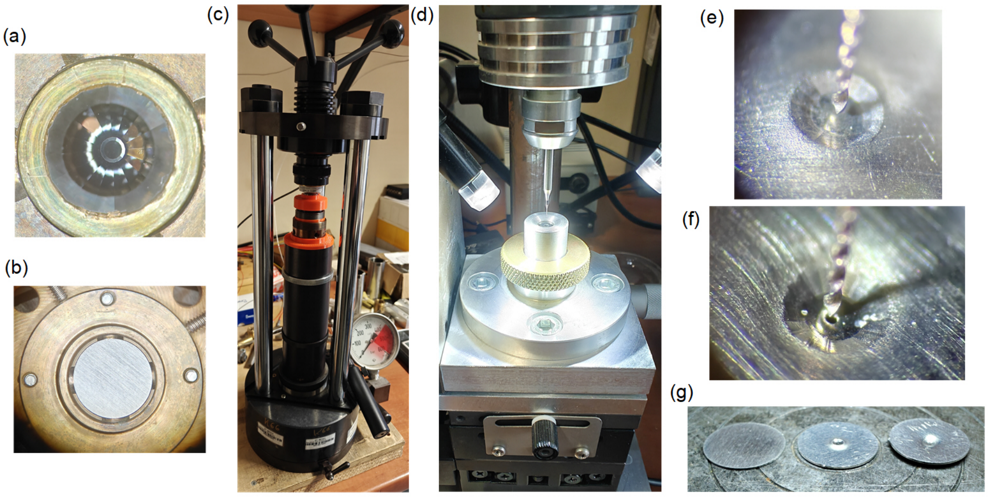

Figure 2.5: Gasket preparation procedure for HP measurements. (a) Bottom diamond anvil of the DAC, (b) placement and alignment of the gasket blank on the diamond culet, (c) external hydraulic press with alignment guides used for controlled pre-indentation, (d) mechanical drilling setup, (e) gasket prior to hole drilling, (f) gasket after drilling of the sample chamber, (g) comparison of unindented, properly prepared, and improperly prepared gaskets.

Gasket preparation is a critical step in ensuring reproducible high-pressure optical measurements. For this study 0.26 mm thick, 10 mm diameter Inconel sheets were used, selected for their high hardness, mechanical durability, and thermal stability. Alternative materials such as tantalum, tungsten, or rhenium may be employed depending on the sample properties and choice of pressure-transmitting medium. The pre-shaped gasket blanks were supplied by Almax easyLab.

The gasket blank is first carefully placed on the bottom diamond culet and aligned relative to the supporting plate (Figure 2.5 (b)). The DAC is then mounted in a hydraulic press equipped with alignment guides to prevent anvil misalignment (Figure 2.5 (c)). Pre-indentation of the gasket is performed in two stages: initially, the load is increased to 250 kg and then released to allow material relaxation, followed by a gradual increase to 500 kg. The loading and unloading rate is maintained at approximately 1 kg/s to ensure uniform compression and prevent micro-cracks. This procedure produces a final gasket thickness of $\sim$50 μm, providing sufficient mechanical support while minimizing interference with pressure transmission. Thickness was measured after pre-indentation using a micrometer, with an estimated uncertainty of ± 2 μm.

After pre-indentation, a central hole is drilled using either mechanical drilling or an electrical discharge machine (Figures 2.5 (c-f)). The hole diameter is chosen to be approximately 1/2 to 1/3 of the diamond culet size, ensuring proper sample containment while minimizing stress concentrations. Correct placement and quality of the hole are essential for uniform pressure distribution and reliable measurements. Figure 2.5 (g) illustrates unindented, properly prepared, and poorly prepared gaskets, highlighting common issues such as off-center holes, uneven thickness, or micro-cracks.

Careful preparation of the gasket ensures quasi-hydrostatic conditions within the sample chamber, which is essential for accurate optical measurements, including PL and transmission spectroscopy. This rigorous procedure maximizes reproducibility and minimizes artifacts arising from pressure gradients or mechanical instability.

Closing Diamond Anvil Cell

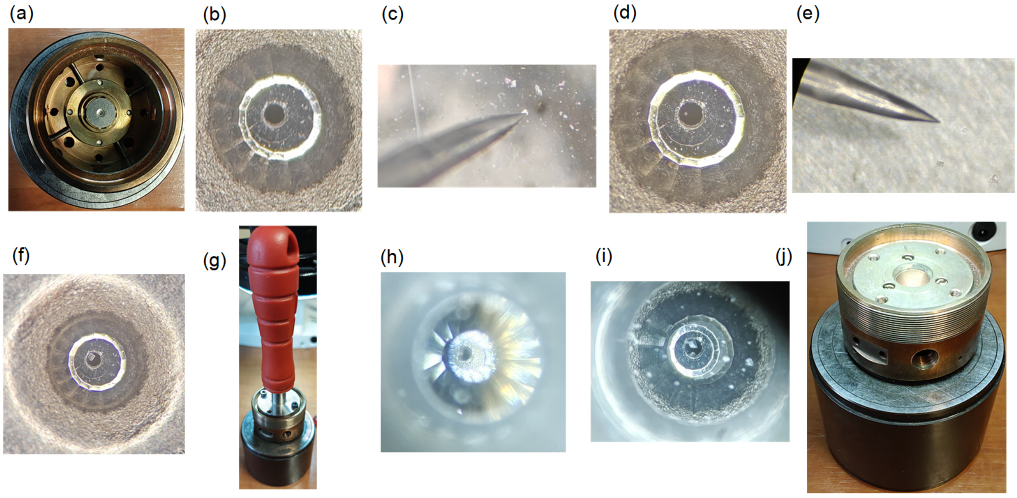

Figure 2.6: Procedure for loading and closing the membrane-driven DAC. (a) Placement of the prepared gasket on the bottom diamond culet, (b) introduction of the pressure-transmitting medium into the gasket chamber, (c) size comparison between the ruby and the loading needle, (d) placement of the ruby sphere inside the gasket hole, (e) size comparison between the sample and loading needle, (f) arrangement of the sample, ruby sphere, and pressure medium within the chamber, (g) extraction tool used to align and connect the two halves of the DAC, (h) intermediate stage during anvil approach, (i) view through the upper diamond after proper alignment, (j) fully assembled DAC ready for HP measurements.

Figure 2.6 (a-j) illustrates the complete procedure for closing the DAC. Prior to assembly, all tools were inspected, and both diamond culets and the upper anvil contact surface were cleaned with acetone to remove contaminants that could compromise gasket sealing or sample integrity. The diamond anvils were verified for parallelism under an optical microscope to ensure uniform stress distribution and prevent asymmetric gasket deformation or potential diamond damage.

The pre-indented and drilled gasket was carefully positioned on the bottom culet. Using the extraction tool, the DAC was brought into partial contact to smooth irregularities and verify alignment (Figure 2.6 (a)). The cell was then reopened for fine adjustment, ensuring proper placement of the gasket and maintaining mechanical stability.

The pressure-transmitting medium was introduced into the gasket hole using a syringe or fine brush (Figure 2.6 b), avoiding overfilling to prevent leakage or sample displacement. A ruby sphere for pressure calibration was placed adjacent to the sample using a fine needle (Figures 2.6 (c-d)), followed by careful positioning of the sample itself (Figures 2.6 (e-f)), maintaining adequate spatial separation to ensure accurate pressure measurements.

Once all components were properly arranged, the upper anvil was gradually lowered using the controlling screw and aligned with the extraction tool (Figure 2.6 (g-i)). Compression was applied incrementally to avoid stress concentration, sample extrusion, or non-hydrostatic conditions. If any displacement of the sample, ruby sphere, or medium occurred, the procedure was repeated to guarantee correct alignment and sealing. The fully assembled DAC is shown in Figure 2.6 (j).

Following this closure protocol ensures uniform pressure distribution, minimizes the risk of non-hydrostatic conditions, and guarantees that all subsequent HP optical measurements reflect intrinsic material behavior.

Pressure Medium

Daphne 7575 oil was employed as the pressure-transmitting medium for all HP optical measurements. The selection was motivated by its high optical transparency in the visible spectral range, which minimizes background absorption in PL and transmission experiments. No chemical interaction or degradation of the investigated HOIPs samples was observed within the applied pressure-temperature range, confirming its suitability for optical studies.[145, 146]

At room temperature, Daphne 7575 exhibits hydrostatic behavior up to approximately 5.3 GPa. However, the hydrostatic limit decreases significantly with decreasing temperature. Above the hydrostatic regime, the medium provides quasi-hydrostatic conditions due to its relatively low shear strength and soft solidification behavior, although pressure gradients may develop across the sample chamber.

Although alternative pressure media such as methanol-ethanol mixtures, NaCl, or noble gases (He, Ar) can provide higher hydrostatic limits, the use of gas-loading systems was not available in the present experimental configuration. Noble gases, while offering excellent hydrostatic conditions over extended pressure ranges, require dedicated loading infrastructure. Therefore, Daphne 7575 represented an optimal compromise between hydrostatic performance, optical compatibility, and experimental feasibility.[147]

Hydrostatic Limit

The content of this sub-chapter (including Figure 2.7) is repeated in Supporting Information in article I, II, and III.

The temperature-dependent hydrostatic behavior of Daphne 7575 was systematically investigated in Publication I of this thesis and therefore Figure 2.7 appears two times more in this dissertation in Publication I, II, and III. The analysis was based on monitoring the pressure-induced splitting and linewidth broadening of the ruby R1 and R2 fluorescence lines at 300, 200, 120, and 40 K. The solidification pressure was defined as the onset of nonlinear broadening of the R1 line accompanied by enhanced R1-R2 peak separation.

From this, analysis, the hydrostatic limits were determined to be approximately 5.3 GPa (300K), 3.8 GPa (200 K), 1.8 GPa (120 K), and 0 GPa (40 K). To our knowledge, this

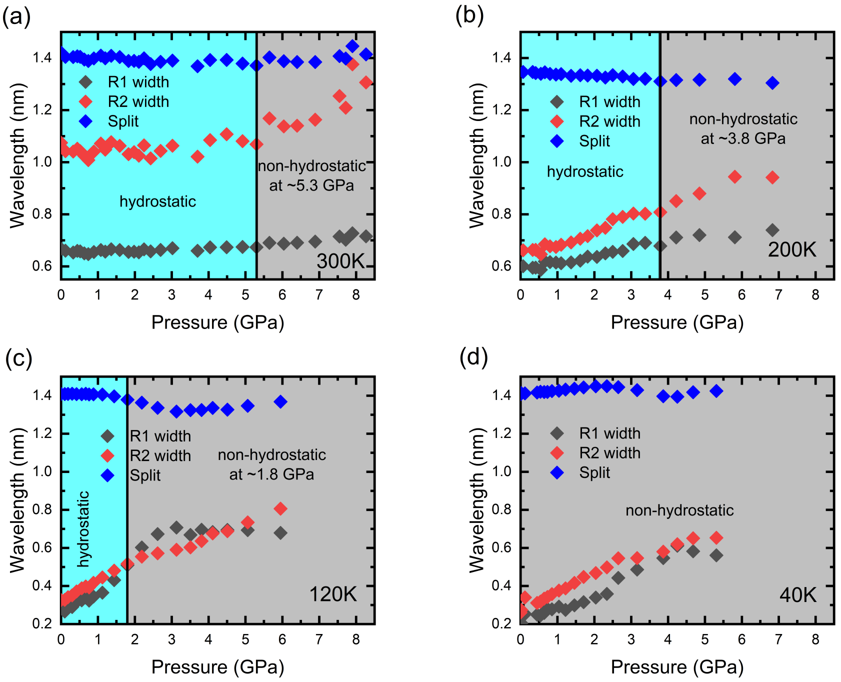

Figure 2.7: Analysis of ruby R1 and R2 peaks split and broadening at (a) 300, (b) 200, (c) 120, and (d) 40 K. Reprinted from Ref. J. Phys. Chem. Lett. 2025, 16, 25, 6372–6377 under CC-BY 4.0 license. Copyright 2025 R. Bartoszewicz et al.

represents the first systematic determination of the hydrostatic stability of Daphne 7575 down to 40 K. The pressure uncertainty derived from ruby fluorescence calibration was estimated to be ±0.05 GPa at room temperature, with slightly larger uncertainties under quasi-hydrostatic conditions.[148, 149, 150]

For combined temperature-pressure measurements, pressure was re-evaluated at each temperature step to account for drift arising from thermal contraction of both the pressure medium and DAC components. This procedure ensures that the measured pressure corresponds accurately to the sample environment, supporting reliable interpretation of pressure-dependent optical spectra.

Non-Hydrostatic Effects

Non-hydrostatic conditions within the DAC can significantly influence optical spectra. Uneven stress distribution within the sample chamber may lead to peak broadening, nonlinear band-gap shifts, artificial splitting of emission lines, or the appearance of defect-related emission features. Such stress-induced artifacts may mimic signatures of structural phase transitions if not carefully considered.[151, 152, 153, 154]

To minimize these effects, the sample dimensions were restricted to below 50 μm to reduce pressure gradients across the chamber. Pressure was increased in small increments (0.1-0.2 GPa) near critical regions, and measurements were repeated upon decompression to verify reversibility. This approach ensured reliable interpretation of pressure-induced spectral changes.

2.4.5 Pressure Calibration Procedure

Pressure inside the DAC was determined using the ruby fluorescence method, which remains the most widely adopted in situ pressure standard for static HP experiments.

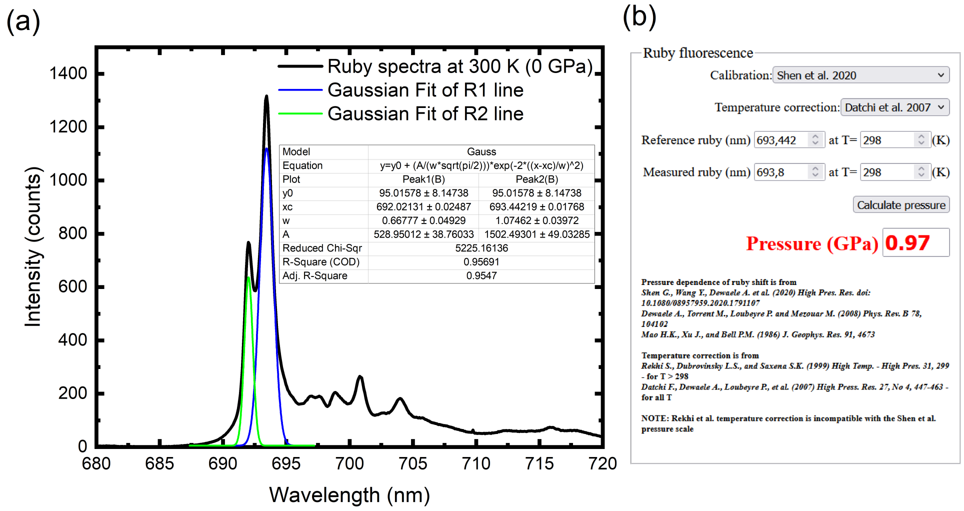

Model	Gauss	
Equation	y=y0 + (A/(w*sqrt(pi/2)))*exp(-2*((x-xc)/w)^2)	
Plot	Peak1(B)	Peak2(B)
y0	95.01578 ± 8.14738	95.01578 ± 8.14738
xc	692.02131 ± 0.02487	693.44219 ± 0.01768
w	0.66777 ± 0.04929	1.07462 ± 0.03972
A	528.95012 ± 38.76033	1502.49301 ± 49.03285
Reduced Chi-Sqr	5225.16136	
R-Square (COD)	0.95691	
Adj. R-Square	0.9547	

Ruby fluorescence

Calibration: Shen et al. 2020

Temperature correction: Datchi et al. 2007

Reference ruby (nm) 693,442 at T= 298 (K)

Measured ruby (nm) 693,8 at T= 298 (K)

Pressure (GPa) 0.97

Pressure dependence of ruby shift is from
Shen G., Wang Y., Dewaele A. et al. (2020) High Pres. Res. doi: 10.1080/08957959.2020.1791107
Dewaele A., Torrent M., Loubeyre P. and Mezouar M. (2008) Phys. Rev. B 78, 104102
Mao H.K., Xu J., and Bell P.M. (1986) J. Geophys. Res. 91, 4673

Temperature correction is from
Rekhi S., Dubrovinsky L.S., and Saxena S.K. (1999) High Temp. - High Pres. 31, 299 **- for T > 298**
Datchi F., Dewaele A., Loubeyre P., et al. (2007) High Press. Res. 27, No 4, 447-463 **- for all T**

NOTE: Rekhi et al. temperature correction is incompatible with the Shen et al. pressure scale

Figure 2.8: (a) Gaussian fitting of the R_1 and R_2 ruby fluorescence lines used to determine the peak position of the R_1 transition. (b) Calculation of pressure from the relative wavelength shift of the R_1 line.

Ruby Fluorescence Method

Pressure was determined from the shift of the R_1 fluorescence line of Cr^{3+}-doped Al_2O_3 (ruby). A single ruby sphere (5-10 μm diameter) was placed adjacent to the sample within the gasket chamber to ensure local pressure determination. The use of a single ruby minimizes line broadening and avoids spectral overlap effects that may arise from multiple fluorescence sources.

Fluorescence was excited using a 532 nm solid-state laser. The emission spectrum was collected using:

- an Avantes ULS4096CL-RS-EVO spectrometer equipped with a DCL-UV/VIS-200 (600 lines/mm, 300 nm blaze) grating for pressure-dependent transimission measurements, and
- an Andor monochromator (600 lines/mm, 500 nm blaze) coupled to a SI CCD detector for pressure-dependent PL measurements.

The ruby spectrum at 300K and ambient pressure is shown in Figure 2.8 (a). The R_1 and R_2 lines were extracted by Gaussian fitting.

Pressure was calculated from the relative wavelength shift $\Delta\lambda = \lambda - \lambda_0$ using the hydrostatic calibration of Shen.[155]

The applied pressure scale is given by:

$$P[GPa] = 1.87(\pm 0.01) \times 10^3 \left(\frac{\Delta\lambda}{\lambda_0}\right) \left[1 + 5.63(\pm 0.03) \left(\frac{\Delta\lambda}{\lambda_0}\right)\right], \tag{2.3}$$

where:

- λ_0 is the R_1 wavelength at ambient conditions,
- $\Delta\lambda$ - is the measured wavelength,
- $\Delta\lambda = \lambda - \lambda_0$.

Temperature Correction

The R_1 fluorescence line of ruby exhibits a small but systematic temperature dependence due to lattice contraction and electron-phonon interactions. If uncorrected, this effect produces an apparent pressure shift, particularly at cryogenic temperatures.

To account for this, a temperature-corrected reference wavelength $\lambda_0(T)$, was used in all low-temperature measurements. Following the formulation of Datchi,[156] the pressure is expressed as:

$$P[GPa] = 1.87(\pm 0.01) \times 10^3 \left(\frac{\Delta\lambda(T)}{\lambda_0(T)}\right) \left[1 + 5.63(\pm 0.03) \left(\frac{\Delta\lambda(T)}{\lambda_0(T)}\right)\right], \tag{2.4}$$

For temperatures between 50 K and 296 K, the temperature-induced shift was calculated as:

$$\Delta\lambda_0(50 < T < 296K) = 0.00664(4)\Delta T + 6.76(52) \times 10^{-6}\Delta T^2 - 2.33(16) \times 10^{-8}\Delta T^3, \tag{2.5}$$

For temperatures below 50 K:

$$\Delta\lambda_0(T < 50K) = -0.887(1), \tag{2.6}$$

Temperature was independently measured using a calibrated sensor near the DAC, ensuring accurate pressure determination across the entire temperature range. This correction allows reliable mapping of pressure-dependent phenomena at low temperatures, minimizing systematic errors arising from thermal effects.

2.4.6 Pressure-Dependent Transmission Measurements at Room Temperature

Pressure-dependent transmission measurements were performed at room temperature using a DAC mounted on a custom XYZ micrometer stage, allowing precise positional alignment. The DAC was positioned between a halogen lamp below, serving as the transmitted light source, and a microscopic objective above to collect light transmitted through the sample chamber. The configuration also enabled observation of color changes during compression.

A camera mounted above the microscope provided live imaging for DAC alignment. For spectral measurements, the camera can be replaced with a custom fiber-optic holder connected to a spectrometer. The microscope back was removed to allow external illumination and facilitate 532 nm laser excitation for ruby fluorescence-based pressure calibration.

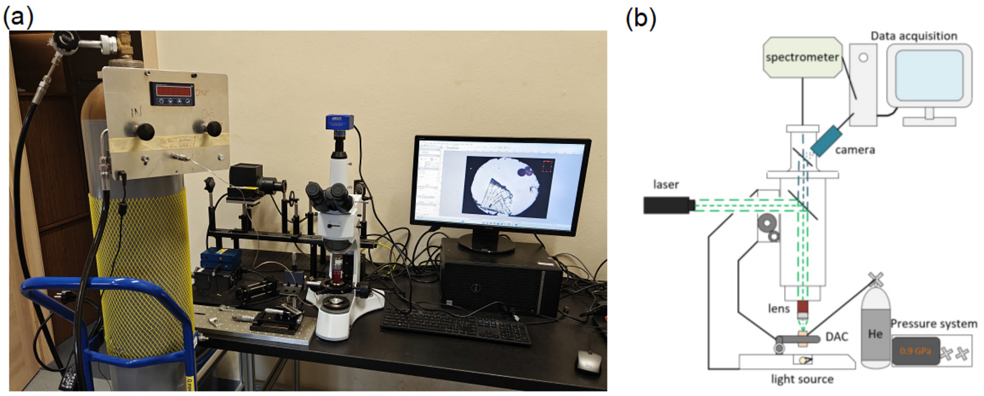

Figure 2.9: Pressure-dependent transmission measurement setup at room temperature. (a) Photograph of the experimental arrangement. (b) Schematic representation of the pressure-driven transmission measurement setup. configuration Reprinted from Ref. J. Phys. Chem. Lett. 2025, 16, 25, 6372–6377 under CC-BY 4.0 license. Copyright 2025 R. Bartoszewicz et al.

Transmitted light intensity depends on both sample thickness and the numerical aperture of the objective which governs light collection efficiency. Ambient light was minimized to reduce measurement artifacts.

Measurements were performed in two steps. First, the DAC contained only the pressure medium and a ruby chip to acquire a reference signal. Subsequently, the DAC was reassembled with the sample, and transmission spectra were measured. This procedure ensures accurate normalization and reproducibility of the optical response under compression.

2.4.7 Pressure-Dependent Photoluminescence Measurements at Room Temperature

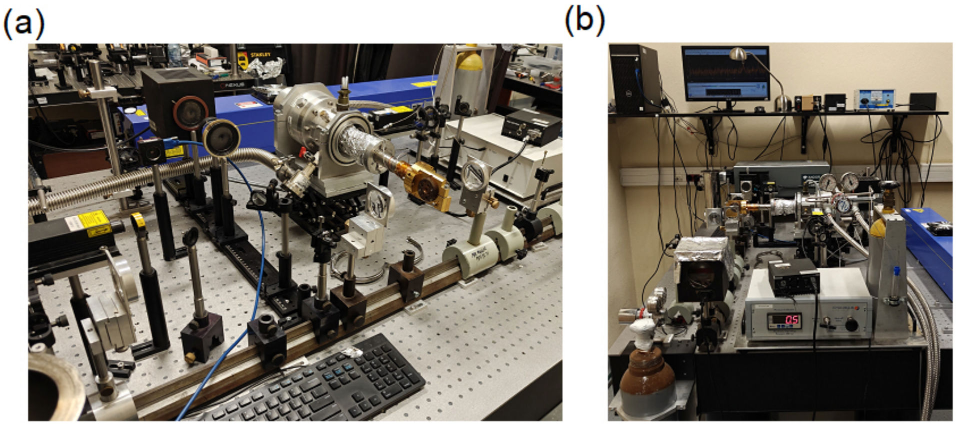

Figure 2.10: Pressure-dependent PL measurement setup at room temperature. (a) Photograph of the experimental arrangement. (b) Photograph of the experimental side-view.

PL measurements under pressure were performed using the same DAC, mounted on the cold finger of a closed-cycle cryostat, which served solely as a mechanically stable holder. PL spectra were collected in a backscattering geometry using continuous-wave excitation with 405 or 325 nm laser line.

Pressure was monitored simultaneously via ruby fluorescence measured in transmission using a 532 nm laser. The excitation beam was focused onto the sample or ruby sphere through 10 cm focal-length lenses, and emitted light was collected by the same objective and directed to a Si CCD detector on the monochromator. A long-pass filter was placed to suppress scattered laser light, ensuring clean detection of PL signals.

Spectral acquisition employed a 150 lines/mm grating blazed at 500 nm for sample PL and a 600 lines/mm grating blazed at 500 nm for ruby fluorescence. Pressure was applied incrementally at room temperature, allowing ∼4 minutes for mechanical stabilization at each step to ensure pressure equilibration in the sample chamber.

This configuration defines the baseline high-pressure optical platform. In the subsequent section, active temperature control is incorporated to enable combined pressure- and temperature-dependent measurements.

2.5 Combined Temperature- and Pressure-Dependent Measurements

2.5.1 Experimental Configuration

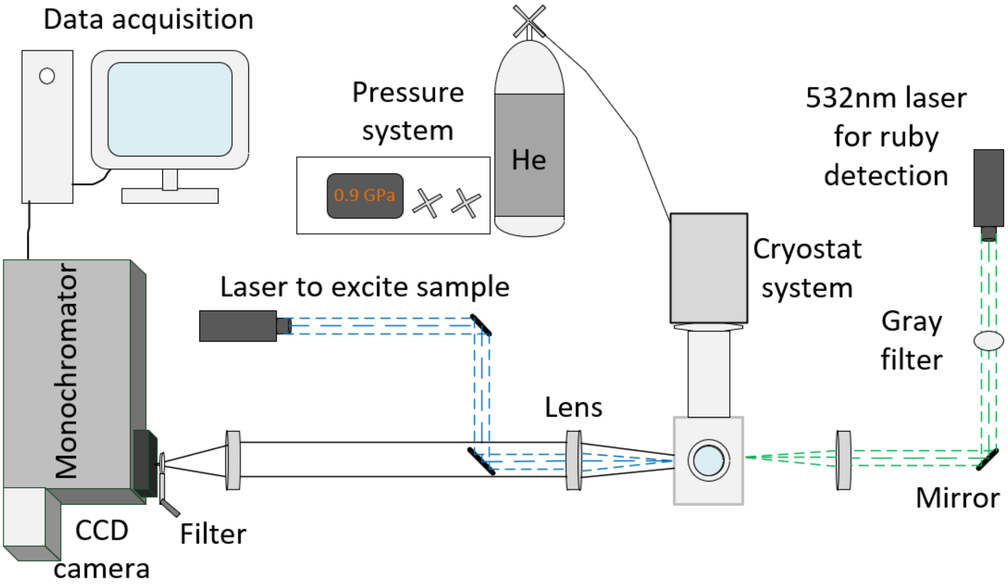

Figure 2.11: Scheme of the system used for combined temperature- and pressure-dependent PL measurements. Reprinted from Ref. J. Phys. Chem. Lett. 2025, 16, 25, 6372–6377 under CC-BY 4.0 license. Copyright 2025 R. Bartoszewicz et al.

Figure 2.11 presents the integrated temperature- and pressure-dependent configuration adapted for PL spectroscopy. DAC was mounted on the cold finger of a closed-cycle cryostat and operated under high-vacuum conditions. The system enables measurements in the 10-300 K temperature range.

Temperature was monitored using a calibrated sensor attached directly to the DAC body in close proximity to the anvil assembly. Since the sensor measures the DAC body rather than the sample chamber itself, a finite thermal gradient across the gasket and pressure medium must be considered. All measurements were performed under strictly isothermal conditions. Prior to spectral acquisition, the system was stabilized at the target temperature for the whole measurement process. Under these conditions, the temperature difference between the sensor and the sample is expected to remain below ± 0.5 K, which is included in the overall temperature uncertainty.

The cryostat was mounted on the same optical table as the excitation and detection components. Consequently, mechanical vibrations generated by the closed-cycle compressor were transmitted throughout the entire setup. However, no measurable influence on the PL spectral position or linewidth was observed within the experimental resolution. This indicated that vibration-induced misalignment or intensity fluctuations were negligible for the measurement conditions employed.

2.5.2 Technical Challenges and Limitations

The implementation of combined temperature- and pressure-dependent PL measurements presents several technical challenges arising from both the DAC construction and the integration of the DAC within a cryogenic optical setup. While many of these limitations were successfully mitigated during this work, some represent intrinsic constraints of the current configuration and define directions for future technical improvements:

- Solidification of Pressure Medium

  The selection of an appropriate pressure-transmitting medium is critical for low-temperature experiments. Many commonly used media solidify upon cooling, leading to non-hydrostatic stress conditions and pressure gradients within the sample chamber. Such non-hydrostatic conditions may induce artificial peak broadening, spectral splitting, or apparent phase-transition-like features unrelated to intrinsic material properties.

  In the present study, Daphne 7575 oil was used as a compromise, maintaining quasi-hydrostatic conditions at low temperatures and moderate pressures. Although noble gases such as helium or argon provide superior hydrostatic conditions over broad pressure and temperature ranges, their gas loading is technically demanding.

- Temperature Gradient at Sample Position

  Finite thermal conductivity of the DAC components and pressure medium may result in small temperature gradients between the cryostat cold finger and the sample. This effect becomes particularly relevant at the lowest temperatures, where even minor differences may influence emission linewidth and peak positions. These gradients are included in the estimated sample temperature uncertainty

- Laser-Induced Local Heating

  Laser excitation inherently introduces local heating at the sample position. In confined DAC geometries, heat dissipation is limited, and the effective local temperature may exceed the nominal cryostat temperature, particularly at higher excitation powers. Excitation power was carefully optimized (20-150 μW). Nevertheless, a residual uncertainty in the effective sample temperature remains and contributes to systematic experimental error.

- Thermal Contraction of the DAC and Pressure Drift

  Cooling the DAC and cryostat introduces thermal contraction, which can cause both pressure drift inside the sample chamber and small shifts of the laser spot relative to the sample. These effects must be considered when analyzing temperature-dependent PL spectra recorded at nominally constant pressure. Periodic optical realignment was performed during cooling cycles to maintain reproducibility.

- Limited Decompression and Safety

  Mechanical access to the DAC is restricted inside the vacuum cryostat. While membrane-type DACs allow pressure increase via gas injection, decompression at low temperature is not possible without manual intervention. Operation of high-pressure cryogenic systems also involves safety considerations, including pressurized helium and vacuum hazards. Strict adherence to established procedures was maintained throughout all experiments.

Future Technical Developments

Implementation of these improvements would bring the setup closer to the state-of-the-art HP optical laboratories, enabling highly accurate, isobaric, and reproducible measurements. Future developments include:

- Implementation of a dual-membrane DAC for dynamic pressure stabilization,
- Introduction of automated pressure control systems,
- Installation of a dedicated helium gas-loading system,
- Integration of in situ pressure monitoring during temperature sweeps.

Despite these limitations, the developed configuration enables stable and reproducible combined temperature- and pressure-dependent PL measurements. Absolute pressure accuracy, local temperature determination, and isobaric stability are affected by the identified constraints. However, all qualitative physical conclusions reported in this thesis remain robust. Systematic evaluation of these limitations further strengthens the reliability of the results and provides a clear roadmap for future technical improvements.

2.6 Data Processing and Error Analysis

Accurate interpretation of optical measurements requires careful data processing, peak extraction, and rigorous estimation of uncertainties. This section outlines the procedures used to ensure reliable and reproducible results. All of the operations reported here, which are connected to the analysis of obtained experimental spectras, were performed in the use of Origin software from OriginLab producer.

2.6.1 Baseline Correction and Normalization

Raw optical spectra, including PL and transmission data, were first corrected for instrumental background and detector response. A baseline was fitted using a third-order polynomial, with fitting regions selected to exclude known sample peaks and minimize contributions from background fluctuations. In some cases, a spline-based baseline was applied to account for broad, slowly varying background features.

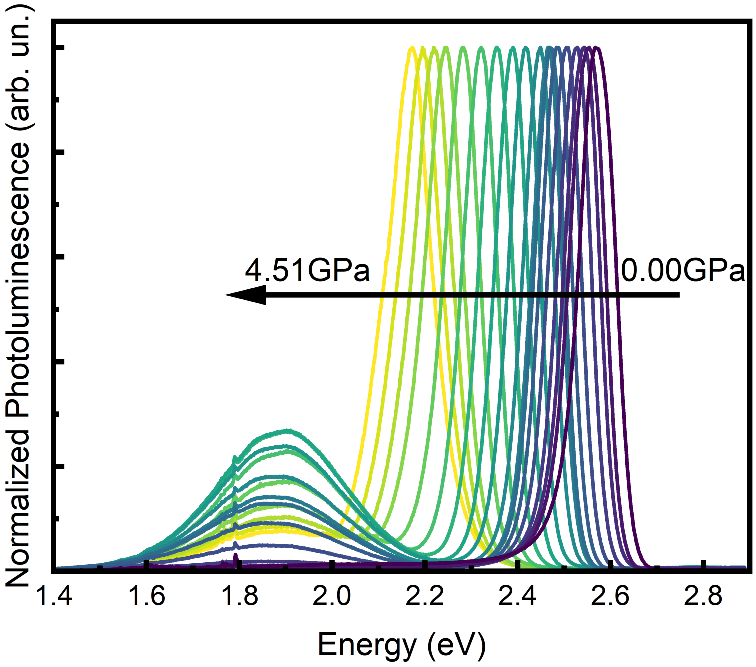

Figure 2.12: Example of normalization of pressure-dependent PL spectra at 120 K for $(4FPEA)_2SnBr_4$.

All spectra were subsequently normalized to either the maximum intensity of a reflectance peak or the integrated intensity over a defined spectral window (Figure 2.12). This normalization facilitates comparison between measurements taken at different pressures or temperatures and ensures that intensity variations reflect intrinsic sample behavior rather than instrumental effects.

As a consequence of broad range of measurement spectra collection, some of the features as emergence of additional peaks from background illumination, noise-induced peaks, or regions without any important features were successfully removed in this pre-analysis process.

2.6.2 Peak Fitting and Parameter Extraction

Spectral peaks were modeled using Gaussian lineshape (Figure 2.13). Initial parameter estimates were obtained from peak maxima, while global fitting routines were used for overlapping or closely spaced peaks to ensure consistent extraction across datasets.

Goodness-of-fit was evaluated using reduced chi-square (χ^2) and R^2 metrics. Only

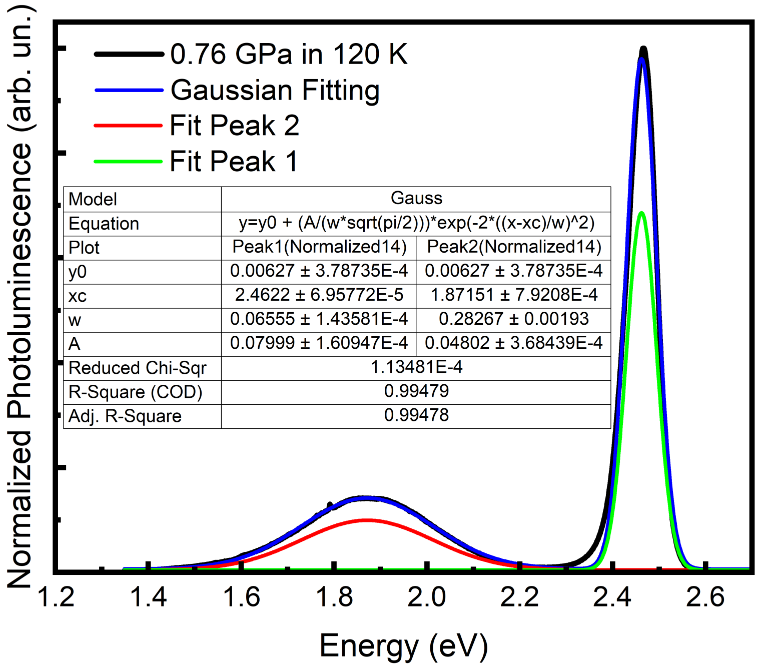

Model	Gauss	
Equation	y=y0 + (A/(w*sqrt(pi/2)))*exp(-2*((x-xc)/w)^2)	
Plot	Peak1(Normalized14)	Peak2(Normalized14)
y0	0.00627 ± 3.78735E-4	0.00627 ± 3.78735E-4
xc	2.4622 ± 6.95772E-5	1.87151 ± 7.9208E-4
w	0.06555 ± 1.43581E-4	0.28267 ± 0.00193
A	0.07999 ± 1.60947E-4	0.04802 ± 3.68439E-4
Reduced Chi-Sqr	1.13481E-4	
R-Square (COD)	0.99479	
Adj. R-Square	0.99478	

Figure 2.13: Example of Gaussian fit of pressure-dependent PL spectra at 120 K and 0.76 GPa for $(4FPEA)_2SnBr_4$.

fits meeting established quality thresholds were used for further analysis. From these fits, key parameters were extracted, including peak position, full width at half maximum, and integrated intensity. These parameters directly probe physical phenomena such as:

- Peak energy evolution - tracked via the pressure- and temperature-dependent peak position,
- Electron-phonon interactions - inferred from linewidth broadening,
- Exciton activation energy and recombination dynamics - deduced from relative peak intensities and their variation under combined pressure-temperature conditions.

Representative fits, including raw, baseline-corrected, and modeled spectra, were inspected visually to confirm the reliability of automated procedures.

In the case of transmission measurements, experimental spectra were redone with the procedures mentioned earlier in this section. To determine the absorption edge position of the investigated sample, a linear fit was used, as shown in Figure 2.14:

2.6.3 Uncertainty Estimation

Uncertainty in extracted parameters was assessed by combining contributions from multiple sources:

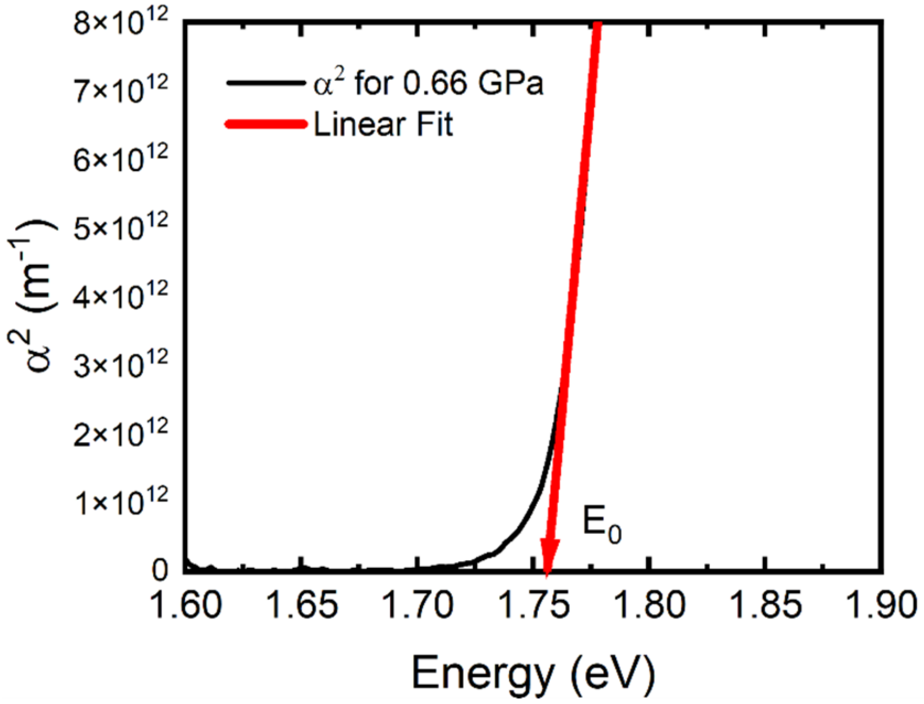

Figure 2.14: Example of linear fit of pressure-dependent transmission spectra at 300 K and 0.66 GPa for $(4FPEA)_2SnI_4$.

- Instrumental uncertainty - including spectral resolution of the monochromator, detector noise, and wavelength calibration accuracy,
- Fitting uncertainty - obtained from the covariance matrix of the least-squares fitting procedure,
- Systematic errors - arising from baseline subtraction, normalization, and pressure calibration.

The combined uncertainty was propagated for derived quantities, such as band gap energy, exciton activation energy, and linewidth, using standard error propagation formulas. Pressure-dependent uncertainties were further updated at each temperature step to account for thermal contraction effects in the DAC and pressure medium.

Where relevant, all pressure- and temperature-dependent measurements were repeated upon decompression or reheating to verify reversibility. This ensures that the reported trends reflect intrinsic sample behavior rather than artifacts from experimental drift or irreversible sample changes.

This workflow, establishes a robust, reproducible framework for analyzing temperature and HP optical data, providing confidence in the quantitative trends and qualitative conclusions presented in this thesis.

Publications

This chapter presents a collection of four peer-reviewed research articles (article 3.2 is published in arXiv) that constitute the primary scientific contribution of this dissertation. The research explores the frontiers of Pb-free,2D HOIPs, specifically focusing on how their "structural softness" can be exploited to tune optoelectronic properties under extreme conditions. By subjecting these materials to hydrostatic pressures reaching 11 GPa and temperatures ranging from 20 to 320 K, we uncover the fundamental mechanisms governing band-edge tuning, phase stability, and excitonic localization.

The sequence of publications is organized as a progressive investigation into the interplay between lattice dynamics and electronic structure:

Publication 3.1 and **Publication 3.2** investigate the record-breaking electronic tunability of Sn-based iodide HOIPs. Using $(4FP)_2SnI_4$ and TMA_2SnI_4 as model systems, these works establish that Sn-based HOIPs possess some of the highest pressure coefficients reported to date (up to -187 meV/GPa). These studies demonstrate that the band gap can be narrowed linearly over several GPa, even across temperature-driven structural phase transitions, positioning these materials as prime candidates for high-sensitivity pressure sensors.

Publication 3.3 explores the complex energy landscape of excitons in $(4FPEA)_2SnBr_4$. This study uncovers a striking dichotomy in the pressure response: while near-band-edge (NBE) emission redshifts under compression, the STE emission exhibits an anomalous blueshift. This research provides a microscopic framework for understanding small polaron formation and demonstrates how halide-specific lattice rigidity and dielectric screening (comparing Br to I analogues) dictate the stabilization of localized versus delocalized excitonic states.

Publication 3.4 transitions the investigation to Cu-based systems, addressing the critical challenge of thermodynamic and structural stability. By utilizing hydrophobic phenylmethylammonium (PMA) cations, we demonstrate that $(PMA)_2CuX_4$ (X = Br, Cl) maintains structural integrity up to $\sim$11 GPa. This work provides a comparative analysis of thermochromism versus piezochromism, revealing that while both temperature and pressure induce significant color changes (redshifts), the underlying lattice mechanisms, thermal expansion versus mechanical compression, interact with the electron-phonon landscape in fundamentally different ways.

Together, these works provide a comprehensive framework for the rational design of stimuli-responsive, Pb-free optoelectronic. For each publication, the specific contributions of the author are detailed in the following sections.

3.1 Giant Band Gap Narrowing under Hydrostatic Pressure in $(4FP)_2SnI_4$ Halide Perovskite

Rafał Bartoszewicz†, Jakub Ziembicki, Ewelina Zdanowicz, Artur P. Herman, Jarosław Serafińczuk, Jesús Sánchez-Diaz, Samrat Das Adhikari, Iván Mora-Seró, Robert Kudrawiec†

The Journal of Physical Chemistry Letters, vol. 16, no. 25, pp. 6372–6377 (2025).
DOI: 10.1021/acs.jpclett.5c00903

Author's Contribution:

Rafał Bartoszewicz with supervisor formulated the physical problem of pressure-induced band gap tuning in layered Sn-based HOIPs and defined the research hypothesis concerning the linear pressure dependence of the fundamental band gap.

The author designed and executed the experimental plan for combined pressure- and temperature-dependent optical spectroscopy, optimizing measurement conditions and data acquisition using the existing HP setup. All high-pressure PL and transmission measurements were performed by the author. Particular attention was devoted to establishing and validating hydrostatic conditions to ensure reliable determination of intrinsic pressure coefficients.

The author contributed to HP X-ray diffraction (XRD) measurements. Data processing and analysis were performed independently, including extraction of pressure coefficients at different temperatures, evaluation of their temperature dependence, uncertainty analysis, and fitting using the third-order Birch-Murnaghan equation of state.

The author established systematic comparisons with Pb-based HOIPs and conventional semiconductors and positioned the results within the broader framework of pressure-dependent electronic structure evolution in structurally soft semiconductors.

The theoretical results were integrated with the experimental findings to provide a microscopic explanation of the observed band gap narrowing, demonstrating that the large and linear pressure coefficient originates primarily from pressure-induced shortening of Sn-I bonds and the resulting modification of orbital overlap within the inorganic layers.

The combined experimental-theoretical analysis allowed for a consistent physical interpretation of the temperature-dependent pressure coefficients and the absence of structural phase transitions in the investigated pressure range.

All figures were prepared by Rafał Bartoszewicz, who also wrote the manuscript, and answered reviewers questions.

---

† corresponding author

THE JOURNAL OF
PHYSICAL CHEMISTRY
LETTERS
A JOURNAL OF THE AMERICAN CHEMICAL SOCIETY

pubs.acs.org/JPCL

Letter

Giant Band Gap Narrowing under Hydrostatic Pressure in $(4FP)_2SnI_4$ Halide Perovskite

Rafał Bartoszewicz,* Jakub Ziembicki, Ewelina Zdanowicz, Artur P. Herman, Jarosław Serafińczuk, Jesús Sánchez-Diaz, Samrat Das Adhikari, Iván Mora-Seró, and Robert Kudrawiec*

Cite This: *J. Phys. Chem. Lett.* 2025, 16, 6372−6377

Read Online

ACCESS | Metrics & More | Article Recommendations | Supporting Information

ABSTRACT: One of the most intriguing properties of hybrid halide perovskites is their structural softness. The interplay between organic and inorganic sublattices leads to a multitude of physical phenomena that are not observed in conventional semiconductors such as III−V materials. One among these is the exceptional band gap tunability under hydrostatic pressure. In this context, tin-based perovskites exhibit a more pronounced effect than their lead-based counterparts. Here, we report on one of the largest band gap tunabilities in this material family. The studied material, layered tin-based $(4FP)_2SnI_4$ perovskite, exhibits an exceptionally strong pressure sensitivity, with a band gap shift of up to −160 meV/GPa at room temperature. Combined experimental and computational studies reveal that its band gap dependence on pressure remains linear in the 0−5 GPa range, making $(4FP)_2SnI_4$ highly attractive for pressure-sensor applications.

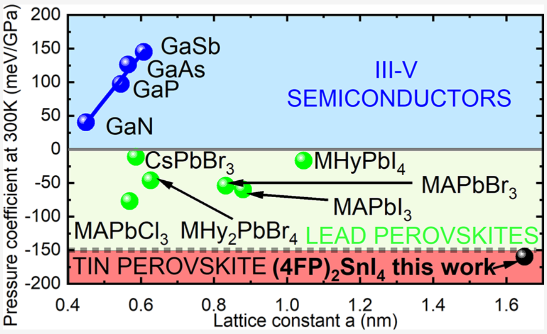

Layered or so-called "two-dimensional" (2D) lead halide perovskites have received considerable attention in recent years due to their high exciton binding energy, high photoluminescence quantum yield, and versatile exciton radiative recombination processes, which are desirable for micro/nanolasers and high-efficiency light-emitting diodes (LED).[1−14] Nevertheless, the utilization of Pb-based perovskites is constrained by the toxicity of the heavy metal component, which restricts their commercial use in optoelectronic devices. In order to optimize the utility of perovskites, researchers have attempted to substitute Pb with less toxic elements, such as Sn.[15,16] Sn-based perovskites demonstrate similar or superior electronic and optical properties compared to Pb-based perovskites, such as higher charge carrier mobilities, long-lived hot carriers, low-cost synthesis, and environmental inertness for use in commercial applications.[17−24] Despite these facts, the main factor that limits the use of Sn-based perovskites for mass-produced devices is their poor structural stability due to the rapid oxidation of the Sn^{2+} state to the Sn^{4+} state under ambient conditions, as well as the abundance of Sn vacancy defects.[25] One of the representatives of Sn-based halide perovskites is 4-fluorophenethylammonium tin iodide ($(4FP)_2SnI_4$), which is a perovskite suitable for applications such as micro/nanolasers, LEDs, or another applications.[12,26] To enhance the application prospects of $(4FP)_2SnI_4$, it is necessary to explore its optical properties, especially its response to hydrostatic pressure. Due to the high flexibility of the crystal structure of perovskites, this approach seems to be an appropriate way to modulate the lattice in a controllable manner to tailor their optoelectronic properties, such as the band gap and the intensity of photoluminescence (PL).[27,28] So far, PL and absorption measurements under hydrostatic pressure have been reported for numerous 2D perovskites.[29−36] However, such studies are rare for tin-based perovskites, and no reports exist for $(4FP)_2SnI_4$, particularly regarding temperature-dependent experiments.

In this Letter, we report on the PL of near-band gap emission (NBE) and absorption edge studies for $(4FP)_2SnI_4$ perovskite under hydrostatic pressure to determine the narrowing of the band gap and compare it with other semiconductor compounds, particularly Pb-based halide perovskites. We have observed a giant pressure coefficient of −160 meV/GPa for $(4FP)_2SnI_4$, which leads to one of the highest band gap tunability potential above halide perovkites and conventional semiconductors (see graphic in the Abstract).[34,37−48] Moreover, unlike in conventional semiconductors, the band gap pressure coefficient significantly changes with temperature.

The synthesis of $(4FP)_2SnI_4$ was carried out using the developed methodology, as detailed in the Supporting Information (SI). Specifically, the microcrystals were synthesized by carefully controlling the amount of hydroiodic acid to

Received: March 26, 2025
Revised: June 9, 2025
Accepted: June 10, 2025
Published: June 16, 2025

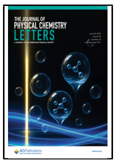

https://doi.org/10.1021/acs.jpclett.5c00903
J. Phys. Chem. Lett. 2025, 16, 6372−6377

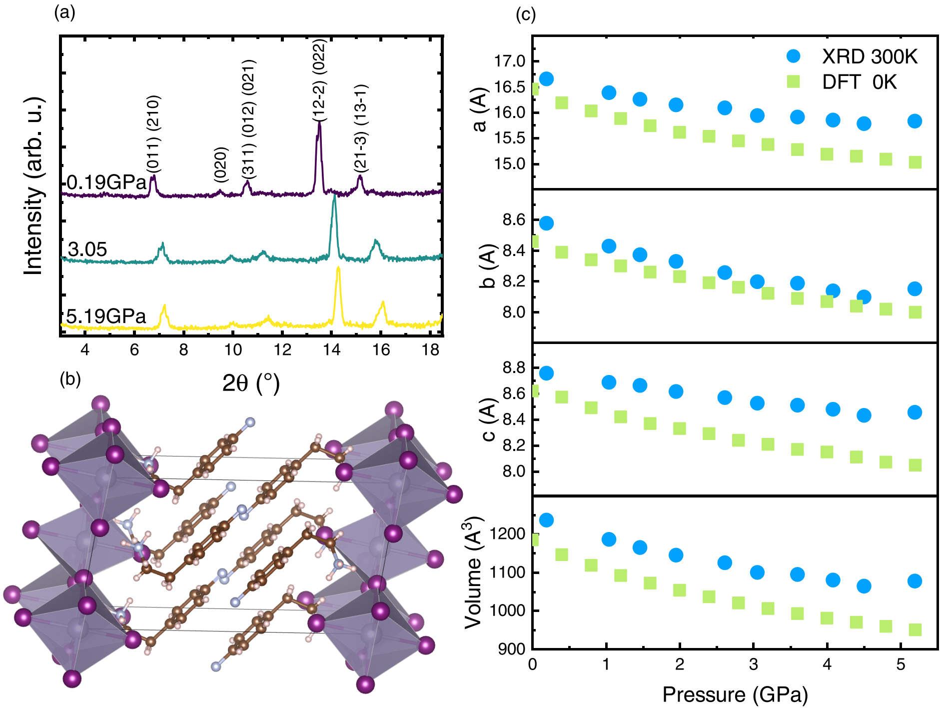

Figure 1. (a) Powder XRD pattern of $(4FP)_2SnI_4$ in three selected pressures, together with interpretation of visible reflections. (b) Crystal structure of $(4FP)_2SnI_4$ used in spectral interpretation and DFT simulations. (c) Lattice parameters and unit cell volume as a function of applied pressure, derived from XRD measurements and DFT calculations.

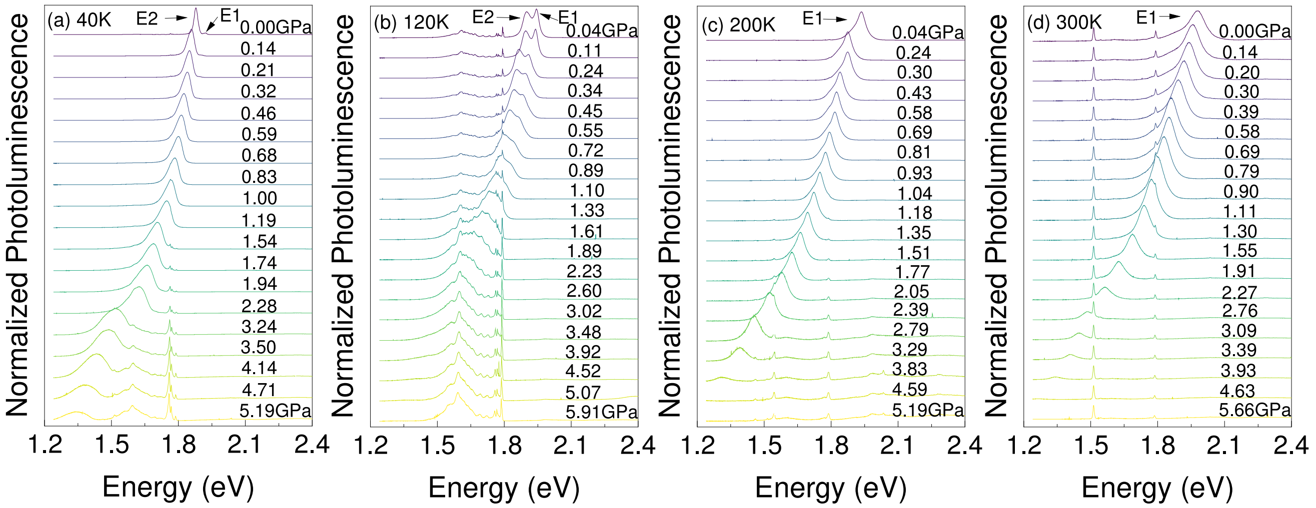

Figure 2. Photoluminescence spectra of $(4FP)_2SnI_4$ as a function of applied pressure at four different temperatures: 40, 120, 200, and 300 K (panels a−d respectively).

prevent an excess of iodide and water, which could otherwise compromise the stability of the material. Acetic acid was employed as the solvent, playing a crucial role in stabilizing the perovskite. It was observed that acetic acid helped maintain structural stability by coordinating with surface iodide and tin atoms,[12,49] thereby reducing the moisture exposure to the material. By following this modified approach, the stability of $(4FP)_2SnI_4$ was significantly enhanced and has been studied in a previous report.[12] After successful synthesis and fundamental optical characterization at room temperature, we measured XRD patterns as a function of the pressure. Figure 1a displays the XRD patterns of $(4FP)_2SnI_4$ under pressure up to 5.19 GPa at 300 K. All visible diffraction peaks are well indexed assuming a monoclinic phase structure with a β angle in the unit cell of 98.65 ± 0.01°, which gradually shifts to higher angle values with increasing pressure. No new peak arises, indicating the structural stability of $(4FP)_2SnI_4$ within the investigated pressure range. Figure 1b presents the monoclinic crystal structure of $(4FP)_2SnI_4$, which was used for the interpretation of the XRD patterns and for DFT simulations presented in this work. Space group of $(4FP)_2SnI_4$ was determined as $P21/c$ while $a = 16.654 \pm 0.008$ Å, $b = 8.6049 \pm 0.0015$ Å, $c = 8.756 \pm 0.004$ Å, $\alpha = 90.00°$, $\gamma = 90.00°$, and $V = 1240.3625$ Å^3 Molecular structure of 4FP is presented in

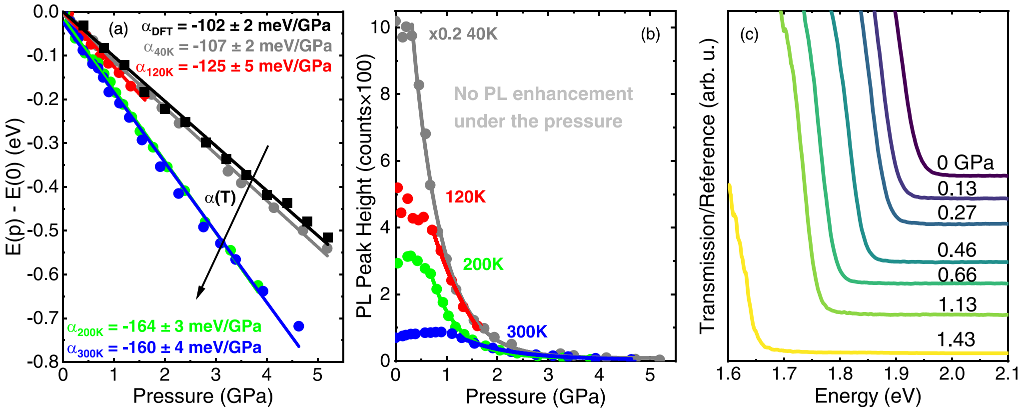

Figure 3. (a) Band gap change $\Delta E = E(P) - E(P = 0)$ as a function of pressure derived from PL spectra for different temperatures (circles), together with linear fits (lines). Clear dependence of the pressure coefficient on temperature can be observed. Results of DFT simulation are also presented as black squares. (b) PL peak high for different temperatures and pressures. (c) Transmission spectra near the absorption edge for different values of applied pressure.

Figure S1 in Supporting Information. Figure 1c shows the refined lattice constants a, b, c, and unit cell volume. The lattice parameters of the unit cell were calculated based on the position of reflections (020), (011), (210), (022), and $(12\bar{2})$ and determined for each pressure, which made it possible to plot the change in lattice parameters and unit cell volume as a function of pressure. The derived trends indicate that no phase transition for $(4FP)_2SnI_4$ occurs. Calculated lattice parameters, angles, volume with uncertainties, and R-factor are presented in Table 1 in the Supporting Information. For comparison, theoretical results are also presented in Figure 1c, which are derived from DFT calculations and compare quite well with the experimental trend. Slightly lower values of the lattice parameters from the theory can be explained on the basis of thermal lattice expansion (DFT calculations correspond to 0 K, while the experimental data are obtained at room temperature). Based on the third-order Birch−Murnaghan equation of state, we derived a bulk modulus of 20.09 ± 1.41 GPa, which is comparable to other perovskite structures.[50−52] Third-order Birch−Murnaghan fitting is presented in Figure S2 in Supporting Information.

Figure 2a−d shows normalized PL spectra of $(4FP)_2SnI_4$ as a function of hydrostatic pressure, i.e., isothermal PL measurements at 40, 120, 200, and 300 K, respectively. A discussion about the hydrostaticity of the used pressure medium is presented in Figure S3 in Supporting Information. The temperature dependence of the PL spectrum is shown in Figure S4, where the redshift of the NBE composed of E1 and E2 peaks is observed as the temperature decreases, but its magnitude is negligible compared to the pressure effect studied in this work. In the spectra presented in panels a−d and in Figure S4, E1 and E2 features are marked. This dual peak structure has also been observed in $(4FP)_2SnI_4$[12] other 2D perovskite microcrystals.[53] Although the specific origins of the E1 and E2 peaks have not been fully clarified, they have been attributed to optical transitions related to isolated Sn−I layers and the edge of the microcrystal, respectively.[12,54] Depending on the temperature, either E1 or E2 is more intensive and remains visible throughout the studied pressure range. Regardless of this, a huge redshift of the NBE position can be observed as the pressure increases. The pressure-independent peak observed at 1.5 eV is associated with the second order of diffraction of the 405 nm laser used in this measurement. Figure 3a shows the energy position of NBE extracted from the spectra presented in Figure 2a−d. The differences in the spectrum intensities at individual temperatures make it difficult to accurately read the energy position at higher pressures for the 120 K case in Figure 2b. In this case, the NBE signal is overlapped by emission from the ruby sphere (used to measure the pressure) at 1.78 eV. Despite this difficulty, robust red-shift of NBE is evident with increasing hydrostatic pressure. The pressure coefficients for NBE were calculated from the linear fitting of the energy of the NBE versus applied pressure. Obtained values are negative, and they decrease with increasing temperature. At the same time, the intensity of the PL drops, whereas peak width increases with applied pressure.

Figure 3b presents the temperature dependence of the intensity of the NBE at varying hydrostatic pressure. As can be seen, the NBE intensity drops rapidly with increasing pressure, and at values around 3 GPa, it becomes difficult to estimate with good accuracy. For each temperature, this trend is maintained. In contrast to many other halide perovskites, no pressure-induced PL enhancement phenomenon or a drastic increase in the band gap value is observed,[55,56] at least up to around 5 GPa of applied pressure.

The very strong red-shift of NBE is attributed to the band gap narrowing in $(4FP)_2SnI_4$ under hydrostatic pressure. In order to further study the pressure-induced changes in the band gap, transmission spectra under hydrostatic pressure were measured. Figure 3c shows normalized transmission spectra for $(4FP)_2SnI_4$ as a function of hydrostatic pressure taken at 300 K. It can be observed that as the pressure increases, the band gap of $(4FP)_2SnI_4$ red-shifts, similar to the behavior of NBE in PL measurements. The pressure coefficient extracted from transmission measurements is equal to −184 ± 16 meV/GPa, which is a value similar to that extracted from room-temperature PL spectra (−160 ± 4 meV/GPa). This indicates a strong correlation of the NBE and the absorption edge. The method by which absorption edge was determined is shown in Figure S5. In Figure S6 optical micrographs of the $(4FP)_2SnI_4$ sample are presented. The change in the crystal color from red at 0 GPa to black at 1.43 GPa is in line with the band gap narrowing observed in transmission and PL.

To obtain further validation of our experimental results, we performed DFT modeling of the band structure evolution

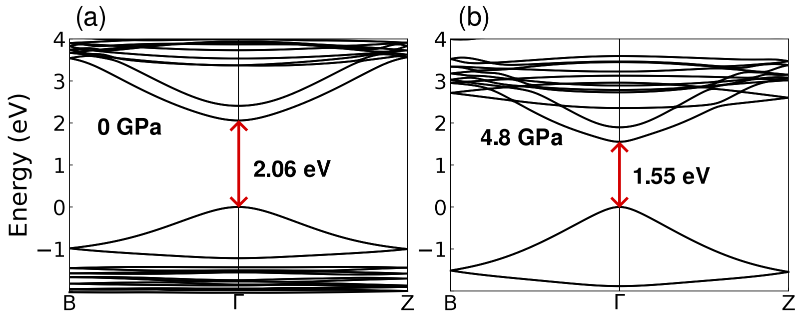

Figure 4. Band structure of $(4FP)_2SnI_4$ for (a) 0 and (b) 4.8 GPa applied pressure. The band gap remains direct for whole range of studied pressures and exhibit significant redshift.

under pressure. Figures 4a,b show representative band structures for 0 and 4.8 GPa of applied pressure, respectively. For the studied pressure range of 0−5.2 GPa, the fundamental band gap is direct and decreases with applied pressure, which is presented in Figure 3a. Derived from calculations, the pressure coefficient is in excellent agreement with low-temperature experimental results, despite the simple level of DFT theory used in this work (see SI for details).

It is worth empathizing that the pressure coefficient derived from measurements and theoretical modeling not only has great absolute value but also stays constant for a wide range of pressures, which gives an opportunity for large band gap tuning by pressure in a linear fashion. Considering the properties of $(4FP)_2SnI_4$ compared to other halide perovskites, it is clear that the value of the pressure coefficient and band gap tunability are among the highest reported to date, making this material a promising candidate for pressure-sensitive applications. The constant pressure coefficient in such a wide range of pressures is also unique among this material group. As mentioned in the Abstract, we attribute this, on the one hand, to its 2D structure and, on the other hand, to the tin occupying metal sites.

It is well-known that the band edges near the fundamental gap in 2D halide perovskites are made from orbitals of atoms from inorganic layers. In the case of $(4FP)_2SnI_4$, the valence band maximum is a combination of *s* orbitals of tin and *p* orbitals of iodine, while the conductive band minimum is mainly from *p* orbitals of tin. Therefore, in order to understand the evolution of the band gap under pressure, it is crucial to examine the changes in the bonds between iodine and tin. Our DFT calculations show that the lengths of these bonds change by almost 0.2 Å, while the changes in the Sn−I bond angles are smaller than 2° in the pressure range studied. Another observation is that the Sn−I bonds directed to the organic spacer exhibit approximately two times smaller changes in lengths (~0.1 Å), which can be explained by noting that in the direction perpendicular to the inorganic layer, most of the pressure is used to squeeze the organic spacer. This picture is in agreement with the mechanism proposed in previous work[52] in which authors show that the initial band gap dependence of perovkites is a steady redshift, accompanied by metal-halide bond shortening (at least if the material does not undergo phase transition in this initial pressure range). According to previous studies[52] at some pressure another regime occurs, after which the band gap increases with pressure due to the change in angles between Sn−I bonds. In our study, $(4FP)_2SnI_4$ remains in the first region up to 5 GPa, which stems from the large width of the organic spacer relative to the width of the inorganic part and the presence of tin instead of lead, as smaller atoms give more space for organic cations to fit in. Such conditions provide material with a linear pressure coefficient and great band gap tunability in a wide pressure range, in agreement with chemical trends derived in previous studies.[52]

In conclusion, a comprehensive study of $(4FP)_2SnI_4$ optical properties under hydrostatic pressure has been carried out. PL spectra show that the NBE position redshifts dramatically under the influence of pressure. The obtained pressure coefficient is negative and increases with increasing temperature. Transmission measurement shows that the near band emission is related to the band gap, and for relatively small value of increased pressure we observe strong redshift resulting in color change. Finally, we validated our observation by DFT simulations and explained a possible reason for such behavior based on geometrical arguments. The pressure at which irreversible amorphization of the crystal occurs has not been determined, and no phase transitions have been observed up to 5 GPa. Compared to other halide perovskites, $(4FP)_2SnI_4$ possesses one of the highest band gap tunabilities reported to date, which marks it as a promising candidate for pressure-sensor applications.

■ ASSOCIATED CONTENT

Supporting Information

The Supporting Information is available free of charge at https://pubs.acs.org/doi/10.1021/acs.jpclett.5c00903.

> Detailed materials and methods; experimental layout; additional photoluminescence spectra of $(4FP)_2SnI_4$; 4FP molecular structure; determination of the absorption edge; optical micrographs of $(4FP)_2SnI_4$ sample mounted in the DAC; analysis of ruby fluorescence peaks; comment about hydrostaticity of Daphne 7575; third-order Birch−Murnaghan fitting; calculated lattice parameters, angles, and volume with uncertainties as a function of pressure (PDF)

■ AUTHOR INFORMATION

Corresponding Authors

Rafał Bartoszewicz − *Department of Semiconductor Materials Engineering, Wrocław University of Science and Technology, 50-370 Wrocław, Poland;* orcid.org/0009-0001-2951-1459; Email: rafal.bartoszewicz@pwr.edu.pl

Robert Kudrawiec − *Department of Semiconductor Materials Engineering, Wrocław University of Science and Technology, 50-370 Wrocław, Poland;* orcid.org/0000-0003-2593-9172; Email: robert.kudrawiec@pwr.edu.pl

Authors

Jakub Ziembicki — *Department of Semiconductor Materials Engineering, Wrocław University of Science and Technology, 50-370 Wrocław, Poland*

Ewelina Zdanowicz — *Department of Semiconductor Materials Engineering, Wrocław University of Science and Technology, 50-370 Wrocław, Poland;* orcid.org/0000-0001-7479-6943

Artur P. Herman — *Department of Semiconductor Materials Engineering, Wrocław University of Science and Technology, 50-370 Wrocław, Poland;* orcid.org/0000-0002-1393-0317

Jarosław Serafińczuk — *Department of Nanometrology, Wrocław University of Science and Technology, 50-372 Wrocław, Poland;* orcid.org/0000-0001-9809-4233

Jesús Sánchez-Diaz — *Institute of Advanced Materials (INAM), Universitat Jaume I., Castellón de la Plana 12006, Spain*

Samrat Das Adhikari — *Institute of Advanced Materials (INAM), Universitat Jaume I., Castellón de la Plana 12006, Spain; Institute of Physical Chemistry, Polish Academy of Sciences, Warsaw 01-224, Poland*

Iván Mora-Seró — *Institute of Advanced Materials (INAM), Universitat Jaume I., Castellón de la Plana 12006, Spain;* orcid.org/0000-0003-2508-0994

Complete contact information is available at:
https://pubs.acs.org/10.1021/acs.jpclett.5c00903

Notes

The authors declare no competing financial interest.

ACKNOWLEDGMENTS

This work was partially funded by the National Science Centre (NCN) in Poland through grant Preludium-21 no. 2022/45/N/ST3/03465. E.Z. was also supported by the Foundation for Polish Science (FNP). I.M.-S. acknowledges the project UJI-B2022-35 funded by University Jaume I for supporting this publication. Calculations have been carried out using resources provided by Wroclaw Centre for Networking and Supercomputing. S.D.A. would like to thank POLONEZ BIS project No, 2022/47/P/ST5/03261 co-funded by the National Science Centre and the Eu's H2020 research and innovation programme under the MSCA 945339.

REFERENCES

(1) Dong, H.; Zhang, C.; Liu, X.; Yao, J.; Zhao, Y. S. Materials chemistry and engineering in metal halide perovskite lasers. *Chem. Soc. Rev.* **2020**, *49*, 951−982.

(2) Fakharuddin, A.; Gangishetty, M. K.; Abdi-Jalebi, M.; Chin, S. H.; bin Mohd Yusoff, A. R.; Congreve, D. N.; Tress, W.; Deschler, F.; Vasilopoulou, M.; Bolink, H. J. Perovskite light-emitting diodes. *Nature. Electronics* **2022**, *5*, 203−216.

(3) Sun, C.; Jiang, Y.; Cui, M.; Qiao, L.; Wei, J.; Huang, Y.; Zhang, L.; He, T.; Li, S.; Hsu, H.-Y.; et al. High performance large-area quasi 2D perovskite light-emitting diodes. *Nat. Commun.* **2021**, *12*, 2207.

(4) Zhang, L.; Sun, C.; He, T.; Jiang, Y.; Wei, J.; Huang, Y.; Yuan, M. High-performance quasi-2D perovskite light-emitting diodes: from materials to devices. *Light: Science & Applications* **2021**, *10*, 61.

(5) Qin, C.; Sandanayaka, A. S. D.; Zhao, C.; Matsushima, T.; Zhang, D.; Fujihara, T.; Adachi, C. Stable room-temperature continuous-wave lasing in quasi-2D perovskite films. *Nature* **2020**, *585*, 53−57.

(6) Yassitepe, E.; Yang, Z.; Voznyy, O.; Kim, Y.; Walters, G.; Casraneda, J. A.; Kanjanaboos, P.; Yuan, M.; Gong, X.; Fan, F.; et al. Amine-Free Synthesis of Cesium Lead Halide Perovskite Quantum Dots for Efficient Light-Emitting Diodes. *Adv. Funct. Mater.* **2016**, *26*, 8757−8763.

(7) Chen, W.; Huang, Z.; Yao, H.; Liu, Y.; Zhang, Y.; Li, Z.; Zhou, H.; Xiao, P.; Chen, T.; Sun, H.; et al. Highly bright and stable single-crystal perovskite light-emitting diodes. *Nat. Photonics* **2023**, *17*, 401.

(8) Marchal, N.; Van Gompel, W.; Gelvez-Rueda, M. C.; Vandewal, K.; Van Hecke, K.; Boyen, H.-G.; Conings, B.; Herckens, R.; Maheshwari, S.; Lutsen, L.; et al. Lead-Halide Perovskites Meet Donor-Acceptor Charge-Transfer Complexes. *Chem. Mater.* **2019**, *31*, 6880−6888.

(9) Eperon, G. E.; Stranks, S. D.; Menelaou, C.; Johnston, M. B.; Herz, L. M.; Snaith, H. J.; et al. Formamidinium lead trihalide: a broadly tunable perovskite for efficient planar heterojunction solar cells. *Energy Environ. Sci.* **2014**, *7*, 982−988.

(10) Yang, W. S.; Noh, J. H.; Jeon, N. J.; Kim, Y. C.; Ryu, S.; Seo, J.; Seok, S. I. High-performance photovoltaic perovskite layers fabricated through intramolecular exchange. *Science* **2015**, *348*, 1234−1237.

(11) Yang, J.; Bao, Q.; Shen, L.; Ding, L. Potential Applications for Perovskite Solar Cells in Space. *Nano Energy* **2020**, *76*, 105019.

(12) Sanchez-Diaz, J.; Rodriguez-Pereira, J.; Das Adhikari, S.; Mora-Sero, I. Synthesis of Hybrid Tin-Based Perovskite Microcrystals for LED Applications. *Advanced Science* **2024**, *11*, 2403835.

(13) Vescio, G.; Dirin, D. N.; González-Torres, S.; Sanchez-Diaz, J.; Vidal, R.; Franco, I. P.; Adhikari, S. D.; Chirvony, V. S.; Martínez-Pastor, J. P.; Vinocour Pacheco, F. A.; et al. Inkjet-Printed Red-Emitting Flexible LEDs Based on Sustainable Inks of Layered Tin Iodide Perovskite. *Advanced Sustainable Systems* **2024**, *8*, 2400060.

(14) Vescio, G.; Sanchez-Diaz, J.; Frieiro, J. L.; Sánchez, R. S.; Hernández, S.; Cirera, A.; Mora-Seró, I.; Garrido, B. 2D PEA2SnI4 Inkjet-Printed Halide Perovskite LEDs on Rigid and Flexible Substrates. *ACS Energy Letters* **2022**, *7*, 3653−3655.

(15) Jokar, E.; Cai, L.; Han, J.; Nacpil, E. J. C.; Jeon, I. Emerging Opportunities in Lead-Free and Lead-Tin Perovskites for Environmentally Viable Photodetector Applications. *Chem. Mater.* **2023**, *35*, 3404−3426.

(16) López-Fernández, I.; Valli, D.; Wang, C.-Y.; Samanta, S.; Okamoto, T.; Huang, Y.-T.; Sun, K.; Liu, Y.; Chirvony, V. S.; Patra, A.; et al. Lead-Free Halide Perovskite Materials and Optoelectronic Devices: Progress and Prospective. *Adv. Funct. Mater.* **2024**, *34*, 2307896.

(17) De Marco, L.; Nasti, G.; Abate, A.; Rizzo, A. Perovskite Single-Crystal Solar Cells: Advances and Challenges. *Solar RRL* **2022**, *6*, 2101085.

(18) Priyadarshini, N.; Mansingh, S.; Das, K. K.; Mohanty, R.; Parida, K.; Barik, G.; Parida, K. Single Crystal Perovskite an Emerging Photocatalytic and Storage Material: Synthesis to Applications via Theoretical Insight. *Phys. Rep.* **2024**, *1061*, 1−53.

(19) Rong, S. S.; Faheem, M. B.; Li, Y. B. Perovskite Single Crystals: Synthesis, Properties, and Applications. *Journal of Electronic Science and Technology* **2021**, *19*, 100081.

(20) Zhang, Y.; Liu, Y.; Liu, S. Composition Engineering of Perovskite Single Crystals for High-Performance Optoelectronics. *Adv. Funct. Mater.* **2023**, *33*, 2210335.

(21) Li, C.; Sun, H.; Gan, S.; Dou, D.; Li, L. Perovskite Single Crystals: Physical Properties and Optoelectronic Applications. *Materials Futures* **2023**, *2*, 042101.

(22) Yan, J.; Li, H.; Aldamasy, M. H.; Frasca, C.; Abate, A.; Zhao, K.; Hu, Y. Advances in the Synthesis of Halide Perovskite Single Crystals for Optoelectronic Applications. *Chem. Mater.* **2023**, *35*, 2683−2712.

(23) Li, H.; Shen, N.; Chen, S.; Guo, F.; Xu, B. Recent Progress on Synthesis, Intrinsic Properties and Optoelectronic Applications of Perovskite Single Crystals. *Adv. Funct. Mater.* **2023**, *33*, 2214339.

(24) Wang, Y.; Sun, X.; Shao, T.; Zhao, D.; Zhang, L.; Li, Y.; Dong, Q.; Liu, C.; Wang, K.; Xiao, G.; et al. Band-gap Narrowing and Electric Transport Regulation of Hybrid Perovskites via Pressure Engineering. *Inorg. Chem.* **2024**, *63*, 11431−11437.

(25) Bhardwaj, A.; Marongiu, D.; Demontic, V.; Simbula, A.; Quochi, F.; Saba, M.; Mura, A.; Bongiovanni, G. Single Crystal Sn-Based Halide Perovskites. *Nanomaterials* **2024**, *14*, 1444.

(26) Jaffe, A.; Lin, Y.; Karunadasa, H. I. Halide Perovskites under Pressure: Accessing New Properties through Lattice Compression. *ACS Energy Letters* **2017**, *2*, 1549−1555.

(27) Zhang, L.; Wang, K.; Lin, Y.; Zou, B. Pressure Effects on the Electronic and Optical Properties in Low-Dimensional Metal Halide Perovskites. *J. Phys. Chem. Lett.* **2020**, *11*, 4693−4701.

(28) Zhao, W.; Xiao, G.; Zou, B. Pressure-induced emission (PIE) in halide perovskites toward promising applications in scintillators and solid-state lighting. *Aggregate* **2024**, *5*, No. e461.

(29) Liu, G.; Kong, L.; Yang, W.; Mao, H.-k. Pressure engineering of photovoltaic perovskites. *Mater. Today* **2019**, *27*, 91−106.

(30) Qin, Y.; Lv, Z.; Chen, S.; Li, W.; Wu, X.; Ye, L.; Li, N.; Lu, P. Tuning Pressure-Induced Phase Transitions, Amorphization, and Excitonic Emissions of 2D Hybrid Perovskites via Varying Organic Amine Cations. *J. Phys. Chem. C* **2019**, *123*, 22491−22498.

(31) Fang, Y.; Zhang, L.; Wu, L.; Yan, J.; Lin, Y.; Wang, K.; Mao, W. L.; Zou, B. Pressure-Induced Emission (PIE) and Phase Transition of a Two-dimensional Halide Double Perovskite $(BA)_4AgBiBr_8$ (BA = $CH_3(CH_2)_3NH_3^+$). *Angew. Chem., Int. Ed.* **2019**, *58*, 15249.

(32) Wang, Y.; Lü, X.; Yang, W.; Wen, T.; Yang, L.; Ren, X.; Wang, L.; Lin, Z.; Zhao, Y. Pressure-Induced Phase Transformation, Reversible Amorphization, and Anomalous Visible Light Response in Organolead Bromide Perovskite. *J. Am. Chem. Soc.* **2015**, *137*, 11144−11149.

(33) Zhao, X.-Z.; Gao, F.-F.; Li, W.; Li, Z.-G.; Zhang, Y.; Li, K.; Hu, H.; Cai, W.; Zhang, J.; Bu, X.-H. Pressure enables high-standard white light emission and significant emission enhancement in a 2D halide perovskite. *Journal of Materials Chemistry C* **2024**, *12*, 4599−4605.

(34) Maczka, M.; Sobczak, S.; Ratajczyk, P.; Leite, F. F.; Paraguassu, W.; Dybała, F.; Herman, A. P.; Kudrawiec, R.; Katrusiak, A. Pressure-Driven Phase Transition in Two-Dimensional Perovskite MHy_2PbBr_4. *Chem. Mater.* **2022**, *34*, 7867−7877.

(35) Celeste, A.; Capitani, F. Hybrid perovskites under pressure: Present and future directions. *J. Appl. Phys.* **2022**, *132*, 220903.

(36) Ma, Z.; Li, F.; Sui, L.; Shi, Y.; Fu, R.; Yuan, K.; Xiao, G.; Zou, B. Tunable Color Temperatures and Emission Enhancement in 1D Halide Perovskites under High Pressure. *Advanced Optical Materials* **2020**, *8*, 2000713.

(37) Francisco-López, A.; Charles, B.; Weber, O. J.; Alonso, M. I.; Garriga, M.; Campoy-Quiles, M.; Weller, M. T.; Goñi, A. R. Pressure-Induced Locking of Methylammonium Cations versus Amorphization in Hybrid Lead Iodide Perovskites. *J. Phys. Chem. C* **2018**, *122*, 22073−22082.

(38) Sobczak, S.; Nowok, A.; Zarȩba, J. K.; Roszak, K.; Półrolniczak, A.; Szeremeta, A. Z.; Dziuk, B.; Dybała, F.; Pawlus, S.; Kudrawiec, R.; et al. Expanding the horizons of the thermodynamic landscape and optoelectronic properties of soft 2D hybrid perovskites MHy2PbX4. *J. Mater. Chem. A* **2024**, *12*, 16803−16814.

(39) Li, H.; Wines, D.; Chen, B.; Yumigeta, K.; Sayyad, Y. M.; Kopaszek, J.; Yang, S.; Ataca, C.; Sargent, E. H.; Tongay, S. Abnormal Phase Transition and Band Renormalization of Guanidinium-Based Organic−Inorganic Hybrid Perovskite. *ACS Appl. Mater. Interfaces* **2021**, *13*, 44964−44971.

(40) Wolf, C.; Lee, T.-W. Exciton and lattice dynamics in low-temperature processable CsPbBr3 thin-films. *Materials Today Energy* **2018**, *7*, 199−207.

(41) Wang, S. Q.; Ye, H. Q. A plane-wave pseudopotential study on III−V zinc-blende and wurtzite semiconductors under pressure. *J. Phys.: Condens. Matter* **2002**, *14*, 9579.

(42) Perlin, P.; Gorczyca, I.; Porowski, S.; Suski, T.; Christensen, N. E.; Polian, A. III−V Semiconducting Nitrides: Physical Properties under Pressure. *Jpn. J. Appl. Phys.* **1993**, *32*, 334.

(43) Jauberthie-Carillon, C.; Guillemin, C. Dependence of the indirect energy gap of GaP on quasihydrostatic pressure and phase transition. *J. Phys.: Condens. Matter* **1989**, *1*, 6807.

(44) Xu, K.; Perez-Fidalgo, L.; Charles, B. L.; Weller, M. T.; Alonso, M. I.; Goni, A. R. Using pressure to unravel the structure-dynamic-disorder relationship in metal halide perovskites. *Sci. Rep* **2023**, *13*, 9300.

(45) Wang, W.; Chen, X.; Wang, K.; Zhang, L.; Wang, L. High-Pressure Stability of LTA Zeolite-Confined $CsPbBr_3$ Nanocrystals. *SSRN* **2022**. DOI: 10.2139/ssrn.4166707

(46) Alouani, M.; Wills, J. M. Calculated optical properties of Si, Ge, and GaAs under hydrostatic pressure. *Phys. Rev. B* **1996**, *54*, 2480−2490.

(47) Christensen, N. E.; Gorczyca, I. Optical and structural properties of III-V nitrides under pressure. *Phys. Rev. B* **1994**, *50*, 4397−4415.

(48) Fasahat, S.; Schäfer, B.; Xu, K.; Fiuza-Maneiro, N.; Gómez-Graña, S.; Alonso, M. I.; Polavarapu, L.; Goñi, A. R. Absence of Anomalous Electron−Phonon Coupling in the Near-Ambient Gap Temperature Renormalization of CsPbBr3 Nanocrystals. *J. Phys. Chem. C* **2025**, *129*, 453−463.

(49) Su, Y.; Yang, J.; Liu, G.; Sheng, W.; Zhang, J.; Zhong, Y.; Tan, L.; Chen, Y. Acetic Acid-Assisted Synergistic Modulation of Crystallization Kinetics and Inhibition of Sn^{2+} Oxidation in Tin-Based Perovskite Solar Cells. *Adv. Funct. Mater.* **2022**, *32*, 2109631.

(50) Lee, Y.; Mitzi, D. B.; Barnes, P. W.; Vogt, T. Pressure-induced phase transitions and templating effect in three-dimensional organic-inorganic hybrid perovskites. *Phys. Rev. B* **2003**, *68*, 020103.

(51) Ratul Hasan, M. D.; Apon, I. A.; Ahmed Ovi, I.; Zahra, F.-T. Impact of Applied Pressure on Tin-Based Cubic Halide Perovskite ASnX3 (A = Li, Na and X = Cl, Br, and I) in Reference to Their Optoelectronic Applications. *International Journal of Energy Research* **2024**, *2024*, 8213804.

(52) Kong, L.; Gong, J.; Spanopoulos, I.; Yan, S.; Li, Z.; Zhu, Z.; Liu, X.; Zhu, Y.; Dong, H.; Shu, H.; et al. Revealing the Universal Pressure-Driven Behavior of Hybrid Halide Perovskites and Unique Optical Modifiability in Extremely Soft 2D Tin-Based System. *Adv. Funct. Mater.* **2024**, *34*, 2414437.

(53) Sheikh, T.; Nawale, V.; Pathoor, N.; Phadnis, C.; Chowdhury, A.; Nag, A. Molecular Intercalation and Electronic Two Dimensionality in Layered Hybrid Perovskites. *Angew. Chem., Int. Ed.* **2020**, *59*, 11653−11659.

(54) Nawale, V. V.; Sheikh, T.; Nag, A. Dual Excitonic Emission in Hybrid 2D Layered Tin Iodide Perovskites. *J. Phys. Chem. C* **2020**, *124*, 21129−21136.

(55) Jung, M.-H. The red light emission in 2D $(C_4SH_3CH_2NH_3)$-SnI_4 and $(C_4OH_7CH_2NH_3)_2SnI_4$ perovskites. *Dalton Transactions* **2021**, *50*, 10261−10274.

(56) Wu, K.; Bera, A.; Ma, C.; Du, Y.; Yang, Y.; Li, L.; Wu, T. Temperature-dependent excitonic photoluminescence of hybrid organometal halide perovskite films. *Phys. Chem. Chem. Phys.* **2014**, *16*, 22476−22481.

Supporting Information for

Giant band gap narrowing under hydrostatic pressure in $(4FP)_2SnI_4$ halide perovskite

*Rafał Bartoszewicz,[1, *] Jakub Ziembicki,[1] Ewelina Zdanowicz,[1] Artur P. Herman,[1] Jarosław Serafińczuk,[2] Jesús Sánchez-Diaz,[3] Samrat Das Adhikari,[3,4] Iván Mora-Seró,[3] and Robert Kudrawiec[1, **]*

[1]Department of Semiconductor Materials Engineering, Wroclaw University of Science and Technology, Wybrzeże Wyspiańskiego 27, 50-370 Wrocław, Poland

[2]Department of Nanometrology, Wroclaw University of Science and Technology, Janiszewskiego 11/17, 50-372 Wrocław, Poland

[3]Institute of Advanced Materials (INAM), Universitat Jaume I. Av. De Vicent Sos Baynat, Castellón de la Plana, 12006 Spain

[4]Institute of Physical Chemistry, Polish Academy of Sciences, Warsaw 01-224, Poland

* e-mail address: rafal.bartoszewicz@pwr.edu.pl

** e-mail address: robert.kudrawiec@pwr.edu.pl

KEYWORDS: Perovskites, Photoluminescence, Absorption, XRD, Hydrostatic pressure

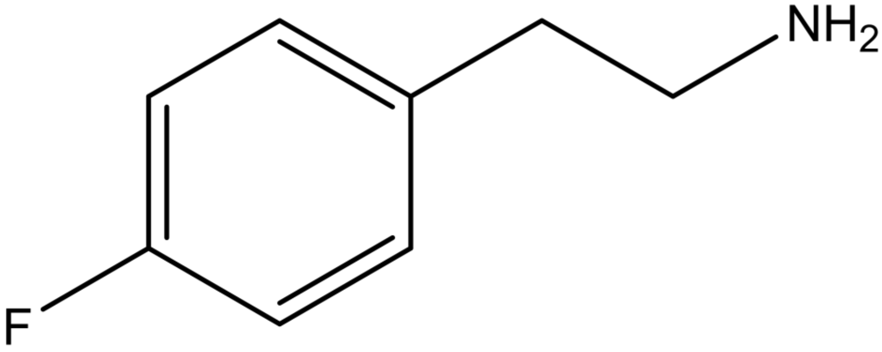

Figure S1. 4FP molecular structure

Table 1. Calculated lattice parameters, angles, volume and R-factor of (4FP)$_2$SnI$_4$ as a function of applied pressure

Pressure [GPa]	a [Å]	Δa [Å]	b [Å]	Δb [Å]	c [Å]	Δc [Å]	β [°]	Δβ [°]	c/a	a/b	c/b	V (Å^3)	ΔV (Å^3)	R-factor [%]
0.19	16.654	0.008	8.5774	0.0015	8.756	0.004	98.65	0.01	0.5257	1.9415	1.0207	1236.41	0.85	0.9
1.04	16.388	0.008	8.4298	0.0015	8.685	0.004	98.72	0.01	0.5299	1.9440	1.0302	1185.85	0.82	0.68
1.46	16.255	0.008	8.3722	0.0014	8.663	0.004	98.80	0.01	0.5329	1.9415	1.0346	1164.96	0.81	0.64
1.95	16.151	0.008	8.3294	0.0014	8.614	0.004	98.84	0.01	0.5333	1.9390	1.0341	1144.96	0.79	0.62
2.61	16.087	0.008	8.2585	0.0014	8.569	0.004	98.91	0.01	0.5326	1.9479	1.0375	1124.60	0.78	0.6
3.05	15.939	0.008	8.1977	0.0014	8.524	0.004	98.95	0.01	0.5347	1.9443	1.0397	1100.11	0.76	0.59
3.60	15.909	0.008	8.1868	0.0014	8.509	0.004	98.98	0.01	0.5348	1.9432	1.0392	1094.57	0.76	0.58
4.08	15.856	0.008	8.1397	0.0014	8.479	0.004	99.00	0.01	0.5347	1.9480	1.0416	1080.76	0.75	0.57
4.50	15.777	0.008	8.0991	0.0014	8.432	0.004	99.03	0.01	0.5344	1.9480	1.0410	1063.99	0.74	0.56
5.19	15.827	0.008	8.1517	0.0014	8.454	0.004	98.99	0.01	0.5341	1.9415	1.0370	1088.21	0.75	0.56

Calculations were performed considering 5 lattice planes: (011), (210), (022), (020) and (12-2), which allowed us to accurately determine both the lattice parameters and the beta angle. In addition, measurement uncertainties were calculated for the measurement step used of 0.0167 degrees.

The R-factor is defined as:

$$R = \frac{\sum |d_{observed} - d_{calculated}|}{\sum d_{observed}} \cdot 100\%$$

Where $d_{observed}$ is derived from the measured 2θ angles using Bragg’s law, and $d_{calculated}$ is computed from the refined lattice parameters.

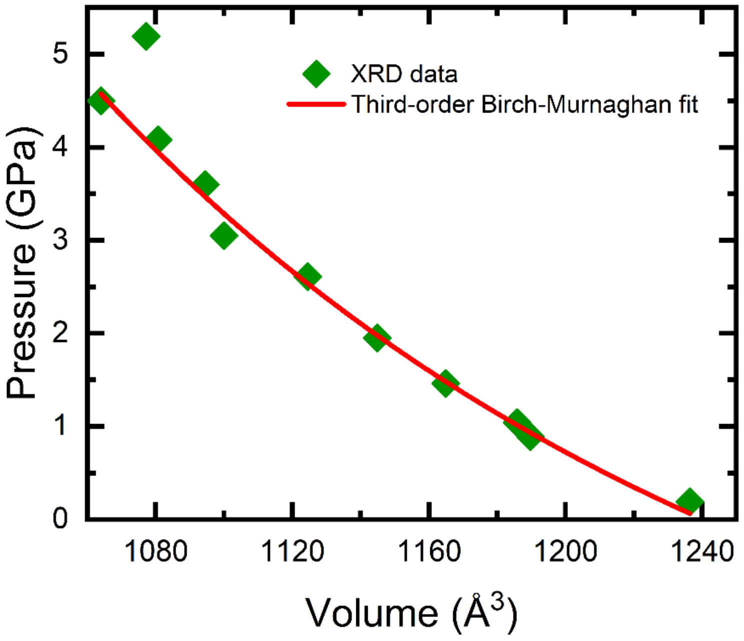

Figure S2. Third-order Birch-Murnaghan fitting of XRD data.

To determine bulk modulus value of $(4FP)_2SnI_4$ we used third-order Birch-Murnaghan EoS :

$$P(V) = \frac{3}{2}B_0\left[\left(\frac{V_0}{V}\right)^{7/3} - \left(\frac{V_0}{V}\right)^{5/3}\right] \times \left\{1 + \frac{3}{4}(B_0' - 4)\left[\left(\frac{V_0}{V}\right)^{2/3} - 1\right]\right\}$$

The approximation was calculated using Origin and also python software. After refitting the third-order Birch-Murnaghan function with a fixed value of V_0 = 1240.3625 Å^3 we received :

B_0 = 20.09 ± 1.41 GPa

B_0' = 5.14 ± 1.12

The measurement at 5.19 GPa was excluded after calculations due to a likely error in determining the pressure within the DAC.

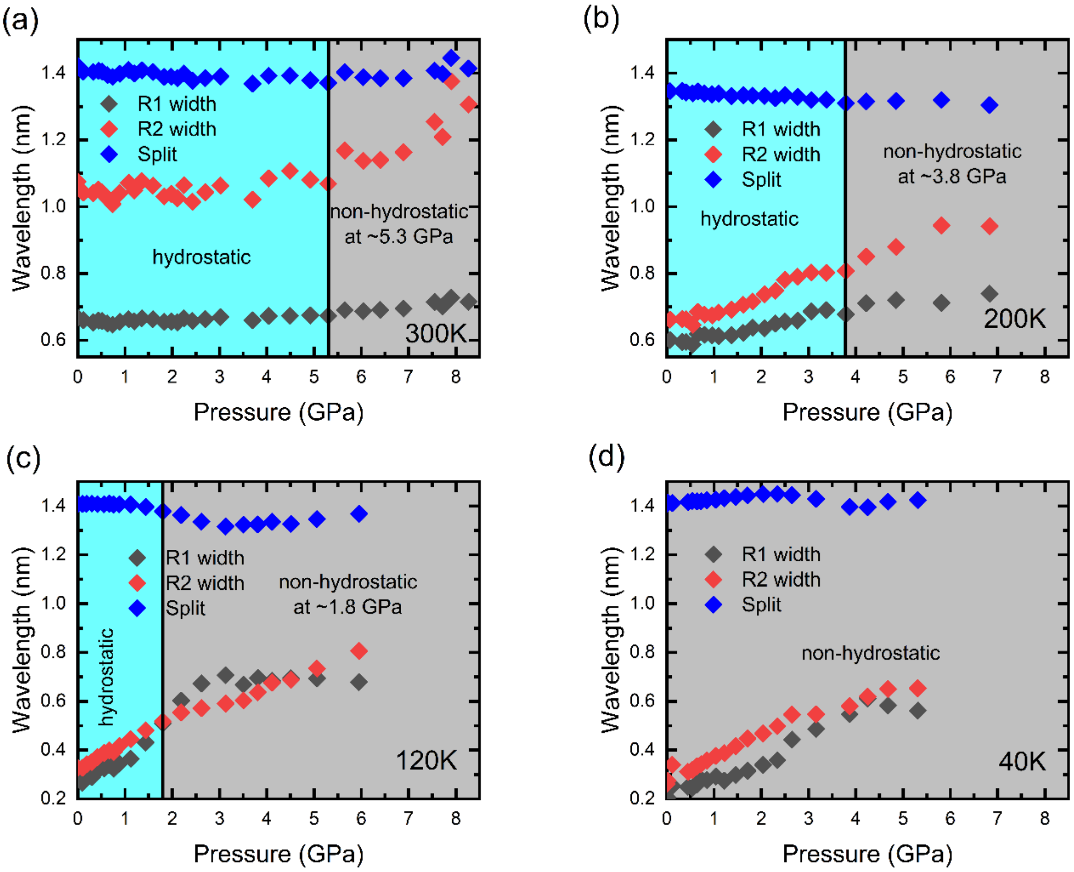

Figure S3. Analysis of ruby R1 and R2 peaks split and broadening at (a) 300, (b) 200, (c) 120, and (d) 40 K.

Figure S3 presents the analysis of the applied pressure using ruby fluorescence. Daphne 7575 is not strictly hydrostatic at low temperatures, and its ability to maintain hydrostatic conditions decreases significantly with both temperature reduction and pressure increase [1,2]. However, while Daphne 7575 does not remain fully hydrostatic at high pressures and low temperature, it maintains quasi-hydrostatic conditions, owing to its relatively low shear strength and soft solidification behavior [2,3]. From R1 and R2 peaks split and broadening we determined solidification points of Daphne 7575 at (a) ~5.3, (b) ~3.8, (c) ~1.8 and (d) 0 GPa for 300, 200, 120 and 40 K respectively. The pressure coefficients we investigated are not highly sensitive to moderate non-hydrostatic stress. As far as we know, such conditions should lead to nonlinear band gap shifts, splitting of emission lines, amorphization, or appearing defect emission due to uneven stress, which could be reported as the presence of phase transition in this material [4-7]. Such effects were not observed in our measurements. Our results remain consistent with theoretical expectations, which support their validity even in the presence of quasi-hydrostatic conditions. Moreover, for perovskite materials such medium is still second best choice (first choice is helium) as it not influence the condition of measured sample, as it is in the case of 4:1 methanol-ethanol mixture [8].

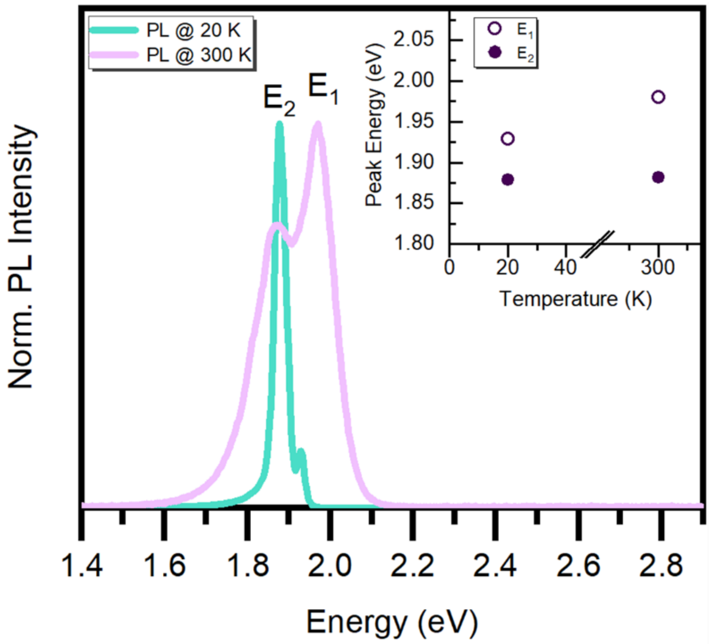

Figure S4. Normalized photoluminescence spectra of $(4FP)_2$ SnI_4. The inset shows energies of E_1 and E_2 at investigated temperatures.

Figure S4 compares the PL spectra recorded at 20 and 300 K, revealing two distinct peaks, E_1 and E_2, at both temperatures. The inset illustrates the temperature dependence of the extracted energies for E_1 and E_2. Notably, E_1 exhibits a blueshift with increasing temperature, while E_2 remains nearly constant. The PL spectra in Figure S1 indicate that $(4FP)_2SnI_4$ maintains strong emission properties across a wide temperature range.

Figure S5 illustrates the method used to determine the energy shift of the absorption edge. Using a linear regression fit, we estimated the energy value from the square of the absorption coefficient (α^2), where α is defined according to the formula:

$$\alpha = -\frac{1}{d} ln \frac{T}{(1-R)^2}$$

where d is the sample thickness (here 50μm), T means– transmission and, R – reflectance signal.

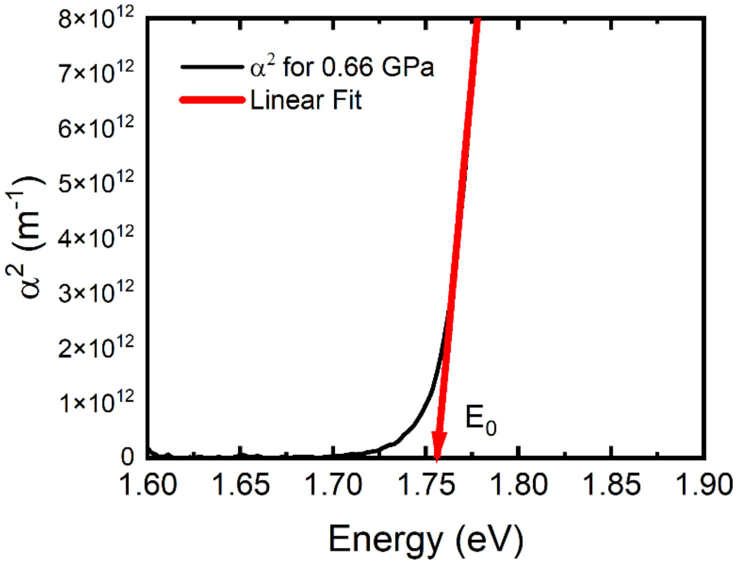

Figure S5. Determination of the absorption edge at 0.66 GPa.

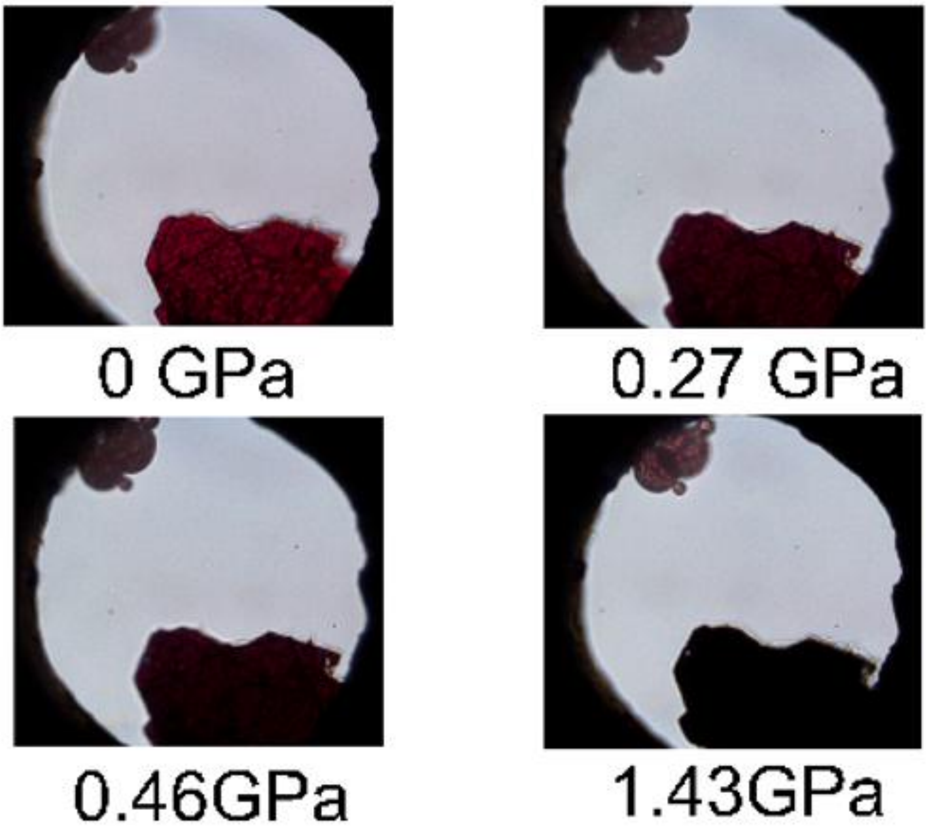

Figure S6. View on the sample for different values of pressure.

MATERIALS AND METHODS

Experimental details:

Materials: Acetic acid (AcOH, 99-100 %, sigma aldrich), hydroiodic acid (HI; 57 wt. % in H_2O, distilled, stabilized, 99.95 %), hypophosphorus acid (H_3PO_2; 50wt. % in H_2O), Tin (II) oxide (SnO; 99%, Alfa Aesar), 4-fluorophenethylamine (4FPEA; TCI) was purchased from. All materials were use as received with no further purifications.

Synthesis of $(4FP)_2SnI_4$ microcrystals powder:

Synthesis of $(4FP)_2SnI_4$ was carried out following the literature report [8, 9]. A mixture consisting of 3 mL of acetic acid, 0.2 mL of hydroiodic acid (HI), and 0.05 mL of hypophosphorous acid (H_3PO_2) was combined in a three-necked flask under an inert nitrogen (N_2) atmosphere. The mixture was stirred at room temperature for 30 minutes, during which a transition from a faint red to a colorless appearance indicated the stabilization of HI in the presence of H_3PO_2. Next, 134 mg of tin(II) oxide (SnO) was introduced into the flask, and the temperature was gradually increased to 100 °C. The solution was stirred for an additional 30 minutes until it developed an orange color. Subsequently, 0.26 mL of 4-fluorophenylethylamine (4FPEA) was added, and the reaction temperature was further raised to 135 °C. The mixture was maintained under these conditions for 15 minutes. Upon completion of the reaction, the solution was rapidly cooled using an ice bath for approximately 2 minutes. The resulting product was collected via vacuum suction filtration. To eleiminate any excess iodine, the collected powder was washed three times with hexane, followed by additional vacuum suction filtration. Finally, the purified product was dried.

Temperature and pressure dependent PL

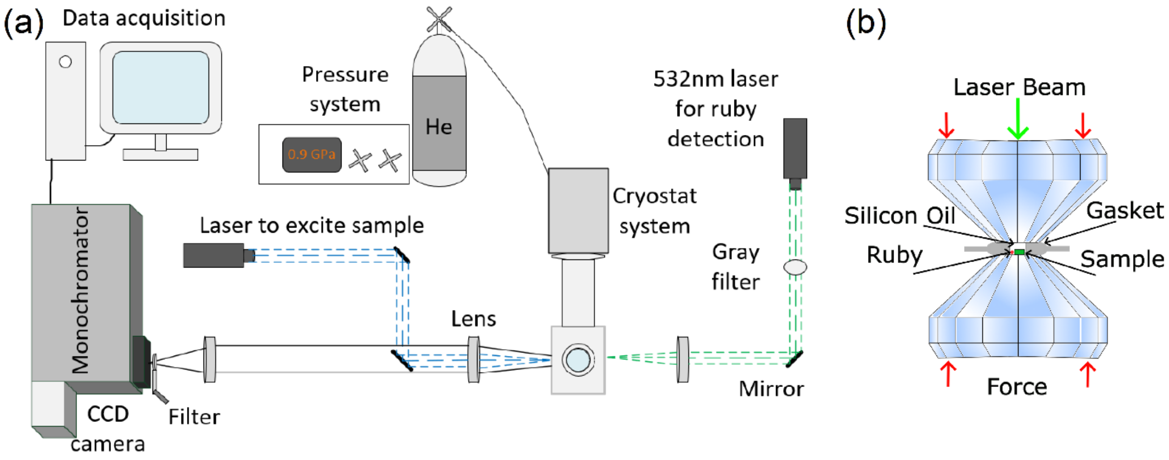

Figure S7. (a) The scheme of the experimental setup for hydrostatic pressure-dependent photoluminescence (b) Cross-section of a diamond anvil cell.

Figure S7 (a) presents schematically the experimental setup of temperature- and pressure-dependent PL carried out in this work. Figure S7 (b) shows a cross-section of a diamond anvil cell (DAC). PL measurements were performed in Diacell design DAC by ‘Almax easyLab’. DAC used in this work is made of beryllium copper (BeCu) alloy, which allows to perform measurements at cryogenic temperature (here 40 K). Diamond with 650 µm culet size was used. The pressurizing mechanism in the DAC was driven using a gas membrane. The pressure in DAC was controlled by the amount of helium injected into the gas membrane. On top of the bottom diamond culet, a gasket was placed. It is a thin sheet (circa 50 µm thickness) of inconel material with a central hole of about 1/3 culet size, where sample, ruby sphere, and silicon oil were placed. Gaskets were prepared by pressing diamonds into a thin sheet, followed by creating a central hole using mechanical drilling. Daphne 7575 was used as the pressure-transmitting medium, which solidifies at about 5.3GPa at room temperature. Whole setup was cooled down in a cryostat with a closed-loop liquid helium system. For PL experiments, the 405 nm CW (with power of 100 µW) laser was used to excite the studied material. Emitted light was dispersed through a 0.5 m Andor monochromator with a 150 l/mm diffraction grating blazed at 500 nm. The signal was recorded by a Si CCD camera cooled to -70 °C by Peltier module. The luminescence of the ruby R1 line at ~1.78 eV (at room temperature) was excited by the 532 nm CW laser, dispersed on the 600 l/mm diffraction grating blazed at 500 nm and detected by CCD camera. To determine pressure value inside DAC we detect pressure-induced redshift of ruby sphere R1 line with calibration taken from Shen [10]. The temperature shift correction of the R1 ruby line was taken from Datchi [11].

Pressure dependent transmission

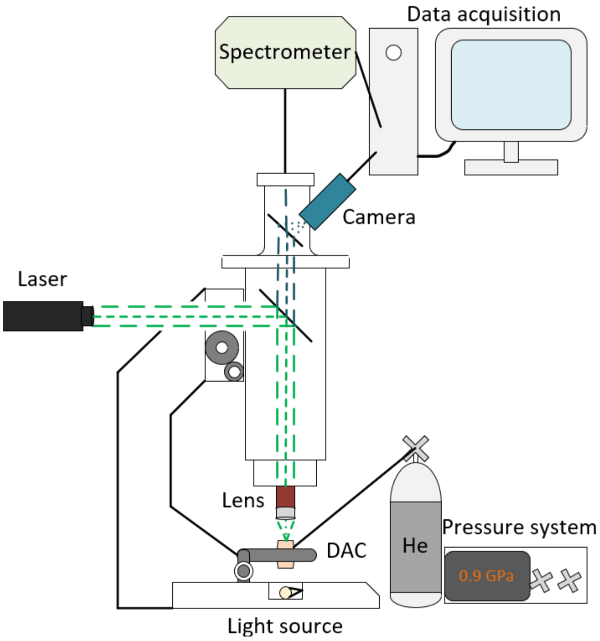

Figure S8. Scheme of the system used for transmission measurements under hydrostatic pressure.

Figure S8 presents a scheme of the experimental setup for hydrostatic pressure-dependent transmission at room temperature. The optical microscope NADE NMM-800TRF and Mitutoyo M PLAN APO NIR 50x/0.42 f = 200 lens was used to properly focus on sample placed inside the DAC chamber. Transmission measurements were carried out using the previously mentioned DAC which was also used for the PL measurements, with Daphne 7575 serving as the pressure-transmitting medium. For transmission measurements, the halogen lamp (with voltage of 24 V and power 100 W) was used as a light source. Transmitted light was recorded by a StellarNet Blue-Wave UVIS 200 spectrometer with a 600 l/mm grating and 200 nm slit with resolution of 1.0. Delta Optical DLT-CAM PRO 3 MP USB 3.0 camera allowed us to investigate the color change of the perovskite. To excite the R1 luminescence of the ruby, a 532 nm CW laser was used (emission power 1 mW). In this case, AVANTES ULS4096CL-RS-EVO with a DCL-UV/VIS-200 600 l/mm diffraction grating blazed at 300 nm was used as a detector. The investigated spectral range is determined by the upper optical limit of the Mitutoyo NIR lens used and the cutoff energy of the optical microscope (approximately 1.6 eV).

Theoretical calculations

DFT calculations have been done in VASP code, using PAW method [12-15]. For geometrical optimization we used PBE with D3 van der Waals correction [16-17], with 600 eV cutoff energy, 3x3x6 kpoint grid, 10^{-7} eV energy tolerance for SCF and 10^{-2} eV/A force tolerance for geometry optimization. Then band structures have been calculated with PBE functional, using the same numerical parameters. To correct the band gap, we used scissor shift to set the band gap to the value derived on the PBE0 level [18] on the same geometry. The spin-orbit coupling (SOC) is included in band structure calculations, as it is well known that SOC greatly affect the band structure in tin and lead based perovskites.

Pressure dependent X-ray diffraction

Structural studies with X-ray diffraction, were carried out using an Malvern-Panalytical Empyrean diffractometer. A molybdenum x-ray tube with $\mathrm{Mo}_{K\alpha 1}$ = 0.7093197 Å was used in the study. Pressure was generated by an ‘Almax easyLab’ Bragg-Mini DAC with diamond culet size of 600 µm allowing pressures up to 20 GPa. Daphne 7575 was used as the pressure-transmitting medium, which solidifies at about 5.3 GPa at room temperature. An x-ray tube was set to point focus and a 135 mm long mono-capillary collimator with an exit beam diameter of 0.3 mm were used to form the incident beam. The diffraction curves were recorded by a multi-strip detector 1Der. Measurements were carried out at range from 3 to 19 degrees which allowed all the strongest reflections for the investigated material to be observed. Counting time was 3400 s/point.

References:

[1] Staško, D., Prchal, J., Klicpera, M., Aoki, S., & Murata, K. (2020). Pressure media for high pressure experiments, Daphne Oil 7000 series. *High Pressure Research*, *40*(4), 525–536. https://doi.org/10.1080/08957959.2020.1825706

[2] Naoyuki Tateiwa and Yoshinori Haga 2010 J. Phys.: Conf. Ser. 215 012178

[3] Y Nakamura et al 2010 J. Phys.: Conf. Ser. 215 012176

[4] Tuson Park et al 2008 J. Phys.: Condens. Matter **20** 322204

[5] Yu, W, Aczel, A. A, Williams, T. J, Bud'ko, S. L, Ni, N, Canfield, P. C, Luke and G. M. Phys. Rev. B 79 020511(R) (2009)

[6] J. Gong, H. Zhong, C. Gao, J. Peng, X. Liu, Q. Lin, G. Fang, S. Yuan, Z. Zhang, X. Xiao, Pressure-Induced Indirect-Direct Bandgap Transition of $CsPbBr_3$ Single Crystal and Its Effect on Photoluminescence Quantum Yield. *Adv. Sci.* 2022, 9, 2201554. https://doi.org/10.1002/advs.202201554

[7] Xujie Lu et al 2017 Chem. Sci. 8, 6764-6776

[8] J. Sanchez-Diaz, J. Rodriguez-Pereira, S. Das Adhikari, I. Mora-Seró, Synthesis of Hybrid Tin-Based Perovskite Microcrystals for LED Applications. Adv. Sci. 2024, 11, 2403835. https://doi.org/10.1002/advs.202403835

[9] Y. Su, J. Yang, G. Liu, W. Sheng, J. Zhang, Y. Zhong, L. Tan, Y. Chen, Acetic Acid-Assisted Synergistic Modulation of Crystallization Kinetics and Inhibition of Sn^{2+} Oxidation in Tin-Based Perovskite Solar Cells, Adv. Funct. Mater. 2022, 32, 2109631. https://doi.org/10.1002/adfm.202109631

[10] Shen, G.; Wang, Y.; Dewaele, A.; Wu, C.; Dayne, E.; Eggert, J.; Klotz, S.; Dziubek, K. F.; Loubeyre, P.; Fat, V.; Asimow, P. D.; Mashimo, T.; Wentzcovitch, R. M. M.; Toward an International Practical Pressure Scale: A Proporsal for an IPPS Ruby Gauge (IPPS-Ruby2020). High Press. Res. 2020, 40, 299-314 10.1080/08957959.2020.1791107

[11] Datchi, F.; Dewaele, A.; Loubeyre, P.; Letoullec, R.; Godec, Y. Le.; Canny, B.; Optical Pressure Sensors for High-Pressure-High-Temperature Studies in a Diamond Anvil Cell. High Press. Res. 2007, 27, 447-463.c https://doi.org/10.1080/08957950701659593

[12] G. Kresse and J. Hafner, Ab initio molecular dynamics for liquid metals, Phys. Rev. B 47, 558 (1993).

[13] G. Kresse and J. Furthm¨uller, Efficient iterative schemes for ab initio total-energy calculations using a plane-wave basis set, Phys. Rev. B 54, 11169–11186 (1996).

[14] G. Kresse and J. Furthm¨uller, Efficiency of ab-initio total energy calculations for metals and semiconductors using a plane-wave basis set, Computational Materials Science 6, 15 (1996).

[15] G. Kresse and D. Joubert, From ultrasoft pseudopotentials to the projector augmented-wave method, Phys. Rev. B 59, 1758 (1999).

[16] J. P. Perdew, K. Burke, and M. Ernzerhof, Phys. Rev. Lett., **77**, 3865 (1996).

[17] Grimme, S., Ehrlich, S. and Goerigk, L. (2011), Effect of the damping function in dispersion corrected density functional theory. J. Comput. Chem., 32: 1456-1465.

[18] C. Adamo and V. Barone, Phys. Rev. Lett., **110**, 6158 (1999).

3.2 Band Gap Tuning by Hydrostatic Pressure in TMA_2SnI_4 Halide Perovskite

Rafał Bartoszewicz[†], Jakub Ziembicki, Artur P. Herman, Magdalena Wietrzyńska, Jarosław Serafińczuk, Łukasz Przypis, Robert Kudrawiec

ACS Materials Letters, vol. 8, no. 4, pp. 1201-1208 (2026). DOI: 10.1021/acsmaterialslett.5c01670

Author's Contribution:

Rafał Bartoszewicz with supervisor conceived and formulated the research problem, focusing on the pressure- and temperature-dependent optical and structural response of TMA_2SnI_4, with the aim of elucidating the mechanisms governing band gap modulation across structural phase transitions. The research hypotheses regarding pressure-induced band gap tuning, excitonic behavior, and the emergence of low-temperature emissive states were defined by the author.

The author independently designed and executed the complete optical experimental program, including temperature-dependent PL and R measurements, as well as combined temperature- and pressure-dependent PL studies. All HP optical measurements were performed by the author. The author contributed to pressure-dependent XRD measurements, and their interpretation.

Data processing, spectral fitting, extraction of pressure coefficients, uncertainty qualification, and temperature-dependent trend analysis were carried out independently. The author performed systematic comparisons with DFT calculations to interpret the evolution of the electronic structure under compression, correlating excitonic features with lattice distortions and polaronic effects.

The mechanistic framework connecting lattice compression, structural flexibility, exciton-phonon coupling, and band gap tuning was developed by the author. All figures, schematics, and the manuscript were prepared by the author, who synthesized the results into a coherent physical model describing pressure- and temperature-dependent optical behavior in TMA_2SnI_4. Author also answered for all questions from the reviewers during review process.

---

† corresponding author

ACS MATERIALS LETTERS

www.acsmaterialsletters.org

Letter

Band Gap Tuning by Hydrostatic Pressure in (2-Thienyl)methylammonium Tin Iodide Halide Perovskite

Rafał Bartoszewicz,* Jakub Ziembicki, Artur P. Herman, Magdalena Wietrzyńska, Jarosław Serafińczuk, Łukasz Przypis, and Robert Kudrawiec

Cite This: https://doi.org/10.1021/acsmaterialslett.5c01670

Read Online

ACCESS | Metrics & More | Article Recommendations | Supporting Information

ABSTRACT: Two-dimensional tin-based halide perovskites are promising lead-free materials for optoelectronics due to their lower toxicity, structural flexibility, and strong polaronic excitonic effects. Here, we investigate the structural and optical response of (2-thienyl)methylammonium tin iodide (TMA_2SnI_4) under hydrostatic pressure and variable temperature. Pressure-dependent photoluminescence reveals substantial band gap narrowing of the optical (excitonic) transition energy with a pressure coefficient of −187 ± 3 meV/GPa. Room-temperature X-ray diffraction confirms that TMA_2SnI_4 maintains a stable orthorhombic phase (*Pbca*) up to ~1.6 GPa followed by a structural transition. Temperature-dependent PL and reflectance measurements identify a reversible phase transition near 180 K and highlight strong electron−phonon coupling and excitonic behavior. At cryogenic temperatures, the pressure induces additional emissive states, likely associated with polaronic excitonic complexes. These results characterize TMA_2SnI_4 as a structurally robust and optoelectronically responsive material with pronounced band gap tunability.

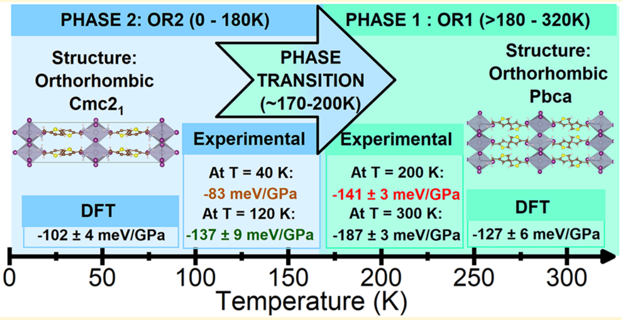

Tin-based halide perovskites have garnered attention as lead-free alternatives, offering reduced toxicity and improved environmental sustainability.[1−4] They exhibit high charge carrier mobility, long hot carrier lifetimes, and strong light−matter interactions, making them suitable candidates for optoelectronic applications, including photovoltaics, photosensors, and light-emitting diodes.[5−9] Among them, layered ("two-dimensional", 2D) Sn-based halide perovskites are particularly attractive due to pronounced quantum confinement and excitonic effects, which enhance photoluminescence quantum yields and enable tunable recombination dynamics.[10] Their facile solution-based synthesis supports cost-effective, scalable device fabrication.[11,12] Sn-based halide perovskites demonstrate resilience to external stimuli such as hydrostatic pressure and temperature,[13,14] which can modulate crystallographic and electronic structures, particularly the band gap, due to the intrinsic softness and flexibility of the perovskite lattice.[15−17] High-pressure studies have demonstrated large pressure-induced band gap modulation in 2D Sn-based systems.[13,14] However, the evolution of pressure coefficients across temperature-driven phase transitions and the emergence of pressure-activated states are characterized here. In particular, TMA_2SnI_4 provides a platform to probe combined structural and excitonic dynamics in a soft, low-dimensional lattice, critical for designing stimuli-responsive materials, temperature sensors, and flexible electronics.[18−20]

(2-Thienyl)methylammonium tin iodide (TMA_2SnI_4) is a 2D Sn-based halide perovskite,[21] exhibiting red photoluminescence, an optical (excitonic) band gap of ~2.00 eV, and a 47 ns carrier lifetime under ambient conditions.[21,22] Despite these promising properties, its response to combined hydrostatic pressure and temperature perturbations, particularly near structural phase boundaries, has not been investigated.

Here, we present a comprehensive investigation of near-band-edge photoluminescence (PL) of TMA_2SnI_4 under a hydrostatic pressure. We report a large pressure-induced band gap narrowing, with a coefficient of −187 ± 3 meV/GPa at room temperature, among the highest known for halide perovskites and traditional semiconductors.[13] This coefficient exhibits a strong cryogenic temperature dependence, persisting through temperature-induced phase transitions, highlighting the significant electronic sensitivity of this material. At cryogenic temperatures, pressure induces additional emissive states, tentatively attributed to pressure- and temperature-stabilized localized states, potentially involving polaronic excitonic complexes.

Received: December 22, 2025
Revised: March 4, 2026
Accepted: March 5, 2026

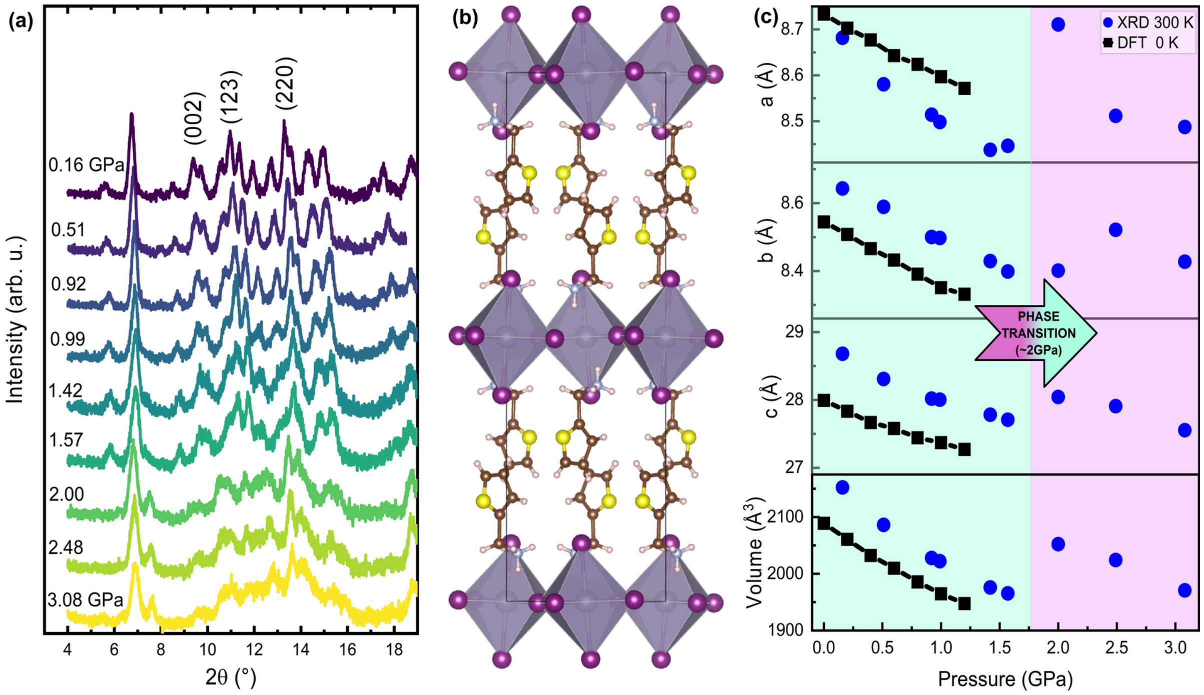

Figure 1. (a) Powder XRD patterns of TMA_2SnI_4 up to 3.08 GPa, together with the interpretation of visible reflections. (b) Crystal structure of TMA_2SnI_4 used in spectra interpretation and DFT calculations. (c) Lattice parameters and unit cell volume as a function of applied pressure, derived from XRD measurements and DFT calculations.

We demonstrate a large negative pressure coefficient (−187 ± 3 meV/GPa), which remains robust across a temperature-induced structural phase transition, exceeding the previously reported values for $(4FP)_2SnI_4$.[13] Combined temperature- and pressure-dependent PL, reflectance, and DFT calculations reveal that the band gap evolution arises from Sn−I bond compression while preserving the octahedral connectivity. These results contribute to understanding pressure-controlled excitonic and electronic phenomena in soft Sn-based halide perovskites and provide a framework for designing tunable, stimuli-responsive optoelectronic materials. While complementary cryogenic high-pressure XRD would further clarify structural origins of low-temperature emissive states, this study establishes clear trends and mechanistic understanding of pressure-dependent optical behavior.

High-quality bulk crystals of TMA_2SnI_4 were synthesized using an optimized method, detailed in the Supporting Information (SI). The stoichiometric combination of freshly prepared tin(II) iodide and commercially available 2-thiophenemethylammonium iodide, followed by solvent evaporation, yielded burgundy-colored, millimeter-sized flakes (see SI, Figure S1).

To investigate the structural resilience, pressure-dependent XRD measurements were performed under hydrostatic conditions of up to 3.08 GPa at room temperature. Diffraction patterns in Figure 1(a) revealed no additional peaks or splitting, indicating the absence of pressure-induced phase transitions up to ~1.6 GPa. All reflections were indexed to an orthorhombic lattice, confirming the structural stability. At ambient pressure, TMA_2SnI_4 adopts a centrosymmetric orthorhombic phase (space group *Pbca*), featuring corner-sharing $[SnI_6]^{4-}$ octahedra, arranged in layered sheets, separated by bilayers of 2-thiophenemethylammonium (TMA) cations.[21] This Ruddlesden−Popper-type structure[22−24] has refined unit cell parameters: a = 8.797 Å, b = 8.688 Å, c = 29.170 Å, $\alpha = \beta = \gamma = 90°$, and V = 2229 Å^3. The molecular structure of TMA and the crystal structure are shown in SI, Figure S1 and Figure 1(b), respectively. Above ~1.6 GPa, a phase transition appears, though its detailed analysis is beyond this study. Figure 1(c) presents the evolution of lattice parameters and unit cell volume with pressure, obtained by fitting key diffraction peaks (002), (123) and (220). Lattice parameters compress smoothly, supporting the absence of structural phase transition up to ~1.6 GPa. Full refinement parameters with uncertainties are summarized in Table 1 of the Supporting Information. For comparison, theoretical results are also presented in Figure 1(c), which are derived from density functional theory (DFT) calculations. The slightly smaller theoretical values reflect thermal expansion in the room-temperature experiments. Pressure−volume data were fitted using the third-order Birch−Murnaghan equation of state[25] over 0−1.6 GPa. The resulting bulk modulus is 9.42 ± 1.50 GPa, consistent with other hybrid perovskites.[14,26,27] The fit is shown in Figure S2 in the Supporting Information.

To gain a deeper insight into the material's optoelectronic properties, we conducted temperature-dependent optical measurements, including photoluminescence (PL) and reflectance (R) spectroscopy, over a temperature range of 20−300 K in 20 K intervals. Measurements were repeated on multiple samples to ensure reproducibility. Figure 2(a) presents the normalized PL spectra for cooling (solid blue and green lines) and heating (dotted red lines) cycles to track thermal hysteresis. At low temperatures, PL exhibits a sharp high-energy peak at 1.99 eV with a full width at a half-maximum of 23 meV, attributed to free exciton (FX) emission. Below 100 K, this FX peak is accompanied by a broader low-energy (LE) emission.[21] The FX peak blueshifts gradually (0.2 meV/K) up to 170 K. Between 170 and 200 K, a sharp redshift

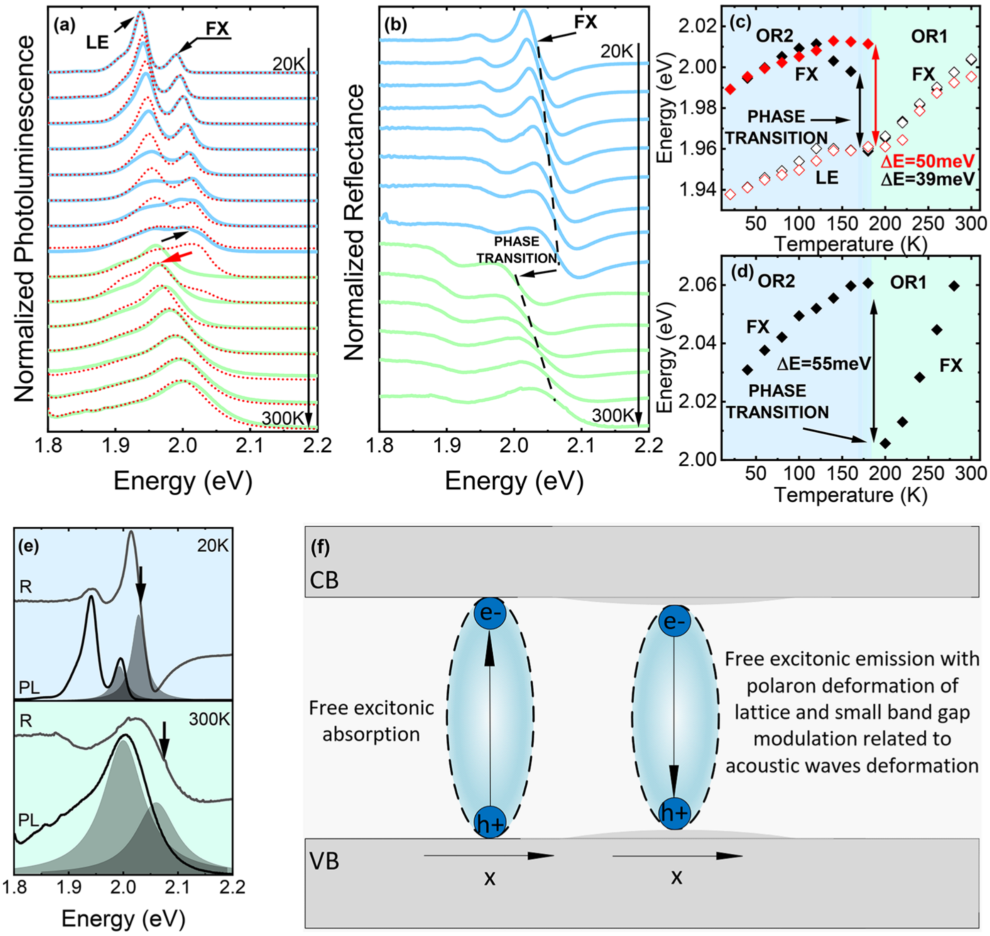

Figure 2. Normalized temperature dependent (a) photoluminescence (PL) and (b) reflectance (*R*) spectra of TMA_2SnI_4. Solid blue and green lines correspond to the cooling cycle, while dotted red lines represent the heating cycle. Blue curves are attributed to the orthorhombic $Cmc2_1$ phase (OR2), and green curves are attributed to the orthorhombic *Pbca* phase (OR1). Temperature dependence of FX (solid black and red diamonds) and LE (open diamonds) energies extracted from (c) PL and (d) *R* measurements. (e) Comparison of PL and *R* spectra measured at 300 and 20 K. (F) Schematic diagrams illustrating the operating principles of the PL and *R* techniques.

indicates a structural phase transition from the orthorhombic $Cmc2_1$ (OR2) phase (the crystal structure is presented in Figure S3 in the Supporting Information) to the orthorhombic *Pbca* (OR1) phase, consistent with prior studies.[21] Temperature-dependent *R* spectra collected during heating, as shown in Figure 2(b), corroborate the PL trends. The FX transition shifts to higher energies with increasing temperature, attributed to enhanced electron−phonon interactions,[28,29] and the phase transition is evident in the 180−200 K range. Figure 2(c) summarizes the FX and LE peak positions were extracted by fitting Gaussian functions to the PL spectra with ±2 meV uncertainty. Black and red diamonds indicate FX peak energies during cooling and heating cycles, respectively, while open diamonds represent LE features. From 20 to 120 K, both emissions remained spectrally stable. A phase transition is observed between 160 and 200 K: during cooling, the FX peak shifts by 39 meV between 160 and 180 K, whereas, during heating, the transition occurs between 180 and 200 K with a larger shift of 50 meV. Beyond 200 K, both transitions change gradually, with a total shift of ∼5 meV. Figure 2(d) shows FX transition energies extracted from *R* spectra fitted with[30]

$$R(E) = R_0 + R_A Re\left(\frac{E_0 - E + i\Gamma}{(E_0 - E)^2 + \Gamma^2} e^{i\Theta}\right) \tag{1}$$

where R_A is the amplitude, E_0 is the transition energy, Γ is the line width, R_0 is the background, and Θ is the phase angle. Fitting parameters (E_0, Γ, and Θ) were allowed to vary freely, and the uncertainty in E_0 is estimated to be ±3 meV from repeated fits. As shown in Figure 2(e) FX features observed in PL and *R* overlap spectrally, but the PL peak maximum is observed at lower energy, further confirming the phase transition near 180−200 K. A systematic offset is observed between the absolute energy positions of the FX feature in PL and *R* measurements. This divergence likely stems from the intrinsic differences between the two techniques: PL is an emission-based process sensitive to exciton recombination and reabsorption effects, whereas *R* probes absorption-like processes that are unsensitive to these phenomena, as schematically shown in Figure 2(f). Overall, the temperature-dependent evolution of FX and LE emissions and the consistent yet technique-dependent discrepancies between PL and *R* underscore the complex optical response of TMA_2SnI_4. These results emphasize the critical role of structural phase transitions and strong electron−phonon coupling in governing the temperature-dependent optical

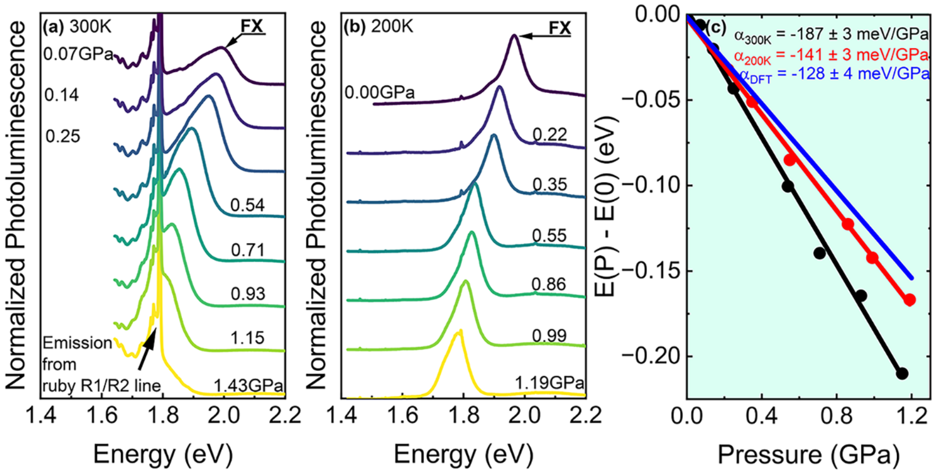

Figure 3. Photoluminescence spectra of TMA_2SnI_4 in the OR1 phase as a function of applied pressure at (a) 300 and (b) 200 K. (c) Pressure-induced band gap shift, defined as $\Delta E = E(P) - E(P = 0)$, extracted from the PL spectra at 300 K (black circles) and 200 K (red circles), along with corresponding linear fits (dashed lines). A clear temperature dependence of the pressure coefficient is observed. Results from DFT calculations are shown for comparison (solid line).

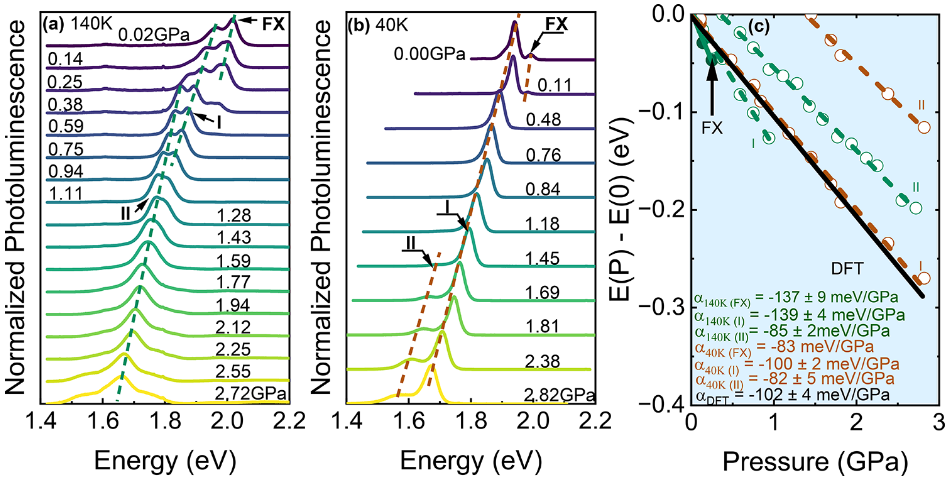

Figure 4. Photoluminescence spectra of TMA_2SnI_4 under varying hydrostatic pressures in the OR2 phase at (a) 140 and (b) 40 K. The divide of the LE feature is indicated as components I and II. (c) Pressure-induced band gap shift $\Delta E = E(P) - E(P = 0)$, extracted from PL spectra at 140 (green circles) and 40 K (brown circles). Solid circles and lines correspond to the FX feature; open circles and dashed lines represent the I and II components of the LE feature. A pronounced temperature dependence of the pressure coefficient is evident. Results from DFT calculations are shown as a solid line for comparison.

properties of 2D hybrid perovskites, distinguishing them from conventional semiconductors.[31,32] While PL and *R* probe excitonic transitions, DFT computes single-particle band-to-band gaps. Comparison focuses on trends and coefficients, assuming smoothly varying exciton binding energy, with residual differences attributed to its pressure sensitivity in 2D systems.

Figure 3(a,b) presents normalized PL spectra of TMA_2SnI_4 under hydrostatic pressure at 300 and 200 K, corresponding to the OR1 phase. A detailed analysis of the pressure-transmitting medium's hydrostaticity is provided in Figure S4 of the Supporting Information, and optical micrographs of the sample are shown in Figure S5 of the Supporting Information. At both temperatures, TMA_2SnI_4 remains in the OR1 phase with PL dominated by FX emission. LE contributions are negligible, consistent with ambient pressure. Upon increasing the pressure, the FX emission redshifts while maintaining line width and intensity at low pressures. At 300 K, the FX emission partially overlaps a 1.78 eV secondary peak originating from ruby fluorescence used for pressure calibration,[33] but the redshift remains clearly observable. The pressure coefficients of the FX optical transition energy were extracted from linear fits of the FX energy versus applied pressure over the pressure range 0−1.6 GPa and compared with DFT calculations of the electronic band gap, as shown in Figure 3(c). Uncertainties reflect the standard error of the slope, and fits were limited to pressure ranges with monotonic peak evolution to ensure reliability. The negative pressure coefficients exhibit a decreasing trend with temperature, e.g., −187 ± 3 and −141 ± 3 meV/GPa at 300 and 200 K respectively, with uncertainties explicitly stated for all reported values. Unlike many other halide perovskites, TMA_2SnI_4 shows no pressure-induced enhancement of PL intensity, band gap widening, additional emission features or amorphization,[17,34−36] at least up to ∼1.6 GPa within the OR1 phase.

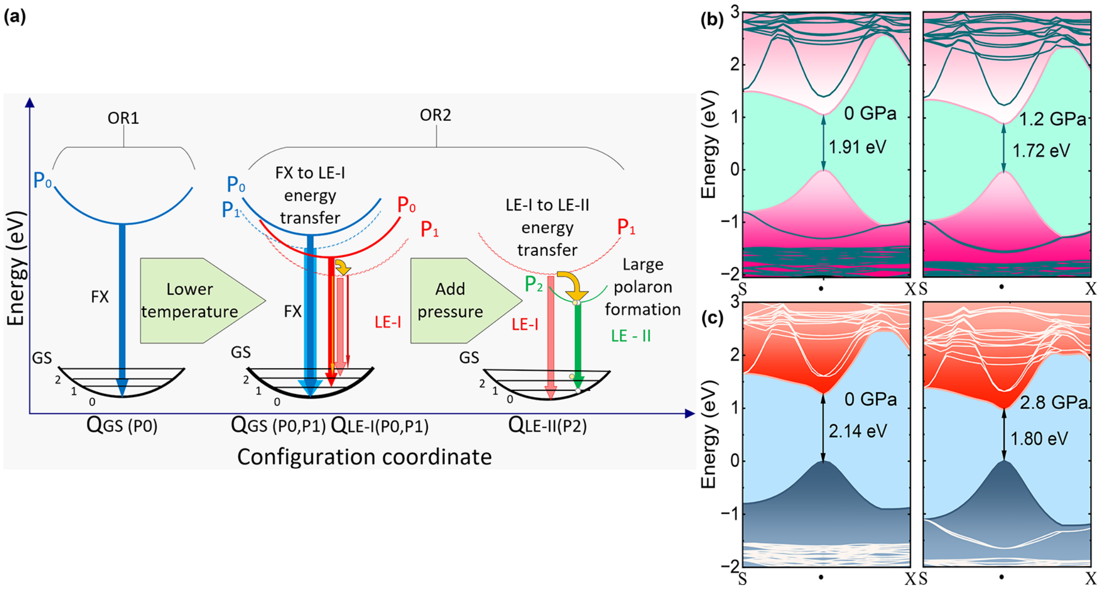

Figure 5. (a) Schematic configuration diagram illustrating the pressure-induced redshift of the FX and LE emissions in TMA_2SnI_4, along with the formation of a large polaron transition. P_0 represents ambient pressure, while P_1 is larger than P_0. GS denotes the ground state of the system. (b) Band structure of TMA_2SnI_4 in the OR1 phase at 0 and 1.2 GPa. (c) Band structure in the OR2 phase at 0 and 2.8 GPa. In both phases, the band gap remains direct and exhibits a pronounced red-shift with increasing pressure.

In contrast, markedly different PL behavior emerges following the thermal phase transition to the OR2 phase structure.

At 140 and 40 K (i.e., OR2 phase), the PL spectra of the material under hydrostatic pressure exhibit distinct behavior, as shown in Figure 4(a,b). At 140 K and low pressure, FX emission dominates, accompanied by weaker LE emission, whereas, at 40 K, LE emission becomes predominant. Upon increasing hydrostatic pressure, both FX and LE emissions redshift. All high-pressure XRD measurements in this study were performed at room temperature; consequently, direct structural information under combined low-temperature and high-pressure conditions is unavailable. Future low-temperature, high-pressure diffraction studies will be required to determine whether a pressure-induced structural phase transition occurs in the OR2 phase. With pressure, the FX peak rapidly diminishes, while the LE response intensifies. At higher pressures, the LE peak splits into two distinct components (labeled I and II). This splitting may arise from pressure-induced reduction in the formation energy of large polarons, consistent with similar hybrid perovskite systems,[37,38] where emergent LE features reflect excitonic complexes coupled to lattice distortions. The energy separation between LE-I and LE-II (~15−20 meV) is comparable to optical phonon binding energies reported in related 2D Sn-perovskites. Alternative mechanisms, including pressure-induced phase coexistence at cryogenic temperatures, defect-assisted radiative recombination, or stabilization of localized excitons in a structurally distorted lattice, cannot be excluded. Direct structural verification at low temperatures, such as cryogenic high-pressure XRD, would be required to definitively confirm these assignments. Pressure may also facilitate emergent emissive states, possibly associated with polaronic excitons,[39−41] or arise from subtle lattice reorganization as seen in hybrid perovskites like $MAPbI_3$.[42] Overall, the spectral evolution is primarily attributed to pressure-enhanced exciton−phonon coupling with structural effects remaining plausible but unverified.

Figure 4(c) summarizes the pressure-dependent energy position of the FX, LE, and emergent peaks, additionally with DFT calculations. Linear fits yield pressure coefficients for both FX and LE emissions. Fits were restricted to pressure ranges where the peak evolution remains monotonic, and the uncertainties shown correspond to one standard deviation of the fitted slope. The pressure coefficients for FX and LE are comparable at 140 and 40 K and exhibit a consistent trend of decreasing magnitude with increasing temperature (at 140 K: −137 ± 9, −139 ± 4, and −85 ± 2 meV/GPa for FX, LE-I, and LE-II, respectively; at 40 K: −83, −100 ± 2, and −82 ± 5 meV/GPa for FX, LE-I, and LE-II, respectively.). The similar pressure response of these features suggests close energetic coupling between the NBE and localized states. In 2D perovskites, strong dielectric confinement and reduced dimensionality produce large exciton binding energies that are moderately sensitive to pressure. Pressure-induced changes in lattice parameters, dielectric screening, and electron−phonon coupling can modify the exciton binding energy, thereby influencing the optical transition energies observed in PL. The approximately linear pressure dependence observed experimentally indicates that these effects vary smoothly over the measured range, yet small variations in exciton binding energy may still contribute to residual differences between experimental and DFT-derived pressure coefficients. The observed pressure-dependent evolution of FX and LE emissions is illustrated by the configuration coordinate model in Figure 5(a).[43−45]

Under ambient conditions, PL is dominated by the FX emission, intrinsic to the OR1 phase. Upon increasing pressure and decreasing temperature, the FX emission is reduced, coinciding with the emergence of LE emission. This LE emission is tentatively attributed to pressure- and temperature-stabilized localized states, which could involve large polarons or self-trapped excitons stabilized by enhanced electron coupling and lattice deformation under the combined effects of lattice compression and reduced thermal energy. The pronounced LE splitting under pressure likely reflects the lattice's ability to accommodate localized distortions, facilitating polaronic stabilization without definitive assignment.

At cryogenic temperatures and elevated pressures, the LE emission further evolves into distinct subfeatures, notably LE-II, suggesting the additional stabilized channels, which may correspond to localized excitonic configurations, defect-assisted recombination pathways, or pressure-induced structural heterogeneity. All photoexcited states, including FX, LE-I and LE-II, relax radiatively, producing the observed PL features. The configuration-coordinate model in Figure 5(a) provides a qualitative framework for interpreting the evolution of LE subfeatures, but it does not uniquely determine their microscopic origin. Deviations between DFT calculated band structures and experimental PL energies likely reflect exciton binding energies that vary under hydrostatic pressure and lattice distortions. This model captures the complex temperature- and pressure-dependent evolution of the emission landscape, highlighting the role of structural dynamics and polaron formation in 2D Sn-based perovskites.

The obtained pressure coefficient for the FX transition is further supported by DFT calculations incorporating the influence of hydrostatic pressure on the electronic band structure. Figure 5(b) presents representative electronic band structures of the OR1 phase under applied pressures of 0 and 1.2 GPa. Across this range, the fundamental band gap remains direct and decreases monotonically with increasing pressure, consistent with the trend observed in Figure 3(c). The pressure coefficient extracted from DFT calculations shows good agreement with the experimental observations. The slight underestimation of theoretical values is attributed to the absence of thermal effects in DFT (0 K), whereas the experimental data were collected at elevated temperatures (200−300 K).

Figure 5(c) shows the corresponding band structures for the OR2 phase at 0 and 2.8 GPa. Similar to OR1, the band gap remains direct and decreases approximately linearly with increasing pressure, consistent with the behavior shown in Figure 4(c). The pressure coefficient predicted by DFT closely matches the experimental values for FX, with only minor deviations. These discrepancies likely arise not only from thermal effects but also from the excitonic nature of the experimentally observed optical transitions, in contrast to the single particle band-to-band gaps obtained from DFT. In particular, pressure-dependent changes in the exciton binding energy, expected in strongly confined 2D perovskites, may contribute to the observed differences between experiment and theory. It is possible that exciton binding energy is varied with the hydrostatic pressure. Notably, both experimental and theoretical pressure coefficients show high linearity across the analyzed pressure ranges, underscoring the robustness of the band gap tuning mechanism in both the OR1 and OR2 phases. Any deviations from linearity are within the experimental uncertainties, justifying the use of linear fits in the reported intervals.

This pressure-induced modulation of the band gap can be directly attributed to the structural characteristics of 2D tin-based perovskites, particularly the role of Sn atoms occupying the metal sites within the inorganic layers. In such systems, the band edges near the fundamental gap are primarily formed by tin and halide orbitals, the valence band maximum typically arises from the hybridization of tin and halide orbitals, and the conduction band minimum is predominantly composed of tin orbitals. Upon compression, significant shortening of the Sn-halide bond lengths occurs, while bond angles remain relatively more stable in comparison. This bond compression induces a systematic redshift in the band gap, particularly evident in the low-pressure regime. The effect is especially pronounced in systems with large organic spacers, which absorb a portion of the applied stress and modulate the extent of distortion within the inorganic lattice. Furthermore, the substitution of lead with tin enhances structural flexibility due to tin's smaller atomic radius, allowing greater accommodation of the organic components and improved pressure resilience.[13,14]

In conclusion, we have shown that TMA_2SnI_4 exhibits pronounced band gap tunability of the optical (excitonic) transiton energies under hydrostatic pressure, with a large negative pressure coefficient (−187 ± 3 meV/GPa) and no phase transition up to ∼1.6 GPa at room temperature. Temperature-dependent studies reveal a reversible phase transition near 180 K and strong excitonic behavior with additional emissive states emerging at low temperatures under pressure, consistent with strong exciton−phonon coupling and polaron formation. While we cannot rule out pressure-induced structural modifications in the OR2 phase, confirmation would require low-temperature, high-pressure structural probes such as XRD. These results highlight the material's structural stability and optoelectronic sensitivity, positioning TMA_2SnI_4 as a candidate for pressure-responsive and thermally adaptive optoelectronic devices.

■ ASSOCIATED CONTENT

Supporting Information

The Supporting Information is available free of charge at https://pubs.acs.org/doi/10.1021/acsmaterialslett.5c01670.

> Detailed materials and methods, experimental layout, TMA molecular structure, comment about hydrostaticity of Daphne 7575, third-order Birch−Murnaghan fitting, calculated lattice parameters, angles, and volume with uncertainties as a function of pressure, low temperature crystal structure of TMA_2SnI_4, and optical micrographs of TMA_2SnI_4 under pressure (PDF)

■ AUTHOR INFORMATION

Corresponding Author

Rafał Bartoszewicz − *Department of Semiconductor Materials Engineering, Wrocław University of Science and Technology, 50-370 Wrocław, Poland;* orcid.org/0009-0001-2951-1459; Email: rafal.bartoszewicz@pwr.edu.pl

Authors

Jakub Ziembicki − *Department of Semiconductor Materials Engineering, Wrocław University of Science and Technology, 50-370 Wrocław, Poland*

Artur P. Herman − *Department of Semiconductor Materials Engineering, Wrocław University of Science and Technology, 50-370 Wrocław, Poland;* orcid.org/0000-0002-1393-0317

Magdalena Wietrzyńska − *Department of Semiconductor Materials Engineering, Wrocław University of Science and Technology, 50-370 Wrocław, Poland*

Jarosław Serafińczuk − *Department of Semiconductor Materials Engineering, Wrocław University of Science and Technology, 50-370 Wrocław, Poland;* orcid.org/0000-0001-9809-4233

Łukasz Przypis − *Department of Semiconductor Materials Engineering, Wrocław University of Science and Technology, 50-370 Wrocław, Poland;* orcid.org/0000-0001-5195-8751

Robert Kudrawiec − *Department of Semiconductor Materials Engineering, Wrocław University of Science and Technology, 50-370 Wrocław, Poland;* orcid.org/0000-0003-2593-9172

Complete contact information is available at:
https://pubs.acs.org/10.1021/acsmaterialslett.5c01670

Author Contributions

CRediT: **Rafał Bartoszewicz** conceptualization, formal analysis, investigation, methodology, resources, supervision, validation, visualization, writing - original draft, writing - review & editing; **Jakub Ziembicki** formal analysis, investigation, methodology, software, writing - review & editing; **Artur P. Herman** resources, writing - review & editing; **Magdalena Wietrzyńska** investigation; **Jarosław Serafińczuk** investigation, methodology; **Łukasz Przypis** resources; **Robert Kudrawiec** funding acquisition, project administration, supervision, validation, writing - review & editing.

Notes

The authors declare no competing financial interest.

ACKNOWLEDGMENTS

This work was financed by the National Science Center (NC) Poland under OPUS 29 grant no. 2025/57/B/ST3/03683. Calculations have been carried out using resources provided by Wroclaw Center for Networking and Supercomputing (https://wcss.pl).

REFERENCES

(1) Jokar, E.; Cai, L.; Han, J.; Nacpil, E. J. C.; Jeon, I. Emerging Opportunities in Lead-Free and Lead−Tin Perovskites for Environmentally Viable Photodetector Applications. *Chem. Mater.* **2023**, *35*, 3404−3426.

(2) López-Fernández, I.; Valli, D.; Wang, C.-Y.; Samanta, S.; Okamoto, T.; Huang, Y.-T.; Sun, K.; Liu, Y.; Chirvony, V. S.; Patra, A.; et al. Lead-Free Halide Perovskite Materials and Optoelectronic Devices: Progress and Prospective. *Adv. Funct. Mater.* **2024**, *34*, 2307896.

(3) Jiang, X.; Zang, Z.; Zhou, Y.; Li, H.; Wei, Q.; Ning, Z. Tin Halide Perovskite Solar Cells: An Emerging Thin-Film Photovoltaic Technology. *Accounts of Materials Research* **2021**, *2*, 210−219.

(4) Babayigit, A.; Thanh, D. D.; Ethirajan, A.; Manca, J.; Muller, M.; Boyen, H.-G.; Conings, B. Assessing the toxicity of Pb- and Sn-based perovskite solar cells in model organism Danio rerio. *Sci. Rep.* **2016**, *6*, 18721.

(5) Fang, H.-H.; Adjokatse, S.; Shao, S.; Even, J.; Loi, M. A. Long-lived hot-carrier light emission and large blue shift in formamidinium tin triiodide perovskites. *Nat. Commun.* **2018**, *9*, 243.

(6) Tong, J.; Song, Z.; Kim, D. H.; Chen, X.; Chen, C.; Palmstrom, A. F.; Ndione, P. F.; Reese, M. O.; Dunfield, S. P.; Reid, O. G.; et al. Carrier lifetimes of > 1 μs in Sn-Pb perovskites enable efficient all-perovskite tandem solar cells. *Science* **2019**, *364*, 475−479.

(7) Sanchez-Diaz, J.; Rodriguez-Pereira, J.; Das Adhikari, S.; Mora-Seró, I. Synthesis of Hybrid Tin-Based Perovskite Microcrystals for LED Applications. *Advanced Science* **2024**, *11*, 2403835.

(8) Żuraw, W.; Kubicki, D.; Kudrawiec, R.; Przypis. Carboxylic Acid-Assisted Synthesis of Tin(II) Iodide: Key for Stable Large-Area Lead-Free Perovskite Solar Cells. *ACS Energy Letters* **2024**, *9*, 4509−4515.

(9) Adl, H. P.; Sánchez-Díaz, J.; Vescio, G.; Cirera, A.; Garrido, B.; Pacheco, F. A. V.; Żuraw, W.; Przypis; Öz, S.; Mora-Seró, I.; et al. Tailoring Single-Mode Random Lasing of Tin Halide Perovskites Integrated in a Vertical Cavity. *Adv. Mater.* **2024**, *36*, 2313252.

(10) Xing, Y.; He, H.; Cui, Z.; Fu, Z.; Qin, S.; Zhang, W.; Mei, S.; Guo, R. Recent Advances in Optical Properties and Light-Emitting Diode Applications for 2D Tin Halide Perovskites. *Advanced Optical Materials* **2024**, *12*, 2302679.

(11) Ran, C.; Li, W.; Dong, H.; Zhou, Y.; Gao, W.; Wu, Z. Seeking for Cost-Effective Tin Iodide Source toward Efficient Lead-Free Tin Triiodide Perovskite Solar Cells: Advances and Prospects. *ACS Applied Energy Materials* **2023**, *6*, 5102−5112.

(12) Altinkaya, C.; Aydin, E.; Ugur, E.; Isikgor, F. H.; Subbiah, A. S.; De Bastiani, M.; Liu, J.; Babayigit, A.; Allen, T. G.; Laquai, F.; et al. Tin Oxide Electron-Selective Layers for Efficient, Stable, and Scalable Perovskite Solar Cells. *Adv. Mater.* **2021**, *33*, 2005504.

(13) Bartoszewicz, R.; Ziembicki, J.; Zdanowicz, E.; Herman, A. P.; Serafińczuk, J.; Sánchez-Diaz, J.; Das Adhikari, S.; Mora-Seró, I.; Kudrawiec, R. Giant Band Gap Narrowing under Hydrostatic Pressure in (4FP)2SnI4 Halide Perovskite. *J. Phys. Chem. Lett.* **2025**, *16*, 6372−6377.

(14) Kong, L.; Gong, J.; Spanopoulos, I.; Yan, S.; Li, Z.; Zhu, Z.; Liu, X.; Zhu, Y.; Dong, H.; Shu, H.; et al. Revealing the Universal Pressure-Driven Behavior of Hybrid Halide Perovskites and Unique Optical Modifiability in Extremely Soft 2D Tin-Based System. *Adv. Funct. Mater.* **2024**, *34*, 2414437.

(15) Jaffe, A.; Lin, Y.; Karunadasa, H. I. Halide Perovskites under Pressure: Accessing New Properties through Lattice Compression. *ACS Energy Letters* **2017**, *2*, 1549−1555.

(16) Wang, S.; Ma, J.; Li, W.; Wang, J.; Wang, H.; Shen, H.; Li, J.; Wang, J.; Luo, H.; Li, D. Temperature-Dependent Band Gap in Two-Dimensional Perovskites: Thermal Expansion Interaction and Electron−Phonon Interaction. *J. Phys. Chem. Lett.* **2019**, *10*, 2546−2553.

(17) Zhao, W.; Xiao, G.; Zou, B. Pressure-induced emission (PIE) in halide perovskites toward promising applications in scintillators and solid-state lighting. *Aggregate* **2024**, *5*, No. e461.

(18) Liu, G.; Kong, L.; Yang, W.; Mao, H.-k Pressure engineering of photovoltaic perovskites. *Mater. Today* **2019**, *27*, 91−106.

(19) Zhu, Y.; Buitenhuis, J.; Förster, B.; Vetrano, M. R.; Koos, E. Development of Perovskite Quantum Dots for Two-Dimensional Temperature Sensors. *ACS Applied Nano Materials* **2023**, *6*, 4661−4671.

(20) Vescio, G.; Dirin, D. N.; González-Torres, S.; Sanchez-Diaz, J.; Vidal, R.; Franco, I. P.; Adhikari, S. D.; Chirvony, V. S.; Martínez-Pastor, J. P.; Vinocour Pacheco, F. A.; et al. Inkjet-Printed Red-Emitting Flexible LEDs Based on Sustainable Inks of Layered Tin Iodide Perovskite. *Advanced Sustainable Systems* **2024**, *8*, 2400060.

(21) Jung, M.-H. The red light emission in 2D (C4SH3CH2NH3)-2SnI4 and (C4OH7CH2NH3)2SnI4 perovskites. *Dalton Trans.* **2021**, *50*, 10261−10274.

(22) Zdanowicz, E.; Przypis; Żuraw, W.; Grodzicki, M.; Chlipała, M.; Skierbiszewski, C.; Herman, A. P.; Kudrawiec, R. Revealing the TMA2SnI4/GaN band alignment and carrier transfer across the interface. *J. Mater. Chem. C* **2024**, *12*, 18356−18362.

(23) Chen, Y.; Sun, Y.; Peng, J.; Tang, J.; Zheng, K.; Liang, Z. 2D Ruddlesden−Popper Perovskites for Optoelectronics. *Adv. Mater.* **2018**, *30*, 1703487.

(24) Gao, X.; Zhang, X.; Yin, W.; Wang, H.; Hu, Y.; Zhang, Q.; Shi, Z.; Colvin, V. L.; Yu, W. W.; Zhang, Y. Ruddlesden−Popper Perovskites: Synthesis and Optical Properties for Optoelectronic Applications. *Advanced Science* **2019**, *6*, 1900941.

(25) Katsura, T.; Tange, Y. A Simple Derivation of the Birch−Murnaghan Equations of State (EOSs) and Comparison with EOSs Derived from Other Definitions of Finite Strain. *Minerals* **2019**, *9*, 745.

(26) Lee, Y.; Mitzi, D. B.; Barnes, P. W.; Vogt, T. Pressure-induced phase transitions and templating effect in three-dimensional organic-inorganic hybrid perovskites. *Phys. Rev. B* **2003**, *68*, No. 020103.

(27) Ratul Hasan, M. D.; Apon, I. A.; Ahmed Ovi, I.; Zahra, F.-T. Impact of Applied Pressure on Tin-Based Cubic Halide Perovskite

ASnX3 (A = Li, Na and X = Cl, Br, and I) in Reference to Their Optoelectronic Applications. *International Journal of Energy Research* **2024**, *2024*, 8213804.

(28) Francisco-López, A.; Charles, B.; Weber, O. J.; Alonso, M. I.; Garriga, M.; Campoy-Quiles, M.; Weller, M. T.; Goñi, A. R. Equal Footing of Thermal Expansion and Electron−Phonon Interaction in the Temperature Dependence of Lead Halide Perovskite Band Gaps. *J. Phys. Chem. Lett.* **2019**, *10*, 2971−2977.

(29) Saran, R.; Heuer-Jungemann, A.; Kanaras, A. G.; Curry, R. J. Giant Bandgap Renormalization and Exciton−Phonon Scattering in Perovskite Nanocrystals. *Advanced Optical Materials* **2017**, *5*, 1700231.

(30) Stępniewski, R.; Korona, K. P.; Wysmołek, A.; Baranowski, J. M.; Pakuła, K.; Potemski, M.; Martinez, G.; Grzegory, I.; Porowski, S. Polariton effects in reflectance and emission spectra of homoepitaxial GaN. *Phys. Rev. B* **1997**, *56*, 15151−15156.

(31) Varshni, Y. Temperature dependence of the energy gap in semiconductors. *Physica* **1967**, *34*, 149−154.

(32) Sarkar, S.; Kamath, N. S.; Gayen, K.; Pal, S. K. Exciton−phonon coupling in quasi-two-dimensional Ruddlesden−Popper perovskites: impact of a mixed-phase structure. *Nanoscale* **2025**, *17*, 10771−10783.

(33) Datchi, F.; Dewaele, A.; Loubeyre, P.; Letoullec, R.; Godec, Y. L.; Canny, B. Optical pressure sensors for high-pressure−high-temperature studies in a diamond anvil cell. *High Pressure Research* **2007**, *27*, 447−463.

(34) Wu, K.; Bera, A.; Ma, C.; Du, Y.; Yang, Y.; Li, L.; Wu, T. Temperature-dependent excitonic photoluminescence of hybrid organometal halide perovskite films. *Phys. Chem. Chem. Phys.* **2014**, *16*, 22476−22481.

(35) Samanta, D.; Chaudhary, S. P.; Ghosh, B.; Bhattacharyya, S.; Shukla, G.; Mukherjee, G. D. Pressure-induced emission enhancement and bandgap narrowing: Experimental investigations and first-principles theoretical simulations on the model halide perovskite $Cs_3Sb_2Br_9$. *Phys. Rev. B* **2022**, *105*, No. 104103.

(36) Lü, X.; Wang, Y.; Stoumpos, C. C.; Hu, Q.; Guo, X.; Chen, H.; Yang, L.; Smith, J. S.; Yang, W.; Zhao, Y.; et al. Enhanced Structural Stability and Photo Responsiveness of CH3NH3SnI3 Perovskite via Pressure-Induced Amorphization and Recrystallization. *Adv. Mater.* **2016**, *28*, 8663−8668.

(37) Brosseau, P.; Ghosh, A.; Seiler, H.; Strandell, D.; Kambhampati, P. Exciton−polaron interactions in metal halide perovskite nanocrystals revealed via two-dimensional electronic spectroscopy. *J. Chem. Phys.* **2023**, *159*, No. 184711.

(38) Muhammad, Z.; Rashid, A. Exciton binding energies and polaron interplay in the optically excited state of organic−inorganic lead halide perovskites. *Mater. Adv.* **2025**, *6*, 13−38.

(39) Chen, B.; Chen, R.; Huang, B. Strong Electron−Phonon Coupling Induced Self-Trapped Excitons in Double Halide Perovskites. *Advanced Energy and Sustainability Research* **2023**, *4*, 2300018.

(40) Yamada, Y.; Kanemitsu, Y. Electron-phonon interactions in halide perovskites. *NPG Asia Materials* **2022**, *14*, 48.

(41) Dybała, F.; Kudrawiec, R.; Polak, M. P.; Herman, A. P.; Sieradzki, A.; Maczka, M. Near-bandgap emission in [HOC2H4NH3]2PbI4 perovskite under hydrostatic pressure: emission of a free exciton and a polaronic exciton. *Mater. Adv.* **2025**, *6*, 569−578.

(42) Pieniążek, A.; Dybała, F.; Polak, M. P.; Przypis; Herman, A. P.; Kopaczek, J.; Kudrawiec, R. Bandgap Pressure Coefficient of a CH3NH3PbI3 Thin Film Perovskite. *J. Phys. Chem. Lett.* **2023**, *14*, 6470−6476.

(43) Zhao, W.; Fu, R.; Yang, J.; Xiao, G.; Zou, B. Building New Structural Distortion Descriptors through Pressure Engineering toward Enhanced Violet Emission in 2D Hybrid Perovskite. *Advanced Optical Materials* **2024**, *12*, 2401732.

(44) Yu, X.; Fang, Y.; Sun, X.; Xie, Y.; Liu, C.; Wang, K.; Xiao, G.; Zou, B. Pressure-Tuning Localized Excitons Toward Enhanced Emission, Photocurrent Enhancement and Piezochromism in Unconventional ACI-Type 2D Hybrid Perovskites. *Angew. Chem., Int. Ed.* **2024**, *63*, No. e202412756.

(45) Ma, Z.; Lv, P.; He, X.; Wang, F.; Li, Y.; Xiao, G.; Zou, B. Self-Trapped Excitons or Bi3+ Ions for Broad Emission in a Lead-Free Double Perovskite? Hearing What Pressure Says. *Nano Lett.* **2025**, *25*, 9345−9352.

Supporting Information for

Band Gap Tuning by Hydrostatic Pressure in (2-thienyl)methylammonium Tin Iodide Halide Perovskite

Rafał Bartoszewicz,[1,*] *Jakub Ziembicki,*[1] *Artur P. Herman,*[1] *Magdalena Wietrzyńska,*[1] *Jarosław Serafińczuk,*[1] *Łukasz Przypis,*[1] *and Robert Kudrawiec*[1]

[1]Department of Semiconductor Materials Engineering, Wroclaw University of Science and Technology, Wybrzeże Wyspiańskiego 27, 50-370 Wrocław, Poland

* e-mail address: rafal.bartoszewicz@pwr.edu.pl

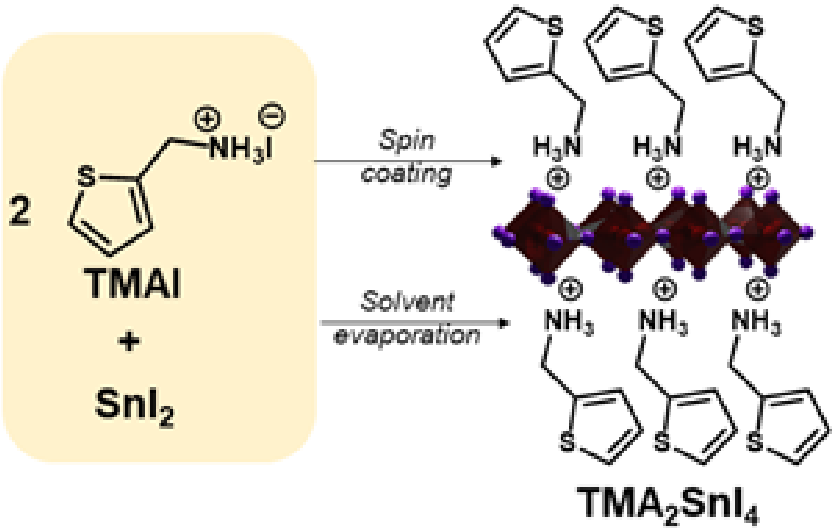

Figure S1. TMA_2SnI_4 employed fabrication methods, and molecular structure with inorganic layer (corner sharing SnI_6 octahedra) enveloped within organic layers (2-thienylmethylammonium cations).

Table 1. Calculated lattice parameters, angles, volume of TMA_2SnI_4 as a function of applied pressure

Pressure [GPa]	a [Å]	Δa [Å]	b [Å]	Δb [Å]	c [Å]	Δc [Å]	V (Å^3)	ΔV (Å3)
0.16	8.682	0.006	8.644	0.005	28.681	0.11	2152.221	8.10
0.51	8.581	0.006	8.589	0.005	28.308	0.09	2086.274	6.69
0.92	8.515	0.006	8.501	0.005	28.019	0.09	2027.825	6.23
0.99	8.499	0.006	8.498	0.005	28.003	0.08	2022.145	5.63
1.42	8.438	0.006	8.429	0.005	27.781	0.08	1975.878	4.63
1.57	8.447	0.006	8.399	0.005	27.708	0.08	1965.559	4.93
2.00	8.711	0.006	8.402	0.005	28.044	0.08	2052.269	5.33
2.49	8.512	0.006	8.522	0.005	27.901	0.08	2024.249	5.21
3.08	8.487	0.006	9.428	0.005	27.554	0.08	1970.816	5.43

Calculations were performed considering 3 lattice planes: (002), (123), and (220), which allowed us to accurately determine both the lattice parameters and the beta angle. In addition, measurement uncertainties were calculated for the measurement step used of 0.0167 degrees.

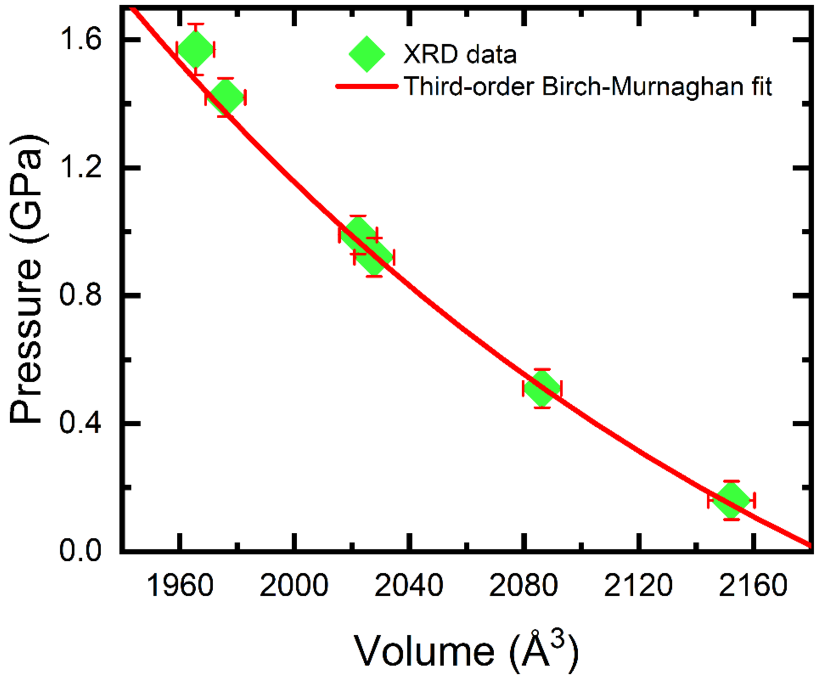

Figure S2. Third-order Birch-Murnaghan fitting of XRD data.

To determine bulk modulus value of TMA_2SnI_4 we used third-order Birch-Murnaghan EoS :

$$P(V) = \frac{3}{2}B_0\left[\left(\frac{V_0}{V}\right)^{7/3} - \left(\frac{V_0}{V}\right)^{5/3}\right] \times \left\{1 + \frac{3}{4}(B_0' - 4)\left[\left(\frac{V_0}{V}\right)^{2/3} - 1\right]\right\}$$

The approximation was calculated using Origin and also EoSFit7 software. After refitting the third-order Birch-Murnaghan function with a fixed value of V_0 = 2229.42 Å^3 we received :

B_0 = 9.42 ± 1.50 GPa

B_0' = 7.68

Pressure was calibrated using the standard ruby fluorescence method [1] with temperature-dependent corrections [2]. The R1 line was fitted using a Gaussian profile, yielding a pressure uncertainty of ± 0.05 GPa. We allowed sufficient time for mechanical relaxation after each pressure change to minimize drift. Pressure stability during long XRD acquisitions was further confirmed by equation-of-state fitting, where no systematic deviations were observed.

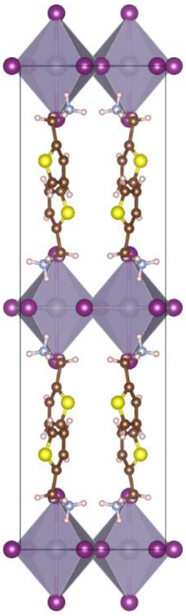

Figure S3. Low temperature crystal structure (orthorhombic Cmc2_1) of TMA_2SnI_4 used in DFT simulations.

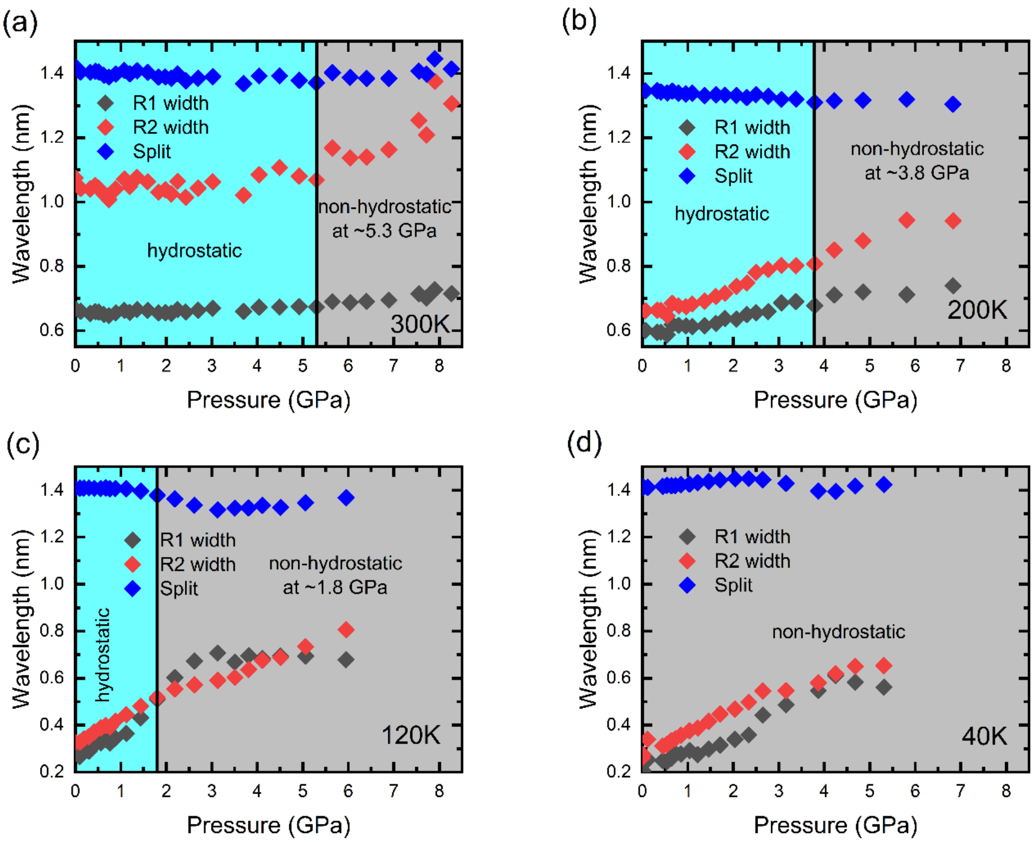

Figure S4. Analysis of ruby R1 and R2 peaks split and broadening at (a) 300, (b) 200, (c) 120, and (d) 40 K. Reprinted from Ref. J. Phys. Chem. Lett. 2025, 16, 25, 6372–6377 under CC-BY 4.0 license. Copyright 2025 R. Bartoszewicz et al.

Figure S4 presents the analysis of the applied pressure using ruby fluorescence. Daphne 7575 is not strictly hydrostatic at low temperatures, and its ability to maintain hydrostatic conditions decreases significantly with both temperature reduction and pressure increase [3,4]. However, while Daphne 7575 does not remain fully hydrostatic at high pressures and low temperature, it maintains quasi-hydrostatic conditions, owing to its relatively low shear strength and soft solidification behavior [4,5]. From R1 and R2 peaks split and broadening we determined solidification points of Daphne 7575 at (a) ~5.3, (b) ~3.8, (c) ~1.8 and (d) 0 GPa for 300, 200, 120 and 40 K respectively. Our results remain consistent with theoretical expectations, which support their validity even in the presence of quasi-hydrostatic conditions. Moreover, for perovskite materials such medium is still second best choice (first choice is helium) as it not influence the condition of measured sample, as it is in the case of 4:1 methanol-ethanol mixture [4].

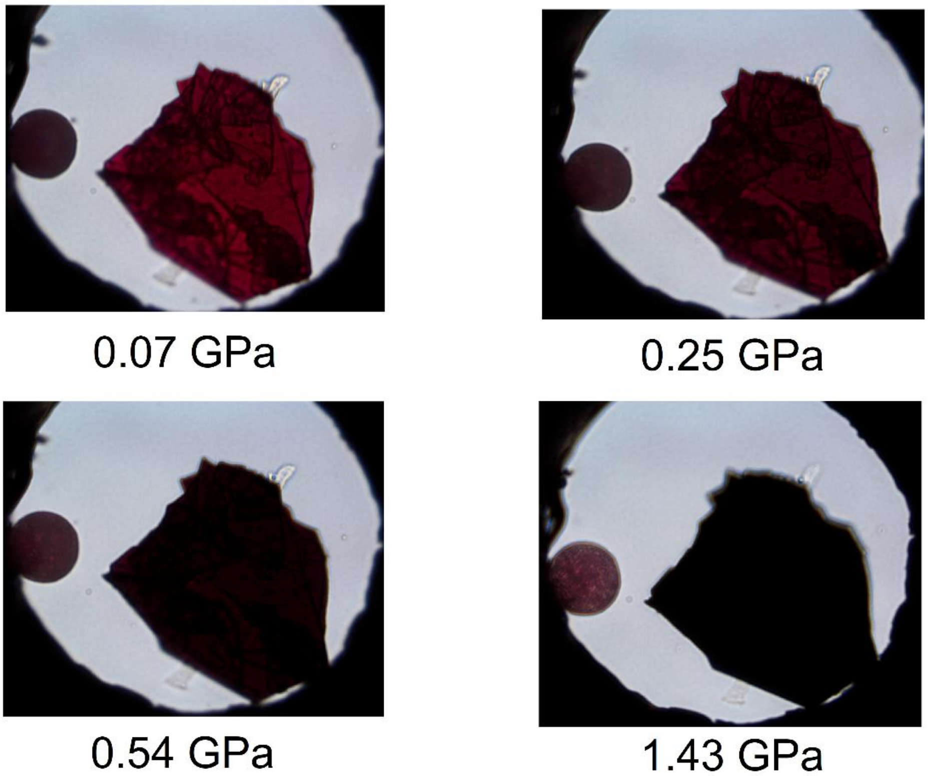

Figure S5. View on the sample for different values of pressure at 300 K.

MATERIALS AND METHODS

Synthesis of TMA_2SnI_4 single crystals:

The synthesis of high-quality TMA_2SnI_4 bulk crystals was accomplished by combining solutions of freshly synthesized tin(II) iodide and commercially available 2-thiophenemethylammonium iodide in stoichiometric amounts, utilizing the solvent evaporation method.

Thin film preparation:

Glass substrates were cleaned by ultrasonication in 2% Hellmanex deionized water solution, deionized water, acetone and isopropanol for 5 minutes in each solvent and dried by nitrogen flow. Before deposition substrates were treated with UV light for 10 minutes in N_2 filled glovebox. Filtered perovskite solution was spin-coated at 6000 rpm for 30 s with a ramping rate of 2000 rpm·s -1 with toluene as an antisolvent. The resulting film was annealed at 100 °C for 10 min.

Temperature and pressure dependent PL

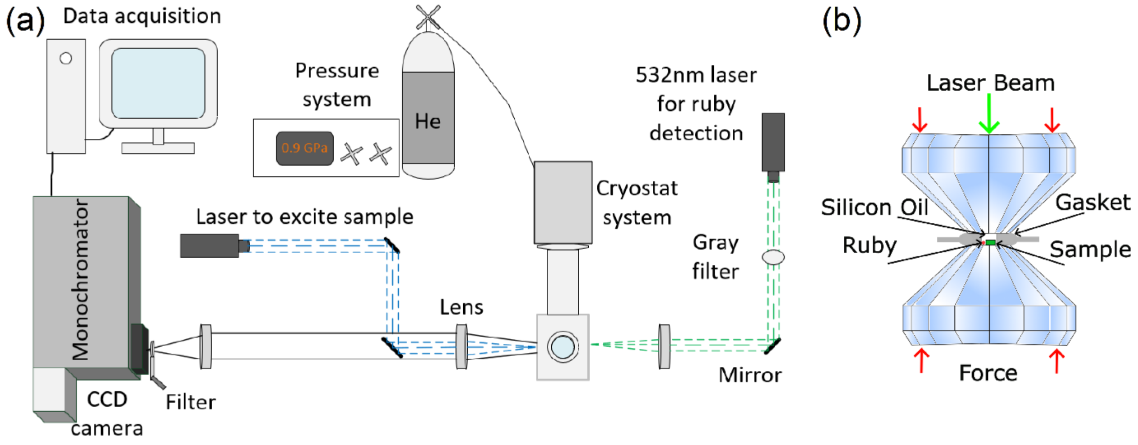

Figure S5. (a) The scheme of the experimental setup for hydrostatic pressure-dependent photoluminescence (b) Cross-section of a diamond anvil cell.

Figure S5 (a) presents schematically the experimental setup of temperature- and pressure-dependent PL carried out in this work. Figure S5 (b) shows a cross-section of a diamond anvil cell (DAC). PL measurements were performed in Diacell design DAC by 'Almax easyLab'. DAC used in this work is made of beryllium copper (BeCu) alloy, which allows to perform measurements at cryogenic temperature (here 40 K). Diamond with 650 µm culet size was used. The pressurizing mechanism in the DAC was driven using a gas membrane. The pressure in DAC was controlled by the amount of helium injected into the gas membrane. On top of the bottom diamond culet, a gasket was placed. It is a thin sheet (circa 50 µm thickness) of inconel material with a central hole of about 1/3 culet size, where sample, ruby sphere, and silicon oil were placed. Gaskets were prepared by pressing diamonds into a thin sheet, followed by creating a central hole using mechanical drilling. Daphne 7575 was used as the pressure-transmitting medium, which solidifies at about 5.3GPa at room temperature. Whole setup was cooled down in a cryostat with a closed-loop liquid helium system. For PL experiments, the 405 nm CW (with power of 100 µW) laser was used to excite the studied material. Emitted light was dispersed through a 0.5 m Andor monochromator with a 150 l/mm diffraction grating blazed at 500 nm. The signal was recorded by a Si CCD camera cooled to -70 °C by Peltier module. The luminescence of the ruby R1 line at

~1.78 eV (at room temperature) was excited by the 532 nm CW laser, dispersed on the 600 l/mm diffraction grating blazed at 500 nm and detected by CCD camera. To determine pressure value inside DAC we detect pressure-induced redshift of ruby sphere R1 line with calibration taken from Shen [1]. The temperature shift correction of the R1 ruby line was taken from Datchi [2]

Temperature Dependent reflectance

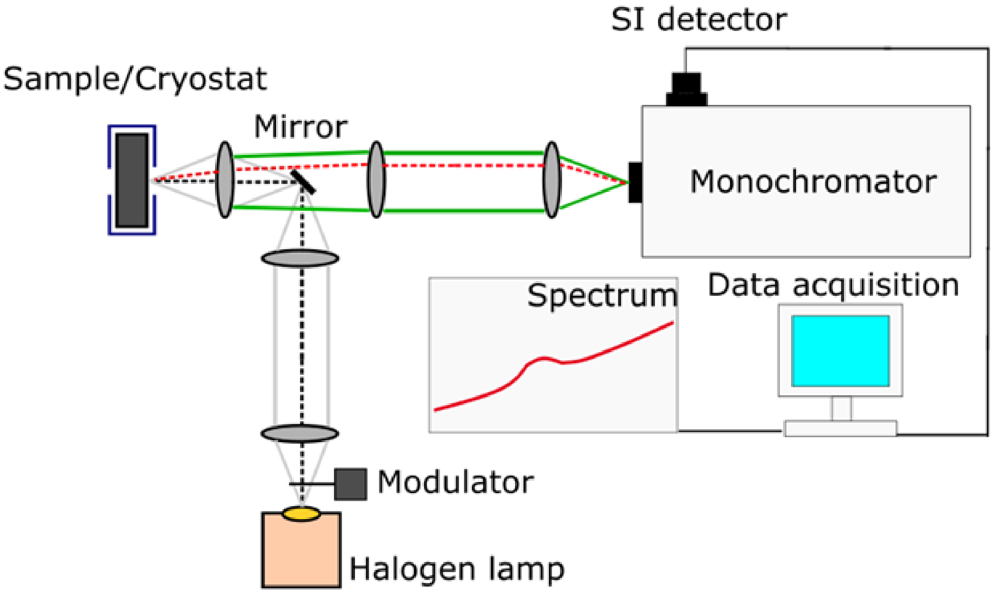

Figure S6. Measurement system for determining the temperature dependent reflectance spectrum.

Figure S6 shows measurement system to collect reflectance spectra in so-called ‘bright configuration’. In this setup, the light emitted from a OSRAM HLX 64655 250 W 24 V halogen lamp was modulated by STANFORD RESEARCH SYSTEMS SR540 CHOPPER at a frequency of 266 Hz and directed to a measured sample. Reflected light from the surface was then directed to a single grating OMNI-λ 500 ZOLIX monochromator. In the monochromator, the probe beam (white light) was dispersed, and finally detected by a SI diode HAMAMATSU S2386. The sample was placed in a closed-cycle helium-cooled SUMITOM DE-202FF cryostat, which allows measurements in the temperature range from 30 to 320 K. The temperature was monitored and stabilized using a LAKESHORE 331 controller. Resultant signal was measured in the lock-in technique with a STANFORD SR830 DSP phase-sensitive nanovoltmeter, which consists in measuring the spectra point by point and the reference signal.

Theoretical calculations

The DFT calculations were performed within the plane-wave representation using the PAW method as implemented in the VASP code [6,7,8,9]. We employed the r^{2}SCAN+rVV10 functional due to its general accuracy in predicting geometries and energies of systems with van der Waals interactions [10]. Geometry optimizations under different hydrostatic pressures were first carried out, starting from experimentally determined structures [11]. The resulting structures were then used for band-gap calculations, where spin-orbit interactions were also included, as they are known to strongly affect the band structures of perovskites. Although, as expected, the employed meta-GGA functional underestimates the absolute band-gap values, the pressure coefficients and the relative differences between the band gaps of the low- and high-temperature phases are in good agreement with experimental results. The convergence criterion for forces was set to 5 meV/Å, the plane-wave energy cutoff was set to 500 eV, and a regular Γ-centered Brillouin zone sampling with a 1 x 4 x 4 k-point mesh was used.

Pressure dependent X-ray diffraction

Structural studies with X-ray diffraction, were carried out using an Malvern-Panalytical Empyrean diffractometer. A molybdenum x-ray tube with $Mo_{K\alpha 1}$ = 0.7093197 Å was used in the study. Pressure was generated by an 'Almax easyLab' Bragg-Mini DAC with diamond culet size of 600 μm allowing pressures up to 20 GPa. Daphne 7575 was used as the pressure-transmitting medium, which solidifies at about 5.3 GPa at room temperature. An x-ray tube was set to point focus and a 135 mm long mono-capillary collimator with an exit beam diameter of 0.3 mm were used to form the incident beam. The diffraction curves were recorded by a multi-strip detector 1Der. Measurements were carried out at range from 3 to 19 degrees which allowed all the strongest reflections for the investigated material to be observed. Counting time was 3400 s/point.

References:

[1] Shen, G.; Wang, Y.; Dewaele, A.; Wu, C.; Dayne, E.; Eggert, J.; Klotz, S.; Dziubek, K. F.; Loubeyre, P.; Fat, V.; Asimow, P. D.; Mashimo, T.; Wentzcovitch, R. M. M.; Toward an International Practical Pressure Scale: A Proporsal for an IPPS Ruby Gauge (IPPS-Ruby2020). High Press. Res. 2020, 40, 299-314 10.1080/08957959.2020.1791107

[2] Datchi, F.; Dewaele, A.; Loubeyre, P.; Letoullec, R.; Godec, Y. Le.; Canny, B.; Optical Pressure Sensors for High-Pressure-High-Temperature Studies in a Diamond Anvil Cell. High Press. Res. 2007, 27, 447-463.c https://doi.org/10.1080/08957950701659593

[3] Staško, D., Prchal, J., Klicpera, M., Aoki, S., & Murata, K. (2020). Pressure media for high pressure experiments, Daphne Oil 7000 series. *High Pressure Research*, *40*(4), 525–536. https://doi.org/10.1080/08957959.2020.1825706

[4] Naoyuki Tateiwa and Yoshinori Haga 2010 J. Phys.: Conf. Ser. 215 012178

[5] Y Nakamura et al 2010 J. Phys.: Conf. Ser. 215 012176

[6] Kresse, G.; Hafner, J.; Ab initio molecular dynamics for liquid metals. Phys. Rev. B 1993, 47, 558(R)

[7] Kresse, G.; Furthmüller, J.; Efficient iterative schemes for ab initio total-energy calculations using a plane-wave basis set. Phys. Rev. B 1996, 54, 11169

[8] Kresse, G.; Furthmüller, J.; Efficiency of ab-initio total energy calculations for metals and semiconductors using a plane-wave basis set. Computational Materials Science, 1996, Vol 6, Issue 1, 15-50

[9] Kresse, G.; Joubert, D.; From ultrasoft pseudopotentials to the projector augmented-wave method. Phys. Rev. B 1999, 59, 1758

[10] Ning, J.; Kothahonda, M.; Furness, J. W.; Kaplan, A. D.; Ehlert, S.; Brandenburg, J. G.; Perdew, J. P.; Sun, J.; Workhorse minimally empirical dispersion-corrected density functional with tests for weakly bound systems: r^2SCAN+rVV10. Phys. Rev. B 2022, 106, 075422

[11] Jung, M.; The red light emission in 2D (C4SH3CH2NH3)2SnI4 and (C4OH7CH2NH3)2SnI4 perovskites. Dalton Trans. 2021, Vol 50, Issue 29, 10261-10274

3.3 Hydrostatic Pressure Driven Band Gap Tuning and Self-Trapped Exciton Formation in $(4FPEA)_2SnBr_4$ Halide Perovskite

Rafał Bartoszewicz† , Jakub Ziembicki, Ewelina Zdanowicz, Artur P. Herman, Jesús Sánchez-Diaz, Samrat Das Adhikari, Iván Mora-Seró, Robert Kudrawiec

arXiv preprint, arXiv:2603.03931 (2026). DOI: 10.48550/arXiv.2603.03931

Author's Contribution:

Rafał Bartoszewicz with supervisor conceived and formulated the research problem, defining the scientific objective of elucidating the interplay between hydrostatic pressure, lattice rigidity, and exciton self-trapping in layered Sn HOIPs.

The author designed and independently conducted all temperature- and pressure-dependent PL experiments, strategically employing halide substitution (Br vs I) to isolate the role of lattice stiffness and dielectric screening.

Comprehensive data analysis, including Gaussian peak deconvolution, extraction of pressure coefficients, quantification of Stokes shifts, and uncertainty assessment was performed solely by the author.

The author identified and demonstrated the contrasting pressure coefficients of NBE and STE emissions, establishing hydrostatic pressure as a direct probe of exciton localization energetics.

Experimental results were interpreted within the framework of exciton-phonon coupling, small polaron formation, and configurational coordinate modeling. The author critically integrated experimental findings with DFT calculations to distinguish band-edge tuning from lattice-relaxation-driven effects.

All figures and schematics were prepared by the author, and the manuscript was written and structured to provide a unified physical interpretation of pressure-tunable exciton localization in 2D lead-free HOIPs.

---

† corresponding author

Hydrostatic Pressure Driven Band Gap Tuning and Self-Trapped Exciton Formation in (4FPEA)$_2$SnBr$_4$ Halide Perovskite

Rafał Bartoszewicz,[*,†] Jakub Ziembicki,[†] Ewelina Zdanowicz,[†] Artur P. Herman,[†] Jesús Sánchez-Diaz,[‡] Samrat Das Adhikari,[‡,¶] Iván Mora-Seró,[‡] and Robert Kudrawiec[†]

†*Department of Semiconductor Materials Engineering, Wrocław University of Science and Technology, Wybrzeże Wyspiańskiego 27, 50-370 Wrocław, Poland*
‡*Institute of Advanced Materials (INAM), Universitat Jaume I. Av. de Vicent Sos Baynat, Castellón de la Plana, 12006 Spain*
¶*Institute of Physical Chemistry, Polish Academy of Sciences, Warsaw 01-224, Poland*

E-mail: rafal.bartoszewicz@pwr.edu.pl

Abstract

Two-dimensional tin halide perovskites provide a highly tunable platform for exciton phonon coupling and local lattice distortions, enabled by their intrinsically soft lattice. We report a combined temperature and pressure dependent photoluminescence study of the layered perovskite (4FPEA)$_2$SnBr$_4$. At room temperature, its optical response is dominated by near band edge (NBE) excitons, which redshift linearly under hydrostatic pressure up to ∼3 GPa, indicating a rigid band edge behavior without phase transitions. Cooling reveals a broad, strongly Stokes shifted self-trapped exciton (STE) emission, evidencing a crossover from delocalized to self localized excitonic states. Strikingly, while NBE emission redshifts under pressure, STE emission exhibits an anomalous blueshift, reflecting pressure induced modification of the exciton phonon energy landscape. In contrast, the iodide analogue (4FPEA)$_2$SnI$_4$ shows no STE emission under identical conditions, highlighting the critical role of lattice rigidity and dielectric screening in stabilizing self-trapped excitons.

TOC Graphic

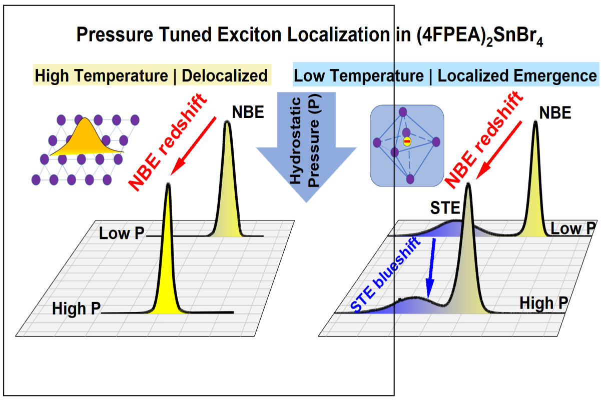

Tin-based halide perovskites have emerged as promising lead-free optoelectronic materials, offering reduced toxicity with strong light-matter interactions and long carrier lifetimes.[1–6] Among them, two-dimensional (2D) Sn-based halide perovskites exhibit pronounced quantum confinement and enhanced excitonic localization,[7–9] making them attractive platforms for studying exciton-phonon coupling phenomena.[10–13] In these materials, the interplay between electronic structure and lattice dynamics governs key processes such as exciton self-trapping, radiative recombination, and carrier-phonon interactions.[14–16]

In particular, the coexistence and competition between free excitons and self-trapped excitons (STE) has attracted growing attention,[17,18] as STE formation is often associated with large Stokes shifts (200-500 meV), broadband emission (100-300 meV), and enhanced exciton-phonon coupling,[19,20] properties that are both technologically appealing and scientifically challenging to control. Here, STEs are interpreted as small polarons, excitons that become tightly localized through strong short-range electron-phonon coupling and consequent local lattice distortion, in contrast to more delocalized large polarons associated with free excitonic state.[20,21] In principle, STEs can be further categorized into those that arise intrinsically from the host lattice and those that are bound to defects or lattice imperfections. In high-quality samples where defect densities are minimal, defect-bound STE signatures are often not resolvable, leaving primarily intrinsic small polaron STE behavior in the optical response.

Exciton self-trapping in halide perovskites is generally attributed to strong coupling between electronic excitations and local lattice distortions.[19] While STE emission has been widely reported in low dimensional and all inorganic halide perovskites, its emergence is highly sensitive to lattice rigidity, dielectric screening, chemical composition, and temperature.[20] Despite extensive experimental and theoretical efforts, an unified understanding of how external perturbations modulate the balance between delocalized and localized excitonic state remains incomplete.[22,23] Hydrostatic pressure provides a powerful, continuous, and reversible means of tuning interatomic distances, orbital overlap, and phonon spectra without introducing chemical disorder.[24] Yet, pressure-dependent behavior of excitons in layered tin-based halide perovskites remain comparatively unexplored.

Notably, Sn-based halide perovskites demonstrate remarkable resilience to external stimuli such as hydrostatic pressure and temperature.[25,26] These stimuli can significantly modulate crystallographic and electronic structures, leading to band gap renormalization, photoluminescence (PL) enhancement, defect-assisted recombination, or even amorphization.[24] In many cases, compression activates new emissive channels or enhances STE formation,[23,27–29] often accompanied by structural instabilities. However, such responses are highly material specific and dependent sensitively on halide chemistry, lattice stiffness and intrinsic structural softness. Understanding, the behavior of these materials under extreme perturbations is therefore important for the development of next generation perovskite-based devices,[30,31] including stimuli-responsive optoelectronic, temperature sensing, mechanical stress detection and flexible electronics.[32–34]

4-fluorophenethylammonium tin bromide ($(4FPEA)_2SnBr_4$) is a recently developed 2D Sn-based halide perovskite.[35] While its structure allows for straightforward optoelectronic characterization, its fundamental optical properties have not yet been reported. In comparison, the closely related $(PEA)_2SnBr_4$ exhibits a direct band gap of ~ 2.7 eV and photoluminescence around $\sim$2.64 eV,[36] suggesting that similar optical behavior may be anticipated in the 4F-substituted derivative. Studies on layered Sn halide perovskites further indicate that both the halide composition and the organic spacer modulate the band gap and emission characteristics.[37] Despite this, the excitonic response of $(4FPEA)_2SnBr_4$ under external perturbations remains largely unexplored.

In this Letter, we present a comprehensive investigation of the excitonic response of $(4FPEA)_2SnBr_4$ under combined control of

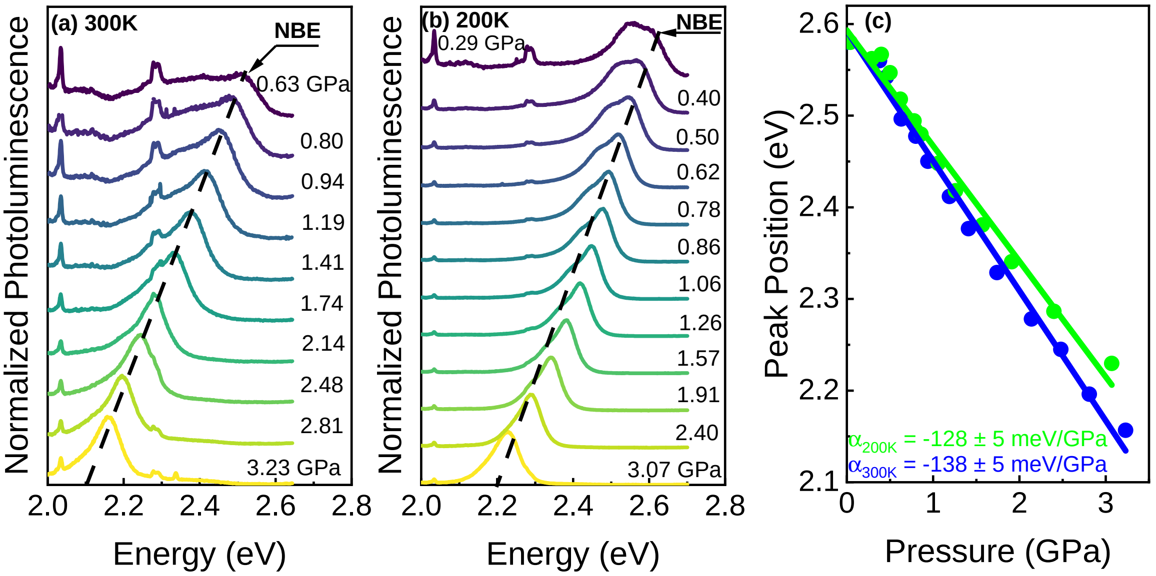

Figure 1: Normalized photoluminescence spectra of $(4FPEA)_2SnBr_4$ under varying hydrostatic pressure at (a) 300 and (b) 200 K. Free exciton is indicated as NBE and position changes are marked by black dashed line. (c) Pressure-induced band gap shift, extracted from the PL spectra at 300 (blue circles) and 200 K (green circles), along with corresponding linear fits (solid lines). A clear temperature dependence of the pressure coefficient is observed.

temperature and hydrostatic pressure. By tracking its PL spectra from room temperature down to cryogenic temperatures and pressures up to ∼ 3 GPa, we uncover a strikingly rigid high temperature excitonic response, characterized by a single near-band-edge (NBE) emission. Here, the high-energy emission close to the optical band edge is referred to as NBE excitonic emission and is commonly attributed to free exciton recombination. This emission redshifts linearly with pressure without any anomalous spectral broadening, intensity enhancement, or evidence of phase transitions what is in line with behavior reported for other perovskites. In contrast, at low temperatures a broad STE emission emerges exclusively in the bromide compound, exhibiting an anomalous blueshift under compression. Direct comparison with iodide analogues shows that STE emission is entirely suppressed in softer, more strongly screened lattices.

The synthesis of $(4FPEA)_2SnBr_4$ microcrystals was performed using the developed methodology elsewhere,[35] as detailed in the Supporting Information (SI). To prove the formation and explore the crystallographic features of the resulting microcrystals, we performed X-ray diffraction (XRD) to identify the crystal phases obtained. Figure S1 in the SI shows the XRD pattern of the $(4FPEA)_2SnBr_4$ microcrystals, exhibiting high crystalinity and uniformity, showing repetitive XRD peaks with intervals of ∼ 5.4°, which corresponds to the interlayer distance of the inorganic layers.

Figure 1 (a-b) presents the evolution of the normalized PL spectra of $(4FPEA)_2SnBr_4$ under hydrostatic pressure, measured isothermally at 300 and 200 K, respectively. Hydrostatic conditions were maintained up to approximately 3 GPa for all measurements. An assessment of the pressure-transmitting medium is provided in Figure S3 in the SI. At both temperatures, the material retains its initial structural phase throughout the investigated pressure range. The PL response is dominated by NBE emission, with no emergence of additional emissive features, consistent with ambient pressure behavior.[35] Upon increasing pressure, the NBE peak exhibits a pronounced redshift, while its linewidth and relative inten-

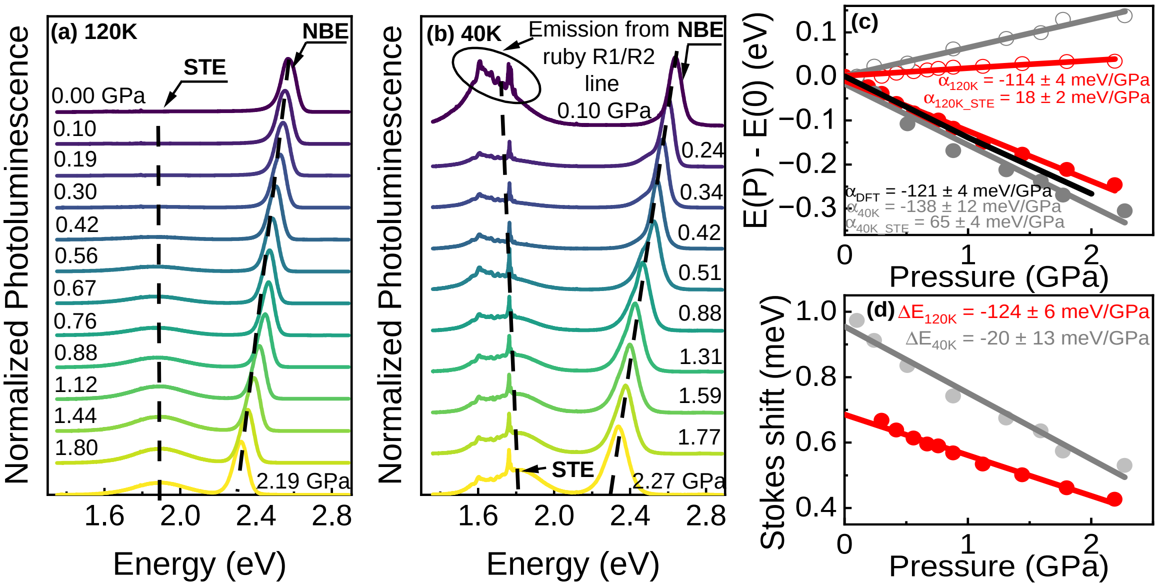

Figure 2: Pressure dependent normalized PL spectra of $(4FPEA)_2SnBr_4$ at (a) 120 and (b) 40 K. Self-Trapped Exciton is indicated as component STE. Positions changes are marked by black dashed lines. (c) Pressure-induced band gap shift $\Delta E = E(P) - E(P = 0)$, extracted at 120 (red circles) and 40 K (grey circles). Solid circles and lines correspond to the NBE feature; open circles and solid lines represent STE feature. Black line shows DFT calculations (crystal strucutre is presented in Figure S2 in the SI). (d) Pressure dependence of the Stokes shift from the same data.

sity remain nearly unchanged compared to low pressures. For clarity in tracking the pressure-induced energy shifts, all spectra are normalized to their maximum intensity. A weak peaks near ~2.3 and 2.0 eV arises from inadvertent illumination by a green and red light source in the experimental environment. However, this artifacts does not affect the determination of the NBE peak position. Pressure coefficients were extracted from linear fits of the NBE peak energy as a function of pressure, with peak positions obtained using Gaussian fitting (Figure 1 (c)). The resulting coefficients are negative and slightly decrease in magnitude with increasing temperature (-138 and -128 meV/GPa at 300 and 200 K, respectively), consistent with pressure-induced band gap narrowing. This behavior reflects enhanced orbital overlap within the Sn-Br framework under compression, which lowers the band edges while preserving the excitonic character of the emission.[25,38] Notably, unlike many halide perovskites, $(4FPEA)_2SnBr_4$ does not exhibit pressure-induced PL enhancement, band gap widening, additional emission channels, or amorphization up to ∼ 3 GPa.[28,39–41] These observations indicate a comparatively rigid pressure response in which compression primarily modifies band dispersion rather than activating defect- or polaron assisted recombination pathways.[29,42,43] In contrast, markedly different PL behavior is observed at lower temperatures.

Figure 2 (a-b) present the pressure-dependent PL spectra measured at 120 and 40 K. At both temperatures and low pressure, the spectra are dominated by NBE emission, together with a weaker and broader STE band which is separated from NBE emission by a large Stokes shift typical of STE containing small polarons.[44,45] With increasing pressure, the NBE emission undergoes a pronounced redshift, whereas the STE emission exhibits a clear blueshift accompanied by a significant increase in intensity. The opposite pressure response of NBE, which can be attributed to free exciton (FX), and STE emissions highlights their distinct physical origins: while NBE emission follows the band-edge

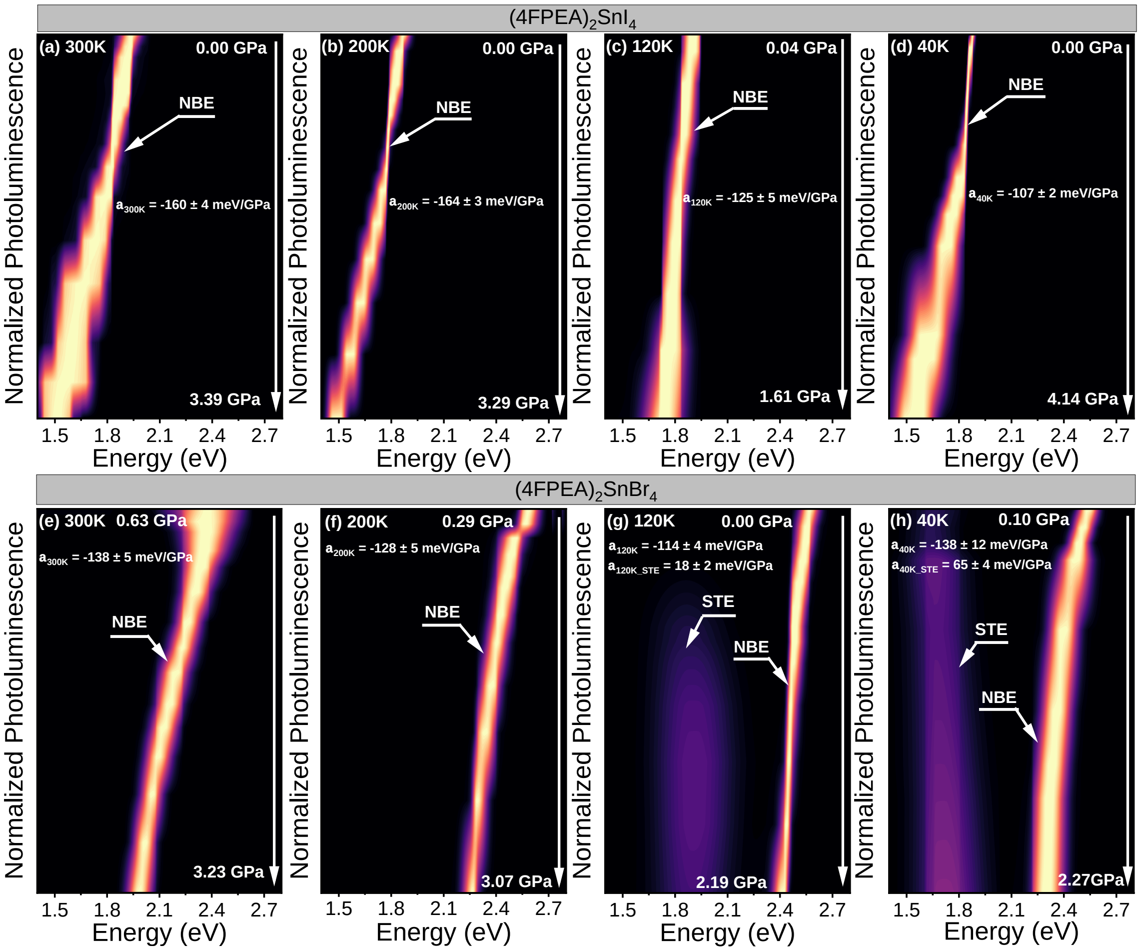

Figure 3: Pressure dependent photoluminescence spectra of two layered halide perovskites measured at variable temperature. (a-d) PL spectra of $(4FPEA)_2SnI_4$ collected at 300, 200, 120, and 40 K under hydrostatic pressure. (e-h) Corresponding PL spectra of $(4FPEA)_2SnBr_4$ acquired under indentical temperature but different pressure conditions. Bright yellow traces denote the evolution of NBE emission, whereas the violet trace indicates the spectral position of STE emission.

electronic structure, STE emission reflects the depth of the local lattice relaxation potential associated with exciton self-trapping.[46] At 40 K, the STE emission partially overlaps with a secondary peak at 1.78 eV arising from ruby fluorescence used for pressure calibration.[47] Despite this overlap, the pressure-induced blueshift of the STE emission remains unambiguous. Pressure coefficients for both NBE and STE emissions were extracted from linear fits of peak energy versus pressure, with peak positions determined by Gaussian fitting, as shown in Figure 2 (c). Representative Gaussian fit is provided in the Figure S4 in SI. Density functional theory (DFT) results are also included for comparison. At 120 K, the NBE emission exhibits a negative pressure coefficient (-114 meV/GPa), consistent with the trend observed at higher temperatures, while the STE emission shows a positive coefficient (18 meV/GPa). At 40 K, this trend is partially disrupted by the freezing of the pressure-transmitting medium, resulting in quasi-hydrostatic conditions. In addition, the strong pressure-induced enhancement of the STE emission hampers reliable detection of the ruby R1/R2 lines, preventing precise determination of the pressure inside the diamond anvil cell. As a consequence, the NBE pressure coefficient at 40 K is reduced (-138 meV/GPa) and exhibits larger uncertainty. Nevertheless, it agrees well with the DFT predicted value (-121 meV/GPa), supporting the consistency between experiment and theory (see below Figure 5). The STE emission at 40 K displays a what is positive pressure coefficient (65 meV/GPa), consistent with pressure-induced STE behavior reported for many halide perovskites.[23,48–50] Up to approximately 2 GPa, no pressure-induced PL enhancement, band gap widening, or amorphization is observed. Importantly, in $(4FPEA)_2SnBr_4$, STE emission becomes pronounced only at low temperatures, confirming its self-trapped nature.[44] Figure 2 (d) presents the pressure dependence of the Stokes shift between NBE and STE emissions. At both temperatures, the Stokes shift decreases monotonically with increasing pressure, reflecting a progressive reduction of the lattice relaxation energy associated with exciton self-trapping. A strong temperature dependence of this effect is observed at 120 K, the Stokes shift is highly pressure sensitive, exhibiting a slope of -124 meV/GPa, whereas at 40 K the pressure induced reduction is much weaker (-20 meV/GPa). This pronounced difference indicates that thermally activated lattice degrees of freedom substantially enhance the pressure response of the NBE-STE energy separation. Upon cooling, lattice stiffening and reduced phonon activity suppress pressure driven modifications of the self-trapping potential, resulting in a markedly smaller Stokes shift variation.

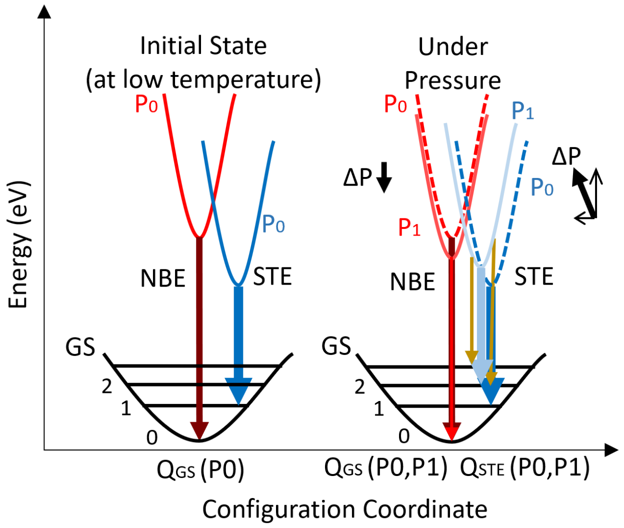

Figure 4: Schematic configuration diagram illustrating the pressure-induced redshift of the NBE emission and blueshift of STE emission in $(4FPEA)_2SnBr_4$. P_0 denotes ambient pressure, while P_1 larger than P_0 represents elevated pressure. GS indicates the ground state of the system.

Temperature and pressure-dependent PL spectra of the layered perovskites $(4FPEA)_2SnI_4$ and $(4FPEA)_2SnBr_4$ shown in Figure 3 (a-d) and (e-h), respectively, as well as it has been reported for their analogues $MAPbI_3$ and $MAPbBr_3$,[25,51,52] reveal a pronounced halide-dependent exciton localization behavior. At 300 and 200 K, all compounds exhibit a single, relatively narrow emission band attributed to FX recombination, indicating that excitonic states remain predominantly delocalized at elevated temperatures.[53] Upon cooling to 120 K and further to 40 K, an additional low-energy emission band emerges exclusively in the bromide-containing compounds, which we assigned in this paper to STE emission. This emission is absent in the iodide analogues over the entire investigated temperature range. The STE emission is broad ($\sim$ 350 meV) and strongly redshifted with respect to the NBE peak, displaying a large Stokes shift that points to a distinct recombination pathway.[45] In addition, STE emission in the bromide perovskites shows a strong sensitivity to hydrostatic pressure. With increasing pressure, its relative intensity increases at the expense of the NBE emission, indicating efficient conversion of photoexcited carriers into localized states.[54] Simultaneously, the NBE emission undergoes a gradual redshift with pressure, whereas the low-energy STE band exhibits an opposite pressure dependence and blueshifts upon compression. The contrasting pressure coefficients of these two emissions unambiguously demonstrate their different physical origins. The emergence of STE emission at low temperatures indicates that thermal fluctuations suppress stable exciton self-trapping at higher temperatures.[44] The pressure-induced enhancement of STE intensity suggests stabilization of exciton localization driven by strengthened exciton-phonon coupling under lattice compression.[48] At the same time, the blueshift of the STE emission under pressure can be rationalized by a reduction of the lattice relaxation energy due to pressure-induced lattice stiffening.[22] The absence of STE emission in the iodide-based compounds, even at low temperatures and elevated pressures (see Figure S5 in the SI), can be rationalized by their softer lattice and stronger dielectric screening, which disfavor the formation of a stable self-trapped exciton state.[55,56] While a definitive identification would require further experiments, the observed temperature and pressure-dependent PL behavior provides strong evidence consistent with STE emission in bromide perovskites, highlighting the critical role of lattice rigidity in governing exciton localization in metal-haldie perovskites.[57]

Next, we explain the evolution of NBE and STE emissions with temperature and pressure using a configurational coordinate diagram,[22,44,45,58–60] shown in Figure 4. In this model, NBE (red) and STE (blue) correspond to distinct energy minima along a lattice distortion coordinate, capturing the dominant exciton-phonon interactions. Optical excitation produces a delocalized NBE state, closely resembling the ground-state lattice. In bromide perovskites, strong exciton-phonon coupling drives relaxation into a shifted STE minimum, producing broad, strongly Stokes-shifted emission. Thermal activation over the barrier separating NBE and STE states governs their relative populations, explaining why STE emission dominates at low temperatures. Hydrostatic pressure reshapes the energy landscape, promoting exciton self-trapping and stiffening the lattice, which enhances the STE population. Notably, we observe that the Stokes shift decreases with increasing pressure. This behavior can be attributed to a reduction in the lattice relaxation energy, reflecting a pressure induced change in the energy formation of small polarons. Consequently, STE emission exhibits a pressure induced blueshift, in contrast to the gradual redshift of NBE emission. In iodide analogues, STE emission is absent (see Figure S5 in SI showing PL spectrum of $(4FPEA)_2SnI_4$ at 40 K and ambient pressure (0 GPa) plotted on a logarithmic scale), as the softer lattice and stronger dielectric screening suppress exciton self-trapping. Displacement along the configurational coordinate reflects lattice relaxation energy, which can be quantitatively inferred from the Stokes shift. These observations underscore the critical role of lattice rigidity and exciton-phonon coupling in controlling exciton self-trapping, while also revealing how external pressure can be used to tune polaron formation and the associated emission properties in layered halide perovskites.

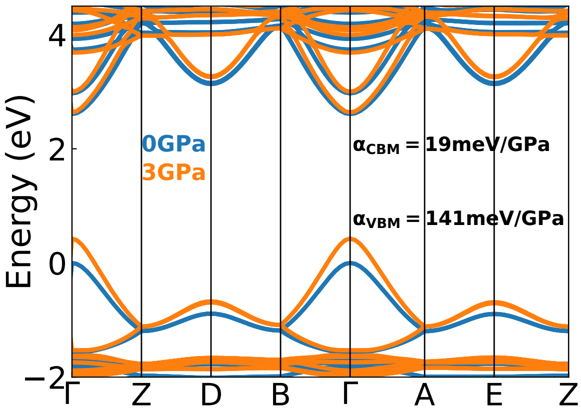

Figure 5: Pressure-dependent band structures of $(4FPEA)_2SnBr_4$ at 0 GPa and 3 GPa, revealing a persistent direct band gap and a significant pressure induced redshift. Values of pressure coefficients for VBM and CBM are also given.

To contextualize the experimental pressure response within an electronic structure framework, we performed DFT calculations of the pressure-dependent band structure of $(4FPEA)_2SnBr_4$. As shown in Figure 5, the material retains a direct band gap up to 3 GPa, demonstrating the robustness of the band edge under moderate hydrostatic compression. Increasing pressure induces a pronounced band gap reduction, consistent with enhanced orbital overlap and lattice compression within the inorganic Sn-Br framework. The calculated band gap pressure coefficient (-121 meV/GPa) closely matches the experimentally extracted NBE pressure coefficient, providing strong evidence that the pressure evolution of the NBE emission is governed predominantly by band edge renormalization. By contrast, the exciton binding energy exhibits only a weak pressure dependence, indicating that changes in excitonic Coulomb interactions play a secondary role. This clear separation of energy scales demonstrates that the anomalous pressure response of the STE emission cannot originate from band edge effects, but instead arises from pressure-induced modifications of lattice relaxation and exciton self-trapping energetics, as captured by the configurational-coordinate model.

In conclusion, we have demonstrated $(4FPEA)_2SnBr_4$ as a model system for elucidating the interplay between lattice dynamics and exciton localization in 2D tin halide perovskites. The contrasting pressure responses of NBE and STE reveal that exciton phonon coupling and lattice rigidity can be systematically tuned to control polaron formation and energy relaxation pathways. The absence of STE in iodide analogue $(4FPEA)_2SnI_4$ underscores the delicate balance between lattice stiffness and dielectric screening in stabilizing self-trapped states. More broadly, our findings demonstrate that external perturbations such as hydrostatic pressure can serve as a precise probe of polaronic phenomena, advancing fundamental understanding and guiding the rational design of next generation lead free perovskite materials.

Acknowledgement This work was financed by the National Science Centre (NC) Poland under OPUS 29 grant no. 2025/57/B/ST3/03683. This work is partially funded by the Ministerio de Ciencia e Innovación of the Spanish Government by the project PLEDs, PID2022-140090OB-C21/AEI/10.13039/501100011033/FEDER. Calculations have been carried out using resources provided by Wroclaw Centre for Networking and Supercomputing (https://wcss.pl)

Supporting Information Available

Detailed materials and methods, experimental layout, 4FPEA molecular structure. Comment about hydrostaticity of Daphne 7575. Example of Gaussian fitting. Photoluminescence spectrum of $(4FPEA)_2SnI_4$ and $(4FPEA)_2SnBr_4$ at 40 K and ambient pressure plotted on a logarithmic intensity scale.

References

(1) Jokar, E.; Cai, L.; Han, J.; Nacpil, E. J. C.; Jeon, I. Emerging Opportunities in Lead-Free and Lead–Tin Perovskites for Environmentally Viable Photodetector Applications. *Chemistry of Materials* **2023**, *35*, 3404–3426.

(2) Li, X.-Z.; Ye, Y.; Cao, Y.; Zhang, D.; Lin, Y.; Chang, J.; Zhu, L.; Wang, N.; Huang, W.; Wang, J. Tin-halide perovskites for light-emitting diodes. *Chem. Soc. Rev.* **2025**, *54*, 6697–6725.

(3) Abate, A. Stable Tin-Based Perovskite Solar Cells. *ACS Energy Letters* **2023**, *8*, 1896–1899.

(4) Zhao, D.; Yu, Y.; Wang, C.; Liao, W.; Shrestha, N.; Grice, C. R.; Cimaroli, A. J.; Guan, L.; Ellingson, R. J.; Zhu, K. et al. Low-bandgap mixed tin–lead iodide perovskite absorbers with long carrier lifetimes for all-perovskite tandem solar cells. *Nature Energy* **2017**, *2*, 17018.

(5) Li, Y.; Wang, D.; Yang, Y.; Ding, C.; Hu, Y.; Liu, F.; Wei, Y.; Liu, D.; Li, H.; Shi, G. et al. Stable Inorganic Colloidal Tin and Tin–Lead Perovskite Nanocrystals with Ultralong Carrier Lifetime via Sn(IV) Control. *Journal of the American Chemical Society* **2024**, *146*, 3094–3101.

(6) Galve-Lahoz, S.; Sánchez-Diaz, J.; Aktas, E.; Rodriguez-Pereira, J.; Abate, A.; Delgado, J. L.; Mora-Seró, I. Reducing Nonradiative Recombination Losses in Tin-Based Perovskite LEDs Utilizing a Self-Assembled Monolayer. *ACS Applied Materials & Interfaces* **2025**, *17*, 60937–60943.

(7) Chakraborty, R.; Paul, G.; Pal, A. J. Quantum Confinement and Dielectric Deconfinement in Quasi-Two-Dimensional

Perovskites: Their Roles in Light-Emitting Diodes. *Phys. Rev. Appl.* **2022**, *17*, 054045.

(8) Hansen, K. R.; McClure, C. E.; Powell, D.; Hsieh, H.-C.; Flannery, L.; Garden, K.; Miller, E. J.; King, D. J.; Sainio, S.; Nordlund, D. et al. Low Exciton Binding Energies and Localized Exciton–Polaron States in 2D Tin Halide Perovskites. *Advanced Optical Materials* **2022**, *10*, 2102698.

(9) Chen, Y.; Wang, Z.; Wei, Y.; Liu, Y.; Hong, M. Exciton Localization for Highly Luminescent Two-Dimensional Tin-Based Hybrid Perovskites through Tin Vacancy Tuning. *Angewandte Chemie International Edition* **2023**, *62*, e202301684.

(10) Zhang, T.; Zhou, C.; Feng, X.; Dong, N.; Chen, H.; Chen, X.; Zhang, L.; Lin, J.; Wang, J. Regulation of the luminescence mechanism of two-dimensional tin halide perovskites. *Nature Communications* **2022**, *13*, 60.

(11) Straus, D. B.; Kagan, C. R. Electrons, Excitons, and Phonons in Two-Dimensional Hybrid Perovskites: Connecting Structural, Optical, and Electronic Properties. *The Journal of Physical Chemistry Letters* **2018**, *9*, 1434–1447.

(12) Jin, L.; Mora Perez, C.; Gao, Y.; Ma, K.; Park, J. Y.; Li, S.; Guo, P.; Dou, L.; Prezhdo, O.; Huang, L. Superior Phonon-Limited Exciton Mobility in Lead-Free Two-Dimensional Perovskites. *Nano Letters* **2024**, *24*, 3638–3646.

(13) Srimath Kandada, A. R.; Silva, C. Exciton Polarons in Two-Dimensional Hybrid Metal-Halide Perovskites. *The Journal of Physical Chemistry Letters* **2020**, *11*, 3173–3184.

(14) Duan, J.; Li, J.; Divitini, G.; Cortecchia, D.; Yuan, F.; You, J.; Liu, S. F.; Petrozza, A.; Wu, Z.; Xi, J. 2D Hybrid Perovskites: From Static and Dynamic Structures to Potential Applications. *Advanced Materials* **2024**, *36*, 2403455.

(15) Zhou, H.; Feng, Q.; Sun, C.; Li, Y.; Tao, W.; Tang, W.; Li, L.; Shi, E.; Nan, G.; Zhu, H. Robust excitonic light emission in 2D tin halide perovskites by weak excited state polaronic effect. *Nature Communications* **2024**, *15*, 8541.

(16) Tao, W.; Zhang, Y.; Zhu, H. Dynamic Exciton Polaron in Two-Dimensional Lead Halide Perovskites and Implications for Optoelectronic Applications. *Accounts of Chemical Research* **2022**, *55*, 345–353.

(17) Gualdrón-Reyes, A. F. Self–Trapped Exciton versus Band–Edge Electron Transitions: Insights of the Factors Affecting the Optical Properties of Lead–Free Sn–Halide Perovskites. *Advanced Optical Materials* **2025**, *13*, 2402043.

(18) Chen, Y.; Wang, Z.; Wei, Y.; Liu, Y.; Hong, M. Exciton Localization for Highly Luminescent Two-Dimensional Tin-Based Hybrid Perovskites through Tin Vacancy Tuning. *Angewandte Chemie International Edition* **2023**, *62*, e202301684.

(19) Li, J.; Wang, H.; Li, D. Self-trapped excitons in two-dimensional perovskites. *Frontiers of Optoelectronics* **2020**, *13*, 225–234.

(20) Li, S.; Luo, J.; Liu, J.; Tang, J. Self-Trapped Excitons in All-Inorganic Halide Perovskites: Fundamentals, Status, and Potential Applications. *The Journal of Physical Chemistry Letters* **2019**, *10*, 1999–2007.

(21) Pan, F.; Li, J.; Ma, X.; Nie, Y.; Liu, B.; Ye, H. Free and Self-Trapped Exciton Emission in Perovskite $CsPbBr_3$ Microcrystals. *RSC Adv.* **2022**, *12*, 1035–1042.

(22) Dai, S.; Xing, X.; Hadjiev, V. G.; Qin, Z.; Tong, T.; Yang, G.; Wang, C.; Hou, L.; Deng, L.; Wang, Z. et al. Theory and experiments of pressure-tunable broadband light emission from self-trapped excitons in metal halide crystals. *Materials Today Physics* **2023**, *30*, 100926.

(23) Mączka, M.; Sobczak, S.; Roszak, K.; Vasconcelos, D. L. M.; Dybała, F.; Herman, A. P.; Kudrawiec, R.; Katrusiak, A.; Freire, P. T. C. Pressure-Induced Detrapping from Self-Trapped Excitons to Free Excitons toward Enhanced Emission and Piezochromism in Ruddlesden–Popper (110)-Oriented Perovskites. *ACS Applied Materials & Interfaces* **2025**, *17*, 58452–58466.

(24) Jaffe, A.; Lin, Y.; Karunadasa, H. I. Halide Perovskites under Pressure: Accessing New Properties through Lattice Compression. *ACS Energy Letters* **2017**, *2*, 1549–1555.

(25) Bartoszewicz, R.; Ziembicki, J.; Zdanowicz, E.; Herman, A. P.; Serafińczuk, J.; Sánchez-Diaz, J.; Das Adhikari, S.; Mora-Seró, I.; Kudrawiec, R. Giant Band Gap Narrowing under Hydrostatic Pressure in (4FP)2SnI4 Halide Perovskite. *The Journal of Physical Chemistry Letters* **2025**, *16*, 6372–6377.

(26) Kong, L.; Gong, J.; Spanopoulos, I.; Yan, S.; Li, Z.; Zhu, Z.; Liu, X.; Zhu, Y.; Dong, H.; Shu, H. et al. Revealing the Universal Pressure-Driven Behavior of Hybrid Halide Perovskites and Unique Optical Modifiability in Extremely Soft 2D Tin-Based System. *Advanced Functional Materials* **2024**, *34*, 2414437.

(27) Fang, Y.-S.; Guo, Y.-F.; Xu, H.-J.; Chen, X.-G.; Zhou, L.; Wang, Z.-X.; Tang, Y.-Y.; Qin, Y. Pressure-Modulated Near-Infrared Photoluminescence of a Two-Dimensional Germanium Halide Perovskite. *The Journal of Physical Chemistry Letters* **2025**, *16*, 10126–10133.

(28) Zhao, W.; Xiao, G.; Zou, B. Pressure-induced emission (PIE) in halide perovskites toward promising applications in scintillators and solid-state lighting. *Aggregate* **2024**, *5*, e461.

(29) Dybała, F.; Kudrawiec, R.; Polak, M. P.; Herman, A. P.; Sieradzki, A.; Mączka, M. Near-bandgap emission in [HOC2H4NH3]2PbI4 perovskite under hydrostatic pressure: emission of a free exciton and a polaronic exciton. *Mater. Adv.* **2025**, *6*, 569–578.

(30) Zhumekenov, A. A.; Saidaminov, M. I.; Mohammed, O. F.; Bakr, O. M. Stimuli-responsive switchable halide perovskites: Taking advantage of instability. *Joule* **2021**, *5*, 2027–2046.

(31) Sun, Y.; Ge, L.; Dai, L.; Cho, C.; Ferrer Orri, J.; Ji, K.; Zelewski, S. J.; Liu, Y.; Mirabelli, A. J.; Zhang, Y. et al. Bright and stable perovskite light-emitting diodes in the near-infrared range. *Nature* **2023**, *615*, 830–835.

(32) Liu, G.; Kong, L.; Yang, W.; Mao, H.-k. Pressure engineering of photovoltaic perovskites. *Materials Today* **2019**, *27*, 91–106.

(33) Zhu, Y.; Buitenhuis, J.; Förster, B.; Vetrano, M. R.; Koos, E. Development of Perovskite Quantum Dots for Two-Dimensional Temperature Sensors. *ACS Applied Nano Materials* **2023**, *6*, 4661–4671.

(34) Vescio, G.; Dirin, D. N.; González-Torres, S.; Sanchez-Diaz, J.; Vidal, R.; Franco, I. P.; Adhikari, S. D.; Chirvony, V. S.; Martínez-Pastor, J. P.; Vinocour Pacheco, F. A. et al. Inkjet-Printed Red-Emitting Flexible LEDs Based on Sustainable Inks of Layered Tin Iodide Perovskite. *Advanced Sustainable Systems* **2024**, *8*, 2400060.

(35) Sanchez-Diaz, J.; Rodriguez-Pereira, J.; Das Adhikari, S.; Mora-Seró, I. Synthesis of Hybrid Tin-Based Perovskite Microcrystals for LED Applications. *Advanced Science* **2024**, *11*, 2403835.

(36) Romani, L.; Bala, A.; Kumar, V.; Speltini, A.; Milella, A.; Fracassi, F.; Listorti, A.; Profumo, A.; Malavasi, L.

PEA2SnBr4: a water-stable lead-free two-dimensional perovskite and demonstration of its use as a co-catalyst in hydrogen photogeneration and organic-dye degradation. *J. Mater. Chem. C* **2020**, *8*, 9189–9194.

(37) Hazra, V.; Mandal, A.; Bhattacharyya, S. Optoelectronic insights of lead-free layered halide perovskites. *Chem. Sci.* **2024**, *15*, 7374–7393.

(38) Coduri, M.; Shiell, T. B.; Strobel, T. A.; Mahata, A.; Cova, F.; Mosconi, E.; De Angelis, F.; Malavasi, L. Origin of pressure-induced band gap tuning in tin halide perovskites††Electronic supplementary information (ESI) available: Experimental and computational details. See DOI: 10.1039/d0ma00731e. *Materials Advances* **2020**, *1*, 2840–2845.

(39) Wu, K.; Bera, A.; Ma, C.; Du, Y.; Yang, Y.; Li, L.; Wu, T. Temperature-dependent excitonic photoluminescence of hybrid organometal halide perovskite films. *Phys. Chem. Chem. Phys.* **2014**, *16*, 22476–22481.

(40) Samanta, D.; Chaudhary, S. P.; Ghosh, B.; Bhattacharyya, S.; Shukla, G.; Mukherjee, G. D. Pressure-induced emission enhancement and bandgap narrowing: Experimental investigations and first-principles theoretical simulations on the model halide perovskite $Cs_3Sb_2Br_9$. *Phys. Rev. B* **2022**, *105*, 104103.

(41) Lü, X.; Wang, Y.; Stoumpos, C. C.; Hu, Q.; Guo, X.; Chen, H.; Yang, L.; Smith, J. S.; Yang, W.; Zhao, Y. et al. Enhanced Structural Stability and Photo Responsiveness of CH3NH3SnI3 Perovskite via Pressure-Induced Amorphization and Recrystallization. *Advanced Materials* **2016**, *28*, 8663–8668.

(42) Yang, B.; Bogachuk, D.; Suo, J.; Wagner, L.; Kim, H.; Lim, J.; Hinsch, A.; Boschloo, G.; Nazeeruddin, M. K.; Hagfeldt, A. Strain effects on halide perovskite solar cells. *Chem. Soc. Rev.* **2022**, *51*, 7509–7530.

(43) Wu, J.; Liu, S.-C.; Li, Z.; Wang, S.; Xue, D.-J.; Lin, Y.; Hu, J.-S. Strain in perovskite solar cells: origins, impacts and regulation. *National Science Review* **2021**, *8*, nwab047.

(44) Han, Y.; Cheng, X.; Cui, B.-B. Factors influencing self-trapped exciton emission of low-dimensional metal halides. *Mater. Adv.* **2023**, *4*, 355–373.

(45) Li, S.; Luo, J.; Liu, J.; Tang, J. Self-Trapped Excitons in All-Inorganic Halide Perovskites: Fundamentals, Status, and Potential Applications. *The Journal of Physical Chemistry Letters* **2019**, *10*, 1999–2007.

(46) Xu, B.; Li, Y.; Hong, P.; Zhang, P.; Han, J.; Xiao, Z.; Quan, Z. Pressure-controlled free exciton and self-trapped exciton emission in quasi-one-dimensional hybrid lead bromides. *Nature Communications* **2024**, *15*, 7403.

(47) Datchi, F.; Dewaele, A.; Loubeyre, P.; Letoullec, R.; Godec, Y. L.; Canny, B. Optical pressure sensors for high-pressure–high-temperature studies in a diamond anvil cell. *High Pressure Research* **2007**, *27*, 447–463.

(48) Jing, X.; Sun, R.; Tian, H.; Liu, R.; Liu, B.; Zhou, D.; Li, Q.; Liu, B. Evolution of self-trapped exciton emission tuned by high pressure in 2D all-inorganic cesium lead halide nanosheets. *J. Mater. Chem. C* **2022**, *10*, 8711–8718.

(49) Gao, F.-F.; Qin, Y.; Li, Z.-G.; Li, W.; Hao, J.; Li, X.; Liu, Y.; Howard, C. J.; Wu, X.; Jiang, X. et al. Unusual Pressure-Induced Self-Trapped Exciton to Free Exciton Transfer in Chiral 2D Lead Bromide Perovskites. *ACS Nano* **2024**, *18*, 3251–3259.

(50) Shi, H.; Chen, L.; Moutaabbid, H.; Feng, Z.; Zhang, G.; Wang, L.; Li, Y.; Guo, H.; Liu, C. Mechanism of Pressure-Modulated Self-Trapped Exciton Emission in Cs2TeCl6 Double Perovskite. *Small* **2024**, *20*, 2405692.

(51) Pieniążek, A.; Dybała, F.; Polak, M. P.; Przypis, L.; Herman, A. P.; Kopaczek, J.; Kudrawiec, R. Bandgap Pressure Coefficient of a CH3NH3PbI3 Thin Film Perovskite. *The Journal of Physical Chemistry Letters* **2023**, *14*, 6470–6476.

(52) Pieniążek, A.; Dybała, F.; Przypis, L.; Polak, M. P.; Norek, M.; Kowalski, B. J.; Kudrawiec, R. Beyond the Cubic Phase: Pressure-Induced Bandgap Modulation in a CH3NH3PbBr3 Perovskite at Low Temperatures. *Advanced Optical Materials* **2026**, *14*, e03177.

(53) Tan, J.; Zhou, Y.; Lu, D.; Feng, X.; Liu, Y.; Zhang, M.; Lu, F.; Huang, Y.; Xu, X. Temperature-dependent photoluminescence of lead-free cesium tin halide perovskite microplates. *Chinese Physics B* **2023**, *32*, 117802.

(54) Rong, Y.; Wang, L.; Wang, Y.; Wang, W.; Wang, J.; Yuan, Y.; Shahzadi, U.; Chen, J.; Zhang, L.; Wang, K. et al. Pressure-Induced Unusual Transition of Luminescence Mechanics from Self-Trapped Exciton to Free Exciton Emission in Lead Bromide Perovskitoids. *Advanced Optical Materials* **2025**, *13*, 2402086.

(55) Gautier, R.; Paris, M.; Massuyeau, F. Exciton Self-Trapping in Hybrid Lead Halides: Role of Halogen. *Journal of the American Chemical Society* **2019**, *141*, 12619–12623.

(56) Xing, Y.; Yin, J.; Qiao, Y.; Zhao, J.; He, H.; Zhao, D.; Zhang, W.; Mei, S.; Guo, R. Gram-Scale Synthesis and Optical Properties of Self-Trapped-Exciton-Emitting Two-Dimensional Tin Halide Perovskites. *Nanomaterials* **2025**, *15*.

(57) Liang, Y.; Jiang, Y.; Du, K.-Z.; Lin, Y.-P.; Ma, X.; Qiu, D.; Wang, Z.; Hou, Y.; Wei, X.; Zhang, Q. A High-Rigidity Organic–Inorganic Metal Halide Hybrid Enabling Reversible and Enhanced Self-Trapped Exciton Emission under High Pressure. *Nano Letters* **2023**, *23*, 7599–7606.

(58) Zhao, W.; Fu, R.; Yang, J.; Xiao, G.; Zou, B. Building New Structural Distortion Descriptors through Pressure Engineering toward Enhanced Violet Emission in 2D Hybrid Perovskite. *Advanced Optical Materials* **2024**, *12*, 2401732.

(59) Yu, X.; Fang, Y.; Sun, X.; Xie, Y.; Liu, C.; Wang, K.; Xiao, G.; Zou, B. Pressure-Tuning Localized Excitons Toward Enhanced Emission, Photocurrent Enhancement and Piezochromism in Unconventional ACI-Type 2D Hybrid Perovskites. *Angewandte Chemie International Edition* **2024**, *63*, e202412756.

(60) Ma, Z.; Lv, P.; He, X.; Wang, F.; Li, Y.; Xiao, G.; Zou, B. Self-Trapped Excitons or Bi3+ Ions for Broad Emission in a Lead-Free Double Perovskite? Hearing What Pressure Says. *Nano Letters* **2025**, *25*, 9345–9352.

Supporting Information for

Hydrostatic Pressure Driven Band Gap Tuning and Self-Trapped Exciton Formation in $(4FPEA)_2SnBr_4$ Halide Perovskite

Rafał Bartoszewicz,[1,*] *Jakub Ziembicki,*[1] *Ewelina Zdanowicz,*[1] *Artur P. Herman,*[1] *Jesús Sánchez-Diaz,*[2] *Samrat Das Adhikari,*[2,3] *Iván Mora-Seró,*[2] *and Robert Kudrawiec*[1,]

[1] Department of Semiconductor Materials Engineering, Wroclaw University of Science and Technology, Wybrzeże Wyspiańskiego 27, 50-370 Wrocław, Poland

[2] Institute of Advanced Materials (INAM), Universitat Jaume I. Av. De Vicent Sos Baynat, Castellón de la Plana, 12006 Spain

[3] Institute of Physical Chemistry, Polish Academy of Sciences, Warsaw 01-224, Poland

* e-mail address: rafal.bartoszewicz@pwr.edu.pl

KEYWORDS: Perovskites, Photoluminescence, Hydrostatic pressure

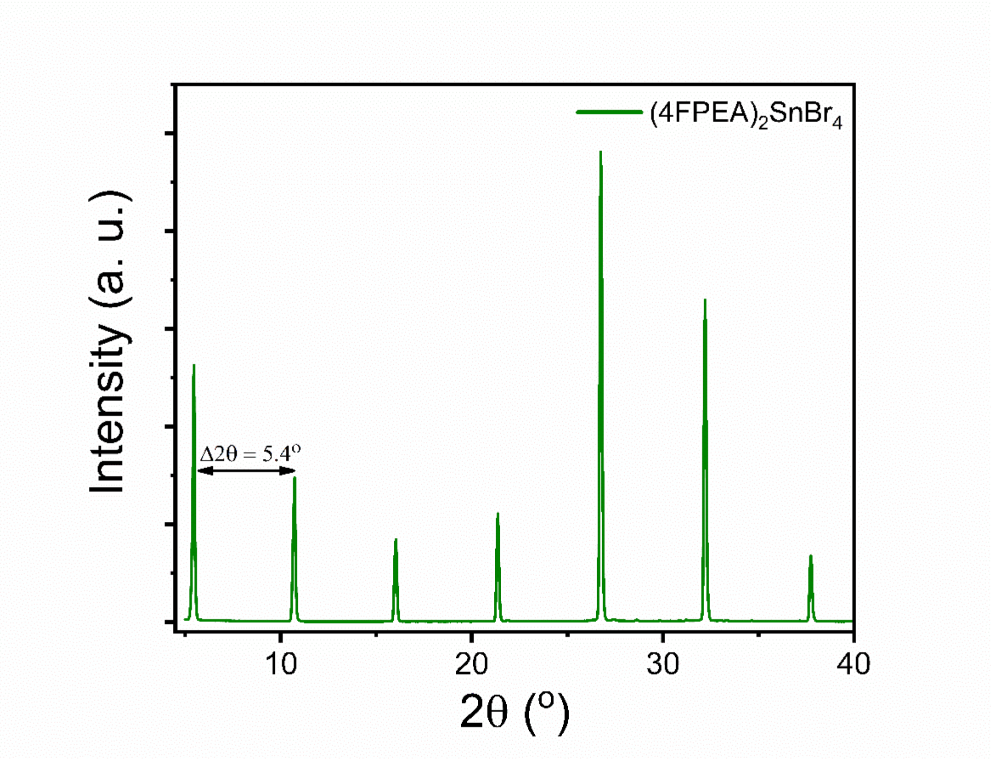

Figure S1. XRD pattern of the $(4FPEA)_2SnI_4$ microcrystals.

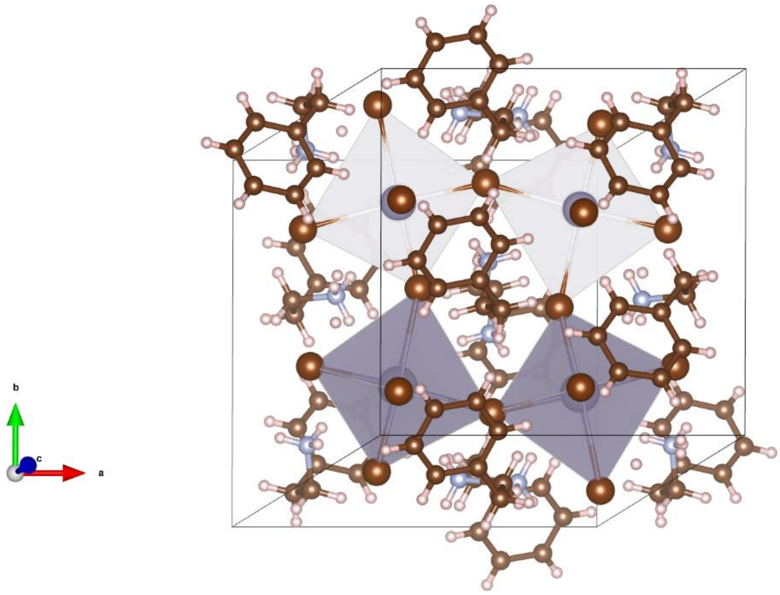

Figure S2. Crystal structure (Triclinic P1) of $(4FPEA_2SnBr_4)$ used in DFT simulations.

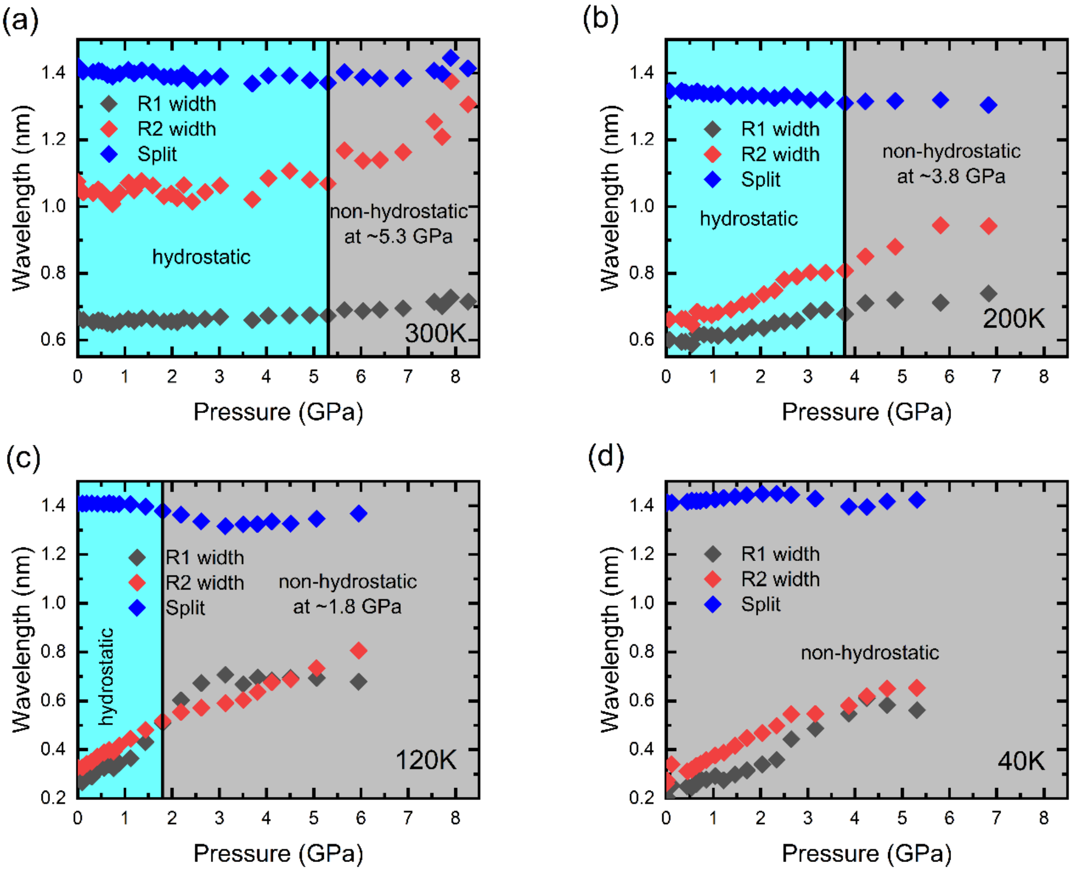

Figure S3. Analysis of ruby R1 and R2 peaks split and broadening at (a) 300, (b) 200, (c) 120, and (d) 40 K.

Figure S3 presents the analysis of the applied pressure using ruby fluorescence. Daphne 7575 is not strictly hydrostatic at low temperatures, and its ability to maintain hydrostatic conditions decreases significantly with both temperature reduction and pressure increase [1,2]. However, while Daphne 7575 does not remain fully hydrostatic at high pressures and low temperature, it maintains quasi-hydrostatic conditions, owing to its relatively low shear strength and soft solidification behavior [2,3]. From R1 and R2 peaks split and broadening we determined solidification points of Daphne 7575 at (a) ~5.3, (b) ~3.8, (c) ~1.8 and (d) 0 GPa for 300, 200, 120 and 40 K respectively. The pressure coefficients we investigated are not highly sensitive to moderate non-hydrostatic stress. As far as we know, such conditions should lead to nonlinear band gap shifts, splitting of emission lines, amorphization, or appearing defect emission due to uneven stress, which could be reported as the presence of phase transition in this material [4-7]. Such effects were not observed in our measurements. Our results remain consistent with theoretical expectations, which support their validity even in the presence of quasi-hydrostatic conditions. Moreover, for perovskite materials such medium is still second-best choice (first choice is helium) as it not influence the condition of measured sample, as it is in the case of 4:1 methanol-ethanol mixture [7].

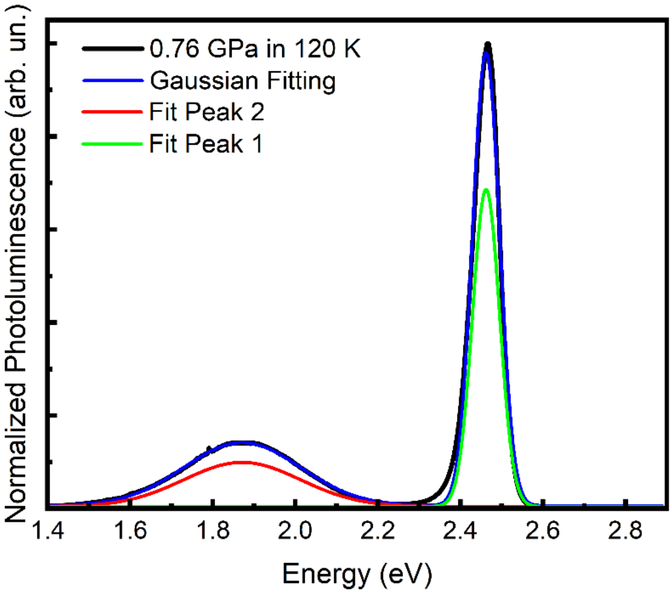

Figure S4. Example of Gaussian fitting performed for photoluminescence spectrum at 0.76 GPa in 120 K.

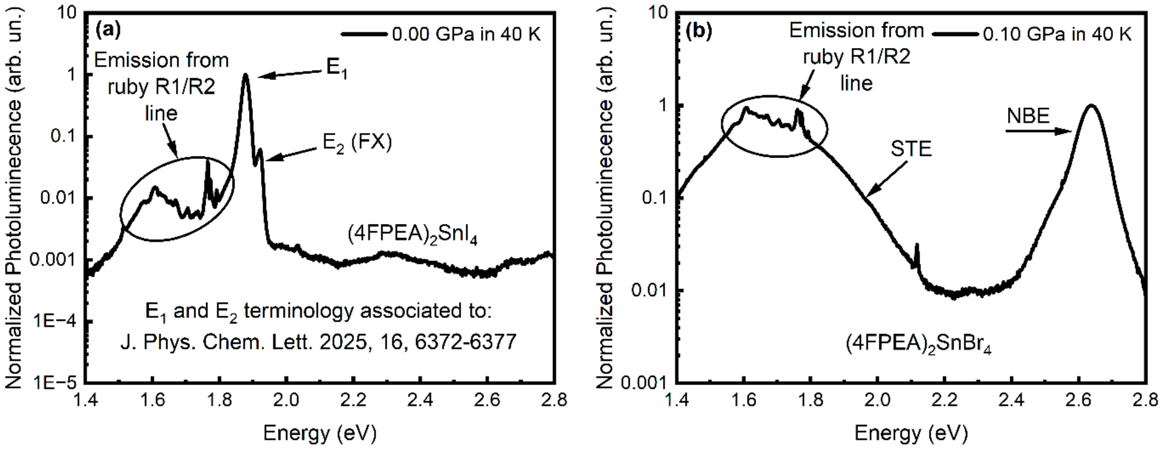

Figure S5. Photoluminescence spectrum of (a) $(4FPEA)_2SnI_4$ and (b) $(4FPEA)_2SnBr_4$ at 40 K and pressure (0 and 0.1 GPa respectively) plotted on a logarithmic intensity scale.

MATERIALS AND METHODS

Experimental details:

Materials: Acetic acid (AcOH, 99-100 %), hydrobromic acid (HBr; 48 wt. % in H_2O), hydroiodic acid (HI; 57 wt. % in H2O, distilled, stabilized, 99.95 %), and hypophosphorus acid (H_3PO_2; 50wt. % in H_2O) were purchased from sigma aldrich. Tin (II) oxide (SnO; 99%) was purchased from Alfa Aesar. 4-fluorophenethylamine (4FPEA; 98%) was purchased from TCI. All materials were use as received with no further purifications.

Synthesis of $(4FPEA)_2SnBr_4$ microcrystals powder:

Synthesis of $(4FP)_2SnBr_4$ was carried out following the literature report [8]. A mixture consisting of 3 mL of acetic acid, and 0.3 mL of hydrobromic acid (HBr) was combined in a three-necked flask under an inert nitrogen (N_2) atmosphere. The mixture was stirred at room temperature for 30 minutes. Next, 134 mg of tin(II) oxide (SnO) was introduced into the flask, and the temperature was gradually increased to 100 °C. The solution was stirred for an additional 30 minutes until it developed a white color. Subsequently, 0.26 mL of 4-fluorophenylethylamine (4FPEA) was added, and the reaction temperature was further raised to 135 °C. The mixture was maintained under these conditions for 15 minutes. Upon completion of the reaction, the solution was rapidly cooled using an ice bath for approximately 2 minutes, in this step, the microcrystalline products were formed having a green-yellow appearance. The resulting product was collected via vacuum suction filtration. To eliminate any excess Bromide, the collected powder was washed three times with hexane, followed by additional vacuum suction filtration. Finally, the purified product was dried.

Synthesis of $(4FPEA)_2SnI_4$ microcrystals powder:

Synthesis of $(4FPEA)_2SnI_4$ was carried out following the same procedure as $(4FPEA)_2SnI_4$. A mixture consisting of 3 mL of acetic acid, 0.2 mL of hydroiodic acid (HI), and 0.05 mL of H_3PO_2 was combined in a three-necked flask under an inert N_2 atmosphere. The mixture was stirred at room temperature for 30 minutes, during which a transition from a faint red to a colorless appearance indicated the stabilization of HI in the presence of H_3PO_2. Next, 134 mg of SnO was introduced into the flask, and the temperature was gradually increased to 100 °C. The solution was stirred for an additional 30 minutes until it developed an orange color. Subsequently, 0.26 mL of 4FPEA was added, and the reaction temperature was further raised to 135 °C. The mixture was maintained under these conditions for 15 minutes. Upon completion of the reaction, the solution was rapidly cooled using an ice bath for approximately 2 minutes. The resulting product was collected via vacuum suction filtration. To eliminate any excess iodine, the collected powder was washed three times with hexane, followed by additional vacuum suction filtration. Finally, the purified product was dried.

XRD measurement

XRD pattern of the microcrystals were measured using X-ray diffractometer (D8 Advance, Bruker-AXS) (Cu Kα, wavelength λ=1.5406 Å) with a Bragg angle range of 4-70° and step size of 0.05°.

Temperature and pressure dependent PL

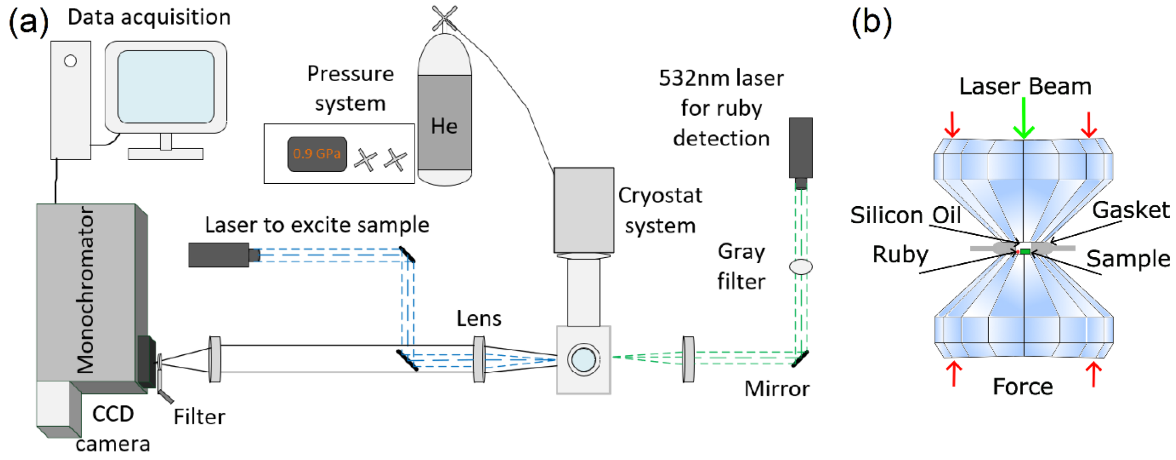

Figure S6. (a) The scheme of the experimental setup for hydrostatic pressure-dependent photoluminescence (b) Cross-section of a diamond anvil cell.

Figure S6 (a) presents schematically the experimental setup of temperature- and pressure-dependent PL carried out in this work. Figure S6 (b) shows a cross-section of a diamond anvil cell (DAC). PL measurements were performed in Diacell design DAC by 'Almax easyLab'. DAC used in this work is made of beryllium copper (BeCu) alloy, which allows to perform measurements at cryogenic temperature (here 40 K). Diamond with 650 μm culet size was used. The pressurizing mechanism in the DAC was driven using a gas membrane. The pressure in DAC was controlled by the amount of helium injected into the gas membrane. On top of the bottom diamond culet, a gasket was placed. It is a thin sheet (circa 50 μm thickness) of inconel material with a central hole of about 1/3 culet size, where sample, ruby sphere, and silicon oil were placed. Gaskets were prepared by pressing diamonds into a thin sheet, followed by creating a central hole using mechanical drilling. Daphne 7575 was used as the pressure-transmitting medium, which solidifies at about 5.3 GPa at room temperature. Whole setup was cooled down in a cryostat with a closed-loop liquid helium system. For PL experiments, the 405 nm CW (with power of 100 μW) laser was used to excite the studied material. Emitted light was dispersed through a 0.5 m Andor monochromator with a 150 l/mm diffraction grating blazed at 500 nm. The signal was recorded by a Si CCD camera cooled to -70 °C by Peltier module. The luminescence of the ruby R1 line at ~1.78 eV (at room temperature) was excited by the 532 nm CW laser, dispersed on the 600 l/mm diffraction grating blazed at 500 nm and detected by CCD camera. To determine pressure value inside DAC we detect pressure-induced redshift of ruby sphere R1 line with calibration taken from Shen [9]. The temperature shift correction of the R1 ruby line was taken from Datchi [10].

Theoretical calculations

Density functional theory (DFT) calculations were performed using the VASP package with standard PBE PAW datasets [11-14]. Geometry optimizations were first carried out over a pressure range of 0–3 GPa using the r^{2}SCAN+rVV10 functional [15]. The optimized geometries were then used for band gap and band structure calculations. In this second step, the same functional was employed with two additional modifications. First, a uniform scissor shift of 1.1 eV was applied to the band gaps at all pressures to match the values obtained from the PBE0 functional, thereby correcting the band gap underestimation inherent to meta-GGA functionals. Second, spin–orbit coupling was included, as it is known to have a significant impact on the band structure of this class of materials. All calculations used identical computational parameters: an energy cutoff of 500 eV, a Γ-centered 3×6×6 k-point mesh, an SCF energy convergence criterion of 10^{-5} eV, and a force convergence criterion of 10^{-2} eV/Å for geometry optimization. For the PBE0 calculations, k-point mesh down-sampling was applied using the VASP flag `NKRED = 3`. To derive the absolute deformation potentials of the valence band maximum (VBM) and conduction band minimum (CBM), a slab supercell approach including an explicit vacuum region was employed. The slab contained a bulk-like region corresponding to three primitive unit cells and was separated by approximately 15 Å of vacuum to avoid spurious interactions between periodic images. The slab was symmetrically terminated at the center of the organic spacer layer to eliminate artificial surface dipoles.

References:

[1] Staško, D., Prchal, J., Klicpera, M., Aoki, S., & Murata, K. (2020). Pressure media for high pressure experiments, Daphne Oil 7000 series. *High Pressure Research*, *40*(4), 525–536. https://doi.org/10.1080/08957959.2020.1825706

[2] Naoyuki Tateiwa and Yoshinori Haga 2010 J. Phys.: Conf. Ser. 215 012178

[3] Y Nakamura et al 2010 J. Phys.: Conf. Ser. 215 012176

[4] Tuson Park et al 2008 J. Phys.: Condens. Matter **20** 322204

[5] Yu, W, Aczel, A. A, Williams, T. J, Bud'ko, S. L, Ni, N, Canfield, P. C, Luke and G. M. Phys. Rev. B 79 020511(R) (2009)

[6] J. Gong, H. Zhong, C. Gao, J. Peng, X. Liu, Q. Lin, G. Fang, S. Yuan, Z. Zhang, X. Xiao, Pressure-Induced Indirect-Direct Bandgap Transition of $CsPbBr_3$ Single Crystal and Its Effect on Photoluminescence Quantum Yield. *Adv. Sci.* 2022, 9, 2201554. https://doi.org/10.1002/advs.202201554

[7] Xujie Lu et al 2017 Chem. Sci. 8, 6764-6776

[8] Sanchez-Diaz, J.; Rodriguez-Pereira, J.; Das Adhikari, S.; Mora-Seró, I.; Synthesis of Hybrid Tin-Based Perovskite Microcrystals for LED Applications, Adv. Sci. 2024, 11, 2403835 https://doi.org/10.1002/advs.202403835

[9] Shen, G.; Wang, Y.; Dewaele, A.; Wu, C.; Dayne, E.; Eggert, J.; Klotz, S.; Dziubek, K. F.; Loubeyre, P.; Fat, V.; Asimow, P. D.; Mashimo, T.; Wentzcovitch, R. M. M.; Toward an International Practical Pressure Scale: A Proporsal for an IPPS Ruby Gauge (IPPS-Ruby2020). High Press. Res. 2020, 40, 299-314 10.1080/08957959.2020.1791107

[10] Datchi, F.; Dewaele, A.; Loubeyre, P.; Letoullec, R.; Godec, Y. Le.; Canny, B.; Optical Pressure Sensors for High-Pressure-High-Temperature Studies in a Diamond Anvil Cell. High Press. Res. 2007, 27, 447-463.c https://doi.org/10.1080/08957950701659593

[11] G. Kresse and J. Hafner, Phys. Rev. B 47, 558 (1993).

[12] G. Kresse and J. Furthmüller, Phys. Rev. B 54, 11169 (1996).

[13] G. Kresse and J. Furthmüller, Computational Materials Science 6, 15 (1996).

[14] G. Kresse and D. Joubert, Phys. Rev. B 59, 1758 (1999).

[15] J. Ning, M. Kothakonda, J. W. Furness, A. D. Kaplan, S. Ehlert, J. G. Brandenburg, J. P. Perdew, and J. Sun, Workhorse minimally empirical dispersion-corrected density functional with tests for weakly bound systems: rSCAN+rVV⊠10, Phys. Rev. B 106, 075422 (2022).

3.4 Thermochromism versus piezochromism in $(PMA)_2CuX_4$ (X = Br, Cl) halide perovskites

Rafał Bartoszewicz†, Jan-Albert Zienkiewicz, Sri Hartati, Arramel Arramel, Jan Kopaczek, Muhammad Danang Birowosuto, Robert Kudrawiec

Journal of Materials Chemistry C., vol. 13, pp. 16929–16936 (2025).
DOI: 10.1039/D5TC02326B

Author's Contribution:

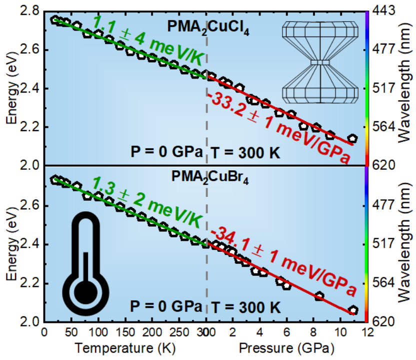

Figure 3.1: Graphical abstract. Reprinted from Ref. J. Mater. Chem. C, 2025, 13, 16929-16936 under CC-BY 3.0 license. Copyright 2025 R. Bartoszewicz et al.

Rafał Bartoszewicz with supervisor conceived and formulated the research problem addressing temperature- and pressure-induced band gap tuning in layered copper HOIPs. The author proposed the working hypothesis that thermochromism and piezochromism originate from fundamentally distinct lattice-electronic coupling mechanisms, rather than representing inverse manifestations of the same structural response.

The author independently designed and executed a comprehensive experimental program combining low-temperature absorption and R spectroscopy with HP transmission measurements. Significant technical improvements to the DAC methodology were introduced, including optimized gasket preparation.

All optical measurements were performed independently. The author developed analysis routines for: extraction of direct and indirect band gaps, discrimination between fundamental transitions and d-d absorption bands, determination of pressure coefficients across structural regimes, quantitative uncertainty analysis. The study led to the correction of previously reported band gap assignments in the literature.

Through systematic comparison of thermo- and piezo-induced band gap evolution, the author demonstrated that lattice expansion (temperature) and lattice compression (pressure) produce qualitatively different modifications of electronic structure, revealing non-equivalent renormalization pathways. This finding challenges the common assumption that pressure effects are simply the inverse of thermal expansion.

All figures were generated by the author, who wrote the manuscript in its entirety. Author also answered for all questions from the reviewers during review process.

---

† corresponding author

Journal of
Materials Chemistry C

ROYAL SOCIETY
OF CHEMISTRY

COMMUNICATION

View Article Online
View Journal | View Issue

Cite this: *J. Mater. Chem. C*, 2025, **13**, 16929

Received 16th June 2025,
Accepted 29th July 2025

DOI: 10.1039/d5tc02326b

rsc.li/materials-c

Thermochromism *versus* piezochromism in $(PMA)_2CuX_4$ (X = Br, Cl) halide perovskites

Rafał Bartoszewicz, *[a] Jan-Albert Zienkiewicz, [b] Sri Hartati, [c] Arramel Arramel, [c] Jan Kopaczek, [a] Muhammad Danang Birowosuto [b] and Robert Kudrawiec [a]

This study addresses the challenges of poor thermodynamic and structural stability in copper-based perovskites under extreme conditions. By replacing hygroscopic cations with hydrophobic ones like phenylmethylammonium (PMA), the stability of these materials is significantly enhanced. Two-dimensional copper-based perovskites, $(PMA)_2CuCl_4$ and $(PMA)_2CuBr_4$, are examined for their large band gap tunability, focusing on thermo- and piezo-chromism. Temperature-dependent transmission and reflectance measurements show that the band gaps narrow by ~70 nm (from 466 to 536 nm) for $(PMA)_2CuCl_4$ and by ~87 nm (from 472 to 559 nm) for $(PMA)_2CuBr_4$ across the temperature range of 20–320 K. Pressure-dependent transmission reveals that a redshift in the band gap occurs, shifting from 476 to 546 nm (~70 nm) up to 10.94 GPa for $(PMA)_2CuCl_4$ and from 482 to 572 nm (~90 nm) up to 10.86 GPa for $(PMA)_2CuBr_4$ under ambient conditions. These changes are reversible, confirming the stability under extreme conditions. The observed significant thermo- and piezo-chromic effects make the materials very functional for use in color tuning and temperature and pressure sensor applications. Additionally, the comparison of thermo- and piezo-chromism shows that even if electron–phonon interactions play an important role in both phenomena, the changes in lattice parameters induced by temperature (expansion) and pressure (compression) are fundamentally different, leading to distinct mechanisms of energy gap narrowing.

1 Introduction

Two-dimensional (2D) lead halide organic–inorganic perovskites have received considerable attention in recent years due to their large exciton binding energy, high photoluminescence quantum yield, and versatile exciton radiative recombination processes, which are desirable for micro/nano-lasers and high-efficiency light-emitting diodes (LEDs).[1–12] However, the widespread use of lead-based perovskites is hindered by the toxicity of the lead component, limiting their commercial applications in optoelectronic devices. In order to optimize the utility of perovskites, researchers have explored alternatives by replacing the toxic Pb with environment-friendly elements, including Sn(II), Ge(II), Bi(II), Sb(II), and the transition metal Cu(II).[13–18] Among these, Cu, a low-cost, earth-abundant, and non-toxic element, has emerged as a promising substitute for Pb in 2D perovskite materials. Cu-based perovskites have demonstrated similar or superior electronic and optical properties compared to Pb-based perovskites, including efficient charge transportation in metal-halide octahedral layers, high thermodynamic stability, low-cost synthesis, and environmental inertness, making them suitable for commercial applications.[16,19,20] Despite these facts, key challenges remain for Cu-based perovskites, such as limited absorption coefficient and insufficient long-term stability.[16] One promising strategy to overcome these limitations involves replacing hygroscopic cations with more hydrophobic cations, like phenylmethylammonium (PMA), which enhances material stability under extreme conditions, including exposure to heat, pressure, UV light, and humidity,[21,22] but further studies of these compounds are still needed.

Piezochromism involves color or luminescence changes under pressure and has gained interest in crystalline systems such as halide perovskites and metal–organic frameworks. So far, only a limited number of studies have explored crystals of perovskites under high pressure.[23–25] In addition, thermochromism refers to the reversible color change of materials in response to temperature variations. This property has attracted increasing interest for applications in smart coatings,[26] energy-saving systems,[27] and temperature sensors.[28] Thermochromic materials are also useful in environments where conventional temperature monitoring is difficult.[29] In hybrid perovskites, thermochromism is often linked to structural changes, including lattice distortion. For example, copper-based layered perovskites

---

[a] *Department of Semiconductor Materials Engineering, Wroclaw University of Science and Technology, Wybrzeże Wyspiańskiego 27, 50-370 Wrocław, Poland. E-mail: rafal.bartoszewicz@pwr.edu.pl*

[b] *Lukasiewicz Research Network-PORT Polish Center for Technology Development, Stabłowicka 147, 54-066 Wrocław, Poland*

[c] *Center of Excellence Applied Physics and Chemistry, Nano Center Indonesia, Jalan Raya PUSPIPTEK, South Tangerang 15314, Indonesia*

show reversible transitions from orange to red, while inorganic compounds like $Cs_3Sb_2I_9$ and $Cs_2AgBiBr_6$ shift from red to brown with temperature.[30–32]

Copper-based halide perovskites, such as $(PMA)_2CuCl_4$ and $(PMA)_2CuBr_4$, are promising materials for applications in solar cell absorbers, scintillators, and LEDs.[33,34] To recognize their utilities in mentioned applications as well as other applications, it is essential to examine their behavior under varying temperature and hydrostatic pressure conditions. The flexible crystal structures of perovskites, combined with significant lattice expansion induced by temperature, provide a viable approach to modulate the material properties in a controlled manner, such as tuning the band gap.[35–37] Understanding the effects of temperature and hydrostatic pressure on these materials is crucial, as both factors can induce significant changes in the crystal structure. This opens new possibilities for copper-based hybrid perovskites to be used as thermometers or impact/stress indicators, thanks to their color and electronic conductivity changes upon temperature and pressure variations.[35,38]

While absorption (α) and reflectance (R) have been extensively studied under varying temperature or hydrostatic pressure conditions for various 2D perovskites,[10,39–48] such studies are rare for copper-based hybrid perovskites. Moreover, there are no reports on temperature-dependent experiments for $(PMA)_2CuCl_4$ and $(PMA)_2CuBr_4$ specifically and no studies on the effect of pressure on $(PMA)_2CuCl_4$.

In this article, we investigate the thermo- and piezo-chromic properties of $(PMA)_2CuCl_4$ and $(PMA)_2CuBr_4$ perovskites. Absorption and reflectance spectra show a temperature-induced redshift of the absorption edge, consistent with band gap narrowing in both investigated perovskites. Similarly, pressure-driven transmission measurements reveal a redshift of the absorption edge under increasing hydrostatic pressure, leading to a visible color change. Moreover, the fundamental energy gap for both was found to be indirect.

2 Results and discussion

Prior to discussing the thermo- and piezo-chromic properties of the $(PMA)_2CuCl_4$ and $(PMA)_2CuBr_4$ perovskites, we first characterized the crystallinity order, vibrational properties, and chemical states of the compounds using X-ray diffraction (XRD), Fourier transform infrared spectroscopy (FTIR), Raman spectroscopy and X-ray photoemission spectroscopy (XPS). The structural characterization of the studied perovskites confirmed their high quality. In particular, the structural order of the 2D Ruddlesden–Popper (RP) phase according to its XRD analysis and inorganic network connectivity and optimized geometric calculations. A detailed description of the experimental results, analysis and methods is provided in Fig. S1–S14 in the SI.

2.1. Thermochromism in $(PMA)_2CuBr_4$ and $(PMA)_2CuCl_4$ halide perovskites

After successful synthesis and fundamental structural characterization under ambient conditions, absorption (α) and reflectance (R) spectra were measured for both perovskites as a function of temperature to investigate their thermochromism. Fig. 1(a) shows the absorption spectra of $(PMA)_2CuBr_4$ as a function of temperature, measured between 20 and 320 K, to analyze the temperature dependence of the fundamental energy gap, while Fig. 1(b) presents the R spectra measured in the range of 30 to 320 K.

From the α measurements, it was observed that the energy gap narrows linearly with increasing temperature for both the direct and indirect band gaps, as shown in Fig. 1(c). Specifically, the energy gap decreases by 342 meV ($\sim$63 nm from 450 to 513 nm) for the direct gap and 426 meV ($\sim$87 nm from 472 to 559 nm) for the indirect gap, respectively, between 20 and 320 K. This exceeds the narrowing typically observed for group III–V semiconductors (70–90 meV)[49] and other perovskites measured in the same temperature range.[50,51] Such a significant temperature-dependent narrowing of the energy gap also leads to visible thermochromism, where the material undergoes a noticeable color change with increasing temperature. As the energy gap decreases, the material absorbs light at different wavelengths, resulting in a visible change in color, from green at 20 K to yellow at 320 K. The reduction in the energy gap and the change in the color of the studied samples are also confirmed by R measurements. However, due to the presence of a transparency region near the indirect transition, accurately determining the transition energy at each temperature was challenging.

As in other semiconductors, the narrowing of the energy gap with increasing temperature is related to lattice expansion and enhanced electron–phonon interactions.[52] The temperature dependence of the band gap can be typically described using the Varshni relation[53]:

$$E_0(T) = E_0(0) - \frac{(\alpha T^2)}{(\beta + T)} \tag{1}$$

where $E_0(0)$ is the energy of the optical transition at $T = 0$ K, and α and β are the material constants. This relation is non-linear at low temperatures but becomes nearly linear when $T \gg \beta$, allowing for a linear approximation as the first-order approach.

To determine the nature of the absorption edge (whether related to a direct or an indirect band gap), the α^2 and $\sqrt{\alpha}$ spectra were compared with the R spectra. From this comparison, it was concluded that the fundamental energy gap in $(PMA)_2CuBr_4$ is indirect with a value of 2.23 eV under ambient conditions.

Previous studies on this material[10,33] identified a fundamental band gap, with a value of approximately 1.80 eV under ambient conditions. According to our studies, this value actually corresponds to the d-d band in the perovskite.[54] The d–d band in perovskites refers to an electronic transition involving the d orbitals of transition metal ions in the structure. This transition can influence the optical absorption and emission properties of perovskites. However, in this case the d–d absorption occurs in the infrared range, making it invisible to the naked eye. Therefore, it is not discussed in detail in the context of thermo- and piezo-chromism of the studied materials.

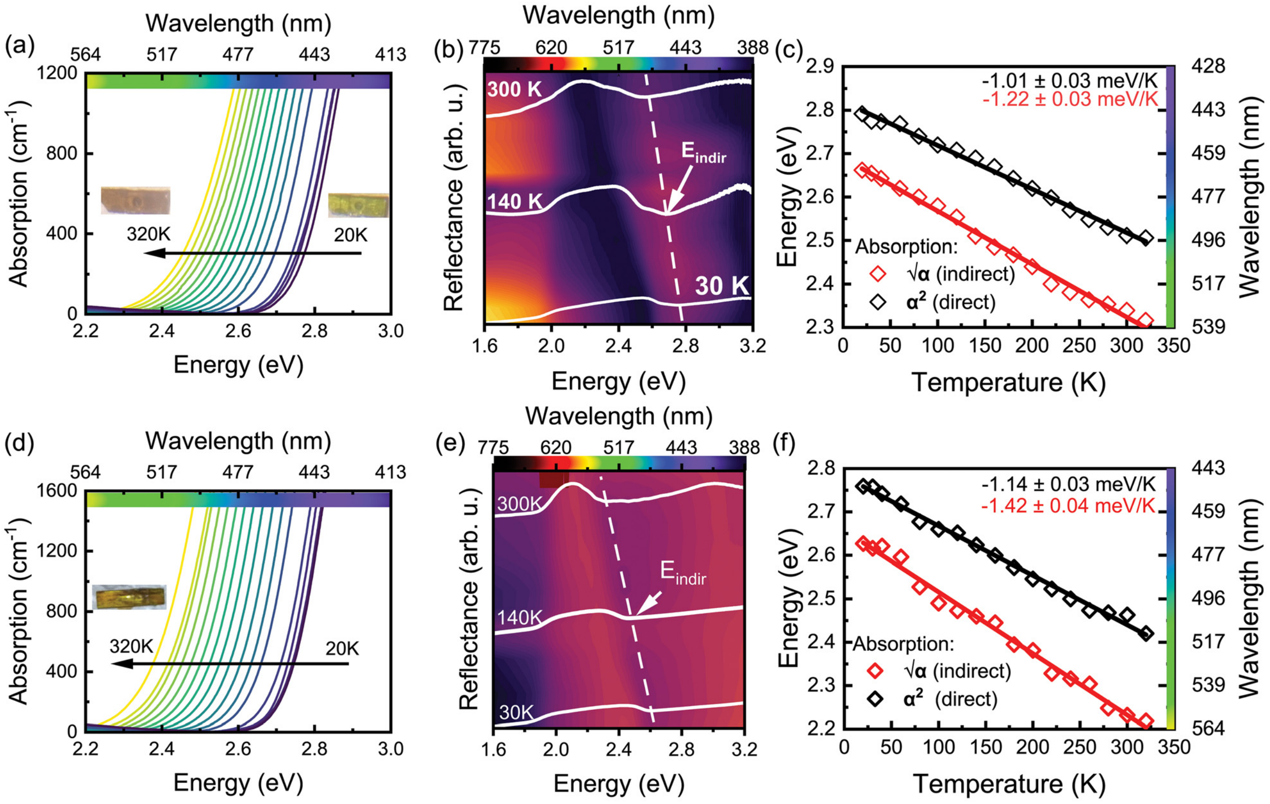

Fig. 1 Temperature dependence of (a) α, (b) *R* spectra for $(PMA)_2CuBr_4$ and (d) α, (e) *R* measurements for $(PMA)_2CuCl_4$. Indirect (open red diamonds) and direct (open black diamonds) gaps extracted from α measurements as a function of temperature for (c) $(PMA)_2CuBr_4$ and (f) $(PMA)_2CuCl_4$.

Fig. 1(d) shows the α spectra of $(PMA)_2CuCl_4$ measured from 20 to 320 K, and Fig. 1(e) illustrates the *R* spectra collected from 30 to 320 K. The α measurements reveal a linear narrowing of both the direct and indirect energy gaps with temperature, with a reduction of 303 meV (∼51 nm from 444 to 495 nm) and 366 meV (∼70 nm from 466 to 536 nm), respectively, from 20 to 320 K. This narrowing causes visible thermochromism, shifting from green at 20 K to yellow at 320 K. Similar to the previous considerations for $(PMA)_2CuBr_4$, the reduction in the energy gap and the color change are confirmed through *R* measurements. However, the presence of a transparency region near the indirect transition complicates the precise determination of the transition position at each temperature for the $(PMA)_2CuCl_4$ perovskite. Comparing the α^2 and $\sqrt{\alpha}$ spectra with the *R* spectra suggests that the fundamental energy gap in $(PMA)_2CuCl_4$ is indirect with a value of 2.33 eV under ambient conditions.

According to the previous studies,[55] an exciton emission for $(PMA)_2CuCl_4$ is observed at 2.12 eV under ambient conditions. This emission is consistent with the fundamental band gap of 2.33 eV determined in this work as there can be a few mechanisms, which can be responsible for the Stokes shift between emission and absorption, see ref. 56–60.

2.2. Piezochromism in $(PMA)_2CuBr_4$ and $(PMA)_2CuCl_4$ halide perovskites

To investigate piezochromism, transmission spectra under hydrostatic pressure were measured. Fig. 2(a) shows the normalized transmission spectra for $(PMA)_2CuBr_4$ as a function of hydrostatic pressure at room temperature. It can be observed that, as the pressure in the diamond anvil cell (DAC) increases, the band gap of $(PMA)_2CuBr_4$ shifts to lower energies (redshifts), similar to other perovskite materials.[61–63] However, this shift is significantly larger compared to other semiconductors.[64,65] The observed redshift is attributed to band gap narrowing in $(PMA)_2CuBr_4$ under hydrostatic pressure, resulting in a ∼400 meV shift (∼90 nm from 482 to 572 nm) up to 10.94 GPa. The decompression process is shown in Fig. S7 in the SI, from which it can be concluded that, during pressure release in the DAC, the band gap of $(PMA)_2CuBr_4$ remains consistent with the data obtained during compression.

This pressure-induced shift in the band gap is accompanied by a visible piezochromic effect. As pressure increases, the color of the material changes, reflecting corresponding shifts in its optical properties. Specifically, the crystal color of $(PMA)_2CuBr_4$ transitions from yellow at 0.00 GPa to red/black at 10.94 GPa, consistent with the observed band gap narrowing. This visible piezochromism results directly from the pressure-induced modification of the material's electronic structure above the band gap, which alters the absorption spectrum, consequently changing the material's perceived color.

The change in the band gap, obtained from pressure-induced transmission spectra, is shown in Fig. 2(b). As seen, the pressure coefficients for $(PMA)_2CuBr_4$ were found to be $\alpha_I = -47 \pm 7$ and $\alpha_{II} = -30 \pm 2$ meV/GPa. The linear fitting used to extract the pressure coefficients from the data was performed

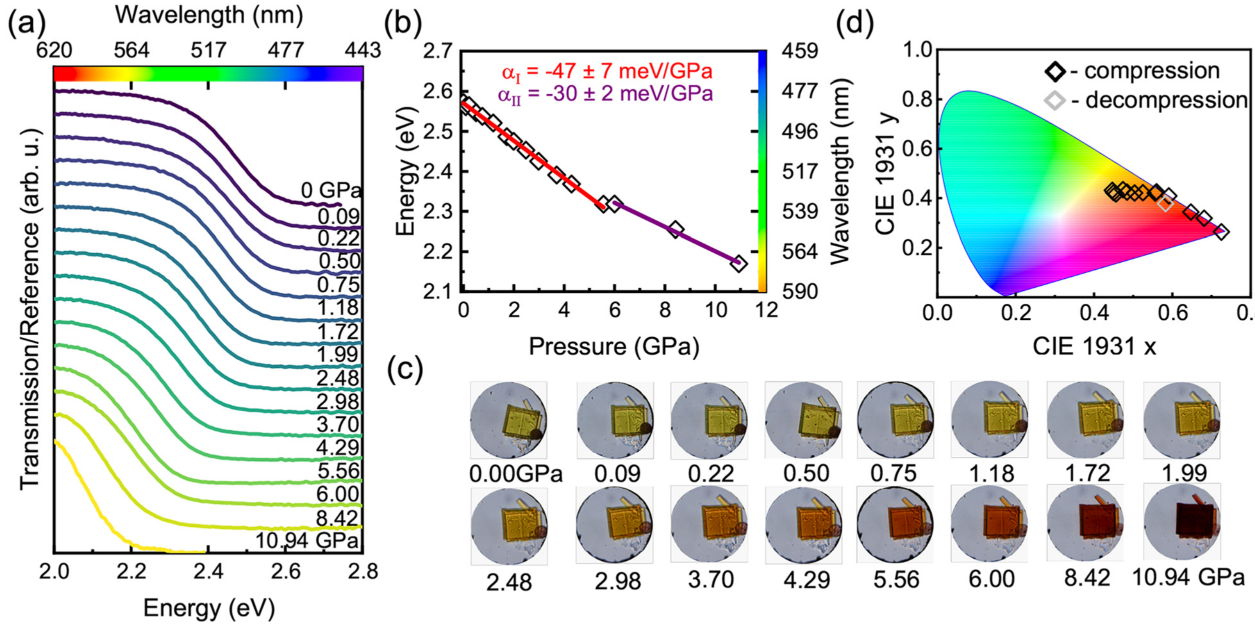

Fig. 2 (a) Transmission spectra showing the near absorption edge of $(PMA)_2CuBr_4$ under ambient conditions. (b) Band gap change as a function of pressure derived from the transmission spectra. (c) Optical micrographs of $(PMA)_2CuBr_4$ in DAC. (d) Pressure-dependent chromaticity coordinates shown in the CIE 1931 format.

in the range of 0.00 to 5.56 GPa for the first phase (P1), and in the range of 6.00 to 10.94 GPa for the second phase (P2). This transition change is attributed to a reduction in structural symmetry and a layer slip in the 2D structure caused by a tilting rotation of the octahedral perovskites.[66] According to previous studies for this material, $(PMA)_2CuBr_4$ exhibits no significant structural phase transitions up to 40 GPa which is associated with the protection of the organic cations by the amino group.[10]

Fig. 2(c) presents optical micrographs of the $(PMA)_2CuBr_4$ sample mounted in the DAC. The crystals' color change from yellow at 0.00 GPa to red/black at 10.94 GPa directly correlates with the band gap narrowing observed in the absorption edge. To further visualize the piezochromic effect, Fig. 2(d) illustrates the CIE 1931 chromaticity diagram.

Fig. 3(a) presents the normalized transmission spectra of $(PMA)_2CuCl_4$ under hydrostatic pressure at 300 K. Similar to the behavior observed for $(PMA)_2CuBr_4$, the band gap of $(PMA)_2CuCl_4$ redshifts with increasing pressure, decreasing by ~330 meV (~70 nm from 476 to 546 nm) up to 10.86 GPa. This indicates that the presence of PMA significantly enhances the structural stability of the material, as is the case of $(PMA)_2CuBr_4$, allowing higher pressures to be applied until irreversible amorphization occurs. During decompression, the band gap of $(PMA)_2CuCl_4$ remains consistent with the data obtained during compression. The pressure coefficients for $(PMA)_2CuCl_4$ were determined to be $\alpha_I = -53 \pm 3$ and $\alpha_{II} = -23 \pm 2$ meV/GPa for P1 and P2, respectively. The pressure coefficient for P1 is slightly larger than that for $(PMA)_2CuBr_4$, whereas for P2 it is smaller. A linear fit was applied to extract these coefficients, with the fitting range set to 0.00–4.43 GPa for P1 and 5.46–10.86 GPa for P2, respectively. As in $(PMA)_2CuBr_4$, the change in the pressure coefficient can be attributed to a phase transition, but a detailed analysis of this phase transition is beyond the scope of this article. Fig. 3(c) displays optical micrographs of $(PMA)_2CuCl_4$. The observed transition of the crystal color from yellow at 0.00 GPa to red/orange at 10.86 GPa is consistent with the band gap narrowing determined from the absorption edge region. Furthermore, to emphasize the thermo- and piezo-chromic effects, the CIE 1931 chart is shown in Fig. 3(d).

2.3. Discussion

In $(PMA)_2CuCl_4$ and $(PMA)_2CuBr_4$ perovskite materials, chlorine (Cl) and bromine (Br) have distinct effects on the materials' optical, electronic, and structural properties. Br has a larger ionic radius (1.96 Å) compared to Cl (1.81 Å), which leads to larger lattice parameters in bromine-based perovskites. This is a well-known chemical trend, which is observed for many crystals including 3D and 2D perovskites.[67] In terms of the optical and electronic properties, Cl-based perovskites typically exhibit a wider band gap absorbing light at shorter wavelengths, while Br-based perovskites have a narrower band gap,[68] this is also true for $(PMA)_2CuX_4$ (X = Br and Cl), although the gap narrowing upon replacement of Cl by Br is only 110 meV, while for other perovskites it is much larger.[69–71]

In these studies, it is worth emphasizing that the band gap tuning induced by the change of composition (*i.e.*, chemical tuning by substituting Cl with Br) is much smaller than the band gap tuning induced by physical factors (*i.e.*, temperature – thermochromism and pressure – piezochromism). The great advantage of the observed phenomenon of thermochromism

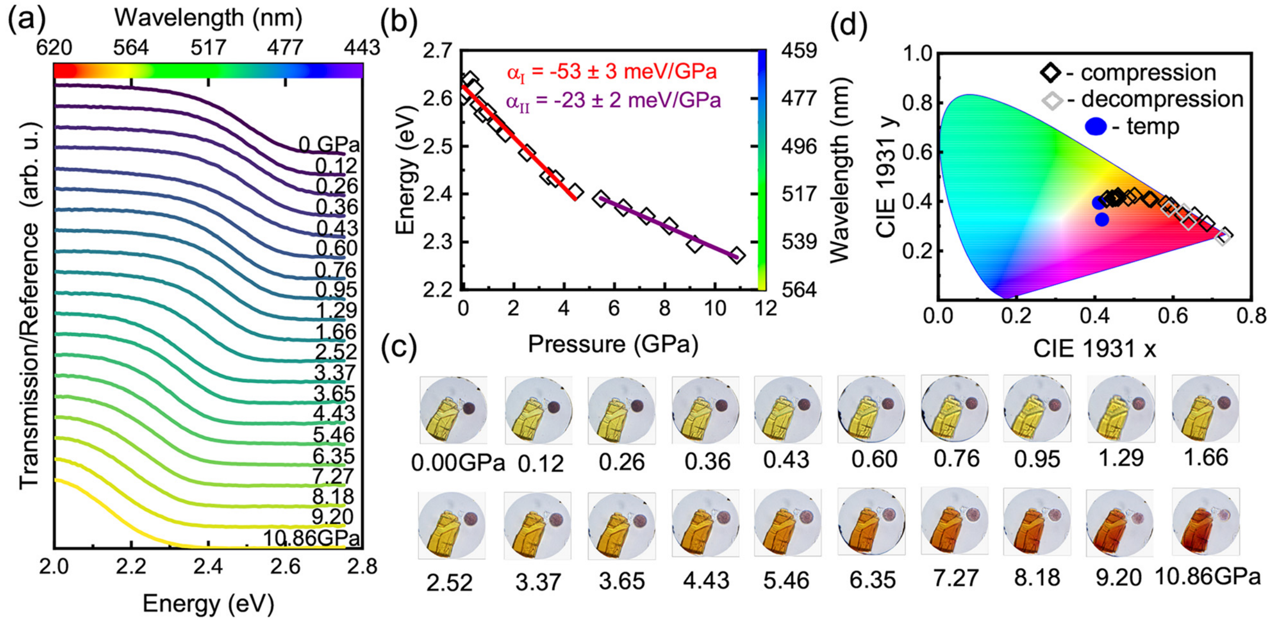

Fig. 3 (a) Transmission spectra showing the near absorption edge of $(PMA)_2CuCl_4$ under ambient conditions. (b) Band gap change as a function of pressure derived from transmission spectra. (c) Optical micrographs of $(PMA)_2CuCl_4$ in DAC. (d) Pressure-dependent chromaticity coordinates shown in the CIE 1931 format.

and piezochromism in these materials is the linear dependence of the absorption edge on external stimuli, which is not typical for many other perovskites. A continuous change in the energy gap with temperature does not indicate the presence of a phase transition. In general, phase transitions in perovskites often lead to a non-monotonic change in the energy gap.[72–74] Linear temperature dependence is crucial in thermo-devices, as it simplifies calibration and operation, ensuring predictable, consistent performance. Such sensors maintain stability in controlled environments and provide accurate data across a wide temperature range. Additionally, they are easy to integrate into systems that do not require high sensitivity to small temperature changes, making them a cost-effective solution for many applications.

Thermochromism and piezochromism both involve color changes in $(PMA)_2CuCl_4$ and $(PMA)_2CuBr_4$ materials, but they are driven by different stimuli – temperature and mechanical stress, respectively. These phenomena are closely related to interactions between electrons and phonons, as well as changes in the crystal lattice parameters. In thermochromism, the increase in lattice parameters caused by the increase in temperature leads to a narrowing of the energy gap, and additionally, the increase in the phonon population affects the narrowing of the energy gap through electron–phonon interactions. In piezochromism, we also deal with a narrowing of the energy gap, but the hydrostatic pressure leads to a decrease in the crystal volume (*i.e.* a decrease in lattice parameters, which is opposite to the thermal expansion of the lattice parameters with increasing temperature). The thermal energy of the crystal does not change during measurements under hydrostatic pressure because the measurements are performed at the same temperature, but the phonon dispersion changes under hydrostatic pressure and therefore the electron–phonon interaction may also change, which may also affect the energy gap narrowing.

The simple comparison of thermo- and piezo-chromism in $(PMA)_2CuCl_4$ and $(PMA)_2CuBr_4$ crystals indicates that the changes in lattice parameters induced by temperature and pressure are not equivalent, even if electron–phonon interactions play an important role in both thermo- and piezo-chromism. This means that the narrowing of the energy gap in the studied perovskites is a complex issue, and the electron–phonon interaction can certainly play a significant role in it and requires deeper research, including theoretical studies.

3 Conclusion

In conclusion, a comprehensive study of the thermo- and piezochromism of $(PMA)_2CuCl_4$ and $(PMA)_2CuBr_4$ has been carried out. We observed significant reductions in the energy gap: 366 meV (~70 nm from 466 to 536 nm) for $(PMA)_2CuCl_4$ and 426 meV (~87 nm from 472 to 559 nm) for $(PMA)_2CuBr_4$ across the 20–320 K temperature range. Additionally, pressure-dependent energy gap reductions were observed: 330 meV (~70 nm from 476 to 546 nm) up to 10.94 GPa for $(PMA)_2CuCl_4$ and by 400 meV (~90 nm from 482 to 572 nm) up to 10.86 GPa for $(PMA)_2CuBr_4$) which manifests as a visible color change. The observed changes in the band gap are continuous without any sudden jumps, which is a great advantage in terms of using these materials in thermochromic and piezochromic sensors. The fundamental energy gap for both was found to be indirect, with values of 2.33 eV for $(PMA)_2CuCl_4$ and 2.23 eV for $(PMA)_2CuBr_4$ under ambient conditions. Compared to other halide perovskites, both materials possess one of the highest band gap tunabilities reported to date. The hydrophobic PMA cation stabilizes the material by preventing moisture absorption and structural degradation due to environmental factors and ensuring that the lattice remains stable under stress. This structural stability allows for controlled band gap tunability with temperature or pressure variations, making these perovskites promising candidates for color or pressure sensing applications.

Author contributions

Rafał Bartoszewicz carried out the experimental work, data analyses, visualization and writing the original draft. He was also equally involved in conceiving the concept and methodology. Muhammad Danang Birowosuto, Jan-Albert Zienkiewicz, Sri Hartati, Arramel were responsible for providing $(PMA)_2CuCl_4$ and $(PMA)_2CuBr_4$ samples and structural measurements. Jan Kopaczek was responsible for the methodology. Robert Kudrawiec conceived the concept and supervised the work. All authors discussed the research progress and contributed to editing the paper.

Conflicts of interest

There are no conflicts to declare.

Data availability

The data supporting this study have been included as part of the SI.

Detailed materials and methods; experimental layout; additional XRD patterns, FTIR, Raman, XPS spectra for $(PMA)_2CuCl_4$ and $(PMA)_2CuBr_4$ obtained at ambient conditions; optimized geometric structure of $(PMA)_2CuCl_4$ built based on CIF; analysis of α^2 and $\sqrt{\alpha}$ from absorption spectra at 20 and 320 K, direct comparison of reflectance spectra with α^2 and $\sqrt{\alpha}$ at 30 K, position of d–d band and band gap, spectral position of band gap during decompression for $(PMA)_2CuCl_4$ and $(PMA)_2CuBr_4$; determination of the absorption edge. See DOI: **https://doi.org/10.1039/d5tc02326b**

Acknowledgements

This work was supported by the National Science Centre Poland, OPUS Grant no. 2020/39/B/ST3/02704.

References

1 H. Dong, C. Zhang, X. Liu, J. Yao and Y. S. Zhao, *Chem. Soc. Rev.*, 2020, **49**, 951–982.
2 A. Fakharuddin, M. K. Gangishetty, M. Abdi-Jalebi, S.-H. Chin, A. R. bin Mohd Yusoff, D. N. Congreve, W. Tress, F. Deschler, M. Vasilopoulou and H. J. Bolink, *Nat. Electron.*, 2022, **5**, 203–216.
3 C. Sun, Y. Jiang, M. Cui, L. Qiao, J. Wei, Y. Huang, L. Zhang, T. He, S. Li, H.-Y. Hsu, C. Qin, R. Long and M. Yuan, *Nat. Commun.*, 2021, **12**, 2207.
4 L. Zhang, C. Sun, T. He, Y. Jiang, J. Wei, Y. Huang and M. Yuan, *Light: Sci. Appl.*, 2021, **10**, 61.
5 C. Qin, A. S. D. Sandanayaka, C. Zhao, T. Matsushima, D. Zhang, T. Fujihara and C. Adachi, *Nature*, 2020, **585**, 53–57.
6 E. Yassitepe, Z. Yang, O. Voznyy, Y. Kim, G. Walters, J. A. Castañeda, P. Kanjanaboos, M. Yuan, X. Gong, F. Fan, J. Pan, S. Hoogland, R. Comin, O. M. Bakr, L. A. Padilha, A. F. Nogueira and E. H. Sargent, *Adv. Funct. Mater.*, 2016, **26**, 8757–8763.
7 W. Chen, Z. Huang, H. Yao, Y. Liu, Y. Zhang, Z. Li, H. Zhou, P. Xiao, T. Chen, H. Sun, J. Huang and Z. Xiao, *Nat. Photonics*, 2023, **17**, 401–407.
8 N. Marchal, W. Van Gompel, M. C. Gélvez-Rueda, K. Vandewal, K. Van Hecke, H.-G. Boyen, B. Conings, R. Herckens, S. Maheshwari, L. Lutsen, C. Quarti, F. C. Grozema, D. Vanderzande and D. Beljonne, *Chem. Mater.*, 2019, **31**, 6880–6888.
9 G. E. Eperon, S. D. Stranks, C. Menelaou, M. B. Johnston, L. M. Herz and H. J. Snaith, *Energy Environ. Sci.*, 2014, **7**, 982–988.
10 X. Zhan, X. Jiang, P. Lv, J. Xu, F. Li, Z. Chen and X. Liu, *Angew. Chem., Int. Ed.*, 2022, **61**, e202205491.
11 W. S. Yang, J. H. Noh, N. J. Jeon, Y. C. Kim, S. Ryu, J. Seo and S. I. Seok, *Science*, 2015, **348**, 1234–1237.
12 J. Yang, Q. Bao, L. Shen and L. Ding, *Nano Energy*, 2020, **76**, 105019.
13 I. Kopacic, B. Friesenbichler, S. F. Höfler, B. Kunert, H. Plank, T. Rath and G. Trimmel, *ACS Appl. Energy Mater.*, 2018, **1**, 343–347.
14 H. C. Sansom, G. Longo, A. D. Wright, L. R. V. Buizza, S. Mahesh, B. Wenger, M. Zanella, M. Abdi-Jalebi, M. J. Pitcher, M. S. Dyer, T. D. Manning, R. H. Friend, L. M. Herz, H. J. Snaith, J. B. Claridge and M. J. Rosseinsky, *J. Am. Chem. Soc.*, 2021, **143**, 3983–3992.
15 Y. Liao, H. Liu, W. Zhou, D. Yang, Y. Shang, Z. Shi, B. Li, X. Jiang, L. Zhang, L. N. Quan, R. Quintero-Bermudez, B. R. Sutherland, Q. Mi, E. H. Sargent and Z. Ning, *J. Am. Chem. Soc.*, 2017, **139**, 6693–6699.
16 D. Cortecchia, H. A. Dewi, J. Yin, A. Bruno, S. Chen, T. Baikie, P. P. Boix, M. Grätzel, S. Mhaisalkar, C. Soci and N. Mathews, *Inorg. Chem.*, 2016, **55**, 1044–1052.
17 Z. Shi, J. Guo, Y. Chen, Q. Li, Y. Pan, H. Zhang, Y. Xia and W. Huang, *Adv. Mater.*, 2017, **29**, 1605005.
18 X. Li, X. Zhong, Y. Hu, B. Li, Y. Sheng, Y. Zhang, C. Weng, M. Feng, H. Han and J. Wang, *J. Phys. Chem. Lett.*, 2017, **8**, 1804–1809.
19 X.-P. Cui, K.-J. Jiang, J.-H. Huang, Q.-Q. Zhang, M.-J. Su, L.-M. Yang, Y.-L. Song and X.-Q. Zhou, *Synth. Met.*, 2015, **209**, 247–250.
20 A. Elattar, H. Suzuki, R. Mishima, K. Nakao, H. Ota, T. Nishikawa, H. Inoue, A. K. K. Kyaw and Y. Hayashi, *J. Mater. Chem. C*, 2021, **9**, 3264–3270.

21 H. Tsai, W. Nie, J.-C. Blancon, C. C. Stoumpos, R. Asadpour, B. Harutyunyan, A. J. Neukirch, R. Verduzco, J. J. Crochet, S. Tretiak, L. Pedesseau, J. Even, M. A. Alam, G. Gupta, J. Lou, P. M. Ajayan, M. J. Bedzyk and M. G. Kanatzidis, *Nature*, 2016, **536**, 312–316.

22 I. C. Smith, E. T. Hoke, D. Solis-Ibarra, M. D. McGehee and H. I. Karunadasa, *Angew. Chem., Int. Ed.*, 2014, **53**, 11232–11235.

23 Q.-Q. Sun, Q. Li, H.-Y. Li, M.-M. Zhang, M.-E. Sun, S. Li, Z. Quan and S.-Q. Zang, *Chem. Commun.*, 2021, **57**, 2372–2375.

24 F.-F. Gao, H. Song, Z.-G. Li, Y. Qin, X. Li, Z.-Q. Yao, J.-H. Fan, X. Wu, W. Li and X.-H. Bu, *Angew. Chem., Int. Ed.*, 2023, **62**, e202218675.

25 X. Wu, Y. Sun, L. Wang, Y. Huang, J. Wang, Y. Yuan, U. Shahzadi, R. Fu, K. Wang and H. Guo, *Adv. Opt. Mater.*, 2025, **13**, 2402136.

26 M. De Bastiani, M. I. Saidaminov, I. Dursun, L. Sinatra, W. Peng, U. Buttner, O. F. Mohammed and O. M. Bakr, *Chem. Mater.*, 2017, **29**, 3367–3370.

27 S. Liu, Y. Li, Y. Wang, K. M. Yu, B. Huang and C. Y. Tso, *Adv. Sci.*, 2022, **9**, 2106090.

28 O. Mapazi, P. K. Matabola, R. M. Moutloali and C. J. Ngila, *Sens. Actuators, B*, 2017, **252**, 671–679.

29 M. Cinquino, C. T. Prontera, A. Giuri, M. Pugliese, R. Giannuzzi, A. Maggiore, D. Altamura, F. Mariano, G. Gigli, C. Esposito Corcione, C. Giannini, A. Rizzo, L. De Marco and V. Maiorano, *Adv. Mater.*, 2024, **36**, 2307564.

30 C. Pareja-Rivera and D. Solis-Ibarra, *Adv. Opt. Mater.*, 2021, **9**, 2100633.

31 A. Singh and S. Satapathi, *Adv. Opt. Mater.*, 2021, **9**, 2101062.

32 W. Ning, X.-G. Zhao, J. Klarbring, S. Bai, F. Ji, F. Wang, S. I. Simak, Y. Tao, X.-M. Ren, L. Zhang, W. Huang, I. A. Abrikosov and F. Gao, *Adv. Funct. Mater.*, 2019, **29**, 1807375.

33 X. Li, B. Li, J. Chang, B. Ding, S. Zheng, Y. Wu, J. Yang, G. Yang, X. Zhong and J. Wang, *ACS Appl. Energy Mater.*, 2018, **1**, 2709–2716.

34 K. Zulfa, B. Zahara, A. Akmal Afkauni, P. Yuniar Diah Maulida, S. Hartati, I. Mulyani, A. Yudhowijoyo, L. Jaya Diguna, M. Haris Mahyuddin, D. Onggo, M. Danang Birowosuto and A. Arramel, *Mater. Today: Proc.*, 2024, DOI: 10.1016/j.matpr.2024.03.058.

35 G. Liu, L. Kong, W. Yang and H.-K. Mao, *Mater. Today: Proc.*, 2019, **27**, 91–106.

36 W. Zhao, G. Xiao and B. Zou, *Aggregate*, 2024, **5**, e461.

37 S. Wang, J. Ma, W. Li, J. Wang, H. Wang, H. Shen, J. Li, J. Wang, H. Luo and D. Li, *J. Phys. Chem. Lett.*, 2019, **10**, 2546–2553.

38 Y. Zhu, J. Buitenhuis, B. Förster, M. R. Vetrano and E. Koos, *ACS Appl. Nano Mater.*, 2023, **6**, 4661–4671.

39 A. Celeste and F. Capitani, *J. Appl. Phys.*, 2022, **132**, 220903.

40 X.-Z. Zhao, F.-F. Gao, W. Li, Z.-G. Li, Y. Zhang, K. Li, H. Hu, W. Cai, J. Zhang and X.-H. Bu, *J. Mater. Chem. C*, 2024, **12**, 4599–4605.

41 J. Xu, S. Yu, X. Shang and X. Chen, *Adv. Photonics Res.*, 2023, **4**, 2200193.

42 J. Ning, L. Zheng, W. Lei, S. Wang, J. Xi and J. Yang, *Phys. Chem. Chem. Phys.*, 2022, **24**, 16003–16010.

43 Y. Zhou, D. Zhao, F. Wang, Y. Shi, Z. Ma, R. Fu, K. Wang, Y. Sui, Q. Dong, G. Xiao and B. Zou, *Phys. Rev. Mater.*, 2023, **7**, 074002.

44 P. Steeger, M. Adnan, T. Deilmann, X. Li, S. Müller, K. Skrzynska, M. Hanfland, E. Kolesnikov, J. Kösters, T. Block, R. Schmidt, I. Kupenko, C. Sanchez-Valle, G. Vijaya Prakash, S. Michaelis de Vasconcellos and R. Bratschitsch, *J. Am. Chem. Soc.*, 2024, **146**, 23205–23211.

45 L. Zhang, L. Wu, K. Wang and B. Zou, *Adv. Sci.*, 2019, **6**, 1801628.

46 N. Hassan, S. Nagaraja, S. Saha, K. Tarafder and N. Ballav, *Chem. Sci.*, 2024, **15**, 4075–4085.

47 R. F. I. Josey and J. L. Fenton, *Inorg. Chem.*, 2024, **63**, 6026–6032.

48 Y.-H. Liu, Y.-F. Wu, L.-J. Feng, R.-R. Zhao, S.-X. Wang, M.-M. Zhang, D.-Y. Wang, X.-W. Kong and X.-W. Lei, *Chem. Commun.*, 2023, **59**, 10267–10270.

49 I. Vurgaftman, J. R. Meyer and L. R. Ram-Mohan, *J. Appl. Phys.*, 2001, **89**, 5815–5875.

50 G. Mannino, I. Deretzis, E. Smecca, A. La Magna, A. Alberti, D. Ceratti and D. Cahen, *J. Phys. Chem. Lett.*, 2020, **11**, 2490–2496.

51 F. Ji, J. Klarbring, F. Wang, W. Ning, L. Wang, C. Yin, J. S. M. Figueroa, C. K. Christensen, M. Etter, T. Ederth, L. Sun, S. I. Simak, I. A. Abrikosov and F. Gao, *Angew. Chem.*, 2020, **132**, 15303–15306.

52 J. Bhosale, A. K. Ramdas, A. Burger, A. Muñoz, A. H. Romero, M. Cardona, R. Lauck and R. K. Kremer, *Phys. Rev. B*, 2012, **86**, 195208.

53 Y. P. Varshni, *Physica*, 1967, **34**, 149–154.

54 A. Jaffe, Y. Lin, W. L. Mao and H. I. Karunadasa, *J. Am. Chem. Soc.*, 2015, **137**, 1673–1678.

55 A. Arramel, A. D. Fauzi, X. Yin, C. S. Tang, M. H. Mahyuddin, M. F. Sahdan, M. Aminah, D. Onggo, G. Shukri, C. Diao, H. Wang, M. D. Birowosuto, A. T. S. Wee and A. Rusydi, *Commun. Mater.*, 2021, **2**, 1–12.

56 J. A. Peters, Z. Liu, M. C. De Siena, M. G. Kanatzidis and B. W. Wessels, *J. Lumin.*, 2022, **243**, 118661.

57 T. Yamada, T. Aharen and Y. Kanemitsu, *Phys. Rev. Lett.*, 2018, **120**, 057404.

58 F. Dybala, R. Kudrawiec, M. P. Polak, A. P. Herman, A. Sieradzki and M. Maczka, *Mater. Adv.*, 2025, **6**, 569–578.

59 A. Pieniazek, F. Dybala, M. P. Polak, U. Przypis, A. P. Herman, J. Kopaczek and R. Kudrawiec, *J. Phys. Chem. Lett.*, 2023, **14**, 6470–6476.

60 H. He, Q. Yu, H. Li, J. Li, J. Si, Y. Jin, N. Wang, J. Wang, J. He, X. Wang, Y. Zhang and Z. Ye, *Nat. Commun.*, 2016, **7**, 10896.

61 H. Li, D. Wines, B. Chen, K. Yumigeta, Y. M. Sayyad, J. Kopaszek, S. Yang, C. Ataca, E. H. Sargent and S. Tongay, *ACS Appl. Mater. Interfaces*, 2021, **13**, 44964–44971.

62 C. Wolf and T.-W. Lee, *Mater. Today Energy*, 2018, **7**, 199–207.

63 M. Maczka, S. Sobczak, P. Ratajczyk, F. F. Leite, W. Paraguassu, F. Dybala, A. P. Herman, R. Kudrawiec and A. Katrusiak, *Chem. Mater.*, 2022, **34**, 7867–7877.

64 N. E. Christensen and I. Gorczyca, *Phys. Rev. B:Condens. Matter Mater. Phys.*, 1994, **50**, 4397–4415.

65 P. E. Van Camp, V. E. Van Doren and J. T. Devreese, *Phys. Rev. B:Condens. Matter Mater. Phys.*, 1990, **41**, 1598–1602.

66 S. Guo, K. Bu, J. Li, Q. Hu, H. Luo, Y. He, Y. Wu, D. Zhang, Y. Zhao, W. Yang, M. G. Kanatzidis and X. Lü, *J. Am. Chem. Soc.*, 2021, **143**, 2545–2551.

67 W. Ning and F. Gao, *Adv. Mater.*, 2019, **31**, 1900326.

68 Y. Liu, Z. Yang, D. Cui, X. Ren, J. Sun, X. Liu, J. Zhang, Q. Wei, H. Fan, F. Yu, X. Zhang, C. Zhao and S. F. Liu, *Adv. Mater.*, 2015, **27**, 5176–5183.

69 M. Szafranski, *J. Mater. Chem. A*, 2024, **12**, 2391–2399.

70 K. Fedoruk, D. Drozdowski, M. Maczka, J. K. Zareba, D. Stefanska, A. Gagor and A. Sieradzki, *Inorg. Chem.*, 2022, **61**, 15520–15531.

71 R. Comin, G. Walters, E. S. Thibau, O. Voznyy, Z.-H. Lu and E. H. Sargent, *J. Mater. Chem. C*, 2015, **3**, 8839–8843.

72 F. Ruf, M. F. Aygüler, N. Giesbrecht, B. Rendenbach, A. Magin, P. Docampo, H. Kalt and M. Hetterich, *APL Mater.*, 2019, **7**, 031113.

73 M. Armer, P. Dörflinger, A. Weis, C. Büchner, A. Gottscholl, J. Höcker, K. Frank, L. Nusser, M. T. Sirtl, B. Nickel, T. Bein and V. Dyakonov, *Adv. Photonics Res.*, 2023, **4**, 2300017.

74 S. Neutzner, A. R. Srimath Kandada, G. Lanzani and A. Petrozza, *J. Mater. Chem. C*, 2016, **4**, 4630–4633.

Supporting Information for

Thermochromism versus piezochromism in $(PMA)_2CuX_4$ (X = Br, Cl) halide perovskites

*Rafał Bartoszewicz,[1, *] Jan-Albert Zienkiewicz,[2] Sri Hartati,[3] Arramel Arramel,[3] Jan Kopaczek,[1] Muhammad Danang Birowosuto,[2] and Robert Kudrawiec[1, **]*

[1]Department of Semiconductor Materials Engineering, Wroclaw University of Science and Technology, Wybrzeże Wyspiańskiego 27, 50-370 Wrocław, Poland

[2]Lukasiewicz Research Network-PORT Polish Center for Technology Development, Stabłowicka 147, 54-066 Wrocław, Poland

[3]Center of Excellence Applied Physics and Chemistry, Nano Center Indonesia, Jalan Raya PUSPIPTEK, South Tangerang 15314, Indonesia

* e-mail address: rafal.bartoszewicz@pwr.edu.pl

** e-mail address: robert.kudrawiec@pwr.edu.pl

KEYWORDS: copper-based perovskites, thermochromism, piezochromism, hydrostatic pressure, absorption, reflectance, temperature

Figure S1 presents the X-ray diffraction (XRD) pattern of (a) $(PMA)_2CuCl_4$ and (b) $(PMA)_2CuBr_4$ in ambient conditions. Previous studies have reported that $(PMA)_2CuCl_4$ crystallizes in an orthorhombic structure (Pbca) with lattice parameters a = 7.59 Å, b = 7.38 Å, c = 31.30 Å [1], while $(PMA)_2CuBr_4$ is reported to possess a hexagonal structure with lattice parameters a = 10.558 Å, b = 10.486 Å and c = 63.473 Å.[2] The XRD results from our study confirm the presence of the expected orthorhombic and hexagonal lattices for the respective crystals. CCDC 2477244 contains the supplementary crystallographic data for this paper. This data can be obtained free of charge via www.ccdc.cam.ac.uk/data_request/cif.

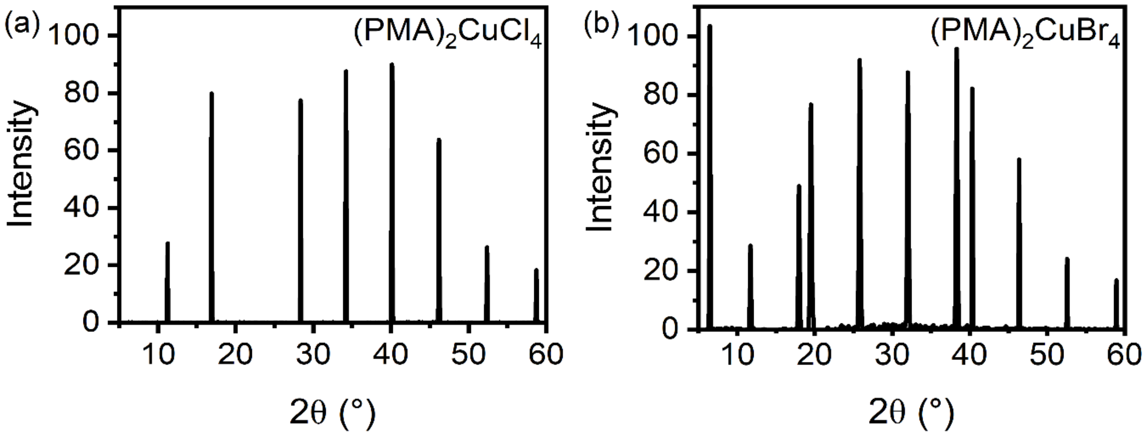

Figure S1. XRD pattern of (a) $(PMA)_2CuCl_4$ and (b) $(PMA)_2CuBr_4$ in ambient conditions.

Based on the previous works[3,4] we confirm $(PMA)_2CuCl_4$ crystals can be categorized as 2D Ruddlesden-Popper (RP) perovskites according to its structural X-ray analysis and optimized geometric calculation. In a conventional 2D RP HOIPs, a distinct layered structure composed of inorganic sheets of corner-sharing BX_6 octahedra (commonly lead, tin, or copper halide units), separated by organic cation layers. The prototypical formula for RP perovskites is $(RNH_3)_2A_{n-1}M_nX_{3n+1}$ for halide-based systems, where in our case the general stoichiometry related to n=1, as previously reported by Dupas et. al, Kim et.al.[5], and Septiany et.al.[4,6] At glance, we noticed that the X-ray diffraction pattern of $(PMA)_2CuCl_4$ is qualitatively different compared to conventional 3D perovskite. In particular, the prominent feature of 2D perovskites display additional peaks that are located at the low-2θ angle (<14°) for $n<\infty$.[7,8] Second consideration is related to the inorganic plane connectivity, corner-sharing between the inorganic networks is the most dominant feature arise within this family, as outlined in Ref[4,9] .

The optimized calculated of geometric $[CuCl_4]^{2-}$ layers is presented in Figure S3 (a). Third contribution is related to the structural studies show that $(PMA)_2CuCl_4$ consists of layers of $[CuCl_4]^{2-}$ anions separated by alternating bilayers of PMA^+ cations. We can relate this aspect by taking into account the observation of prominent periodicity of *hkl* (0 0 l) reflections. The observed reflections correspond to the interlayer distance separating the inorganic sheets. strong and sharp XRD peaks are assigned: (004), (006), (008), (0010), (0012) and (0014) planes at 2θ 11.25°, 16.9°, 22.57°, 28.35°, 34.2°, and 40.1°, respectively (see Figure S2). The pattern show periodical main peaks with relative equal 2θ separation on each peak.[10] These periodical pattern also found in other studies of 2D RP perovskite such as $(C_6H_5C_2H_4NH_3)_2SnI_4$,[10,11] $(C_6H_5(CH_2)_2NH_3)_2SnBr_4$,[12]

$(PMA)_2SnBr_3I$,[13,14] $(BZA)_2PbBr_4$ and $(OA)_2PbBr_4$,[15] $(BA)_2Pb(Br_xI_{1-x})_4$,[16] $(C_6H_5C_2H_4NH_2CH_3)_2CuBr_4$,[17] $(CH_3NH_3)_2CuCl_xBr_{4-x}$,[18] and $(CH_3(CH_2)_3NH_3)_2(CH_3NH_3)_{n-1}Pb_nI_{3n+1}$.[8] To provide clarity, representative optimized geometric structure (Fig. S3 (b)) composed the typical periodic layers of corner-sharing octahedra networks separated by the bilayer of organic ligand cations is outlined.

Table 1. Structural parameters of $(PMA)_2CuCl_4$ deduced from the CIF calculation results.

Crystal system	Orthorhombic
Space group	P −1
a/Å	7.80653
b/Å	7.41954
c/Å	33.8336
α/°	90.1824
β/°	90.0165
γ/°	89.9704
2θ range	6° − 60°

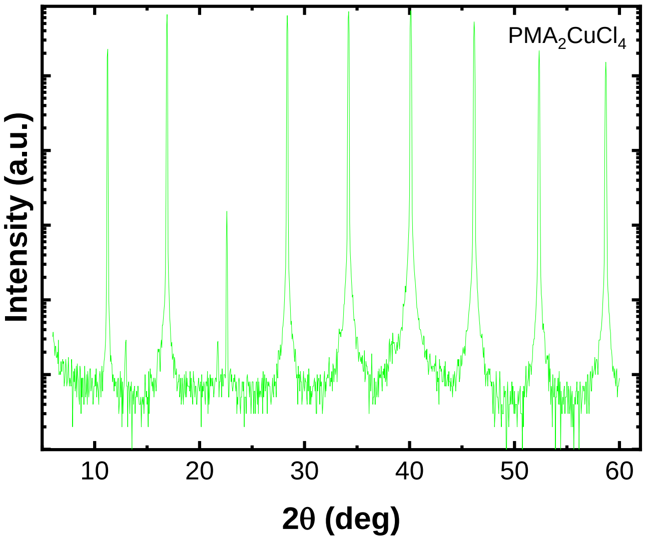

Fig. S2 XRD pattern of $(PMA)_2CuCl_4$ crystals based on previous study.[3]

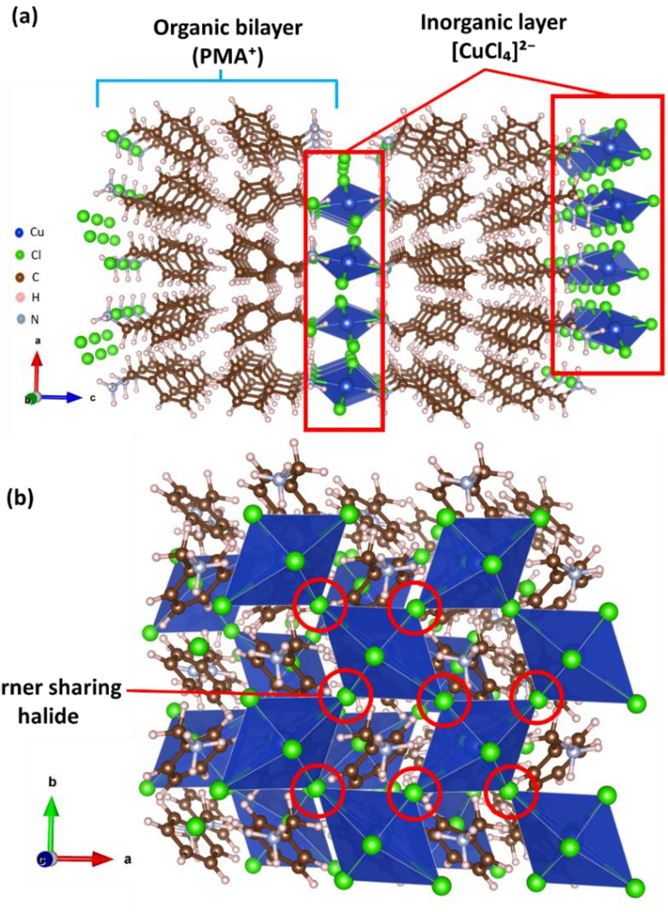

Fig. S3 The optimized geometric structure of PMA_2CuCl_4 built based on CIF. (a) a-c plane and (b) a-b plane.

Fourier transform infrared (FTIR) spectrum analysis in Figure S4 (a), reveals that both samples exhibit similar characteristic peaks within the 3250-2800 cm^{-1} absorption range. These vibration peaks are associated with C-H stretching, with sp^2 C-H stretching observed between 3100-3000 cm^{-1} and sp^3 C-H stretching around 2900 cm^{-1}. The functional group related to C-N is detected in the 1180-1360 cm^{-1} range, while a secondary amine (δ NH bending) is observed at approximately 1570 cm^{-1}. Both materials also show an aromatic C=C ring stretching between 1615-1495 cm^{-1}. Additionally, a peak near 750 cm^{-1}, corresponding to C-H rocking, is observed in the fingerprint region, and the 780-800 cm^{-1} range is associated with the C-Cl stretch of aliphatic chloro-compounds in $(PMA)_2CuCl_4$. A C-Br stretch for $(PMA)_2CuBr_4$ is observed between 500-600 cm^{-1}.[19]

The Raman spectrum displayed in Figure S4 (b) revealed several distinct peaks for $(PMA)_2CuCl_4$, associated with Cu-Cl bond vibrations, specifically at 177.14, 243.28 and 281.43 cm^{-1}. These peaks are attributed to the equatorial planar vibration, out-of-phase coupling of terminal Cu-Cl vibrations, and axial plane vibration, respectively. In contrast, four Raman-active modes are observed for $(PMA)_2CuBr_4$ at 113.0, 176.8, 265.4 and 333.4 cm^{-1}, corresponding to the Br-Cu-Br tilt rotation deformation vibration, Cu-Br axial stretching asymmetric vibration, Cu-Br equatorial plane stretching symmetric vibration, and Cu-Br equatorial plane stretching asymmetric vibration. The obtained results are in agreement with previously reported data.[19]

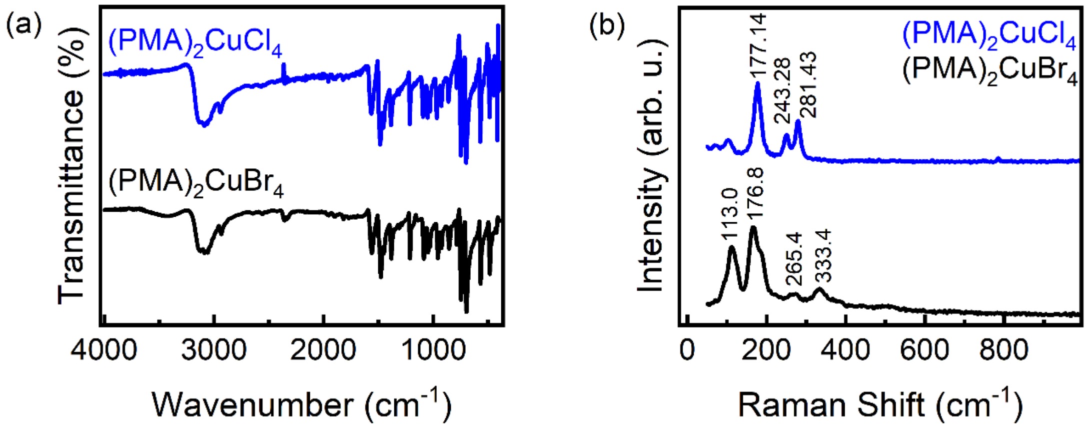

Figure S4. (a) FTIR and (b) Raman spectra collected at ambient conditions. Black line corresponds to $(PMA)_2CuCl_4$ while blue line reveals $(PMA)_2CuBr_4$ spectrum.

Figure S5 shows the chemical states of $(PMA)_2CuCl_4$ and $(PMA)_2CuBr_4$ are successfully resolved using X-ray photoelectron spectroscopy (XPS) at room temperature. The main component of C 1s peak in Figure S3 (a) is attributed to the C-N bond at 286.6 eV. The XPS spectrum of Cu 2p in Figure S5 (b) shows two prominent peaks corresponding to Cu $2p_{1/2}$ and Cu $2p_{3/2}$ within the 948-957 and 928-937 eV ranges, respectively. These peaks can be further deconvoluted into three components: Cu^0 (931.9 and 951.2 eV), Cu^+ (932.1 and 951.7 eV), and Cu^{2+} (933.2 and 952.9 eV). In addition, a satellite peak related to the Cu $2p_{3/2}$ of Cu^{2+} can be obtained between 939 to 948 eV. In the N 1s spectrum (Figure S5 (c)), a single peak located at 402.6 eV is obtained, which is assigned to the protonated nitrogen ($C\text{-}NH_3^+$). The Br 3d spectrum (Figure S5 (d)) was deconvoluted into two peaks corresponding to Br $3d_{5/2}$ (68.3 eV) and Br $3d_{3/2}$ (69.4 eV). Finally, Figure S5 (e) presents the Cl 2p core level spectrum, which reveals two components: Cl $2p_{3/2}$ at 198.5 eV and Cl $2p_{1/2}$ at 199 eV.[20]

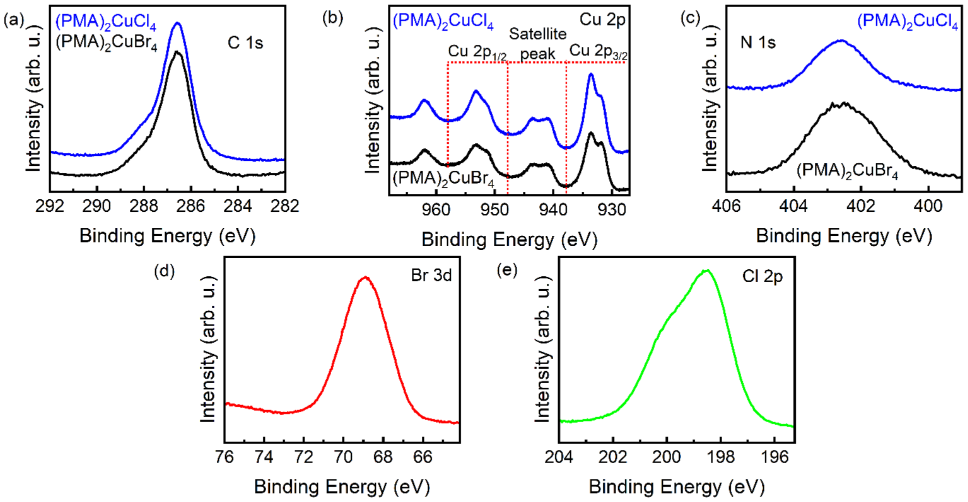

Figure S5. Analysis (a) C 1s core level display a prominent peak centered at 286.6 eV, correspond to the C-N bonding. (b) Cu 2p core level, each of the contributing signals are labeled as Cu $2p_{1/2}$, Cu $2p_{3/2}$ and their satellite peaks, respectively. (Black, $(PMA)_2CuCl_4$ and Blue, $(PMA)_2CuBr_4$). (c) N 1s core level with the maximum intensity is concentrated at 402.6 eV. (d) Br 3d core level containing two deconvoluted peaks of Br $3d_{5/2}$ and $3d_{3/2}$. (e) Cl 2p core level has two components, which outlines the presence of Cl $2p_{3/2}$ and Cl $2p_{1/2}$.

Figure S6 presents the example analysis for determining the absorption edge related to the indirect and direct band gap from temperature dependent transmission measurements. To determine the indirect gap, $\sqrt{\alpha}$ spectrum was drawn at 20 and 320 K. The linear dependence was extrapolated to zero and thus the indirect energy gap was determined. Additionally, the α^2 was plotted, and by linear extrapolation of this spectrum to zero the direct band gap was estimated.

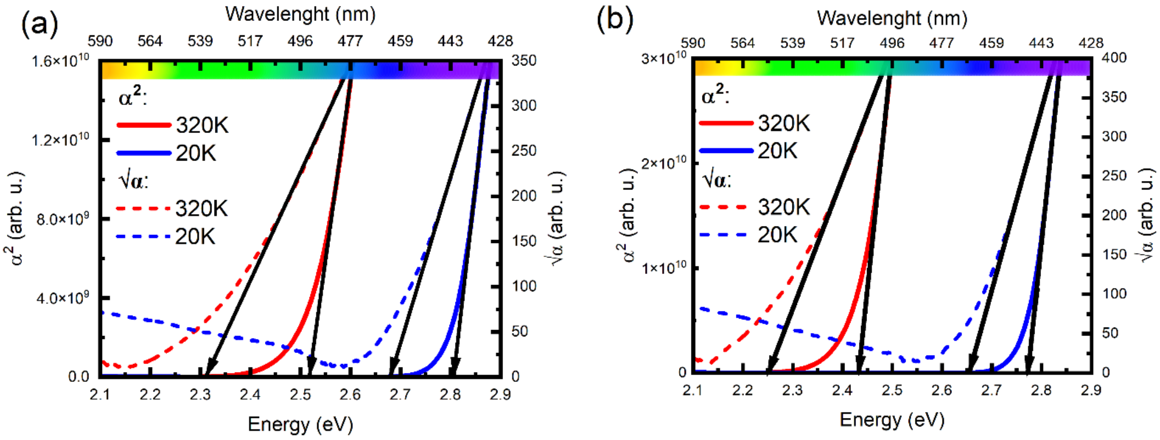

Figure S6. Analysis of α^2 and $\sqrt{\alpha}$ from absorption spectra at 20 and 320 K for (a) $(PMA)_2CuCl_4$ and (b) $(PMA)_2CuBr_4$.

Figure S7 illustrates method by which character of fundamental energy gap in $(PMA)_2CuCl_4$ (black solid line) and $(PMA)_2CuBr_4$ (red solid line) was determined. By using the direct comparison between reflectance spectra with (a) α^2 and (b) $\sqrt{\alpha}$ we determine this gap to be indirect for both materials, due to achieving similar position of visible resonance in reflectance spectrum with $\sqrt{\alpha}$ in each case.

As shown in Figure S7 (b), two regions are observed: from 2.5 to 3.2 eV (from 496 to 388 nm) and from 1.4 to 2.0 eV (886 to 620 nm), which correspond to the opacity region of the material. The opacity region refers to the wavelength range in which the material becomes non-transparent, and a lot of the light is reflected rather than transmitted. In this region, the reflectance is high, as the material absorbs or reflects the majority of incident light, limiting its ability to transmit light. This region is significant for optical studies as it provides insight into how optical properties of material change with structural variations. In contrast, the range from 2.0 to 2.5 eV (from 620 to 496 nm) corresponds to the transparency region, where the material allows light to pass through with low reflection. Here, the reflectance is low, as the material is transparent to these wavelengths, with most light transmitting through rather than being reflected. However a part of transmitted light reflects from the back of the sample, resulting in an increase in the measured signal intensity, thus complicating the accurate determination of energy gap from reflectance spectra, as changes in reflectance are less pronounced. Therefore, optical transmission measurements were also performed to more precisely characterize the electronic transitions.

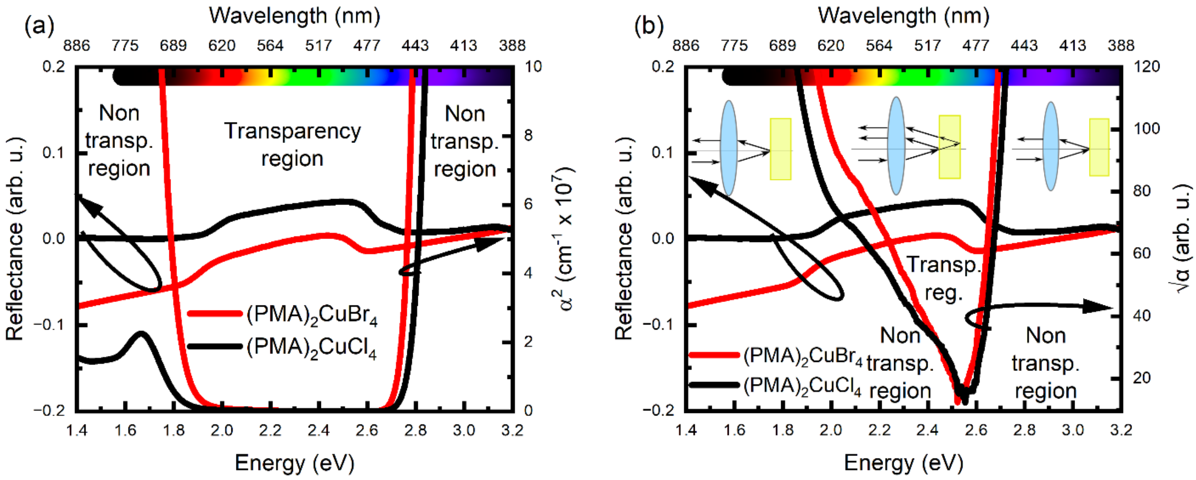

Figure S7. Direct comparison of reflectance spectra with (a) α^2 and (b) $\sqrt{\alpha}$ at 30 K. Black solid line corresponds to (PMA)$_2$CuCl$_4$ and (PMA)$_2$CuBr$_4$ is described by red solid line.

Figure S8 displays absorption spectra measured in the range from 1.35 to 2.9 eV (from 886 to 413 nm). As can be seen, both perovskites show the presence of d-d band, which starts to be visible at ~2 eV (620 nm).

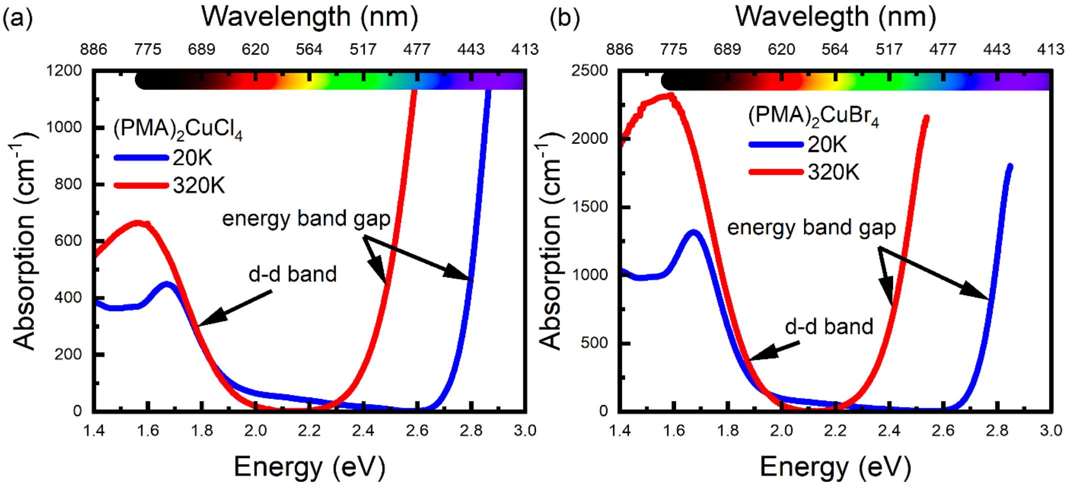

Figure S8. Position of d-d band and band gap for (a) (PMA)$_2$CuCl$_4$ and (b) (PMA)$_2$CuBr$_4$. Blue/red solid line presents absorption spectra measured at 20 and 320 K respectively.

Figure S9 shows the pressure-dependent absorption edge extracted from transmission measurements during decompression. For each obtained pressure value, optical micrographs are presented under respected graphs. It can be observed that as the pressure in the DAC decreases, the band gap of (PMA)$_2$CuBr$_4$ and (PMA)$_2$CuCl$_4$ retains its previous position in comparison to data obtained during compression. The small number of measurement points is due to the design of the DAC used, which does not allow for non-invasive reduction of pressure to a value close to zero. The change in the crystal color from red/orange at 8.72 and 9.02 GPa to yellow at 3.72 and 3.97 GPa (for (PMA)$_2$CuBr$_4$ and (PMA)$_2$CuCl$_4$ respectively) is also in line with data obtained during the compression process.

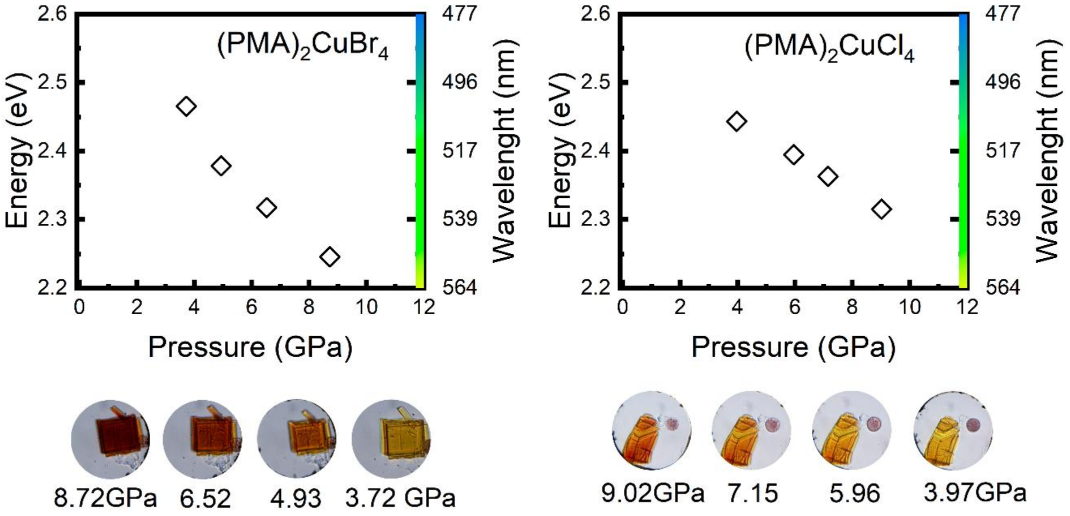

Figure S9. Spectral position of band gap/Optical micrographs as a function of pressure during decompression for $(PMA)_2CuBr_4$ and $(PMA)_2CuCl_4$ perovskites.

Figure S10 illustrates the method used to determine the energy shift of the absorption edge. Using a linear regression fit, we estimated the energy value from the square of the absorption coefficient (α^2), where α is defined according to the formula:

$$\alpha = -\frac{1}{d} ln \frac{T}{(1-R)^2}$$

where d is the sample thickness (here 50 μm), T mean– transmission and, R – reflectance signal.

It is worth noting, that 50 μm thickness is too large for an accurate determination of direct band gap, and therefore the value of direct gap can be underestimated by several lens of meV. Preparing a few micrometer thick sample for absorption measurements is very challenging in this case.

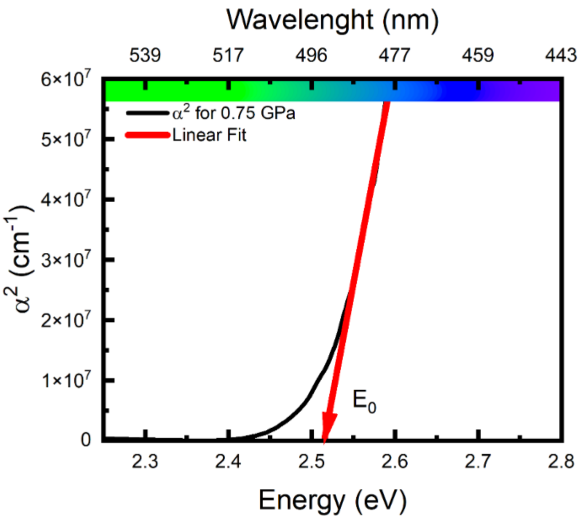

Figure S10. Determination of the absorption edge at 0.75 GPa for $(PMA)_2CuBr_4$.

MATERIALS AND METHODS

Sample synthesis

The process for growing $(PMA)_2CuX_4$ (X= Br, Cl) perovskite single crystals was adapted from established protocols in the literature. Initially, 1.79 g of copper(II) bromide or chloride dihydrate (CuX2·2H2O) was dissolved in 10 mL of distilled water to form a solution. Next, 2.86 g of phenylmethylamine hydrochloride (PMA, C7H10NCl) and 3-4 mL of 32% hydrohalic acid (HX) were added to the solution. The mixture was continuously stirred and heated to a temperature of 70 °C to achieve thorough mixing and create a uniform solution. After maintaining the mixture at 70 °C for one hour, the solution was left to cool slowly to room temperature, allowing single crystals to form. This procedure was repeated several times to ensure the production of high-quality crystals.[21,22]

Sample preparation for thermochromic measurements

Macroscopic samples of $(PMA)_2CuBr_4$ and $(PMA)_2CuCl_4$ were used to study thermochromic effect by transmission and reflectance spectroscopy. Samples used for transmission measurements were sizes of ~3x3 mm with thickness varying from 30 and 40 μm for $(PMA)_2CuBr_4$ and $(PMA)_2CuCl_4$ respectively. This was achieved by using the exfoliation method which provide mirror-like surface for both sides of the sample. For reflectance measurements, samples were made in the form of a wedge (~3x5 mm with thickness up to 1 mm). To achieve this, polishing/lapping Kemet 300L machine was used (Fig. S11 (a)). With the Si Waterproof Abrasive Disc (Grit P4000) wedge form was achieved. For reflectance measurements, the reflective side should be mirrored. This was done as previously by using the exfoliation method. The other sides have been dulled by using the Si Waterproof Abrasive Disc (Grit P1200). Figure S11 (b) shows that each sample was attached to a brass holder by a silver paste, distributed on the sides of the sample by 100 μm copper wire to eliminate the possibility of non-parallel attachment.

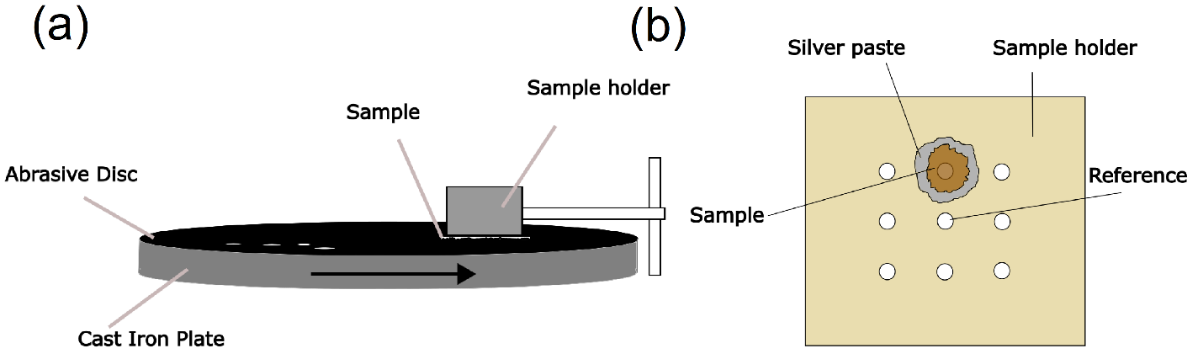

Figure S11. (a) The process of lapping/polishing $(PMA)_2CuBr_4$ and $(PMA)_2CuCl_4$ crystals with Si abrasive disc. (b) Preparation of perovskite crystals for transmission and reflectance measurements: samples attached to a brass sample holder using silver paste.

Temperature dependent transmission

Figure S12 shows measurement system to collect transmission (absorption) spectra in so-called 'dark configuration'. In this setup, the light emitted from a OSRAM HLX 64642 150 W 24 V halogen lamp was modulated by STANFORD RESEARCH SYSTEMS SR540 CHOPPER at a frequency of 266 Hz and directed to a single grating OMNI-λ 300 ZOLIX monochromator. In the monochromator, the probe beam (white light) was dispersed, and then passed through the sample. The sample was placed in a closed-cycle helium-cooled CTI-CRYOGENICS 22 JANIS cryostat, which allows measurements in the temperature range from 20 to 325 K. The temperature was monitored and stabilized using a LAKESHORE 325 controller. Transmission through the sample was detected by a SI diode HAMAMATSU S2386. Resultant signal was measured in the lock-in technique with a STANFORD SR810 DSP phase-sensitive nanovoltmeter, which consists in measuring the spectra point by point and the reference signal.

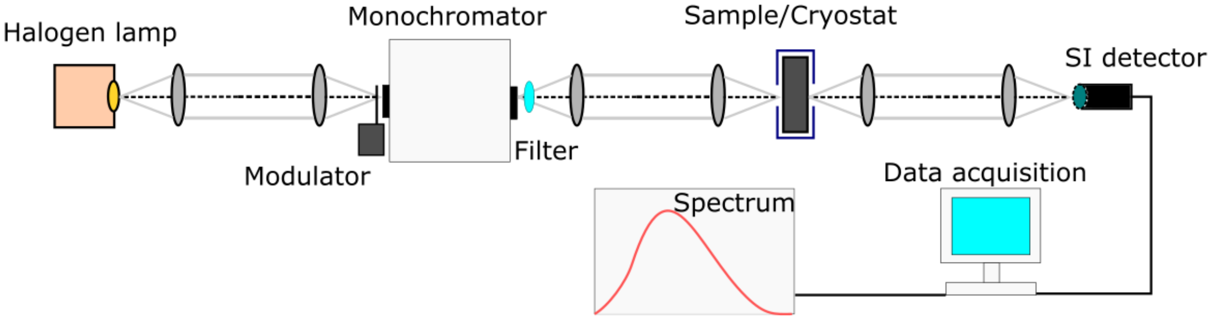

Figure S12. Scheme of the system used for determining the temperature dependent transmission measurements.

Temperature dependent reflectance

Figure S13 shows measurement system to collect reflectance spectra in so-called 'bright configuration'. In this setup, the light emitted from a OSRAM HLX 64655 250 W 24 V halogen lamp was modulated by STANFORD RESEARCH SYSTEMS SR540 CHOPPER at a frequency of 266 Hz and directed to a measured sample. Reflected light from the surface was then directed to a single grating OMNI-λ 500 ZOLIX monochromator. In the monochromator, the probe beam (white light) was dispersed, and finally detected by a SI diode HAMAMATSU S2386. The sample was placed in a closed-cycle helium-cooled SUMITOM DE-202FF cryostat, which allows measurements in the temperature range from 30 to 320 K. The temperature was monitored and stabilized using a LAKESHORE 331 controller. Resultant signal was measured in the lock-in technique with a STANFORD SR830 DSP phase-sensitive nanovoltmeter, which consists in measuring the spectra point by point and the reference signal.

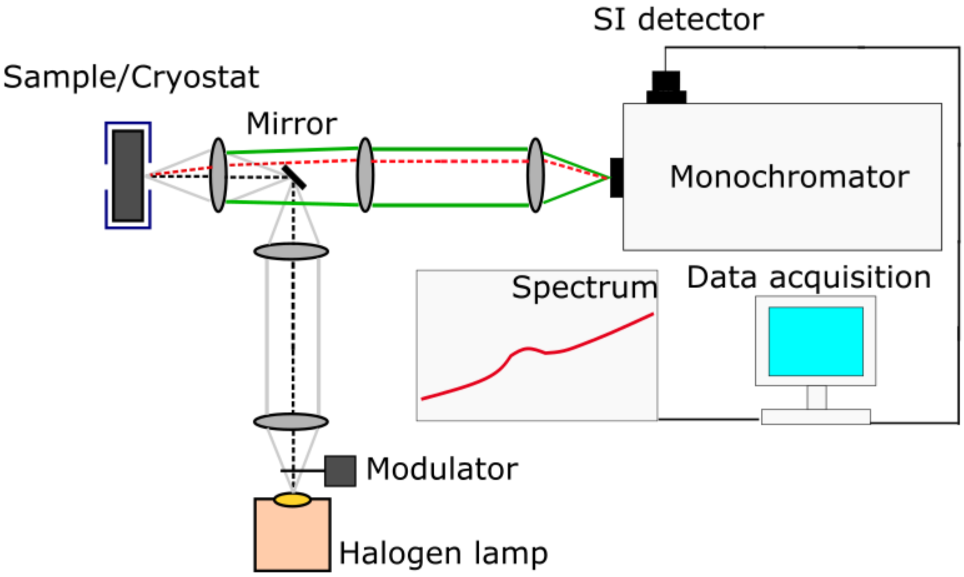

Figure S13. Measurement system for determining the temperature dependent reflectance spectrum.

Pressure dependent transmission

Figure S14 (a) presents schematically the experimental setup of pressure-dependent transmission carried out in this work. Figure S14 (b) shows a cross-section of a diamond anvil cell (DAC). Transmission measurements were performed in Diacell design DAC by ‘Almax easyLab’. Diamond with 650 µm culet size was used. The pressurizing mechanism in the DAC was driven using a gas membrane. The pressure in DAC was controlled by the amount of helium injected into the gas membrane. On top of the bottom diamond culet, a gasket was placed. It is a thin sheet (circa 50 µm thickness) of inconel material with a central hole of about 1/3 culet size, where sample, ruby sphere, and silicon oil were placed. Gaskets were prepared by pressing diamonds into a thin sheet, followed by creating a central hole using mechanical drilling. Daphne 7575 was used as the pressure-transmitting medium, which solidifies at about 4GPa at room temperature.[23] The optical microscope NADE NMM-800TRF and Mitutoyo M PLAN APO NIR 50x/0.42 f = 200 lens was used to properly focus on sample placed inside the DAC chamber. For transmission measurements, the halogen lamp (with voltage of 24 V and power 100 W) was used as a light source. Transmitted light was recorded by a StellarNet Blue-Wave UVIS 200 spectrometer with a 600 l/mm grating and 200 nm slit with resolution of 1.0. Delta Optical DLT-CAM PRO 3 MP USB 3.0 camera allowed us to investigate the color change of the perovskite. To excite the R1 luminescence of the ruby, a 532 nm CW laser was used (emission power 100 mW). In this case, AVANTES ULS4096CL-RS-EVO with a DCL-UV/VIS-200 600 l/mm diffraction grating blazed at 300 nm was used as a detector. To determine pressure value inside DAC we detect pressure-induced redshift of ruby sphere R1 line with calibration taken from Shen.[24]

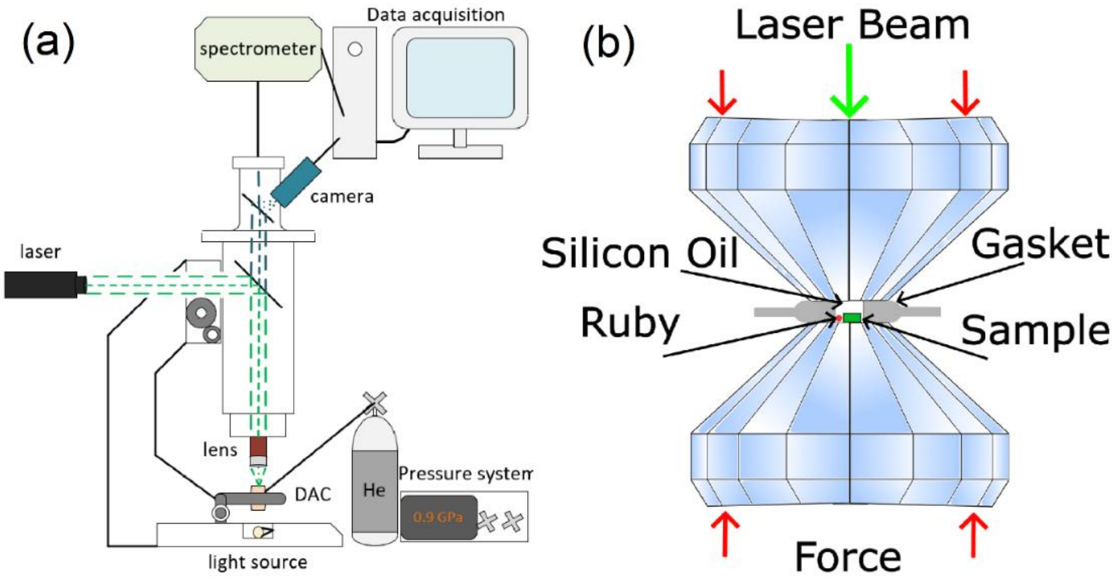

Figure S14. (a) Scheme of the system used for transmission measurements under hydrostatic pressure. (b) Cross-section of a diamond anvil cell.

X-ray diffractometer

To collect the diffraction patterns, we used a high-resolution X-ray diffractometer (Empyrean, PANalytical) equipped with a hybrid monochromator on the incident beam path and a Pixcel3D detector on the diffracted beam path. The measurements were performed using Cu Kα1 (1.540591 Å) emissions. The angular resolution of 2θ was 0.0002°. The diffraction patterns were collected after crystals alignment in the range from 6° to 65° 2θ.

Fourier transform infrared spectroscopy measurements

Fourier transform infrared (FTIR) spectra were obtained at room temperature using ATR-FTIR Thermo Scientific Nicolet iS10 spectrometer (ThermoFisher Scientific, USA), covering a spectral range of 4000-400 cm^{-1} with the spectrum resolution is 0.4 cm^{-1}

Raman spectroscopy measurements

Raman spectra of perovskites samples were collected using a DXR3xi Raman imaging microscope (Thermo Fisher Scientific Raman, USA) with a 532 nm excitation laser source at room temperature with a typical laser power of 1 mW, exposure time 280 Hz and 500 scans.

X-ray photoelectron spectroscopy measurements

XPS were performed using a magnesium Kα X-ray source (excitation energy output 1253.6 eV) with an impingement area of approximately 1mm in diameter. The experiments were performed at room temperature with a typical VG-ESCA vacuum chamber with a base pressure close to 10^{-10} mbar. XPS spectra were calibrated with reference to the Ag $3d_{5/2}$ peak position (centered at 368.10 eV) obtained from silver polycrystalline foil cleaned via a standard argon ion sputtering treatment. The authors also acknowledged Prof. Andrew T. S. Wee (National University of Singapore) to use the room-temperature XPS setup in the Surface Science Laboratory.

References:

[1] A. Dupas, K. Le Dang, J. -P. Renard, P. Veillet, A. Daoud, R. Perret, *The Journal of Chemical Physics* **1976**, *65*, 4099.
[2] X. Li, B. Li, J. Chang, B. Ding, S. Zheng, Y. Wu, J. Yang, G. Yang, X. Zhong, J. Wang, *ACS Appl. Energy Mater.* **2018**, *1*, 2709.
[3] A. Arramel, A. D. Fauzi, X. Yin, C. S. Tang, M. H. Mahyuddin, M. F. Sahdan, M. Aminah, D. Onggo, G. Shukri, C. Diao et al., Commun. Mater. 2021, 2, 1.
[4] Y. H. Kim, N. Hur, J. Korean Phys, Soc. 2020, 77, 1026.
[5] L. Septiany, G. R. Blake, J. Magn. Magn. Mater. 2022, 542, 168598
[6] A. Dupas, K. Le Dang, J. -P. Renard, P. Veillet, A. Daoud, R. Perret, J. Chem. Phys. 1976, 65, 4099.
[7] F. Fiorentino, M. D. Albaqami, I. Poli, A. Petrozza, ACS Appl. Mater. Interfaces 2022, 14, 34180.
[8] C. C. Stoumpos, D. H. Cao, D. J. Clark, J. Young, J. M. Rondinelli, J. I. Jang, J. T. Hupp, M. G. Kanatzidis, Chem. Mater. 2016, 28, 2852.
[9] C. Han, A. J. Bradford, A. M. Z. Slawin, B. E. Bode, E. Fusco, S. L. Lee, C. C. Tang, P. Lightfoot, Inorg. Chem. 2021, 60, 11014.
[10] L. Lanzetta, J. M. Marin-Beloqui, I. Sanchez-Molina, D. Ding, S. A. Haque, ACS Energy Lett. 2017, 2, 1662
[11] C. R. Kagan, D. B. Mitzi, C. D. Dimitrakopoulos, Science 1999, 286, 945.
[12] L. J. Diguna, S. Kaffah, M. H. Mahyuddin, Arramel, F. Maddalena, S. A. Bakar, M. Aminah, D. Onggo, M. E. Witkowski, M. Makowski, W. Drozdowski, M. D. Birowosuto, RSC Adv. 2021, 11, 20635.
[13] S. Hartati, T. Haposan, A. A. Afkauni, S. Anasha, N. S. Anwari, R. Marlina, M. Makowski, D. Kowal, L. Zhang, M. E. Witkowski, L. J. Diguna, M. H. Mahyuddin, W. Drozdowski, A. Arramel, M. D. Birowosuto, J. Mater. Chem. C 2025, https://doi.org/10.1039/D5TC01768H.
[14] S. Hartati, P. Y. D. Maulida, T. Zakly, I. Mulyani, D. Onggo, M. H. Mahyuddin, A. Noviyanto, A. Arramel, N. T. Rochman, Nano Hybrids Compos. 2023, 40, 1.
[15] P. Y. D. Maulida, S. Hartati, D. Kowal, L. J. Diguna, M. A. K. Sheikh, M. H. Mahyuddin, I. Mulyani, D. Onggo, F. Maddalena, A. Bachiri, M. E. Witkowski, M. Makowski, W. Drozdowski, N. Arramel, M. D. Birowosuto, ACS Appl. Energy Mater. 2023, https://doi.org/10.1021/acsaem.3c00340.
[16] H. Wang, Q. Wang, M. Ning, S. Li, R. Xue, P. Chen, Z. Li, RSC Adv. 2023, 13, 22886.
[17] X. Li, B. Li, J. Chang, B. Ding, S. Zheng, Y. Wu, J. Yang, G. Yang, X. Zhong, J. Wang, ACS Appl. Energy Mater. 2018, 1, 2709.
[18] D. Cortecchia, H. A. Dewi, J. Yin, A. Bruno, S. Chen, T. Baikie, P. P. Boix, M. Grätzel, S. Mhaisalkar, C. Soci, N. Mathews, Inorg. Chem. 2016, 55, 1044.

[19] K. Zulfa, B. Zahara, A. Akmal Afkauni, P. Yuniar Diah Maulida, S. Hartati, I. Mulyani, A. Yudhowijoyo, L. Jaya Diguna, M. Haris Mahyuddin, D. Onggo, M. Danang Birowosuto, Arramel, *Materials Today: Proceedings* **2024**.

[20] K. Kang, W. Niu, Y. Zhang, A. Li, X. Zou, W. Hu, *J. Phys. Chem. Lett.* **2023**, *14*, 347.

[21] A. Arramel, A. D. Fauzi, X. Yin, C. S. Tang, M. H. Mahyuddin, M. F. Sahdan, M. Aminah, D. Onggo, G. Shukri, C. Diao, H. Wang, M. D. Birowosuto, A. T. S. Wee, A. Rusydi, *Commun Mater* **2021**, *2*, 1.

[22] A. H. Arkenbout, *Organic-inorganic hybrids: a route towards soluble magnetic electronics*, s.n., Groningen, **2010**.

[23] D. Staško, J. Prchal, M. Klicpera, S. Aoki, K. Murata, *High Pressure Research* **2020**, *40*, 525.

[24] G. Shen, Y. Wang, A. Dewaele, C. Wu, D. E. Fratanduono, J. Eggert, S. Klotz, K. F. Dziubek, P. Loubeyre, O. V. Fat'yanov, P. D. Asimow, T. Mashimo, R. M. M. Wentzcovitch, *High Pressure Research* **2020**, *40*, 299.

Summary

The research presented in this dissertation provides a comprehensive map of the structural and electronic landscapes of lead-free 2D HOIPs under various temperature and hydrostatic pressure. By moving away from toxic Pb-based systems and toward Sn and Cu alternatives, we have demonstrated that "low-toxicity" does not come without compromising functional properties. On the contrary, these systems exhibit unique physics, specifically extreme electronic tunability, that surpasses their Pb-based counterparts.

Table 4.1: Comparison of pressure coefficients at 300 K (α_{300K}(P)) and temperature coefficients (α(T)) of the band gap energy for selected HOIPs.

Materials	α_{300K}(P)	α(T)	Ref.
	[meV/GPa]	[meV/K]	
$(4FP)_2SnI_4$	-160	-	Publication 1
$(4FPEA)_2SnBr_4$	-138	-	Publication 3
TMA_2SnI_4	-187	-	Publication 2
$(PMA)_2CuCl_4$	-53	1.42	Publication 4
$(PMA)_2CuBr_4$	-47	1.22	
$MHyPbI_4$	-63	-	[157]
$MAPbI_3$	-60	0.34	[143, 158]
MHy_2PbBr_4	-47	-	[103]
$MAPbBr_3$	-54	0.30	[159, 160]
$CsPbI_3$	-17	0.23	[161, 162]
$CsPbBr_3$	-11	0.25	[163, 164]
$MAPbCl_3$	-77	0.22	[165, 166]
$MA_{0.2}FA_{0.8}PbI_3$	-54	0.35	[166]
$MA_{0.4}FA_{0.6}PbI_3$	-55	0.25	
$MA_{0.6}FA_{0.4}PbI_3$	-58	0.20	
$MA_{0.8}FA_{0.2}PbI_3$	-46	0.27	
$MA_{0.9}Cs_{0.1}PbI_3$	-65	0.11	
$MA_{0.95}Cs_{0.05}PbI_3$	-65	0.13	
$MA_{0.13}EA_{0.87}PbBr_3$	-61	2.81	
$(PEA)_2PbBr_4$	50	0.80	[167, 168, 169]
$(PEA)_2PbI_4$	63	0.09	

4.1 Summary of Key Findings

- Record-Breaking Sensitivity

  We established that the "structural softness" of the Sn-I framework in TMA_2SnI_4 and $(4FP)_2SnI_4$ allows for the highest reported pressure-induced band gap tuning in the HOIPs family (-187 meV/GPa). This linear response across phase boundaries marks these materials as ideal candidates for the next generation of high-precision optical pressure sensors.

- Tunable Emission States in Low Temperature Regime

  Hydrostatic pressure and low temperature reveal emergence of additional emissive states in TMA_2SnI_4 likely due to polaronic excitons. A close energetic coupling between free excitons and localized excitons enables precise control over optical emission, suggesting avenues for white-light emission and excitonic devices. Pressure-induced LE splitting at cryogenic temperatures indicates the emergence of multiple excitonic channels, reflecting the interplay between lattice compression, exciton-phonon coupling, and polaron formation.

- Influence of Temperature versus Pressure in Lattice Mechanisms

  Thermal expansion of the material lattice versus mechanical compression, interact with the electron-phonon landscape in fundamentally different way.

- Exciton-Phonon Control

  We uncovered the delicate balance between delocalized free excitons and localized STEs. The discovery that pressure can simultaneously close the band gap (redshift) while stiffening the self-trapping potential (blueshift) provides a new way for controlling white-light emission and polaronic transport in 2D systems.

4.2 Concluding Perspective

The findings in this thesis open multiple avenues for both fundamental research and applied technologies:

- Direct Integration into Flexible Electronics:

  The extreme pressure- and strain-sensitivity of these 2D HOIPs suggests that mechanical, thermal, and optical stimuli could be combined to create multifunctional devices. Such platforms could enable advanced strain sensors, adaptive optics, photodetectors, and optoelectronic that operate under diverse conditions.

- Ultrafast Exciton and Polaron Dynamics

  While this work focuses on steady-state spectroscopy, the femtosecond scale dynamics of free and STE under external stimuli remain unexplored. Time-resolved studies could reveal mechanisms for exciton control and polaron transport, guiding the design of high-efficiency LEDs, scintillators.

- Beyond Hydrostatic Pressure

  Uniform hydrostatic compression provides a clean model system, but practical devices often experience uniaxial or anisotropic strain during thin-film growth, bending, or mechanical deformation. Investigating these conditions is crucial for enhancing device reliability, and optimizing performance under realistic operating conditions.

- Computational Discovery

  The high degree of agreement between our DFT models and experimental results suggests that machine learning and high-throughput DFT could be used to predict new organic-inorganic combinations with even higher stability or specific "target" pressure coefficients.

- Advanced Multi Experimental Techniques

  Future studies could expand the experimental toolkit by combining hydrostatic pressure with complementary techniques such as time-resolved photoluminescence, Raman spectroscopy, infrared and R measurements, and electrical transport characterization. Extending these experiments to low- and high-temperature regimes would allow detailed exploration of temperature-dependent exciton-phonon interactions, phase transitions, and polaron dynamics. Coupling pressure with additional external stimuli, such as electric fields, could further enable precise control over electronic and optical properties, advancing the development of multifunctional devices.

- Stability, Scalability, and Device Integration

  Future work should address the chemical and environmental stability of these materials under moisture, temperature cycling, and prolonged optical or mechanical stress. Ensuring scalable synthesis and integration into device architectures will be critical to translating these findings from laboratory demonstrations to commercial applications.

In conclusion, the transition to Pb-free 2D HOIPs is not merely a move toward environmental sustainability. It is entry into a playground of complex, tunable physics. By combining tunable structural softness with precise excitonic control and a roadmap for advanced experimental probing, this work provides a foundation for designing stimuli-responsive materials and devices. The insights gained here will guide both fundamental understanding and practical engineering of high-performance, flexible, and adaptive optoelectronics.

Bibliography

[1] Martin A. Green, Anita Ho-Baillie, and Henry J. Snaith. The emergence of perovskite solar cells. *Nature Photonics*, 8(7):506–514, 2014.

[2] Tze Chien Sum and Nripan Mathews. Advancements in perovskite solar cells: photophysics behind the photovoltaics. *Energy Environ. Sci.*, 7:2518–2534, 2014.

[3] Akihiro Kojima, Kenjiro Teshima, Yasuo Shirai, and Tsutomu Miyasaka. Organometal halide perovskites as visible-light sensitizers for photovoltaic cells. *Journal of the American Chemical Society*, 131(17):6050–6051, 2009.

[4] Wan-Jian Yin, Ji-Hui Yang, Joongoo Kang, Yanfa Yan, and Su-Huai Wei. Halide perovskite materials for solar cells: a theoretical review. *J. Mater. Chem. A*, 3:8926–8942, 2015.

[5] Hui-Seon Kim, Jin-Wook Lee, Natalia Yantara, Pablo P. Boix, Sneha A. Kulkarni, Subodh Mhaisalkar, Michael Grätzel, and Nam-Gyu Park. High efficiency solid-state sensitized solar cell-based on submicrometer rutile tio2 nanorod and ch3nh3pbi3 perovskite sensitizer. *Nano Letters*, 13(6):2412–2417, 2013.

[6] Lioz Etgar, Peng Gao, Zhaosheng Xue, Qin Peng, Aravind Kumar Chandiran, Bin Liu, Md. K. Nazeeruddin, and Michael Grätzel. Mesoscopic ch3nh3pbi3/tio2 heterojunction solar cells. *Journal of the American Chemical Society*, 134(42):17396–17399, 2012.

[7] Giovanni Vescio, Dmitry N. Dirin, Sergio González-Torres, Jesús Sanchez-Diaz, Rosario Vidal, Iván P. Franco, Samrat Das Adhikari, Vladimir S. Chirvony, Juan P. Martínez-Pastor, Felipe A. Vinocour Pacheco, Lukasz Przypis, Senol Öz, Sergi Hernández, Albert Cirera, Iván Mora-Seró, Maksym V. Kovalenko, and Blas Garrido. Inkjet-printed red-emitting flexible leds based on sustainable inks of layered tin iodide perovskite. *Advanced Sustainable Systems*, 8(9):2400060, 2024.

[8] Yanshen Zhu, Johan Buitenhuis, Beate Förster, Maria Rosaria Vetrano, and Erin Koos. Development of Perovskite Quantum Dots for Two-Dimensional Temperature Sensors. *ACS Applied Nano Materials*, 6(6):4661–4671, March 2023.

[9] Yuqin Liao, Hefei Liu, Wenjia Zhou, Dongwen Yang, Yuequn Shang, Zhifang Shi, Binghan Li, Xianyuan Jiang, Lijun Zhang, Li Na Quan, Rafael Quintero-Bermudez, Brandon R. Sutherland, Qixi Mi, Edward H. Sargent, and Zhijun Ning. Highly Oriented Low-Dimensional Tin Halide Perovskites with Enhanced Stability and Photovoltaic Performance. *Journal of the American Chemical Society*, 139(19):6693–6699, May 2017.

[10] Li Zhang, Changjiu Sun, Tingwei He, Yuanzhi Jiang, Junli Wei, Yanmin Huang, and Mingjian Yuan. High-performance quasi-2D perovskite light-emitting diodes: from materials to devices. *Light: Science & Applications*, 10(1):61, March 2021.

[11] Changjiu Sun, Yuanzhi Jiang, Minghuan Cui, Lu Qiao, Junli Wei, Yanmin Huang, Li Zhang, Tingwei He, Saisai Li, Hsien-Yi Hsu, Chaochao Qin, Run Long, and Mingjian Yuan. High-performance large-area quasi-2D perovskite light-emitting diodes. *Nature Communications*, 12(1):2207, April 2021.

[12] Xiao-Zhen Li, Yilong Ye, Yu Cao, Diwei Zhang, Yuan Lin, Jin Chang, Lin Zhu, Nana Wang, Wei Huang, and Jianpu Wang. Tin-halide perovskites for light-emitting diodes. *Chem. Soc. Rev.*, 54:6697–6725, 2025.

[13] E. Jokar, L. Cai, J. Han, E. J. C. Nacpil, and I. Jeon. Emerging opportunities in lead-free and lead-tin perovskites for environmentally viable photodetector applications. *Chemistry of Materials*, 35:3404–3426, 2023.

[14] Qi Jiang, Zema Chu, Pengyang Wang, Xiaolei Yang, Heng Liu, Ye Wang, Zhigang Yin, Jinliang Wu, Xingwang Zhang, and Jingbi You. Planar-structure perovskite solar cells with efficiency beyond 21%. *Advanced Materials*, 29(46):1703852, 2017.

[15] Jin Young Kim, Jin-Wook Lee, Hyun Suk Jung, Hyunjung Shin, and Nam-Gyu Park. High-efficiency perovskite solar cells. *Chemical Reviews*, 120(15):7867–7918, 2020.

[16] Hailin Zhang, Xu Ji, Haoyi Yao, Quanhai Fan, Bowen Yu, and Jishu Li. Review on efficiency improvement effort of perovskite solar cell. *Solar Energy*, 233:421–434, 2022.

[17] Wenhao Bai, Tongtong Xuan, Haiyan Zhao, Haorui Dong, Xinru Cheng, Le Wang, and Rong-Jun Xie. Perovskite light-emitting diodes with an external quantum efficiency exceeding 30%. *Advanced Materials*, 35(39):2302283, 2023.

[18] Azhar Fakharuddin, Mahesh K. Gangishetty, Mojtaba Abdi-Jalebi, Sang-Hyun Chin, Abd. Rashid bin Mohd Yusoff, Daniel N. Congreve, Wolfgang Tress, Felix Deschler, Maria Vasilopoulou, and Henk J. Bolink. Perovskite light-emitting diodes. *Nature Electronics*, 5(4):203–216, 2022.

[19] Chuangye Ge, Qianru Fang, Haoran Lin, and Hanlin Hu. Review on blue perovskite light-emitting diodes: Recent advances and future prospects. *Frontiers in Materials*, Volume 8 - 2021, 2021.

[20] Deepika Tyagi, Vijay Laxmi, Nilanjan Basu, Leelakrishna Reddy, Yibin Tian, Zhengbiao Ouyang, and Pramoda K. Nayak. Recent advances in two-dimensional perovskite materials for light-emitting diodes. *Discover Nano*, 19(1):109, 2024.

[21] Paramesh Chandra and Swapan K. Mandal. Bi-based perovskite materials for high-sensitivity gamma ray detection. *Materials Proceedings*, 26(1):13–0, 2025.

[22] Fang Yao, Kailian Dong, Weijun Ke, and Guojia Fang. Micro/nano perovskite materials for advanced x-ray detection and imaging. *ACS Nano*, 18(8):6095–6110, 2024.

[23] Seung Ju Kim, Hyeon-Ji Lee, Gi-Baek Nam, Ju-Young Kim, and Ho Won Jang. Halide perovskites for neuromorphic sensing and computing. *ACS Applied Materials & Interfaces*, 17(44):59951–59978, 2025.

[24] Siddharth Singh, Zeinab Hamid, Ramavath Babu, Sergio Gómez-Graña, Xiaowen Hu, Iain McCulloch, Robert L. Z. Hoye, Vishal Govind Rao, and Lakshminarayana Polavarapu. Halide perovskite photocatalysts for clean fuel production and organic synthesis: Opportunities and challenges. *Advanced Materials*, 37(28):2419603, 2025.

[25] Y. Li, Z. Qiu, J. L. Lai, Q. Xu, Y. Wu, C. Jiang, B. Li, Y. Li, and W. Li. The advanced application of halide perovskite materials for gas sensor. *International Journal of Nanomedicine*, 20:15415–15440, 2025.

[26] Laura M. Herz. Charge-carrier mobilities in metal halide perovskites: Fundamental mechanisms and limits. *ACS Energy Letters*, 2(7):1539–1548, 2017.

[27] Maria Ibáñez, Simon C. Boehme, Raffaella Buonsanti, Jonathan De Roo, Delia J. Milliron, Sandrine Ithurria, Andrey L. Rogach, Andreu Cabot, Maksym Yarema, Brandi M. Cossairt, Peter Reiss, Dmitri V. Talapin, Loredana Protesescu, Zeger Hens, Ivan Infante, Maryna I. Bodnarchuk, Xingchen Ye, Yuanyuan Wang, Hao Zhang, Emmanuel Lhuillier, Victor I. Klimov, Hendrik Utzat, Gabriele Rainò, Cherie R. Kagan, Matteo Cargnello, Jae Sung Son, and Maksym V. Kovalenko. Prospects of nanoscience with nanocrystals: 2025 edition. *ACS Nano*, 19(36):31969–32051, 2025.

[28] Aron Walsh, David O. Scanlon, Shiyou Chen, X. G. Gong, and Su-Huai Wei. Self-regulation mechanism for charged point defects in hybrid halide perovskites. *Angewandte Chemie International Edition*, 54(6):1791–1794, 2015.

[29] Samuel D. Stranks, Giles E. Eperon, Giulia Grancini, Christopher Menelaou, Marcelo J. P. Alcocer, Tomas Leijtens, Laura M. Herz, Annamaria Petrozza, and Henry J. Snaith. Electron-hole diffusion lengths exceeding 1 micrometer in an organometal trihalide perovskite absorber. *Science*, 342(6156):341–344, 2013.

[30] Alexander N. Beecher, Octavi E. Semonin, Jonathan M. Skelton, Jarvist M. Frost, Maxwell W. Terban, Haowei Zhai, Ahmet Alatas, Jonathan S. Owen, Aron Walsh, and Simon J. L. Billinge. Direct observation of dynamic symmetry breaking above room temperature in methylammonium lead iodide perovskite. *ACS Energy Letters*, 1(4):880–887, 2016.

[31] Christopher Eames, Jarvist M. Frost, Piers R. F. Barnes, Brian C. O'Regan, Aron Walsh, and M. Saiful Islam. Ionic transport in hybrid lead iodide perovskite solar cells. *Nature Communications*, 6(1):7497, 2015.

[32] Xinjiang Wang, Tianshu Li, Bangyu Xing, Muhammad Faizan, Koushik Biswas, and Lijun Zhang. Metal halide semiconductors beyond lead-based perovskites for promising optoelectronic applications. *The Journal of Physical Chemistry Letters*, 12(43):10532–10550, 2021.

[33] Matteo Pitaro, Eelco Kinsa Tekelenburg, Shuyan Shao, and Maria Antonietta Loi. Tin halide perovskites: From fundamental properties to solar cells. *Advanced Materials*, 34(1):2105844, 2022.

[34] Qianqian Fan, Gill V. Biesold-McGee, Jianzhong Ma, Qunna Xu, Shuang Pan, Juan Peng, and Zhiqun Lin. Lead-free halide perovskite nanocrystals: Crystal structures, synthesis, stabilities, and optical properties. *Angewandte Chemie International Edition*, 59(3):1030–1046, 2020.

[35] V. M. Goldschmidt. Die gesetze der krystallochemie. *Naturwissenschaften*, 14(21):477–485, 1926.

[36] Gregor Kieslich, Shijing Sun, and Anthony K. Cheetham. An extended tolerance factor approach for organic–inorganic perovskites. *Chem. Sci.*, 6:3430–3433, 2015.

[37] Na Wang, Shasha Zhang, Shiheng Wang, Xiaodong Yang, Fengmin Guo, Yiqiang Zhang, Zhenkun Gu, and Yanlin Song. Pressure engineering on perovskite structures, properties, and devices. *Advanced Functional Materials*, 34(27):2315918, 2024.

[38] Qian Li, Liming Zhang, Zhongwei Chen, and Zewei Quan. Metal halide perovskites under compression. *J. Mater. Chem. A*, 7:16089–16108, 2019.

[39] Mantas Simenas, Anna Gagor, Juras Banys, and Miroslaw Maczka. Phase transitions and dynamics in mixed three- and low-dimensional lead halide perovskites. *Chemical Reviews*, 124(5):2281–2326, 2024.

[40] Giovanni Mannino, Ioannis Deretzis, Emanuele Smecca, Antonino La Magna, Alessandra Alberti, Davide Ceratti, and David Cahen. Temperature-Dependent Optical Band Gap in CsPbBr3, MAPbBr3, and FAPbBr3 Single Crystals. *The Journal of Physical Chemistry Letters*, 11(7):2490–2496, April 2020.

[41] Alexander N. Beecher, Octavi E. Semonin, Jonathan M. Skelton, Jarvist M. Frost, Maxwell W. Terban, Haowei Zhai, Ahmet Alatas, Jonathan S. Owen, Aron Walsh, and Simon J. L. Billinge. Direct observation of dynamic symmetry breaking above room temperature in methylammonium lead iodide perovskite. *ACS Energy Letters*, 1(4):880–887, 2016.

[42] Paolo Umari, Edoardo Mosconi, and Filippo De Angelis. Relativistic gw calculations on ch3nh3pbi3 and ch3nh3sni3 perovskites for solar cell applications. *Scientific Reports*, 4(1):4467, 2014.

[43] Constantinos C. Stoumpos, Christos D. Malliakas, and Mercouri G. Kanatzidis. Semiconducting tin and lead iodide perovskites with organic cations: Phase transitions, high mobilities, and near-infrared photoluminescent properties. *Inorganic Chemistry*, 52(15):9019–9038, 2013.

[44] Jacky Even, Laurent Pedesseau, Jean-Marc Jancu, and Claudine Katan. Importance of spin–orbit coupling in hybrid organic/inorganic perovskites for photovoltaic applications. *The Journal of Physical Chemistry Letters*, 4(17):2999–3005, 2013.

[45] Marina R. Filip and Linn Leppert. Halide perovskites from first principles: from fundamental optoelectronic properties to the impact of structural and chemical heterogeneity. *Electronic Structure*, 6(3):033002, 2024. Published 22 July 2024 by IOP Publishing Ltd.

[46] Zhuangzhuang Ma, Lintao Wang, Xinzhen Ji, Xu Chen, and Zhifeng Shi. Lead-free metal halide perovskites and perovskite derivatives as an environmentally friendly emitter for light-emitting device applications. *The Journal of Physical Chemistry Letters*, 11(14):5517–5530, 2020.

[47] Junze Li, Haizhen Wang, and Dehui Li. Self-trapped excitons in two-dimensional perovskites. *Frontiers of Optoelectronics*, 13(3):225–234, 2020.

[48] Lingling Mao, Constantinos C. Stoumpos, and Mercouri G. Kanatzidis. Two-dimensional hybrid halide perovskites: Principles and promises. *Journal of the American Chemical Society*, 141(3):1171–1190, 2019.

[49] Nourdine Zibouche and M. Saiful Islam. Structure–electronic property relationships of 2d ruddlesden–popper tin- and lead-based iodide perovskites. *ACS Applied Materials & Interfaces*, 12(13):15328–15337, 2020.

[50] Yulin Liu, Songyang Yuan, Huiqun Zheng, Min Wu, Shiting Zhang, Jing Lan, Wenzhe Li, and Jiandong Fan. Structurally dimensional engineering in perovskite photovoltaics. *Advanced Energy Materials*, 13(23):2300188, 2023.

[51] Xin Li, Sikandar Aftab, Sajjad Hussain, Fahmid Kabir, A. M. A. Henaish, Abdullah G. Al-Sehemi, Mohan Reddy Pallavolu, and Ganesh Koyyada. Dimensional diversity (0d, 1d, 2d, and 3d) in perovskite solar cells: exploring the potential of mixed-dimensional integrations. *J. Mater. Chem. A*, 12:4421–4440, 2024.

[52] Abd. Rashid bin Mohd. Yusoff and Mohammad Khaja Nazeeruddin. Low-dimensional perovskites: From synthesis to stability in perovskite solar cells. *Advanced Energy Materials*, 8(26):1702073, 2018.

[53] Cheng Liu, Yi Yang, Hao Chen, Ioannis Spanopoulos, Abdulaziz S. R. Bati, Isaiah W. Gilley, Jianhua Chen, Aidan Maxwell, Badri Vishal, Robert P. Reynolds, Taylor E. Wiggins, Zaiwei Wang, Chuying Huang, Jared Fletcher, Yuan Liu, Lin X. Chen, Stefaan De Wolf, Bin Chen, Ding Zheng, Tobin J. Marks, Antonio Facchetti, Edward H. Sargent, and Mercouri G. Kanatzidis. Two-dimensional perovskitoids enhance stability in perovskite solar cells. *Nature*, 633(8029):359–364, 2024.

[54] Sung-Doo Baek, Seok Joo Yang, Hanjun Yang, Wenhao Shao, Yu-Ting Yang, and Letian Dou. Exciton dynamics in layered halide perovskite light-emitting diodes. *Advanced Materials*, 37(25):2411998, 2025.

[55] Gang Liu, Lingping Kong, Peijun Guo, Constantinos C. Stoumpos, Qingyang Hu, Zhenxian Liu, Zhonghou Cai, David J. Gosztola, Ho-kwang Mao, Mercouri G. Kanatzidis, and Richard D. Schaller. Two regimes of bandgap red shift and partial ambient retention in pressure-treated two-dimensional perovskites. *ACS Energy Letters*, 2(11):2518–2524, 2017.

[56] A. Jaffe, Y. Lin, and H. I. Karunadasa. Halide perovskites under pressure: Accessing new properties through lattice compression. *ACS Energy Letters*, 2:1549–1555, 2017.

[57] B. Zou, Y. Han, Z. Yang, Q. Wang, G. Wang, G. Zhang, Y. Li, and C. Liu. Pressure-induced emission enhancement: A review. *APL Materials*, 12:030601, 2024.

[58] J. Sanchez-Diaz, J. Rodriguez-Pereira, S. Das Adhikari, and I. Mora-Sero. Synthesis of hybrid tin-based perovskite microcrystals for led applications. *Advanced Science*, 11:2403835, 2024.

[59] W. Żuraw, D. Kubicki, R. Kudrawiec, and Ł. Przypis. Carboxylic acid-assisted synthesis of tin(ii) iodide: Key for stable large-area lead-free perovskite solar cells. *ACS Energy Letters*, 9:2509–4515, 2024.

[60] Chenjian Lin, Yuanhao Tang, Zhichen Nian, Aidan H. Coffey, Yunfei Wang, Hanjun Yang, Pengfei Wu, Yu-Ting Yang, Syed Joy, Kenneth R. Graham, Wenzhan Xu, Chenhui Zhu, Brett M. Savoie, and Letian Dou. Intralayer bidentate diammoniums for stable two-dimensional perovskites. *Nature Chemistry*, 18(2):275–282, 2026.

[61] Yani Chen, Yong Sun, Jiajun Peng, Junhui Tang, Kaibo Zheng, and Ziqi Liang. 2d ruddlesden–popper perovskites for optoelectronics. *Advanced Materials*, 30(2):1703487, 2018.

[62] Hsinhan Tsai, Wanyi Nie, Jean-Christophe Blancon, Constantinos C. Stoumpos, Reza Asadpour, Boris Harutyunyan, Amanda J. Neukirch, Rafael Verduzco, Jared J. Crochet, Sergei Tretiak, Laurent Pedesseau, Jacky Even, Muhammad A. Alam, Gautam Gupta, Jun Lou, Pulickel M. Ajayan, Michael J. Bedzyk, and Mercouri G. Kanatzidis. High-efficiency two-dimensional Ruddlesden-Popper perovskite solar cells. *Nature*, 536(7616):312–316, August 2016.

[63] Mirosław Mączka, Szymon Sobczak, Kinga Roszak, Daniel Linhares Militão Vasconcelos, Filip Dybała, Artur P. Herman, Robert Kudrawiec, Andrzej Katrusiak, and Paulo T. C. Freire. Pressure-induced detrapping from self-trapped excitons to free excitons toward enhanced emission and piezochromism in ruddlesden–popper (110)-oriented perovskites. *ACS Applied Materials & Interfaces*, 17(42):58452–58466, 2025.

[64] Rafał Bartoszewicz, Jakub Ziembicki, Ewelina Zdanowicz, Artur P. Herman, Jarosław Serafińczuk, Jesús Sánchez-Diaz, Samrat Das Adhikari, Iván Mora-Seró, and Robert Kudrawiec. Giant band gap narrowing under hydrostatic pressure in (4fp)2sni4 halide perovskite. *The Journal of Physical Chemistry Letters*, 16(25):6372–6377, 2025.

[65] Kameron R. Hansen, C. Emma McClure, Daniel Powell, Hao-Chieh Hsieh, Laura Flannery, Kelsey Garden, Edwin J. Miller, Daniel J. King, Sami Sainio, Dennis Nordlund, John S. Colton, and Luisa Whittaker-Brooks. Low exciton binding energies and localized exciton–polaron states in 2d tin halide perovskites. *Advanced Optical Materials*, 10(9):2102698, 2022.

[66] Wenguang Li, Tianci Mi, Tian Tian, Meifang Yang, and Huan Pang. Mitigating lead toxicity in halide perovskite solar cells: Strategies for sustainable development. *Inorganics*, 13(4), 2025.

[67] Aslihan Babayigit, Dinh Duy Thanh, Anitha Ethirajan, Jean Manca, Marc Muller, Hans-Gerd Boyen, and Bert Conings. Assessing the toxicity of pb- and sn-based perovskite solar cells in model organism danio rerio. *Scientific Reports*, 6(1):18721, 2016.

[68] Christa E. Torrence, Cara S. Libby, Wanyi Nie, and Joshua S. Stein. Environmental and health risks of perovskite solar modules: Case for better test standards and risk mitigation solutions. *iScience*, 26(1), 2023.

[69] Efat Jokar, Liang Cai, Jiye Han, Edric John Cruz Nacpil, and Il Jeon. Emerging opportunities in lead-free and lead–tin perovskites for environmentally viable photodetector applications. *Chemistry of Materials*, 35(9):3404–3426, 2023.

[70] Cesur Altinkaya, Erkan Aydin, Esma Ugur, Furkan H. Isikgor, Anand S. Subbiah, Michele De Bastiani, Jiang Liu, Aslihan Babayigit, Thomas G. Allen, Frédéric Laquai, Abdullah Yildiz, and Stefaan De Wolf. Tin oxide electron-selective layers for efficient, stable, and scalable perovskite solar cells. *Advanced Materials*, 33(15):2005504, 2021.

[71] Lingping Kong, Jue Gong, Ioannis Spanopoulos, Shuai Yan, Zhongyang Li, Zhikai Zhu, Xingyi Liu, Yinning Zhu, Hongliang Dong, Haiyun Shu, Qingyang Hu, Wenge Yang, Ho-kwang Mao, Mercouri G. Kanatzidis, and Gang Liu. Revealing the universal pressure-driven behavior of hybrid halide perovskites and unique optical modifiability in extremely soft 2d tin-based system. *Advanced Functional Materials*, 34(46):2414437, 2024.

[72] Jia Zhang, Ting Wu, Jiashun Duan, Mahshid Ahmadi, Fangyuan Jiang, Yinhua Zhou, and Bin Hu. Exploring spin-orbital coupling effects on photovoltaic actions in sn and pb based perovskite solar cells. *Nano Energy*, 38:297–303, 2017.

[73] Anna Amat, Edoardo Mosconi, Enrico Ronca, Claudio Quarti, Paolo Umari, Md. K. Nazeeruddin, Michael Grätzel, and Filippo De Angelis. Cation-induced bandgap tuning in organohalide perovskites: Interplay of spin–orbit coupling and octahedra tilting. *Nano Letters*, 14(6):3608–3616, 2014.

[74] Weihai Zhang, Yating Cai, Heng Liu, Yu Xia, Jieshun Cui, Yueqing Shi, Rui Chen, Tingting Shi, and Hsing-Lin Wang. Organic-free and lead-free perovskite solar cells with efficiency over 11%. *Advanced Energy Materials*, 12(42):2202491, 2022.

[75] Joshua Leveillee, George Volonakis, and Feliciano Giustino. Phonon-limited mobility and electron–phonon coupling in lead-free halide double perovskites. *The Journal of Physical Chemistry Letters*, 12(18):4474–4482, 2021.

[76] Long Zhang, Yuanyuan Fang, Laizhi Sui, Jiejuan Yan, Kai Wang, Kaijun Yuan, Wendy L. Mao, and Bo Zou. Tuning emission and electron–phonon coupling in lead-free halide double perovskite cs2agbicl6 under pressure. *ACS Energy Letters*, 4(12):2975–2982, 2019.

[77] Yasuhiro Yamada and Yoshihiko Kanemitsu. Electron-phonon interactions in halide perovskites. *NPG Asia Materials*, 14(1):48, 2022.

[78] Weijun Ke, Constantinos C. Stoumpos, and Mercouri G. Kanatzidis. "unleaded" perovskites: Status quo and future prospects of tin-based perovskite solar cells. *Advanced Materials*, 31(47):1803230, 2019.

[79] He Zhu, Junjie Ma, Pengwei Li, Shuangquan Zang, Yiqiang Zhang, and Yanlin Song. Low-dimensional sn-based perovskites: Evolution and future prospects of solar cells. *Chem*, 8(11):2939–2960, 2022.

[80] Towhid H. Chowdhury, Youjin Reo, Abd Rashid Bin Mohd Yusoff, and Yong-Young Noh. Sn-based perovskite halides for electronic devices. *Advanced Science*, 9(33):2203749, 2022.

[81] Suvankar Sen, Saianand Gopalan, Raja Sellappan, Andrews Nirmala Grace, and Prashant Sonar. Tin-based eco-friendly perovskites for sustainable future. *Advanced Energy and Sustainability Research*, 4(12):2300110, 2023.

[82] Intissar Hamdi, Yeasin Khan, Fatma Aouaini, Jung Hwa Seo, Hyun-Joo Koo, Mark M. Turnbull, Bright Walker, and Houcine Naïli. A copper-based 2d hybrid perovskite solar absorber as a potential eco-friendly alternative to lead halide perovskites. *J. Mater. Chem. C*, 10:3738–3745, 2022.

[83] Khursheed Ahmad and Shaikh M. Mobin. Organic–inorganic copper (ii)-based perovskites: A benign approach toward low-toxicity and water-stable light absorbers for photovoltaic applications. *Energy Technology*, 8(3):1901185, 2020.

[84] Xiaolei Li, Xiangli Zhong, Yue Hu, Bochao Li, Yusong Sheng, Yang Zhang, Chao Weng, Ming Feng, Hongwei Han, and Jinbin Wang. Organic–inorganic copper(ii)-based material: A low-toxic, highly stable light absorber for photovoltaic application. *The Journal of Physical Chemistry Letters*, 8(8):1804–1809, 2017.

[85] Tao Zhu, Yongrui Yang, and Xiong Gong. Recent advancements and challenges for low-toxicity perovskite materials. *ACS Applied Materials & Interfaces*, 12(24):26776–26811, 2020.

[86] A.S. Verma and A. Kumar. Bulk modulus of cubic perovskites. *Journal of Alloys and Compounds*, 541:210–214, 2012.

[87] V. Klinger, T. Roesener, G. Lorenz, M. Petzold, and F. Dimroth. Determination of hardness and young's modulus for important iii–v compound semiconductors. *Thin Solid Films*, 548:358–365, 2013.

[88] V. Kumar, A.K. Shrivastava, and Vijeta Jha. Bulk modulus and microhardness of tetrahedral semiconductors. *Journal of Physics and Chemistry of Solids*, 71(11):1513–1520, 2010.

[89] A. F. Wright. Elastic properties of zinc-blende and wurtzite aln, gan, and inn. *Journal of Applied Physics*, 82(6):2833–2839, 09 1997.

[90] I. Vurgaftman, J. R. Meyer, and L. R. Ram-Mohan. Band parameters for iii–v compound semiconductors and their alloys. *Journal of Applied Physics*, 89(11):5815–5875, 06 2001.

[91] Riccardo Comin, Michael K. Crawford, Ayman H. Said, Norman Herron, William E. Guise, Xiaoping Wang, Pamela S. Whitfield, Ankit Jain, Xiwen Gong, Alan J. H. McGaughey, and Edward H. Sargent. Lattice dynamics and the nature of structural transitions in organolead halide perovskites. *Phys. Rev. B*, 94:094301, Sep 2016.

[92] Ying Han, Xiaohua Cheng, and Bin-Bin Cui. Factors influencing self-trapped exciton emission of low-dimensional metal halides. *Mater. Adv.*, 4:355–373, 2023.

[93] Zeeshan Muhammad and Arooj Rashid. Exciton binding energies and polaron interplay in the optically excited state of organic–inorganic lead halide perovskites. *Mater. Adv.*, 6:13–38, 2025.

[94] Daniel B. Straus and Cherie R. Kagan. Electrons, excitons, and phonons in two-dimensional hybrid perovskites: Connecting structural, optical, and electronic properties. *The Journal of Physical Chemistry Letters*, 9(6):1434–1447, 2018.

[95] Shuai Wang, Jiaqi Ma, Wancai Li, Jun Wang, Haizhen Wang, Hongzhi Shen, Junze Li, Jiaqi Wang, Hongmei Luo, and Dehui Li. Temperature-dependent band gap in two-dimensional perovskites: Thermal expansion interaction and electron–phonon interaction. *The Journal of Physical Chemistry Letters*, 10(10):2546–2553, 2019.

[96] Kewei Wu, Ashok Bera, Chun Ma, Yuanmin Du, Yang Yang, Liang Li, and Tom Wu. Temperature-dependent excitonic photoluminescence of hybrid organometal halide perovskite films. *Phys. Chem. Chem. Phys.*, 16:22476–22481, 2014.

[97] Fang Pan, Jinrui Li, Xiaoman Ma, Yang Nie, Beichen Liu, and Honggang Ye. Free and self-trapped exciton emission in perovskite cspbbr$_3$ microcrystals. *RSC Adv.*, 12:1035–1042, 2022.

[98] Justas Deveikis, Marcin Giza, David Walker, Jie Liu, Claire Wilson, Nathaniel P. Gallop, Pablo Docampo, James Lloyd-Hughes, and Rebecca L. Milot. Temperature-dependent structural and optoelectronic properties of the layered perovskite 2-thiophenemethylammonium lead iodide. *The Journal of Physical Chemistry C*, 128(31):13108–13120, 2024.

[99] Y.P. Varshni. Temperature dependence of the energy gap in semiconductors. *Physica*, 34(1):149–154, 1967.

[100] J. Bhosale, A. K. Ramdas, A. Burger, A. Muñoz, A. H. Romero, M. Cardona, R. Lauck, and R. K. Kremer. Temperature dependence of band gaps in semiconductors: Electron-phonon interaction. *Phys. Rev. B*, 86:195208, Nov 2012.

[101] Yongjae Lee, David B. Mitzi, Paris W. Barnes, and Thomas Vogt. Pressure-induced phase transitions and templating effect in three-dimensional organic-inorganic hybrid perovskites. *Phys. Rev. B*, 68:020103, Jul 2003.

[102] Mirosław Mączka, Szymon Smółka, Dagmara Stefańska, Anna Gągor, Jan K. Zaręba, Katarzyna Fedoruk-Piskorska, Maciej Ptak, Dawid Drozdowski, and Adam Sieradzki. Multinoncentrosymmetric two-dimensional trilayered lead bromide perovskites with methylhydrazinium cations: Lattice dynamics, phase transitions, dielectric response, and optical properties. *Chemistry of Materials*, 36(17):8286–8299, 2024.

[103] Mirosław Mączka, Szymon Sobczak, Paulina Ratajczyk, Fabio Furtado Leite, Waldeci Paraguassu, Filip Dybała, Artur P. Herman, Robert Kudrawiec, and Andrzej Katrusiak. Pressure-driven phase transition in two-dimensional perovskite mhy2pbbr4. *Chemistry of Materials*, 34(17):7867–7877, 2022.

[104] Agnieszka Noculak, Simon C. Boehme, Marcel Aebli, Yevhen Shynkarenko, Kyle M. McCall, and Maksym V. Kovalenko. Pressure-induced perovskite-to-non-perovskite phase transition in cspbbr3. *Helvetica Chimica Acta*, 104(2):e2000222, 2021.

[105] Bin Xu, Yawen Li, Peibin Hong, Peijie Zhang, Jiang Han, Zewen Xiao, and Zewei Quan. Pressure-controlled free exciton and self-trapped exciton emission in quasi-one-dimensional hybrid lead bromides. *Nature Communications*, 15(1):7403, 2024.

[106] Rafał Bartoszewicz, Jan-Albert Zienkiewicz, Sri Hartati, Arramel Arramel, Jan Kopaczek, Muhammad Danang Birowosuto, and Robert Kudrawiec. Thermochromism versus piezochromism in (pma)2cux4 (x = br, cl) halide perovskites. *J. Mater. Chem. C*, 13:16929–16936, 2025.

[107] Agnieszka Pieniażek, Filip Dybała, Maciej P. Polak, Łukasz Przypis, Artur P. Herman, Jan Kopaczek, and Robert Kudrawiec. Bandgap pressure coefficient of a ch3nh3pbi3 thin film perovskite. *The Journal of Physical Chemistry Letters*, 14(28):6470–6476, 2023.

[108] R. J. Angel, J. Zhao, and N. L. Ross. General rules for predicting phase transitions in perovskites due to octahedral tilting. *Phys. Rev. Lett.*, 95:025503, Jul 2005.

[109] Feng Ke, Chenxu Wang, Chunjing Jia, Nathan R. Wolf, Jiejuan Yan, Shanyuan Niu, Thomas P. Devereaux, Hemamala I. Karunadasa, Wendy L. Mao, and Yu Lin. Preserving a robust cspbi3 perovskite phase via pressure-directed octahedral tilt. *Nature Communications*, 12(1):461, 2021.

[110] H. J. Xiang, Mael Guennou, Jorge Íñiguez, Jens Kreisel, and L. Bellaiche. Rules and mechanisms governing octahedral tilts in perovskites under pressure. *Phys. Rev. B*, 96:054102, Aug 2017.

[111] Yonggang Wang, Xujie Lü, Wenge Yang, Ting Wen, Liuxiang Yang, Xiangting Ren, Lin Wang, Zheshuai Lin, and Yusheng Zhao. Pressure-induced phase transformation, reversible amorphization, and anomalous visible light response in organolead bromide perovskite. *Journal of the American Chemical Society*, 137(34):11144–11149, 2015.

[112] Akun Liang, Robin Turnbull, Catalin Popescu, Ismael Fernandez-Guillen, Rafael Abargues, Pablo P. Boix, and Daniel Errandonea. Pressure-induced phase transition versus amorphization in hybrid methylammonium lead bromide perovskite. *The Journal of Physical Chemistry C*, 127(26):12821–12826, 2023.

[113] Marek Szafrański and Andrzej Katrusiak. Mechanism of pressure-induced phase transitions, amorphization, and absorption-edge shift in photovoltaic methylammonium lead iodide. *The Journal of Physical Chemistry Letters*, 7(17):3458–3466, 2016.

[114] Yongfu Liang, Yuping Yang, Hui Xie, Xuerui Cheng, Xiang Zhu, Chaosheng Yuan, Zheng Wang, Haining Li, and Kun Yang. Pressure-induced abnormal blue-shift emission enhancement and phase transition of perovskite dmapbi3. *Journal of Molecular Structure*, 1321:139787, 2025.

[115] Long Zhang, Qingxin Zeng, and Kai Wang. Pressure-induced structural and optical properties of inorganic halide perovskite cspbbr3. *The Journal of Physical Chemistry Letters*, 8(16):3752–3758, 2017.

[116] Ao Chen, Xiaoling Jing, Tianyuan Wang, Tingting Zhao, Yu Zhang, Donglei Zhou, Rui Sun, Xueting Zhang, Ran Liu, Bo Liu, Quanjun Li, and Bingbing Liu. Pressure-driven abnormal emission blue-shift of lead-free halide double perovskite cs2agincl6 nanocrystals. *Inorganic Chemistry*, 61(17):6488–6492, 2022.

[117] David Carrasco-Busturia, Inés Sánchez-Movellán, Alexander Sougaard Tygesen, Arghya Bhowmik, Juan María García-Lastra, José Antonio Aramburu, and Miguel Moreno. Red shift in optical excitations on layered copper perovskites under pressure: Role of the orthorhombic instability. *Chemistry – A European Journal*, 29(5):e202202933, 2023.

[118] Xiaoling Jing, Rui Sun, Hui Tian, Ran Liu, Bo Liu, Donglei Zhou, Quanjun Li, and Bingbing Liu. Evolution of self-trapped exciton emission tuned by high pressure in 2d all-inorganic cesium lead halide nanosheets. *J. Mater. Chem. C*, 10:8711–8718, 2022.

[119] Bin Xu, Yawen Li, Peibin Hong, Peijie Zhang, Jiang Han, Zewen Xiao, and Zewei Quan. Pressure-controlled free exciton and self-trapped exciton emission in quasi-one-dimensional hybrid lead bromides. *Nature Communications*, 15(1):7403, 2024.

[120] Qinghe Li, Masakazu Anpo, Jinmao You, Tingjiang Yan, and Xinchen Wang. *Photoluminescence (PL) Spectroscopy*, pages 295–321. Springer International Publishing, Cham, 2023.

[121] Brian M. Tissue. *Ultraviolet and Visible Absorption Spectroscopy.* John Wiley Sons, Ltd, 2002.

[122] Weiwei Zhang, Gang Tang, M. P. K. Sahoo, Yunting Liang, and Yajun Zhang. Unified picture for the pressure-controlled band gap in inorganic halide perovskites: Role of strain-phonon and phonon-phonon couplings. *Phys. Rev. B*, 105:075150, Feb 2022.

[123] Zhiwei Ma, Zhun Liu, Siyu Lu, Lingrui Wang, Xiaolei Feng, Dongwen Yang, Kai Wang, Guanjun Xiao, Lijun Zhang, Simon A. T. Redfern, and Bo Zou. Pressure-induced emission of cesium lead halide perovskite nanocrystals. *Nature Communications*, 9(1):4506, 2018.

[124] Chih-Wei Wang, Ebube E. Oyeka, Alison B. Altman, and Dong Hee Son. Effects of pressure on exciton absorption and emission in strongly quantum-confined cspbbr3 quantum dots and nanoplatelets. *The Journal of Physical Chemistry C*, 128(5):2062–2069, 2024.

[125] Filip Dybała, Robert Kudrawiec, Maciej P. Polak, Artur P. Herman, Adam Sieradzki, and Mirosław Mączka. Near-bandgap emission in [hoc2h4nh3]2pbi4 perovskite under hydrostatic pressure: emission of a free exciton and a polaronic exciton. *Mater. Adv.*, 6:569–578, 2025.

[126] Agnieszka Pieniążek, Filip Dybała, ukasz Przypis, Maciej P. Polak, Małgorzata Norek, Bogdan J. Kowalski, and Robert Kudrawiec. Beyond the cubic phase: Pressure-induced bandgap modulation in a ch3nh3pbbr3 perovskite at low temperatures. *Advanced Optical Materials*, 14(5):e03177, 2026.

[127] Xihan Yu, Yuanyuan Fang, Xuening Sun, Ying Xie, Cailong Liu, Kai Wang, Guanjun Xiao, and Bo Zou. Pressure-tuning localized excitons toward enhanced emission, photocurrent enhancement and piezochromism in unconventional aci-type 2d hybrid perovskites. *Angewandte Chemie International Edition*, 63(46):e202412756, 2024.

[128] Wenya Zhao, Guanjun Xiao, and Bo Zou. Pressure-induced emission (PIE) in halide perovskites toward promising applications in scintillators and solid-state lighting. *Aggregate*, 5(1):e461, 2024.

[129] Xue-Zhou Zhao, Fei-Fei Gao, Wei Li, Zhi-Gang Li, Ying Zhang, Kai Li, Huan Hu, Weizhao Cai, Jijie Zhang, and Xian-He Bu. Pressure enables high-standard white light emission and significant emission enhancement in a 2D halide perovskite. *Journal of Materials Chemistry C*, 12(13):4599–4605, March 2024.

[130] Han Li, Daniel Wines, Bin Chen, Kentaro Yumigeta, Yasir Mohammed Sayyad, Jan Kopaszek, Sui Yang, Can Ataca, Edward H. Sargent, and Sefaattin Tongay. Abnormal Phase Transition and Band Renormalization of Guanidinium-Based Organic–Inorganic Hybrid Perovskite. *ACS Applied Materials & Interfaces*, 13(37):44964–44971, September 2021.

[131] J. Bhosale, A. K. Ramdas, A. Burger, A. Muñoz, A. H. Romero, M. Cardona, R. Lauck, and R. K. Kremer. Temperature dependence of band gaps in semiconductors: Electron-phonon interaction. *Phys. Rev. B*, 86:195208, Nov 2012.

[132] Shaojie Jiang, Yiliang Luan, Joon I. Jang, Tom Baikie, Xin Huang, Ruipeng Li, Felix O. Saouma, Zhongwu Wang, Timothy J. White, and Jiye Fang. Phase transitions of formamidinium lead iodide perovskite under pressure. *Journal of the American Chemical Society*, 140(42):13952–13957, 2018.

[133] Akun Liang, Javier Gonzalez-Platas, Robin Turnbull, Catalin Popescu, Ismael Fernandez-Guillen, Rafael Abargues, Pablo P. Boix, Lan-Ting Shi, and Daniel Errandonea. Reassigning the pressure-induced phase transitions of methylammonium lead bromide perovskite. *Journal of the American Chemical Society*, 144(43):20099–20108, 2022.

[134] Xiangting Ren, Xiaozhi Yan, Azkar Saeed Ahmad, Hu Cheng, Yanchun Li, Yusheng Zhao, Lin Wang, and Shanmin Wang. Pressure-induced phase transition and band gap engineering in propylammonium lead bromide perovskite. *The Journal of Physical Chemistry C*, 123(24):15204–15208, 2019.

[135] Md. Sajib Hossain, Md. Majibul Haque Babu, Tusar Saha, Md. Sazzad Hossain, Jiban Podder, Md. Shohel Rana, Abdul Barik, and Protima Rani. Pressure induced semiconductor to metal phase transition in cubic cssnbr3 perovskite. *AIP Advances*, 11(5):055024, 05 2021.

[136] Jung-Hoon Lee, Adam Jaffe, Yu Lin, Hemamala I. Karunadasa, and Jeffrey B. Neaton. Origins of the pressure-induced phase transition and metallization in the halide perovskite (ch3nh3)pbi3. *ACS Energy Letters*, 5(7):2174–2181, 2020.

[137] Marek Szafrański, Andrzej Katrusiak, and Kenny Ståhl. Time-dependent transformation routes of perovskites cspbbr3 and cspbcl3 under high pressure. *J. Mater. Chem. A*, 9:10769–10779, 2021.

[138] Long Zhang, Yuanyuan Fang, Laizhi Sui, Jiejuan Yan, Kai Wang, Kaijun Yuan, Wendy L. Mao, and Bo Zou. Tuning emission and electron–phonon coupling in lead-free halide double perovskite cs2agbicl6 under pressure. *ACS Energy Letters*, 4(12):2975–2982, 2019.

[139] Xujie Lü, Yonggang Wang, Constantinos C. Stoumpos, Qingyang Hu, Xiaofeng Guo, Haijie Chen, Liuxiang Yang, Jesse S. Smith, Wenge Yang, Yusheng Zhao, Hongwu Xu, Mercouri G. Kanatzidis, and Quanxi Jia. Enhanced structural stability and photo responsiveness of ch3nh3sni3 perovskite via pressure-induced amorphization and recrystallization. *Advanced Materials*, 28(39):8663–8668, 2016.

[140] Junsheng Luo, Jianxing Xia, Hua Yang, Chunlin Sun, Ning Li, Haseeb Ashraf Malik, Hongyu Shu, Zhongquan Wan, Haoli Zhang, Christoph J. Brabec, and Chunyang Jia. A pressure process for efficient and stable perovskite solar cells. *Nano Energy*, 77:105063, 2020.

[141] Xinhui Zhan, Xiaomei Jiang, Pin Lv, Jie Xu, Fengjiao Li, Zhaolai Chen, and Xiaobing Liu. Enhanced structural stability and pressure-induced photoconductivity in two-dimensional hybrid perovskite (c6h5ch2nh3)2cubr4. *Angewandte Chemie International Edition*, 61(28):e202205491, 2022.

[142] Kiyoshi Fujino, Daisuke Nishio-Hamane, Keisuke Suzuki, Hiroyuki Izumi, Yusuke Seto, and Takaya Nagai. Stability of the perovskite structure and possibility of the transition to the post-perovskite structure in casio3, fesio3, mnsio3 and cosio3. *Physics of the Earth and Planetary Interiors*, 177(3):147–151, 2009.

[143] Adrián Francisco-López, Bethan Charles, Oliver J. Weber, M. Isabel Alonso, Miquel Garriga, Mariano Campoy-Quiles, Mark T. Weller, and Alejandro R. Goñi. Pressure-induced locking of methylammonium cations versus amorphization in hybrid lead iodide perovskites. *The Journal of Physical Chemistry C*, 122(38):22073–22082, 2018.

[144] R. Letoullec, J. P. Pinceaux, and P. Loubeyre. The membrane diamond anvil cell. *High Pressure Research*, 5(1-6):871–873, 1990.

[145] Keizo Murata, Keiichi Yokogawa, Harukazu Yoshino, Stefan Klotz, Pascal Munsch, Akinori Irizawa, Mototsugu Nishiyama, Kenzo Iizuka, Takao Nanba, Tahei Okada, Yoshitaka Shiraga, and Shoji Aoyama. Pressure transmitting medium daphne 7474 solidifying at 3.7 gpa at room temperature. *Review of Scientific Instruments*, 79(8):085101, 08 2008.

[146] D. Staško, J. Prchal, M. Klicpera, S. Aoki, and K. Murata. Pressure media for high pressure experiments, daphne oil 7000 series. *High Pressure Research*, 40(4):525–536, 2020.

[147] S Klotz, J-C Chervin, P Munsch, and G Le Marchand. Hydrostatic limits of 11 pressure transmitting media. *Journal of Physics D: Applied Physics*, 42(7):075413, mar 2009.

[148] D. Staško, J. Prchal, M. Klicpera, S. Aoki, and K. Murata. Pressure media for high pressure experiments, daphne oil 7000 series. *High Pressure Research*, 40(4):525–536, 2020.

[149] Naoyuki Tateiwa and Yoshinori Haga. Appropriate pressure-transmitting media for cryogenic experiment in the diamond anvil cell up to 10 gpa. 215:012178, 2010.

[150] Y. Nakamura, A. Takimoto, and M. Matsui. Rheology and nonhydrostatic pressure evaluation of solidified oils including daphne oils by observing microsphere deformation, 2010.

[151] Tuson Park, Eunsung Park, Hanoh Lee, T Klimczuk, E D Bauer, F Ronning, and J D Thompson. Pressure-induced superconductivity in cafe2as2. *Journal of Physics: Condensed Matter*, 20(32):322204, jul 2008.

[152] W. Yu, A. A. Aczel, T. J. Williams, S. L. Bud'ko, N. Ni, P. C. Canfield, and G. M. Luke. Absence of superconductivity in single-phase cafe$_2$as$_2$ under hydrostatic pressure. *Phys. Rev. B*, 79:020511, Jan 2009.

[153] Junbo Gong, Hongxia Zhong, Chan Gao, Jiali Peng, Xinxing Liu, Qianqian Lin, Guojia Fang, Shengjun Yuan, Zengming Zhang, and Xudong Xiao. Pressure-induced indirect-direct bandgap transition of cspbbr3 single crystal and its effect on photoluminescence quantum yield. *Advanced Science*, 9(29):2201554, 2022.

[154] Xujie Lü, Wenge Yang, Quanxi Jia, and Hongwu Xu. Pressure-induced dramatic changes in organic–inorganic halide perovskites. *Chem. Sci.*, 8:6764–6776, 2017.

[155] Guoyin Shen, Yanbin Wang, Agnes Dewaele, Christine Wu, Dayne E. Fratanduono, Jon Eggert, Stefan Klotz, Kamil F. Dziubek, Paul Loubeyre, Oleg V. Fat'yanov,

Paul D. Asimow, Tsutomu Mashimo, and Renata M. M. Wentzcovitch and. Toward an international practical pressure scale: A proposal for an ipps ruby gauge (ipps-ruby2020). *High Pressure Research*, 40(3):299–314, 2020.

[156] F. Datchi, A. Dewaele, P. Loubeyre, R. Letoullec, Y. Le Godec, and B. Canny. Optical pressure sensors for high-pressure–high-temperature studies in a diamond anvil cell. *High Pressure Research*, 27(4):447–463, 2007.

[157] Szymon Sobczak, Andrzej Nowok, Jan K. Zaręba, Kinga Roszak, Aleksandra Półrolniczak, Anna Z. Szeremeta, Błażej Dziuk, Filip Dybała, Sebastian Pawlus, Robert Kudrawiec, Adam Sieradzki, Mirosław Mączka, and Andrzej Katrusiak. Expanding the horizons of the thermodynamic landscape and optoelectronic properties of soft 2d hybrid perovskites mhy2pbx4. *J. Mater. Chem. A*, 12:16803–16814, 2024.

[158] Benjamin J. Foley, Daniel L. Marlowe, Keye Sun, Wissam A. Saidi, Louis Scudiero, Mool C. Gupta, and Joshua J. Choi. Temperature dependent energy levels of methylammonium lead iodide perovskite. *Applied Physics Letters*, 106(24):243904, 06 2015.

[159] Kai Xu, Luis Pérez-Fidalgo, Bethan L. Charles, Mark T. Weller, M. Isabel Alonso, and Alejandro R. Goñi. Using pressure to unravel the structure–dynamic-disorder relationship in metal halide perovskites. *Scientific Reports*, 13(1):9300, 2023.

[160] Qi Shi, Supriya Ghosh, Pushpendra Kumar, Laura C. Folkers, Suman Kalyan Pal, Tõnu Pullerits, and Khadga J. Karki. Variations in the composition of the phases lead to the differences in the optoelectronic properties of mapbbr3 thin films and crystals. *The Journal of Physical Chemistry C*, 122(38):21817–21823, 2018.

[161] Ye Cao, Guangyu Qi, Chuang Liu, Lingrui Wang, Zhiwei Ma, Kai Wang, Fei Du, Guanjun Xiao, and Bo Zou. Pressure-tailored band gap engineering and structure evolution of cubic cesium lead iodide perovskite nanocrystals. *The Journal of Physical Chemistry C*, 122(17):9332–9338, 2018.

[162] Albert Liu, Luiz G. Bonato, Francesco Sessa, Diogo B. Almeida, Erik Isele, Gabriel Nagamine, Luiz F. Zagonel, Ana F. Nogueira, Lazaro A. Padilha, and Steven T. Cundiff. Effect of dimensionality on the optical absorption properties of cspbi3 perovskite nanocrystals. *The Journal of Chemical Physics*, 151(19):191103, 11 2019.

[163] Christoph Wolf and Tae-Woo Lee. Exciton and lattice dynamics in low-temperature processable cspbbr3 thin-films. *Materials Today Energy*, 7:199–207, 2018.

[164] Ke Wei, Zhongjie Xu, Runze Chen, Xin Zheng, Xiangai Cheng, and Tian Jiang. Temperature-dependent excitonic photoluminescence excited by two-photon absorption in perovskite cspbbr3 quantum dots. *Opt. Lett.*, 41(16):3821–3824, Aug 2016.

[165] Dae Young Park, Yong Ho Shin, and Yongmin Kim. Electron–phonon-mediated temperature-dependent optical bandgap of mapbclxbr3−x single crystals. *The Journal of Physical Chemistry C*, 127(43):21235–21241, 2023.

[166] Shima Fasahat, Benedikt Schäfer, Kai Xu, Nadesh Fiuza-Maneiro, Sergio Gómez-Graña, M. Isabel Alonso, Lakshminarayana Polavarapu, and Alejandro R. Goñi. Absence of anomalous electron–phonon coupling in the near-ambient gap temperature renormalization of cspbbr3 nanocrystals. *The Journal of Physical Chemistry C*, 129(1):453–463, 2025.

[167] Zhiyuan Ma, Wei Wang, Mengmeng Jiao, Chuanlu Yang, Kai Wang, and Qinfeng Xu. Pressure-induced distinct conformational evolution of organic spacer cations in 2d perovskites. *Advanced Optical Materials*, 14(14):e02003, 2026.

[168] Xiaoyu Song, Xinsheng Liu, Danwen Zhang, Jingyan Liao, Siqi Zhu, and Wei Zheng. High-contrast thermochromism in room-temperature transparent layered perovskite pea2pbbr4 with a high temperature-induced bandgap change rate of 0.8 mev/k. *Journal of the American Chemical Society*, 146(35):24670–24680, 2024.

[169] Supriya Ghosh, Bapi Pradhan, Arkamita Bandyopadhyay, Irina Skvortsova, Yiyue Zhang, Christian Sternemann, Michael Paulus, Sara Bals, Johan Hofkens, Khadga J. Karki, and Arnulf Materny. Rashba-type band splitting effect in 2d (pea)2pbi4 perovskites and its impact on exciton–phonon coupling. *The Journal of Physical Chemistry Letters*, 15(31):7970–7978, 2024.

Appendix A

Publications and Conferences

Publications presented in this thesis:

1. **R. Bartoszewicz**, J. Ziembicki, E. Zdanowicz, A. P. Herman, J. Serafińczuk, J. Sánchez-Diaz, S. Das Adhikari, I. Mora-Seró, R. Kudrawiec
   "Giant Band Gap Narrowing under Hydrostatic Pressure in (4FP)$_2$SnI$_4$ Halide Perovskite"
   The Journal of Physical Chemistry Letters, vol. 16, no. 25, pp. 6372–6377 (2025).
   doi: 10.1021/acs.jpclett.5c00903

2. **R. Bartoszewicz**, A. P. Herman, M. Wietrzyńska, J. Serafińczuk, Ł. Przypis, R. Kudrawiec
   "Band Gap Tuning by Hydrostatic Pressure in (2-Thienyl)methylammonium Tin Iodide Halide Perovskite"
   ACS Materials Letters, vol. 8, no. 4, pp. 1201-1208 (2026).
   doi: 10.1021/acsmaterialslett.5c01670

3. **R. Bartoszewicz**, J.-A. Zienkiewicz, S. Hartati, A. Arramel, J. Kopaczek, M. D. Birowosuto, R. Kudrawiec
   "Thermochromism versus piezochromism in (PMA)$_2$CuX$_4$ (X = Br, Cl) halide perovskites"
   Journal of Materials Chemistry C., vol. 13, pp. 16929–16936 (2025).
   doi: 10.1039/D5TC02326B

4. **R. Bartoszewicz**, J. Ziembicki, E. Zdanowicz, A. P. Herman, J. Sánchez-Diaz, S. Das Adhikari, I. Mora-Seró, R. Kudrawiec
   "Hydrostatic Pressure Driven Band Gap Tuning and Self-Trapped Exciton Formation in (4FPEA)$_2$SnBr$_4$ Halide Perovskite"
   arXiv preprint, arXiv:2603.03931 (2026).
   doi: 10.48550/arXiv.2603.03931

Other published articles:

1. D. Majchrzak*†, M. Rybak*†, **R. Bartoszewicz**, J. Plutnar, U. Ahsan, M. Grodzicki, D. Hommel, M. Birowska, Z. Sofer, R. Kudrawiec
   "Experimental and theoretical band alignment study of MPS_3 *(M = Mn, Fe, Co, Ni) for designing tailored 2D heterostructures"*
   npj 2D Materials and Applications, vol. 9, no. 1, art. 53 (2025).
   doi: 10.1038/s41699-025-00578-w

2. M. Wełna†, J. Kopaczek, Ł. Przypis, **R. Bartoszewicz**, B. Wilk, A. P. Herman, R. Kudrawiec
   "Piezoreflectance: A sensitive method for studying optical and phase transitions in metal halide films"
   APL Materials, vol. 13, no. 7, art. 071126 (2025).
   doi: 10.1063/5.0273480

3. J. Ziembicki*†, **R. Bartoszewicz**, M. Grodzicki, P. Scharoch, R. Kudrawiec†, W. Olszewski*, D. Pucicki, D. Hommel, M. P. Polak
   "Electronic band structure of GaN diluted and overdiluted with group-V elements"
   Physical Review Applied, vol. 23, art. 024005 (2025).
   doi: 10.1103/PhysRevApplied.23.024005

4. M. Serra*†, N. Antonatos, L. Lajaunie, J. Albero, H. Garcia, M. Weng, L. Bastonero, K. J. Sarkar, R. Gusmão, J. Luxa, **R. Bartoszewicz**, J. Ziembicki, I. Plutnarová, N. Marzari, R. Kudrawiec, Z. Sofer*
   "A photodetector based on the non-centrosymmetric 2D pseudo-binary chalcogenide $MnIn_2Se_4$*"*
   Journal of Materials Chemistry C, vol. 13, pp. 5356–5369 (2025).
   doi: 10.1039/D4TC04380D

5. J. Kopaczek, **R. Bartoszewicz**, K. Ciesiołkiewicz, A. P. Herman, V. Mazánek, I. Plutnarova, Z. Sofer, R. Kudrawiec
   "Strain Modulation in van der Waals Crystals Directly Exfoliated onto Piezoceramics—Application in Micropiezoreflectance Spectroscopy"
   ACS Applied Electronic Materials, vol. 6, no. 11, pp. 7857–7864 (2024).
   doi: 10.1021/acsaelm.4c01227

Scientific Conferences:

1. 8th International Conference on Perovskite Solar Cells and Optoelectronics, Perugia, Italy, 15–18 September 2025.
   "Giant Band Gap Narrowing under Hydrostatic Pressure in $(4FP)_2SnI_4$ *Halide Perovskite"*
   "Thermochromism versus piezochromism in $(PMA)_2CuX_4$ *(X = Br, Cl) halide perovskites"*

---

* equal contribution; † corresponding author